EFFECT OF CHARGE PREPARATION STRATEGY ON HCCI COMBUSTION

by

Janardhan Kodavasal

A dissertation submitted in partial fulfillment
of the requirements for the degree of
Doctor of Philosophy
(Mechanical Engineering)
in The University of Michigan
2013

Doctoral Committee:

Professor Dionissios N. Assanis, Stony Brook University, Co-Chair
Professor Hong G. Im, Co-Chair
Assistant Professor Aristotelis Babajimopoulos, Stony Brook University
Associate Professor Claus Borgnakke
Professor James F. Driscoll
Research Scientist George A. Lavoie
Assistant Research Scientist Jason B. Martz

To my Parents
Ananth and Rama

ACKNOWLEDGMENTS

I would like to start off by thanking Professor Dennis Assanis for having faith in me and giving me the opportunity to do research in his group when I first met him in December 2007. It is because of his constant encouragement and support through the years that I have been able to reach this stage today. I have learned a great deal from Professor Assanis, who has an innate ability to inspire students.

I would like to acknowledge Professor Hong Im for accepting my invitation to serve as a co-chair on my committee, and for the many valuable discussions over the years. Further, I would like to express my gratitude towards Professors Jim Driscoll and Claus Borgnakke for devoting their time to serve on my Ph.D. committee.

Over the past five years working at the Walter E. Lay Automotive Lab, I have come across many kind and intelligent people who have guided me in my research and have always been selfless with their help, friendship and advice.

One among them is Dr. Aris Babajimopoulos who started off by spending many hours patiently guiding me step by step through the KIVA-3V code back in Winter 2008. Since then, he has always been available to advise me on several issues and invariably seems to have a solution to any problem. I have indeed learned a great deal from Aris about HCCI in particular and performing independent research in general. For this I will always be indebted to him.

Dr. Jason Martz is another person whom I would like to sincerely thank for providing me valuable guidance and encouragement in the latter part of my Ph.D. research. In-spite of having multiple responsibilities, he has always been extremely

approachable and collaborative. His high standards, critical input and genuine interest have definitely helped in ensuring the quality and relevance of this work.

I would like to thank Dr. George Lavoie for serving on my committee, and also for his insightful questions and suggestions. I am also grateful to Dr. SeungHwan Keum and Dr. Stani Bohac for their interest in my work and their encouragement.

During the Fall 2011 term, I had the good fortune of interning at Lawrence Livermore National Laboratory (LLNL) with Dr. Dan Flowers. The excellent combustion group at LLNL - Dan, Matt, Salvador, Nick, Joel, Russell, Jonas, Francisco and Guillaume made work really fun. My 4-month internship at LLNL and stay in Livermore represent one of the most productive and memorable periods of my Ph.D.

I thank Robert Bosch LLC for providing the major portion of the funding for this work. I am grateful to Alan Mond, Dr. Li Jiang, Jeff Sterniak, Oliver Miersch-Wiemers and Hakan Yilmaz of Bosch Advanced System Engineering at Farmington Hills for their support over the past three years. I was fortunate to work more closely with this team as part of two internships I undertook at Bosch towards the end of my Ph.D. Their collegiality and genuine interest in my academic and career objectives means a lot to me. I would also like to express my gratitude towards Dr. Sergei Chumakov, Dr. Dave Cook and Dr. Aleksandar Kojic of Bosch Corporate Research for granting me access to their computing cluster. The simulations performed on this cluster form a critical component of this research. I acknowledge Laura Olesky for providing experimental data for CFD model set up and evaluation, and thank Rob Middleton for his collaboration on CFD code development. I am grateful to my friends from the Autolab, particularly Prasad, Sotiris, Stefan and Mehdi, who have always kept my spirits high through the ups and downs of grad school with their friendship, humor and support.

Finally, I would like to thank my parents, Ananth and Rama, and sister Puja, for always being there for me and believing in me.

TABLE OF CONTENTS

DEDICATION ..... **ii**
ACKNOWLEDGMENTS ..... **iii**
LIST OF FIGURES ..... **x**
LIST OF TABLES ..... **xx**
ABSTRACT ..... **xxi**
CHAPTER 1 INTRODUCTION **1**

1.1 Homogeneous Charge Compression Ignition 2
1.2 Benefits and Challenges associated with HCCI 3
1.3 Strategies to achieve HCCI 5
1.3.1 Exhaust gas recompression using Negative Valve Overlap 6
1.3.2 Direct Injection 7
1.3.3 Boosting 8
1.3.4 Spark Assisted Compression Ignition (SACI) 9
1.4 Competing charge preparation strategies for HCCI 9
1.4.1 Effect of diluent composition 10
1.4.2 NVO versus PVO 11
1.4.3 Premixed fueling versus DI 12
1.5 Objective and Document Organization 13
1.6 References 18
CHAPTER 2 TOOLS USED/DEVELOPED AND RESEARCH METHOD **23**

2.1 Overview of CFD software used 24
2.2 Chemical kinetic modeling 27

2.3 The fully-coupled CFD/ kinetics approach 28
2.4 Fully coupled CFD/kinetics model performance evaluation 32
2.4.1 HCCI Engine Configuration 32
2.4.2 CFD model setup 33
2.4.3 Performance evaluation 34
2.5 Quasi-dimensional multi-zone model development 38
2.5.1 Model setup 38
2.5.2 Numerical solution of system states 39
2.6 Sequential multi-zone approach 44
2.6.1 Modeling approach 44
2.6.2 Effect of turbulent diffusion and heat loss during combustion 45
2.6.3 Performance evaluation of sequential MZ against fully coupled CFD/kinetics 50
2.7 Reaction space analysis method 52
2.8 References 77
CHAPTER 3 EFFECT OF DILUENT COMPOSITION 80
3.1 Background 80
3.2 Conditions for current CFD study 83
3.3 Differences in pressure traces and burn profiles 84
3.4 Analysis of pre-ignition reaction space at 10°bTDC 84
3.5 Decoupling thermodynamic effects from chemical kinetic effects 86
3.6 Analysis of NOx emissions 88
3.7 Summary 90
3.8 References 101
CHAPTER 4 IMPACT OF STRATIFICATION FROM NVO 102
4.1 Conditions for study 103

4.2 In-cylinder pressure traces and burn profiles 104
4.3 Analysis of the pre-ignition reaction space (at 10° CA bTDC) 104
4.4 Decoupling thermal and compositional stratification 106
4.5 Analysis of NOx emissions 108
4.6 Summary 109
4.8 References 117
CHAPTER 5 EFFECT OF FUELING STRATEGY 119
5.1 Direct injection under NVO conditions 119
5.1.1 In-cylinder pressure traces and burn profiles 120
5.1.2 Analysis of the pre-ignition reaction space at 10° CA bTDC 120
5.1.3 Effect of ϕ_{FO} distribution from injecting into residuals 122
5.1.4 Comparison of thermal and reactivity stratification 123
5.1.5 Comparison of NOx emissions 125
5.2 Reaction space effects of early DI versus PFI for PVO operation 127
5.2.1 Conditions for study 127
5.2.2 In-cylinder pressure and burn profiles 127
5.2.3 Comparison of pre-ignition reaction space at 10° CA bTDC 128
5.2.4 Comparison of NOx emissions 130
5.3 Comparison of DI effects under PVO and NVO conditions 130
5.4 Summary 133
5.5 References 157
CHAPTER 6 ACCELERATED MULTI-ZONE COMBUSTION MODEL FOR HCCI 158
6.1 Guidelines for a simplified HCCI combustion model 158
6.2 Multi-zone Combustion Modeling for HCCI 159
6.2.1 Balloon-type multi-zone models 160
6.2.2 Onion-skin models 161

6.2.3 Probability Density Function based models 162
6.3 Motivation for a rapid thermal stratification methodology 163
6.4 AMECS combustion model 164
6.4.1 Model setup 164
6.4.2 Block preconditioning for accelerated calculations 165
6.4.3 Calculation of system states 167
6.5 Thermal Stratification 168
6.5.1 Background 168
6.5.2 The Adiabatic Core Concept 169
6.5.3 Thermal Stratification Methodology 170
6.6 Model performance evaluation with respect to CFD 174
6.6.1 Thermal Stratification Prediction 175
6.6.2 Prediction of combustion characteristics 176
6.6.3 Computational cost savings compared to CFD 178
6.7 Model performance evaluation with respect to experiments 178
6.7.1 Comparison with boosted gasoline HCCI experiments 179
6.7.2 Effect of zonal resolution 181
6.8 GT-Power Implementation 182
6.9 Additional applications of thermal stratification methodology 183
6.10 Summary 183
6.11 References 204
CHAPTER 7 CONTRIBUTIONS AND RECOMMENDATIONS 210
7.1 Main findings and insights from this doctoral work 210
7.1.1 Relative importance of thermal and compositional stratification 210
7.1.2 Effect of diluent composition on HCCI combustion 211
7.1.3 Stratification from NVO and effects on burn duration 212

7.1.4 Impact of fueling strategy 213
7.2 Development of a sequential CFD-MZ approach as a diagnostic 214
7.3 Thermal stratification methodology for simple combustion models 215
7.4 Standalone balloon multi-zone HCCI combustion model 216
7.5 Recommendations for future work 216
7.6 References 219

LIST OF FIGURES

Figure 1.1 – Sample positive valve overlap (PVO) and negative valve overlap (NVO) valve lift profiles shown with reference to in-cylinder pressure trace 17

Figure 2.1 – CFD mesh of FFVA engine used in simulations 60

Figure 2.2 – Pressure traces from combustion phasing sweep; experiments versus CFD: 9.4 mg/cycle injected, fixed NVO (157°), T_{in} = 106°C (top), 86°C (middle), 64°C (bottom), RGF (experiment) = 48%, RGF (CFD) = 43%, Φ (experiment) = 0.6, Φ (CFD) = 0.55, Φ'(experiment) = 0.3, Φ'(CFD) = 0.3 61

Figure 2.3 – Pressure traces from combustion phasing sweep; experiments versus CFD: 9.4 mg/cycle injected, fixed NVO (157°), T_{in} = 106°C (top), 86°C (middle), 64°C (bottom), RGF (experiment) = 48%, RGF (CFD) = 43%, Φ (experiment) = 0.6, Φ (CFD) = 0.55, Φ'(experiment) = 0.3, Φ'(CFD) = 0.3. Experimental cycle with closest peak pressure to CFD predictions shown. 62

Figure 2.4 – Comparison of burn profiles for high and low NVO cases – experiments and CFD results, experiment: high NVO = 179°, low NVO = 157°; CFD: high NVO = 181°, low NVO = 157° 63

Figure 2.5 – Illustration of balloon MZ setup 64

Figure 2.6 – Illustration of sequential MZ setup 65

Figure 2.7 – Mass percentage burned profiles for PVO-air dilution, PVO-eEGR dilution and NVO-iEGR dilution; predictions from CFD with turbulent diffusion effects considered and non-adiabatic walls during combustion 66

Figure 2.8 – Mass percentage burned profiles for PVO-air dilution, PVO-eEGR dilution and NVO-iEGR dilution; predictions from CFD with turbulent diffusion effects

neglected along with the assumption of adiabatic walls during combustion (after 718° CA) 66

Figure 2.9 – Mass percentage burned profiles for PVO-air dilution, PVO-eEGR dilution and NVO-iEGR dilution; predictions from CFD with turbulent heat diffusion effects neglected during combustion (post 718° CA) while turbulent mass diffusion considered along with non-adiabatic walls (It must be noted that turning off turbulent heat diffusion in effect turns off wall heat losses too in KIVA-3V, since wall heat loss fluxes are based on the turbulent Prandtl number)..... 67

Figure 2.10 – Mass percentage burned profiles for PVO-air dilution, PVO-eEGR dilution and NVO-iEGR dilution; predictions from CFD with turbulent mass diffusion effects neglected during combustion (post 718° CA) while turbulent heat diffusion is allowed throughout along with non-adiabatic walls throughout..... 68

Figure 2.11 – Mass percentage burned profiles for PVO-air dilution, PVO-eEGR dilution and NVO-iEGR dilution; predictions from CFD with adiabatic walls during combustion (post 718° CA) while turbulent heat and mass diffusion are allowed throughout the simulation 68

Figure 2.12 – Effect of turbulent heat diffusion on sequential autoignition: Mass percentage burned profiles for PVO-air dilution, PVO-eEGR dilution and NVO-iEGR dilution; predictions from CFD based on variation (a) – adiabatic walls during combustion (post 718° CA) with turbulent heat and mass diffusion included and variation (b) – adiabatic walls and no turbulent heat diffusion during combustion (post 718°CA), with turbulent mass diffusion allowed throughout..... 69

Figure 2.13 – Effect of turbulent mass diffusion on sequential autoignition: Mass percentage burned profiles for PVO-air dilution, PVO-eEGR dilution and NVO-iEGR dilution; predictions from CFD based on variation (a) – adiabatic walls during combustion (post 718° CA) with turbulent heat and mass diffusion included and

variation (c) – adiabatic walls and no turbulent mass diffusion during combustion (post 718°CA), with turbulent heat diffusion allowed throughout 70
Figure 2.14 – Ignition delay computations for CFD (in every cell) versus computation in every zone based on binning resolution used 71
Figure 2.15 – In-cylinder pressure traces for PVO-air dilution, PVO-eEGR dilution and NVO-iEGR dilution; predictions from CFD (top) and sequential multi-zone (bottom)..... 72
Figure 2.16 – Mass percentage burned profiles for PVO-air dilution, PVO-eEGR dilution and NVO-iEGR dilution; predictions from CFD (top) and sequential multi-zone (bottom)..... 73
Figure 2.17 – Comparison of ignition delay predictions based on the He et al. [16] correlation against ignition delay predictions (where ignition is considered at 10% mass fraction burned) from adiabatic, constant volume reactor simulations using the 312-species gasoline kinetics [5] under pre-ignition conditions (at 10° CA bTDC) corresponding to CFD simulations 74
Figure 2.18 – Pre-ignition reaction space (at 10° CA bTDC), visualized in T and ϕ_{FO}space for a case with 157° NVO, direct injection with SOI at 330° CA bTDC, and CA10 at approximately 2° CA bTDC; computed from CFD simulation..... 75
Figure 2.19 – Pre-ignition reaction space (at 10° CA bTDC) visualized in terms of cumulative charge mass below a certain ignition delay, for a case with 157° NVO, direct injection with SOI at 330° CA bTDC, and CA10 at approximately 2° CA bTDC; computed from CFD simulation 76
Figure 3.1 – In-cylinder pressure traces from full CFD simulation for air dilution and eEGR dilution cases..... 92
Figure 3.2 – Mass percentage burned profiles from full CFD simulation for air dilution and eEGR dilution cases 92

Figure 3.3 – Pre-ignition reaction space (10° CA bTDC) for air dilution case (top) and eEGR dilution case (bottom) from CFD simulations 93
Figure 3.4 – Pre-ignition (10° CA bTDC) temperature distribution from CFD simulation for air dilution and eEGR dilution cases 94
Figure 3.5 – Pre-ignition (10° CA bTDC) ignition delay scatter from CFD simulation for air dilution and eEGR dilution cases 94
Figure 3.6 – Pre-ignition (10° CA bTDC) reactivity distribution from CFD simulation for air dilution and eEGR dilution cases 95
Figure 3.7 – Pre-ignition (10° CA bTDC) distribution of γ from CFD simulation for air dilution and eEGR dilution cases 95
Figure 3.8 – Application of sequential MZ to decouple thermodynamic effects; air dilution, eEGR dilution and N_2 dilution shown 96
Figure 3.9 – Variation of γ with the progress of combustion 96
Figure 3.10 – Variation of C_p with the progress of combustion 97
Figure 3.11 – Post-combustion (6° CA aTDC) distribution in ϕ_{atomic} and T colored by NO from CFD simulation for air dilution and eEGR dilution cases 98
Figure 3.12 – Post-combustion (6° CA aTDC) distribution in χ_{O2} and T colored by NO from CFD simulation for air dilution and eEGR dilution cases 99
Figure 3.13 – Post-combustion (6° CA aTDC) distribution in ϕ_{atomic} and T colored by NO, showing mass fraction contained in ϕ_{atomic} -T bins from CFD simulation of eEGR dilution case 100
Figure 4.1 – In-cylinder pressure traces from CFD simulation of PVO-eEGR-PFI case and NVO-iEGR-PFI case 111
Figure 4.2 –Burn profiles from CFD simulation of PVO-eEGR-PFI case and NVO-iEGR-PFI case 111
Figure 4.3 – Pre-ignition (10° CA bTDC) reaction space from CFD simulation visualized in terms of reaction space variables ϕ_{FO}, χ_{O2} and T 112

Figure 4.4 – Pre-ignition (10° CA bTDC) cumulative distribution in temperature from CFD simulation 113
Figure 4.5 – Pre-ignition (10° CA bTDC) ignition delay scatter from CFD simulation 113
Figure 4.6 – Pre-ignition (10° CA bTDC) reactivity distribution in cumulative terms from CFD simulation 114
Figure 4.7 – Pre-ignition (10° CA bTDC) reactivity distribution in cumulative terms from CFD simulation of PVO-eEGR-PFI, NVO-iEGR-PFI and NVO-iEGR-PFI with mean composition assumed in all cells 114
Figure 4.8 – Sequential MZ used to decouple thermal stratification from compositional stratification; burn profiles obtained from the sequential MZ for PVO-eEGR-PFI, NVO-iEGR-PFI and NVO-iEGR-PFI with mean composition shown 115
Figure 4.9 – Pre-ignition (10° CA bTDC) scatter in γ from CFD simulation 115
Figure 4.10 – Post-combustion (6°CA aTDC) reaction space from CFD simulation showing distribution of NO formation 116
Figure 5.1 – In-cylinder pressure traces from CFD simulation of NVO-iEGR-PFI and NVO-iEGR-DI cases 136
Figure 5.2 – Burn profiles from CFD simulation of NVO-iEGR-PFI and NVO-iEGR-DI cases 136
Figure 5.3 – Pre-ignition (10° CA bTDC) visualized in T and χ_{O2} dimensions from CFD simulation of NVO-iEGR-PFI and NVO-iEGR-DI cases 137
Figure 5.4 – Pre-ignition (10° CA bTDC) visualized in T and ϕ_{FO} dimensions from CFD simulation of NVO-iEGR-PFI and NVO-iEGR-DI cases 138
Figure 5.5 – Decoupling ϕ_{FO} stratification from T stratification for NVO-iEGR-DI case. Pre-ignition (10° CA bTDC) reactivity distribution (in terms of ignition delay) from CFD simulation of NVO-iEGR-DI shown with and without considering ϕFO stratification 139

Figure 5.6 – Pre-ignition (10° CA bTDC) distribution of ϕ_{FO} over ignition delay for NVO-iEGR-PFI and NVO-iEGR-DI 139
Figure 5.7 – Pre-ignition (10° CA bTDC) temperature distribution in cumulative terms from CFD simulation of NVO-iEGR-PFI and NVO-iEGR-DI cases 140
Figure 5.8 – Pre-ignition (10° CA bTDC) ignition delay scatter from CFD simulation of NVO-iEGR-PFI and NVO-iEGR-DI cases 140
Figure 5.9 – Pre-ignition (10° CA bTDC) reactivity distribution (in terms of ignition delay) from CFD simulation of NVO-iEGR-PFI and NVO-iEGR-DI cases 141
Figure 5.10 – In-cylinder temperature traces from CFD simulation of NVO-iEGR-PFI and NVO-iEGR-DI cases 141
Figure 5.11 – NO formation with respect to crank angle (in terms of $EINO_X$) from CFD simulation of NVO-iEGR-PFI and NVO-iEGR-DI cases 142
Figure 5.12 – Post-combustion (6° CA aTDC) reaction space from CFD simulation of NVO-iEGR-PFI and NVO-iEGR-DI cases showing NO distribution 143
Figure 5.13 – In-cylinder pressure traces from CFD simulation of PVO-eEGR-PFI and PVO-eEGR-DI cases 144
Figure 5.14 – Burn profiles from CFD simulation of PVO-eEGR-PFI and PVO-eEGR-DI cases 144
Figure 5.15 – Pre-ignition (10° CA bTDC) reaction space visualized in terms of *T* and χ_{O2} 145
Figure 5.16 – Pre-ignition (10° CA bTDC) reaction space visualized in terms of *T* and ϕ_{FO} 146
Figure 5.17 – Cumulative distribution of reactivity in terms of ignition delay for PVO-PFI and PVO-DI cases 147
Figure 5.18 – Average temperature distribution over ignition delay for PVO-PFI and PVO-DI cases 147

Figure 5.19 – Cumulative distribution in temperature for PVO-PFI and PVO-DI cases 148
Figure 5.20 – Average ϕ_{FO} over ignition delay for PVO-PFI and PVO-DI cases 148
Figure 5.21 – Cumulative distribution of reactivity in terms of ignition delay for PVO-DI and PVO-DI with mean ϕ_{FO} 149
Figure 5.22 – In-cylinder temperature trace for PVO-PFI and PVO-DI cases 149
Figure 5.23 – Evolution of NOx with respect to crank angle for PVO-PFI and PVO-DI cases 150
Figure 5.24 – Post-combustion (6° CA aTDC) reaction space from CFD simulation of PVO-eEGR-PFI and PVO-eEGR-DI cases showing NO distribution 151
Figure 5.25 – In-cylinder pressure traces from CFD simulation of PVO-eEGR-DI and NVO-iEGR-DI cases 152
Figure 5.26 – Burn profiles from CFD simulation of PVO-eEGR-PFI and NVO-iEGR-DI cases 152
Figure 5.27 – Pre- ignition (10° CA bTDC) reactivity distribution (in terms of ignition delay) from CFD simulation of PVO-eEGR-DI and NVO-iEGR-DI cases 153
Figure 5.28 – Pre-ignition (10° CA bTDC) reaction space visualized in terms of *T* and ϕ_{FO} from CFD simulations of the PVO-eEGR-DI and NVO-iEGR-DI cases 154
Figure 5.29 – Evolution of turbulent kinetic energy (TKE) for PVO-DI compared to NVO-DI showing injection event and intake events 155
Figure 5.30 – Post- combustion (6° CA aTDC) reaction space from CFD simulation of PVO-eEGR-DI and NVO-iEGR-DI cases showing NO distribution 156
Figure 6.1 – Conceptual picture of the AMECS combustion model 188
Figure 6.2 – Prescribed zone mass fractions for binning CFD results sequentially from highest temperature (lower zone number) to lowest temperature (higher zone number) 189

Figure 6.3 – CFD results at TDC from the baseline condition (1200 RPM, 100 kPa P_{in}) binned into 40 temperature zones based on a specified mass fraction distribution (Figure 6.2). As an example, zone 35 is highlighted to illustrate the procedure for obtaining the heat loss multipliers used by AMECS. 190

Figure 6.4 – 2D CFD mesh of the Sandia engine used in simulations, shown at TDC.. 191

Figure 6.5 – University of Michigan FFVA engine CFD mesh. 192

Figure 6.6 – Sandia engine (CR = 13.83): comparison of thermal stratification – motoring CFD results binned into 40 predefined zones compared with temperature distribution prediction from AMECS using the thermal stratification methodology at -20° CA aTDC, -10° CA aTDC and 0° CA aTDC for three cases: Case (a) 1200 RPM, 100 kPa P_{in} (baseline); Case (b) 2000 RPM, 100 kPa P_{in} and Case (c) 1200 RPM, 240 kPa $P_{in.}$..... 193

Figure 6.7 – UM-FFVA engine (CR = 12.22): comparison of thermal stratification – motoring CFD results binned into 40 predefined zones compared with temperature distribution prediction from AMECS using the thermal stratification methodology at -20° CA aTDC, -10° CA aTDC and 0° CA aTDC for three cases: Case (a) 2000 RPM, 100 kPa P_{in} (baseline); Case (b) 3000 RPM, 100 kPa P_{in} and Case (c) 2000 RPM, 200 kPa $P_{in.}$ 194

Figure 6.8 – Comparison of AMECS (40 zones) predictions with CFD (fully-coupled CFD/kinetics) results; $\Phi = 0.3$ (PRF 90 and 33-species Tsurushima mechanism [43] used) for the Sandia engine..... 195

Figure 6.9 – Comparison of AMECS (40 zones) predictions with CFD (fully-coupled CFD/kinetics) results; $\Phi = 0.3$ (PRF 90 and 33-species Tsurushima mechanism [43] used) for the UM-FFVA engine..... 196

Figure 6.10 – Comparison of AMECS (40 zones) predictions (using the 252-species gasoline mechanism [2]) and surrogate formulation given in Table 6.4 with Sandia boosted gasoline HCCI experiments by Dec and Yang [39]. The dashed box

indicates a “bump” in the pressure trace during the main heat release (highlighted here for the 10 kPa P_{in} case), which is possibly an artifact of the gasoline mechanism used. 197

Figure 6.11 – Heat release rates (HRRs) – comparison of AMECS (40 zones using the 252-species gasoline mechanism [2]) predictions with Sandia experiments of Dec and Yang [39]. The dashed box in the AMECS results indicates a “bump” in the HRR predictions from AMECS during the main heat release (highlighted here for the 100 kPa P_{in} case), which is possibly an artifact of the gasoline mechanism used. 198

Figure 6.12 – Pressure traces from single-zone adiabatic simulations, with intake pressure of 240 kPa P_{in} and composition as in Sandia experiments, using the 1389-species LLNL detailed gasoline mechanism [44] and the 252-species reduced gasoline mechanism [2]/ The dashed box indicates the “bump” in the pressure trace during the main heat release for both mechanisms. 199

Figure 6.13 – Normalized HRR – comparison of AMECS (40 zones using the 252-species gasoline mechanism [2]) predictions with Sandia experiments of Dec and Yang [39]. Curves are shifted to align peak heat release rate with TDC. The dashed boxes indicate the ITHR (prior to the main heat release) observed by Dec and Yang [39] (top) and that predicted by AMECS (bottom) for boosted conditions. 200

Figure 6.14 – CO and HC emissions (top) and peak charge temperature and NO emissions (bottom) – comparison of AMECS (40 zones using the 252-species gasoline mechanism [2]) predictions with Sandia experiments of Dec and Yang [39]. 201

Figure 6.15 – In-cylinder pressure predictions by AMECS using the 252-species gasoline mechanism [2] based on the Sandia data [39] with different zone resolutions. 202

Figure 6.16 –HRR predictions by AMECS using the 252-species gasoline mechanism [2] based on the Sandia data [39] with different zone resolutions. 203

LIST OF TABLES

Table 2.1 – Gasoline surrogate composition taken from Mehl et al. [5] 57

Table 2.2 – UM-FFVA engine specifications used in CFD simulations 57

Table 2.3 – Component temperatures used in CFD simulation 58

Table 2.4 – Peak pressure rise rates –CFD versus experimental cycle (with closest peak pressure to CFD), for combustion phasing sweep with fixed NVO of 157° 58

Table 2.5 – Operating conditions for test cases based on three different charge preparation strategies 59

Table 2.6 – Burn duration predictions from CFD and sequential MZ for the three test cases (charge preparation strategies) studied 59

Table 3.1 – Operating conditions: Air versus eEGR dilution 91

Table 4.1 – Operating conditions: eEGR (PVO) versus iEGR (NVO) dilution 110

Table 5.1 – Operating conditions: NVO-PFI versus NVO-DI 134

Table 5.2 – Operating conditions: PVO-PFI versus PVO-DI 134

Table 5.3 – Operating conditions: PVO-DI versus NVO-DI 135

Table 6.1 – Sandia engine specifications used in CFD simulations 185

Table 6.2 – UM-FFVA engine specifications used in CFD simulations 185

Table 6.3 – Computation times (CFD vs. AMECS) using the 33 species Tsurushima PRF mechanism [43] 186

Table 6.4 – Gasoline surrogate composition taken from Mehl et al. [2] 186

Table 6.5 – Computation times for different AMECS zone resolutions (Gasoline 252 species mechanism [2], Sandia engine, 100 kPa P_{in}) 187

ABSTRACT

A critical factor determining Homogeneous Charge Compression Ignition (HCCI) combustion characteristics and emissions is preparation of the fuel-diluent charge prior to ignition. The choice of charge preparation strategy impacts diluent composition and stratification. Presently, there is a gap in fundamental understanding as to the impact of these strategies on charge distribution within the reaction space and consequent effects on HCCI combustion.

In this doctoral work, fully-coupled CFD/chemical kinetics simulations are performed for various competing charge preparation strategies at a typical HCCI operating point to study the differences in burn duration and emissions arising from these strategies. The strategies studied are: air versus external EGR dilution, Negative Valve Overlap (NVO) versus Positive Valve Overlap (PVO) operation, and premixed fueling versus direct injection. The CFD reaction space is analyzed to determine the reactivity stratification prior to ignition arising from each of these strategies. A sequential CFD-multi-zone model is developed as a diagnostic tool wherein CFD simulation is performed over the gas exchange period until a transition point before TDC, after which the CFD reaction space is mapped onto a multi-zone chemical kinetic model. This tool is used to decouple various concurrent effects. For example, by selectively choosing to map thermal stratification from the CFD domain onto the multi-zone model while ignoring compositional stratification, the relative contributions of thermal and compositional stratification arising from NVO operation are isolated.

Based on these insights from CFD, a standalone quasi-dimensional HCCI combustion model incorporating kinetics is built, featuring a computationally efficient methodology (developed as part of this work) to capture wall heat loss driven thermal stratification, as an alternative to expensive CFD simulation. It is shown that predictions from this model correspond well with results from detailed CFD/kinetics simulations over a range of operating conditions, for different engine geometries, while being up to two-orders of magnitude faster than CFD, making this model ideal for use in system-level codes.

CHAPTER 1

INTRODUCTION

The non-renewable nature of our primary energy reserves such as coal, oil and natural gas, coupled with growing environmental concerns such as global climate change, requires a paradigm shift in our approach to the use of energy resources. The automotive sector is a major consumer of these energy reserves (oil in particular), and also a major contributor to global warming in terms of CO_2 generation. Rising fuel prices, increasing consumer awareness and environmental legislation have spurred research into improving energy-efficiency as well as reducing the environmental impact from the automobile.

One direction is developing new technologies such as electrification of the powertrain, expanding the use of renewable fuels, development of fuel-cell technology, using hydrogen as an energy carrier and so forth. Another direction is improving efficiency associated with currently available systems such as gasoline and diesel internal combustion engines by employing advanced combustion coupled with sophisticated controls and after-treatment. The advantage of improving on currently available technologies is that this approach does not require significant changes to hardware (which is extremely attractive from an Original Equipment Manufacturer, OEM standpoint) and minimizes inconvenience to consumers by allowing them to continue with their traditional use patterns such as refueling at gas-stations, enjoying long driving ranges and so on.

Improving on current technology (internal combustion) while concurrently developing new technologies (gasoline-/diesel-electric hybrids, fuel-cells, electric powertrains, hydrogen etc.) will ensure a smooth transition to long-term mobility solutions that are cheap, environmentally friendly and accessible to a large number of people.

1.1 Homogeneous Charge Compression Ignition

Homogeneous Charge Compression Ignition (HCCI) is an advanced combustion mode which aims achieve to diesel-like efficiency while minimizing NOx and soot emissions. HCCI has been demonstrated on existing hardware with minimal changes. The first description of HCCI was given by Onishi et al. [1] who reported running a two-stroke gasoline engine wherein the charge (fuel and air) was ignited purely by compression without the use of a spark. They termed this Active Thermo-Atmospheric Combustion (ATAC). Around the same time, Noguchi et al. [2] demonstrated HCCI on a two-stroke opposed piston engine.

In 1983, Najt and Foster [3] were the first to demonstrate HCCI on a four-stroke Cooperative Fuels Research (CFR) engine, and reported gains in efficiency and reduction in emissions. They also postulated that HCCI combustion is primarily controlled by chemical kinetics, and is not influenced by turbulence and mixing. They proposed a simple model to predict ignition (based on the Shell ignition model by Halstead et al. [4]) coupled with an expression for average energy release rate. The term HCCI itself is attributed to Thring [5], who in 1989 reported operating a four-stroke gasoline fueled HCCI engine with Exhaust Gas Recirculation (EGR) over a range of loads. Heating of intake air was used as a means to facilitate autoignition of the charge.

To achieve HCCI operation, a near-homogenous fuel-air mixture is prepared and ignited purely by piston compression. Hultqvist et al. [6, 7, 8] used Planar Laser Induced

Fluorescence (PLIF) along with chemiluminescence imaging to gain insights into the HCCI combustion process. Their results indicate that HCCI combustion occurs without the presence of a flame front and is characterized by multiple autoignition sites within the cylinder determined by local thermo-chemical conditions.

There is now a general consensus within the engine community that HCCI combustion is primarily driven by chemical kinetic rates and not diffusion of unburned gas mixture into a flame front. This results in near constant-volume combustion and is accompanied by high energy release rates compared to Spark Ignited (SI) gasoline and conventional diesel combustion modes.

1.2 Benefits and Challenges associated with HCCI

HCCI offers a potential fuel-economy benefit of 15-20% [9] over conventional gasoline SI operation with diesel-like thermal efficiencies due to the following factors:

1. Absence of a flame allows HCCI to operate lean of stoichiometric, thus eliminating the need for throttling incoming air at lower loads. This leads to reduced pumping losses compared to SI.
2. The near constant-volume combustion with HCCI results in thermodynamic benefits due to higher peak pressures compared to SI, which results in higher work out during expansion.
3. Lean operation also results in the charge (fuel-air mixture) having a higher ratio of specific heats (γ) which translates to higher thermal efficiencies.
4. HCCI typically operates with high levels of dilution either with air or with products of combustion. The diluents act as a thermal sink and bring down combustion temperatures (<2000 K), which results in lower heat transfer losses near Top Dead Center (TDC).

Operating lean of stoichiometric could pose problems with Nitrogen Oxides (NOx) after-treatment, which is typically done by employing a Three Way Catalyst (TWC) for gasoline SI engines. The TWC requires stoichiometric operation for effective NOx removal. Fortunately, as a consequence of low combustion temperatures associated with HCCI, engine-out NOx emissions are *typically* comparable to tail-pipe out NOx emissions for gasoline SI with a TWC (generally < 20 parts per million, ppm). This allows bypass of the TWC altogether under HCCI mode, while still meeting emission regulations. However, under certain HCCI operating conditions such as higher loads and lower dilution levels, NOx emissions could pose a serious concern. The main benefit of HCCI over conventional diesel combustion is much lower soot emissions, due to homogeneous operation and absence of fuel-rich regions within the charge.

In spite of these benefits, there are some critical challenges associated with the practical realization of HCCI and implementation into mass-production vehicles.

1. It is difficult to control HCCI ignition as there is no spark (as in gasoline SI) or fuel injection near TDC (as in diesel) to initiate combustion. Ignition is purely driven by chemical kinetics which depend on the composition of the charge and its pressure-temperature history through compression. In essence, unlike conventional SI or diesel combustion, HCCI ignition is primarily determined by conditions at Intake Valve Close (IVC) and is very sensitive to these conditions as well as to external factors such as heat losses, which makes controlling ignition very difficult.
2. HCCI is also handicapped by a limited operating range in terms of speed and load. At lower loads, the high levels of dilution make it difficult to ignite the charge and the lower combustion temperatures (<1300 K) at these low loads has also been shown to drastically drop combustion efficiencies to the point of partial burn or misfire. At higher loads, it is difficult to achieve sufficient dilution to slow down energy release rates; this can lead to unacceptable combustion noise,

impacting the integrity of engine components as well as drivability. Due to residence time effects on chemical kinetics, at lower speeds it is difficult to control premature autoignition of the charge, and at higher speeds, HCCI tends to misfire, thus limiting the range of speeds over which HCCI may be achieved.

3. The low combustion temperatures also result in elevated Hydro-Carbon (HC) and Carbon Monoxide (CO) emissions compared to gasoline SI and diesel modes. HC and CO are typically formed when portions of the fuel mixture are trapped in the cooler regions of crevices and ring-packs. This results in incomplete combustion of these portions of the fuel mixture and HC and CO formation. In traditional gasoline SI and diesel engines, the HC and CO thus formed outgas into the cylinder during the expansion portion of the cycle and get oxidized due to the high post-combustion temperatures associated with these combustion modes. However, in the case of HCCI, these outgased emissions do not get completely oxidized due to lower post-combustion temperatures, leading to higher engine-out HC and CO emissions [9].
4. NOx emissions can become an issue with HCCI under higher loads, where higher combustion temperatures lead to engine-out NOx levels no longer low enough to avoid using the TWC. However, the TWC cannot be used when the combustion is lean of stoichiometric as is the case even with higher load HCCI.

1.3 Strategies to achieve HCCI

HCCI relies on achieving a thermochemical environment favorable for autoignition of the charge near TDC while having sufficient dilution to achieve low combustion temperatures and acceptable energy release rates. There are various strategies and key enabling technologies that help realize HCCI operation. Some of the more widely adopted strategies are discussed in this section.

1.3.1 Exhaust gas recompression using Negative Valve Overlap

HCCI ignition is driven by chemical kinetics and there is no spark discharge as in SI or fuel injection near TDC as in diesel to initiate combustion. HCCI needs higher charge temperatures than SI or diesel through the compression stroke to enable ignition through chemical kinetic reactions, and thus requires some form of charge heating. This heating may be achieved externally, with intake air heaters, or internally, by trapping hot residuals from the previous combustion cycle as shown by Kontarakis et al. [10]. The latter approach is generally preferred for automotive applications due to the ease of implementation and higher control authority under transient conditions.

The trapped hot residuals from the previous cycle are also known as internal EGR or iEGR. This is made possible by the use of flexible valve trains which allow the modification of valve lift and timing based on operating condition and the level of iEGR desired. A valve strategy known as Negative Valve Overlap (NVO) is employed to trap iEGR by prematurely closing the exhaust valve, which results in both the intake and exhaust valves being simultaneously closed for a period of time (known as NVO) around the gas exchange TDC. Thus, the portion of the hot exhaust gases trapped due to premature closure of the exhaust valve undergo “recompression” and are subsequently mixed with the cooler fresh incoming charge. Mixing of the fresh charge with the hot iEGR results in an overall increase in the charge temperature that serves to provide the required thermal inertia needed to achieve autoignition. Koopmans et al. [11] demonstrated the use of NVO to achieve HCCI combustion on a single cylinder research engine. They were able to achieve HCCI over a load range of 0.1 bar to 3.5 bar with engine speeds going from 1200 RPM to 3000 RPM. They noted that Exhaust Valve Close (EVC) timing had the strongest effect on autoignition delay of all the valve events. Other researchers [12, 13, 14] have also employed NVO operation to achieve HCCI operation.

This sort of NVO operation is in contrast to the conventional SI valve strategy which is characterized by Positive Valve Overlap (PVO) wherein both the exhaust and intake valves are open simultaneously for a short period of time around the gas exchange TDC. An illustration of PVO and NVO valve profiles with relation to the in-cylinder pressure trace is shown in Figure 1.1.

In this case the PVO valve profile is shown to have negligible overlap between intake and exhaust events. It may also be seen, that for the NVO case, the advance in EVC timing is accompanied by a corresponding and equal retard in Intake Valve Open (IVO) timing resulting in what is known as “symmetric” NVO. This is done to minimize pumping losses associated with recompression. Another strategy that has been used to internally heat the charge is called “rebreathing”, wherein there is a secondary, shorter, exhaust event during the intake stroke, which results in hot gases from the exhaust “back-flowing” into the cylinder and heating up the fresh charge [15]. Some researchers [16] also employ a very late EVC, resulting in a longer “exhaust” event. The intake event is unchanged and occurs within this long exhaust event, resulting in re-induction of exhaust gases in this manner.

1.3.2 Direct Injection

In addition to charge heating, HCCI relies on compression of the charge to achieve temperatures high enough to achieve auto-ignition. It is thus desirable to have a relatively high compression ratio (CR) in HCCI engines compared to gasoline SI engines. However, any future production gasoline HCCI engine will inevitably be a multi-mode combustion engine with SI being the preferred combustion mode at high loads. This is due to the challenges associated with high-load HCCI operation, namely combustion noise and NOx emissions. This restriction puts an upper limit on the CR arising from the tendency of SI to knock at high-loads with increased CR. Direct Injection (DI) provides a

means for SI engines to tolerate higher CR by providing fuel vaporization cooling of the charge, which reduces the tendency of end-gas to auto-ignite (knock) under SI conditions. Mitsubishi was one of the first auto manufacturers to develop Direct Injection SI (DISI) engines [17].

1.3.3 Boosting

Boosting is a means of achieving the required dilution for HCCI especially at higher loads and allows lean operation with increasing fueling rate. Several researchers such as Christensen et al. [18], Christensen and Johansson[19], Olsson et al. [20,21], Hyvonen et al. [22], Cairns and Blaxill [23], and others have used turbocharging and supercharging as means to achieve boosted HCCI operation. The primary benefit of boosting is to control post-combustion temperatures and energy release rates by increasing dilution. An additional advantage of boosting is increased chemical reactivity which reduces the level of charge heating required. It has been shown that certain fuels, including gasoline, exhibit low temperature and intermediate temperature reactions under higher pressures which tend to advance autoignition [24, 25, 26]. When boosting is achieved by means of a turbocharger, there are also system level benefits achieved by recovering some of the enthalpy from the exhaust gases.

Higher in-cylinder pressures as a result of boosting accelerate kinetics and this tends to advance combustion phasing. Thus, boosting is generally accompanied with lower levels of NVO and iEGR, as less thermal inertia is needed at higher pressures to initiate autoignition. In addition, external EGR (eEGR) may also be employed under boosted conditions if lower NVO (or even zero NVO) is not sufficient to compensate for the acceleration of kinetics with boost. The function of eEGR in this case is to retard combustion by lowering the γ of the mixture and thus compression temperatures of the mixture. It must be noted that eEGR is generally cooled to the temperature of the fresh

intake charge and does not bring with it any thermal inertia that would promote or advance auto-ignition.

1.3.4 Spark Assisted Compression Ignition (SACI)

Spark Assisted Compression Ignition (SACI) is a variation of HCCI wherein a spark discharge is used to initiate combustion. This combustion mode is characterized by a certain amount of flame propagation followed by autoignition of the end gas. In a matter of speaking this mode may be thought of as “controlled SI knock”. The overall charge is still dilute like HCCI with residuals used to bring the equivalence ratio close to stoichiometric to sustain flames. The spark discharge provides an added degree of control over combustion phasing while preserving benefits associated with dilution such as lower combustion temperatures than SI (thus lower heat losses) as well as near constant volume ignition of the end-gas (thermodynamic benefit from higher expansion ratio). With the availability of spark plugs in most experimental HCCI engine setups, several researchers such as Hyvonen et al. [27], Daw et al. [28], Manofsky et al. [29] and others have demonstrated SACI. Lavoie et al. [30] proposed a multi-mode combustion diagram outlining the regions in space spanned by unburned temperature, burned temperature and fuel-charge dilution where HCCI, SACI and SI could operate in a multi-mode combustion engine.

1.4 Competing charge preparation strategies for HCCI

Charge preparation refers to dilution method, charge heating method and fuel delivery strategy. With the availability of multiple enabling systems for HCCI there are multiple, often competing, charge preparation strategies. To choose one strategy over another it is important to understand the strengths and weaknesses of each strategy. For this, it is critical develop a fundamental understanding about how the choice of dilution,

charge heating and fueling method impacts the thermochemical distribution within the cylinder, which in turn affects combustion characteristics such as burn duration and emissions.

1.4.1 Effect of diluent composition

HCCI is characterized by high levels of dilution. Lavoie et al. [30] define a fuel to charge equivalence ratio (Φ') which accounts for both air and EGR dilution. It is defined as follows:

$$\Phi' = \Phi(1 - \mathrm{RGF}) \tag{1.1}$$

In the above equation, Φ refers to the fuel-air equivalence ratio and RGF refers to the Residual Gas Fraction which is a combination of iEGR and eEGR. EGR has different thermodynamic and chemical properties compared to air, which affects combustion characteristics such as phasing, burn rates and emissions. Various attempts have been made to understand the impact of using air versus eEGR as a diluent on HCCI combustion. Researchers such as Christensen and Johansson [19], Olsson et al. [21], Sjöberg et al. [31] showed that displacing air with cooled eEGR serves to retard combustion phasing for HCCI and increase burn duration. A single zone computational study by Dec [32] showed that eEGR serves to significantly slow down HCCI heat release rates (HRR) when combustion phasing is matched with an air-dilute case. However, Olsson et al. [21] and Dec et al. [33] reported that when combustion phasing is matched, the effect of eEGR displacing air as diluent is small in terms of heat release rate (HRR). Further, Dec et al. [33] also noted that NOx levels actually rise with the use of eEGR under some conditions, which they attributed to higher temperatures during the expansion stroke owing to lower γ of the mixture, which is contrary to the standard understanding within the engine community.

There seems to be a gap in fundamental understanding within the literature in terms of relating thermodynamic and chemical kinetic effects of eEGR dilution (versus air dilution) to HCCI burn duration and NOx emissions.

1.4.2 NVO versus PVO

In engines with relatively low compression ratios (<13) intended to run as multi-mode engines switching to SI at higher loads, residuals often are used as a means of initiating HCCI autoignition. In such engines NVO is typically used to trap large amounts of hot iEGR. The iEGR broadly has the same thermodynamic and chemical kinetic properties as eEGR; however using iEGR also brings about significant thermal and compositional stratification within the charge as hot residuals mix with the fresh incoming charge.

In 2009, Rothamer et al. [34] compared what they call “pure HCCI” operation with conventional valve events (similar to the PVO case shown in Figure 1.1) with NVO operation at 1200 RPM. For the pure HCCI case, they used *n*-heptane as fuel, and inject directly into the cylinder during the intake stroke. They claim that this generates a homogeneous fuel distribution prior to ignition. They operated this case with an elevated intake air temperature of 375 K. Based on Planar Laser Induced Fluorescence (PLIF) images, they reported that the distributions of EGR and temperature in-cylinder prior to combustion achieved a uniform state with 1σ distribution widths of 2.2 mole fraction % for the EGR distribution and 4.9 K for the temperature distribution. The second case was an NVO case, with an NVO of 147°. For this case, the fuel used was a mixture of 90% isooctane and 10% *n*-heptane by volume. They used a split injection strategy with about 30% of the fuel mass being injected right after EVC and the rest being injected at the beginning of the main compression stroke. They noticed some NVO heat release from the fuel injection during recompression, based on the pressure-volume diagram for this case.

From PLIF images taken prior to ignition, they noted a significant increase in EGR and temperature stratification compared to the pure HCCI case, with 1σ distribution widths of 6.2 mole fraction % for the EGR distribution and 24.5 K for the temperature distribution. They speculate that this increase in thermal and compositional stratification could extend burn duration.

Olesky et al. [35] in 2012 reported that trading air dilution for iEGR dilution results in increased burn duration, though it is not clear whether this is because of a mean composition effect or stratification effects. All the cases studied in this work used an NVO of at least 157°, and due to limitations in the setup an NVO versus PVO comparison could not be done.

In summary, it is not really clear if the level of stratification introduced by NVO operation has a significant impact on HCCI burn duration. Further, it is not clear whether the primary effect of iEGR on HCCI burn duration is by means of altering the mean composition of the mixture, or by introducing stratification. Also, the relative importance of thermal versus compositional stratification is presently unclear.

1.4.3 Premixed fueling versus DI

With the increasing use of direct injection in gasoline engines, it is important to understand the impact of fuel stratification caused by DI over premixed operation. Sjöberg et al. [36] demonstrated HCCI operation using a Gasoline Direct Injection (GDI) system. They found that with an intake pressure of ~ 1 bar and intake temperatures ranging from 75-100°C, they were able to achieve satisfactory HCCI combustion with low NOx and HC/CO emissions, which they speculated was due to a homogeneous mixture prior to ignition. However, as they retarded the injection timing, past the optimal timing, they observed higher NOx and CO. They attributed this to a possible increase in stratification with richer regions burning hotter (generating NOx) and leaner regions

burning cooler (generating CO) compared to the case with the optimal injection timing.

Dec et al. [37] show that fuel stratification might be used as a means to extend burn duration for HCCI under boosted conditions with gasoline operation. Herold et al. [38] speculate that any effect on burn duration due to equivalence ratio stratification brought about by direct injection might be mitigated by having γ stratification in the opposite direction.

It is currently unclear how equivalence ratio stratification brought about by direct injection interacts with other concurrent phenomena such as thermal stratification as well as local composition. The understanding of these interactions assumes an even greater importance when injecting during NVO, as is the case with most engines operating HCCI with internal residual. With DI during NVO, fuel is associated with a hot, oxygen-deprived environment unlike in the premixed fueling case, where the fuel is associated with the intake (cool and oxygen rich). Moreover, NVO injection happens when the valves are closed, and compared to PVO, the intake event is generally shorter from the intake stream (as is generally the case with GDI) to completely mix the fuel with the rest of the charge.

1.5 Objective and Document Organization

There is currently a gap in fundamental understanding regarding the impact of various charge preparation strategies on the HCCI reaction space, and the ultimate effect on HCCI combustion characteristics. Experimental work done so far has been limited by hardware restrictions such as having to employ a minimum level of NVO to achieve HCCI [35] or the ability to examine stratification only in a small, 2-D viewing window [34, 39]. Further, it is not possible to get an accurate estimation of in-cylinder temperatures, especially when high levels of iEGR are used due to the uncertainties associated with residual gas estimation methods. Experiments are also often handicapped

by their inability to completely decouple various concurrent effects such as thermal and compositional stratification.

Considering the difficulties and limitations associated with experimental investigation into the effect of various charge preparation strategies on HCCI combustion, it would seem that detailed CFD simulation coupled with chemical kinetics could yield fundamental insights into reaction space development. However, there is an absence in the literature of a thorough CFD-based reaction space analysis of various charge preparation strategies. From a simplified model development standpoint there is not a clear understanding about the major effects that need to be captured in order to predict HCCI combustion duration and emissions. The main goals of this doctoral work are to

- Provide fundamental combustion insights to guide HCCI charge preparation strategy
- Identify the major effects contributing to HCCI burn duration and emissions by systematically decoupling concurrent effects

Based on the understanding from the CFD studies, a rapid methodology to capture wall-driven thermal stratification for use in system level multi-zone codes is developed. Using this methodology, a high-speed quasi-dimensional multi-zone HCCI combustion model intended for use in system-level codes is developed and evaluated based on its performance compared to CFD simulations as well as experiments (Kodavasal et al. [40]).

The rest of the document is organized as follows. Chapter 2 describes the simulation tools used to investigate the various charge preparation strategies. These include the CFD code (KIVA-3V) as well as quasi-dimensional multi-zone models developed as part of this work. Description of an ignition delay correlation is given, which is then used as a metric within the reaction space to characterize stratification in reaction space dimensions of temperature, equivalence ratio and oxygen concentration.

Chapter 3 describes investigation into the effect of diluent composition on HCCI combustion characteristics. Air dilution is compared with external EGR (eEGR) dilution in an attempt to explain the fundamental chemical kinetic and thermodynamic implications of trading air dilution for eEGR dilution for a fixed operating point.

In Chapter 4, the effect of NVO operation on thermal and compositional stratification is studied. The effect of NVO-induced stratification on burn duration is studied, and is compared with PVO operation keeping the mean composition and ignition timing the same between the NVO and PVO strategies to isolate stratification caused by trapping internal residual.

The impact of fueling strategy is studied in Chapter 5. The effect of switching from premixed operation, where fuel is mixed in the intake port (PFI), to DI is studied with respect to development of the reaction space, and consequent impact on burn duration and NOx emissions.

In Chapter 6, a thermal stratification methodology to capture wall heat loss driven thermal stratification is outlined. The development of an Accelerated Multi-zone model for Engine Cycle Simulation (AMECS) of HCCI combustion using this thermal stratification methodology is outlined; and the performance of AMECS is evaluated against CFD simulations as well as experiments.

Chapter 7 summarizes the main contributions and insights from this work and provides recommendations for further study.

The original contributions presented in this dissertation have also been reported/ are to be reported in the following publications:

Kodavasal, J., McNenly, M., Babajimopoulos, A., Aceves, S., Assanis, D., Havstad, M. and Flowers, D. "An accelerated multi-zone model for engine cycle simulation of homogeneous charge compression ignition combustion", *International Journal of Engine Research*, in press, 2013.

Kodavasal, J., Martz, J. B., Assanis, D. N., “Effect of diluent composition on HCCI combustion characteristics at a fixed operating condition”, Publication in preparation.

Kodavasal, J., Martz, J. B., and Assanis, D. N., “Thermal and compositional stratification from NVO operation; and effects on HCCI combustion characteristics,” Publication in preparation.

Kodavasal, J., Martz, J. B., and Assanis, D. N., “Reaction-space analysis of premixed and direct injected fueling in the context of NVO HCCI operation,” Publication in preparation.

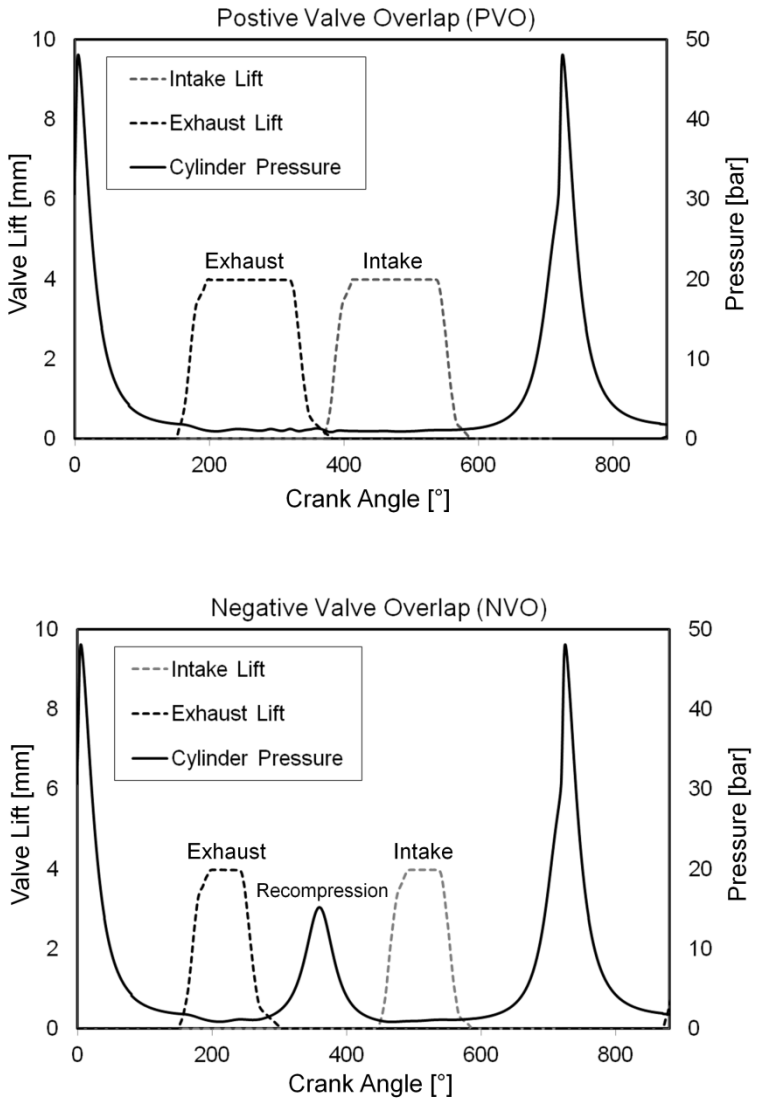

Figure 1.1 – Sample positive valve overlap (PVO) and negative valve overlap (NVO) valve lift profiles shown with reference to in-cylinder pressure trace

1.6 References

1. Onishi, S., Jo, S. H., Shoda, K., Jo, P. D., and Kato, S., "Active Thermo-Atmosphere Combustion (ATAC) – A New Combustion Process for Internal Combustion Engines," SAE Paper 790501, 1979.

2. Noguchi, M., Tanaka, Y., Tanaka, T., and Takeuchi, Y., "A Study on Gasoline Engine Combustion by Observation of Intermediate Reactive Products during Combustion," SAE Paper 790840, 1979.

3. Najt P. M., and Foster D. E., "Compression Ignited Homogeneous Charge Combustion," SAE Paper 830264, 1983.

4. Halstead, M. P., Kirsch, L. J., Prothero, A., and Quinn, C. P., "A mathematical model for hydrocarbon autoignition at high pressures," *Proc. Roy. Soc. London*, 1975, A346, pp. 515-538.

5. Thring R. H., "Homogeneous-Charge Compression-Ignition (HCCI) Engines," SAE Paper 892068, 1989.

6. Hultqvist, A., Christensen, M., Johansson, B., Franke, A., Richter, M., and Alden, ., "A Study of the Homogeneous Charge Compression Ignition Combustion Process by Chemiluminescence Imaging," SAE Paper 1999-01-3680, 1999.

7. Hultqvist, A., Engdar, U., Johansson, B., and Klingmann, J., "Reacting Boundary Layers in a Homogeneous Charge Compression Ignition (HCCI) Engine," SAE Paper 2001-01-1032, 2001.

8. Hultqvist, A., Christensen, M., Johansson, B., Richter, M., Nygren, J., Hult, J., and Alden, M., "The HCCI Combustion Process in a Single Cycle~High-Speed fuel Tracer LIF and Chemiluminescence Imaging," SAE Paper 2002-01-0424, 2002.

9. F. Zhao, T.W. Asmus, D.N. Assanis, J.E. Dec, J.A. Eng, and P.M. Najt (eds.), *Homogeneous Charge Compression Ignition (HCCI) Engines: Key Research and Development Issues*, SAE, Warrendale, PA, 2003.

10. Kontarakis, G., Collings, N., and Ma, T., “Demonstration of HCCI Using a Single Cylinder, Four-Stroke SI Engine with Modified Valve Timing,” SAE Paper 2000-01-2870, 2000.

11. Koopmans, L., and Denbratt, I., “A Four Stroke Camless Engine, Operated in Homogeneous Charge Compression Ignition Mode with Commercial Gasoline,” SAE Paper 2001-01-3610, 2001.

12. Allen, J., and Law, D., “Variable Valve Actuated Controlled Auto-Ignition: Speed Load Maps and Strategic Regimes of Operation,” SAE Paper 2002-01-0422, 2002.

13. Hiraya, K., Hasegawa, K., Urushihara, T., Iiyama, A., and Itoh, T., “A Study on Gasoline Fueled Compression Ignition Engine ~ A Trial of Operation Region Expansion,” SAE Paper 2002-01-0416, 2002.

14. Milovanovic N., Chen R., and Turner J., “Influence of the Variable Valve Timing Strategy on the Control of a Homogeneous Charge Compression Ignition Engine”, SAE Paper 2004-01-1899.

15. Chang, J., Guralp, O., Filipi, Z., Assanis, D., Kuo, T.-W., Najt, P., and Rask, R., “New Heat Transfer Correlation for an HCCI Engine Derived from Measurements of Instantaneous Surface Heat Flux,” SAE Paper 2004-01-2996, 2004.

16. Kaahaaina, N. B., Simon, A. J., Caton, P. A., and Edwards, C. F., “Use of Dynamic Valving to Achieve Residual-Affected Combustion,” SAE Paper 2001-01-0549, 2001.

17. Ando, H., Noma, K., Iida, K., Nakayama, O. and Yamauchi, T., “Mitsubishi GDI engine – Strategies to meet the European requirements,” SAE Paper 1997-29-0017, 1997.

18. Christensen M., Johansson, B., Amneus P., and Mauss F., “Supercharged Homogeneous Charge Compression Ignition,” SAE Paper 980787, 1998.

19. Christensen, M., and Johansson, B., “Supercharged Homogeneous Charge Compression Ignition (HCCI) with Exhaust Gas Recirculation and Pilot Fuel,” SAE Paper 2000-01-1835, 2000.

20. Olsson J., Tunestal P., Haraldsson G., and Johansson B., “A Turbo Charged Dual Fuel HCCI Engine,” SAE Paper 2001-01-1896, 2001.

21. Olsson, J., Tunestal, P., Ulfvik, J., and Johansson, B., “The Effect of Cooled EGR on Emissions and Performance of a Turbocharged HCCI Engine,” SAE Paper 2003-01-0743, 2003.

22. Hyvonen J., Haraldsson G., and Johansson B., “Supercharging HCCI to Extend the Operating Range in a Multi-Cylinder VCR-HCCI Engine,” SAE Paper 2003-01-3214, 2003.

23. Cairns A., and Blaxill H., “Lean Boost and External Exhaust Gas Recirculation for High Load Controlled Auto-Ignition,” SAE Paper 2005-01-3744, 2005.

24. Sjoberg M., and Dec J., “EGR and Intake Boost for Managing HCCI Low Temperature Heat Release over Wide Ranges of Engine Speed,” SAE Paper 2007-01-0051, 2007.

25. Silke E., Pitz W., Westbrook C., Sjoberg M., and Dec J., “Understanding the Chemical Effects of Increased Boost Pressure under HCCI Conditions,” SAE Paper 2008-01-0019, 2008.

26. Dec. J., and Yang. Y., “Boosted HCCI for High Power without Engine Knock and Ultra-Low NO_x Emissions using a Conventional Fuel,” SAE Paper 2010-01-1086, 2010.

27. Hyvonen, J., Haraldsson, G., and Johansson, B., “Operating Conditions Using Spark Assisted HCCI Combustion During Combustion Mode Transfer to SI in a Multi-Cylinder VCD-HCCI Engine”, SAE Paper 2005-01-0109, 2005

28. Daw, C. S., Edwards, K. D., Wagner, R. M., and Green, J.J.B Jr., "Modeling Cyclic Variability in Spark-Assisted HCCI", *Journal of Engineering for Gas Turbines and Power*, Vol. 130: 052801-1-6, 2008.

29. Manofsky, L., Vavra, J., Assanis, D., and Babajimopoulos, A., "Bridging the Gap between HCCI and SI: Spark-Assisted Compression Ignition," SAE Paper 2011-01-1179, 2011.

30. Lavoie, G. A., Martz, J., Wooldridge, M., and Assanis, D., "A Multi-mode Combustion Diagram for Spark Assisted Compression Ignition", *Combustion and Flame*, Vol. 157: 1106-1110, 2010.

31. Sjöberg, M., Dec, J. E., and Hwang, W., "Thermodynamic and Chemical Effects of EGR and Its Constituents on HCCI Autoignition," SAE Paper 2007-01-0207, 2007.

32. Dec, J., "A Computational Study of the Effects of Low Fuel Loading and EGR and Heat Release Rates and Combustion Limits in HCCI Engines," SAE Paper 2002-01-1309, 2002.

33. Dec, J. E., Sjöberg, M., and Hwang, W., "Isolating the Effects of EGR on HCCI Heat-Release Rates and NOx Emissions," SAE Paper 2009-01-2665, 2009.

34. Rothamer, D. A., Snyder, J. A., Hanson, R. K., Steeper, R. R., and Fitzgerald, R. P., "Simultaneous imaging of exhaust gas residuals and temperature during HCCI combustion," *Proceedings of the Combustion Institute* 32: 2869-2876, 2009.

35. Olesky, L. M., Vavra, J., Assanis, D., and Babajimopoulos, A., "Internal residual vs. elevated intake temperature: how the method of charge preheating affects the phasing limitations of HCCI combustion," *Proceedings of the ASME 2012 Internal Combustion Engine Spring Technical Conference*, May 6-9, 2012, Torino, Piemonte, Italy.

36. Sjöberg, M., Edling, L-O., Eliassen, L. M., and Ångström, "GDI HCCI: Effects of Injection Timing and Air Swirl on Fuel Stratification, Combustion and Emissions Formation," SAE Paper 2002-01-0106, 2002.

37. Dec, J. E., Yang, Y., and Dronniou, N., “Boosted HCCI – Controlling Pressure-Rise Rates for Performance Improvements using Partial Fuel Stratification with Conventional Gasoline,” SAE Paper 2011-01-0897, 2011.

38. Herold, R.E., Krasselt, J. M., Foster, D. E., Ghandhi, J. B., Reuss, D. L., and Najt, P. M., “Investigations into the Effects of Thermal and Compositional Stratification on HCCI Combustion – Part II: Optical Engine Results,” SAE Paper 2009-01-1106, 2009.

39. Snyder, J., Dronniou, N., Dec, J., and Hanson, R., “PLIF Measurements of Thermal Stratification in an HCCI Engine under Fired Operation,” SAE Paper 2011-01-1291, 2011.

40. Kodavasal, J., McNenly, M. J., Babajimopoulos, A., Aceves, S. M., Assanis, D. N., Havstad, M. A., and Flowers, D. L., “An accelerated multi-zone model for engine cycle simulation of HCCI combustion,” *International Journal of Engine Research*, in press, 2013.

CHAPTER 2

TOOLS USED/DEVELOPED AND RESEARCH METHOD

This chapter introduces the tools used, as well as tools developed as part of this work to understand the effect of charge preparation strategy on HCCI combustion. First, a brief overview of the CFD software used in this work is provided. The chemical kinetics and fuel surrogate used are then introduced. A description of the fully-coupled CFD/kinetics approach is given along with a modified zoning scheme developed. The performance of the fully-coupled CFD/kinetics approach is evaluated against HCCI engine experiments.

A quasi-dimensional multi-zone model is developed to capture stratification effects on HCCI combustion. This multi-zone is coupled to cold-flow CFD simulations in a sequential manner. The objective to this sequential multi-zone approach is to systematically decouple concurrent effects such as thermal and compositional stratification to understand the effect of each phenomenon in isolation.

An approach to analyze the reaction space based on an ignition delay correlation is proposed. The application of this approach to understanding stratification effects on reactivity is described as a prelude to the studies and analysis performed in the following chapters.

2.1 Overview of CFD software used

The CFD software used in this work is KIVA-3V [1], which uses a Reynolds Averaged Navier Stokes (RANS) solver for fluid dynamics calculations. It is a free, open-source FORTRAN code intended for two- and three-dimensional (2-D, 3-D) engine simulations, developed by Los Alamos National Laboratory (LANL). The first version of this code was called KIVA [2] and was made available for public use in 1985. KIVA-3V features significant improvements over previous versions of the code and enables modeling of ports and moving valves, allowing for simulation of complete engine cycles including breathing events. Further features of KIVA-3V include sub-models for sprays and chemical kinetics solution.

The governing equations for the fluid phase are described in the KIVA-II manual [3], and are reproduced here. These governing equations may be applied to both laminar and turbulent flows.

The equation of continuity for species *m* is

$$\frac{\partial \rho_k}{\partial t} + \boldsymbol{\nabla}.(\rho_k \mathbf{u}) = \boldsymbol{\nabla}.\left[\rho D \boldsymbol{\nabla}\left(\frac{\rho_k}{\rho}\right)\right] + \dot{\rho_k^c} + \dot{\rho^s}\delta_{k1}\,, \tag{2.1}$$

where ρ_m is the mass density of species *m*, ρ the total mass density, and **u** the fluid velocity vector. Fick's Law diffusion with single diffusion coefficient *D* is assumed. Equations for *D* and the source terms due to chemistry $\dot{\rho_m^c}$ and the spray $\dot{\rho^s}$ are given in the KIVA-II manual, and omitted here. Based on the KIVA convention, species 1 is the species which the spray droplets are composed of, and δ is the Dirac delta function. The total fluid density is obtained by the equation

$$\frac{\partial \rho}{\partial t} + \boldsymbol{\nabla}.(\rho \mathbf{u}) = \dot{\rho^s}\,, \tag{2.2}$$

since mass is conserved in chemical reactions.

The momentum equation for the fluid mixture is

$$\frac{\partial(\rho\mathbf{u})}{\partial t} + \boldsymbol{\nabla}.(\rho\mathbf{u}\mathbf{u}) = -\frac{1}{\alpha^2}\boldsymbol{\nabla}p - A_0\boldsymbol{\nabla}\left(\frac{2}{3}\rho k\right) + \boldsymbol{\nabla}.\boldsymbol{\sigma} + \mathbf{F^S} + \rho\mathbf{g}\,, \tag{2.3}$$

where p is the fluid pressure. The dimensionless quantity α is used in conjunction with the Pressure Gradient Scaling (PGS) Method, which is used to enhance computational efficiency in low Mach number flows, where the pressure is nearly uniform. The parameter A_0 is set to zero for laminar calculations and unity when one of the turbulence models within the code is used. The viscous stress tensor is Newtonian in form:

$$\boldsymbol{\sigma} = \mu[\boldsymbol{\nabla}\mathbf{u} + (\boldsymbol{\nabla}\mathbf{u})^T] + \lambda\boldsymbol{\nabla}.\mathbf{u}\,\mathbf{I} \tag{2.4}$$

The first and second coefficients of viscosity are represented by μ and λ respectively. The superscript T denotes the transpose and **I** is the unit dyadic. $\mathbf{F^s}$ is the rate of momentum gain per unit volume due to the spray. The specific body force **g** is assumed constant.

The internal energy equation is

$$\frac{\partial(\rho I)}{\partial t} + \boldsymbol{\nabla}.(\rho\mathbf{u}I) = -p\boldsymbol{\nabla}.\mathbf{u} + (1 - A_0)\boldsymbol{\sigma}\!:\!\boldsymbol{\nabla}\,\mathbf{u} - \boldsymbol{\nabla}.\mathbf{J} + A_0\rho\varepsilon + \dot{Q}^C + \dot{Q}^S\,, \tag{2.5}$$

where I is the specific internal energy, exclusive of chemical energy. The heat flux vector **J** is the sum of contributions of heat conduction and enthalpy diffusion. The quantity ε is the rate of dissipation of the turbulent kinetic energy k, and $\dot{Q}^C$ and $\dot{Q}^S$ are the source terms due to chemical heat release and fuel spray respectively.

When one of the turbulence models is used (A_0=1), two additional transport equations for turbulent kinetic energy k and its dissipation rate ε are solved:

$$\frac{\partial\rho k}{\partial t} + \boldsymbol{\nabla}.(\rho\mathbf{u}k) = -\frac{2}{3}\rho k\boldsymbol{\nabla}.\mathbf{u} + \boldsymbol{\sigma}\!:\!\boldsymbol{\nabla}\,\mathbf{u} + \boldsymbol{\nabla}.\left[\left(\frac{\mu}{Pr_k}\right)\boldsymbol{\nabla}k\right] - \rho\varepsilon + \dot{W}^S\,, \tag{2.6}$$

and

$$\frac{\partial \rho\varepsilon}{\partial t} + \boldsymbol{\nabla}.(\rho \mathbf{u}\varepsilon) = -\left(\frac{2}{3}c_{\varepsilon_1} - c_{\varepsilon_3}\right)\rho\varepsilon\boldsymbol{\nabla}.\mathbf{u} + \boldsymbol{\nabla}.\left[\left(\frac{\mu}{Pr_\varepsilon}\right)\boldsymbol{\nabla}\varepsilon\right] \tag{2.7}$$

$$+\frac{\varepsilon}{k}\left[c_{\varepsilon_1}\boldsymbol{\sigma}:\boldsymbol{\nabla}\,\mathbf{u} - c_{\varepsilon_2}\rho\varepsilon + c_S\dot{W^S}\right]\ ,$$

These are the standard *k*-ε (SKE) equations with some additional terms. The source term $-\left(\frac{2}{3}c_{\varepsilon_1} - c_{\varepsilon_3}\right)\rho\varepsilon\boldsymbol{\nabla}.\mathbf{u}$ in the ε-equation accounts for changes in length scale resulting from velocity dilation. The source terms containing $\dot{W}^S$ account for interaction of the gas phase with the spray. When the optional subgrid-scale (SGS) turbulence model is used, the value of ε is governed by the inequality

$$\varepsilon \geq \left[\frac{c_\mu}{Pr_\varepsilon\left(c_{\varepsilon_2} - c_{\varepsilon_1}\right)}\right]^{\frac{1}{2}}\frac{k^{3/2}}{L_{SGS}}, \tag{2.8}$$

where L_{SGS} is a length scale determined by the user in the input file. The recommended value for this length scale is 4 times the dimension of a representative computational cell. The recommended values for various constants are as follows

c_{ε_1} = 1.44	c_S = 1.50
c_{ε_2} = 1.92	Pr_k = 1.0
c_{ε_3} = -1.0	Pr_ε = 1.3

Besides the SKE and the SGS turbulence models, KIVA-3V also features a Renormalization Group (RNG) theory variant of the *k*-ε developed by Han and Reitz [4], which includes the effects of compressibility using a rapid distortion analysis.

Based on ideal gas relationships, the internal energy is related to temperature in the following manner:

$$p = R_0 T \sum_k \left(\frac{\rho_k}{MW_k}\right) \tag{2.9}$$

$$I(T) = \sum_k \left(\frac{\rho_k}{\rho}\right) I_k(T) \tag{2.10}$$

$$I_k(T) = h_k(T) - \frac{R_0}{MW_k} T \tag{2.11}$$

where R_0 is the universal gas constant, $I_k(T)$ is the specific internal energy of species k at temperature T, $h_k(T)$ is the specific enthalpy of species k taken from the JANAF thermodynamic tables, and MW_k is the molecular weight of the species k.

KIVA-3V also includes several other sub-models to simulate injection, breakup, collision and evaporation of spray droplets and wall film formation, details of which may be found in the KIVA manuals. The numerical solution scheme is based on the Arbitrary Lagrangian Eulerian (ALE) method, which is detailed in the KIVA-II manual.

2.2 Chemical kinetic modeling

In this work a 4-component surrogate is used to model gasoline fuel. This surrogate was developed by Mehl et al. [5] at Lawrence Livermore National Laboratory (LLNL). The surrogate is comprised of isooctane, *n*-heptane, toluene and 2-pentene, and the relative proportion of each component by mass fraction is given in Table 2.1. In order to determine the composition of the surrogate, Mehl and coworkers used both composition of real gasoline (in terms of aromatics, olefins, alkanes and average molecular weight) as well as reactivity of gasoline (autoignition properties) to formulate a surrogate having a similar overall representation of various kinds of hydrocarbons and having similar (RON + MON)/2 as gasoline where RON stands for Research Octane Number and MON stands for Motor Octane Number. The choice of isooctane, *n*-heptane and toluene has been attributed to historical reasons, since they fit well within the

molecular weight range of interest, and have been traditionally well understood within the combustion community. The addition of 2-pentene to represent olefins has been attributed to this molecule matching the typical molecular weight of olefins found in gasoline, and also because it has the highest octane number and sensitivity.

A detailed chemical kinetic mechanism for this surrogate was developed by Mehl et al. [6], which consists of roughly 1400 species and 5000 reactions. This mechanism was validated against gasoline shock tube data over a range of temperatures and pressures. However, it is computationally infeasible to incorporate such a large mechanism within a 3-D CFD simulation; hence the same group (Mehl et al. [5]) also developed a reduced 312-species, 1488-reaction chemical kinetic mechanism based on the detailed mechanism, intended for 3-D CFD simulation of HCCI engines. This model was validated against HCCI engine experiments by Mehl et al. [7] over a range of intake pressure and load conditions, and was found to capture features such as Intermediate Temperature Heat Release (ITHR, Dec et al. [8]) which are thought to be unique to gasoline fuel chemistry at higher near Top Dead Center (TDC) pressures.

This 312-species mechanism along with the 4-component gasoline surrogate has been used in the studies performed in chapters 3, 4 and 5.

2.3 The fully-coupled CFD/ kinetics approach

In order to capture the effect of chemical reactions in conjunction with the fluid-dynamics calculations, chemical kinetics is fully-coupled with the CFD solution. Researchers such as Kong et al. [9] and Agarwal et al. [10] have described approaches to couple multi-dimensional fluid dynamics to detailed chemical kinetics in every cell. The ALE method used in KIVA-3V for temporal differencing permits the computation of the chemistry source terms in the species continuity and energy equations in the Lagrangian phase A. The solution of the chemistry source terms is decoupled from the computation

of the advective-diffusive terms, in essence treating each computational cell as an isothermal reactor. Based on the species generated at the end of the chemistry calculation, a change in the internal energy of formation is computed which is turn is reflected as a change in the sensible internal energy (SIE) of that cell in the internal energy equation.

This sort of operator-splitting approach is traditionally accepted in HCCI simulations, due to the absence of diffusive fronts from flames. Overall energy release rates in HCCI are thought to be *primarily* dominated by sequential autoignition based on local ignition delays. Sankaran and Im [11] studied the effect of dissipation rate and mixture inhomogeneity on HCCI autoignition. They found that at conditions typical of TDC in an HCCI engine (lower mixing rates and higher pressures) chemical kinetics, and not dissipation due to mixture inhomogeneities, dominate the sequential auto-ignition process.

Performing chemical kinetics in every CFD cell can quickly become computationally intensive and prohibitive when the number of cells is increased (as is the case with detailed 3-D meshes) or when the size of the kinetic mechanism is increased. To overcome this, Babajimopoulos et al. [12] developed a method to of grouping cells with similar thermochemical properties into “chemistry zones”. By performing chemistry calculations in hundreds of “chemistry zones” rather than tens of thousands of individual CFD cells, significant computational speed-up is achieved with minimal loss to fidelity of results compared to the detailed approach.

Babajimopoulos et al. [12] group the cells based on a so-called “progress equivalence ratio” φ and temperature. The progress equivalence ratio φ of a CFD cell is defined as based on the number of carbon atoms ($C^{\#}$), hydrogen atoms ($H^{\#}$) and oxygen atoms ($O^{\#}$) within the CFD cell, excluding the number of carbon (C), hydrogen (H) and oxygen(O) atoms contained in products of complete combustion (carbon dioxide, CO_2 and water, H_2O):

$$\varphi = \frac{2C^{\#}_{-CO_2} + \frac{H^{\#}_{-H_2O}}{2} - z'C^{\#}_{-CO_2}}{O^{\#}_{-CO_2-H_2O} - z'C^{\#}_{-CO_2}} \ , \tag{2.12}$$

Here z' is the ratio of oxygen atoms per carbon atom in the fuel which is zero for pure hydrocarbon fuels, such as the 4-component gasoline fuel surrogate described earlier. Babajimopoulos et al. [12] proposed creating zones in the following manner:

1. The cells in the CFD domain are sorted in ascending order of temperature, and divided into five temperature zones, based on a prescribed mass fraction distribution.

2. The cells in each temperature zone are then sorted in ascending order of φ and zones for chemistry are created within each temperature zone by grouping cells together, starting from the cell with the lowest φ within each temperature zone, such that $\Delta\varphi$ within each chemistry zone is no greater than 0.02.
3. The final step is to loop through all the T/φ zones to identify zones that contain more than 1% of the total mass within the cylinder. In such zones, the cells are sorted by temperature and divided into smaller temperature zones in such a way that none of these newly created zones exceeds 1% of the total mass contained within the cylinder.

There are two shortcomings associated with this zoning method:

- There is no way of explicitly enforcing a limit on ΔT within each chemistry zone. It was observed that zones with ΔT of over 100 K could be created using this zoning method in cases with high levels of stratification, resulting in incorrect prediction of ignition timing.
- Adding additional variables to the zoning criteria is not straight-forward, and requires multiple nested loops.

To address these issues, a new simplified mapping method to create chemistry zones from CFD cells is developed, which is also reported in Kodavasal et al. [13]):

1. The cells in the CFD domain are sorted based on descending order of temperature
2. Cells are added into chemistry zones, starting from the hottest cell in this sorted domain, as long as adding a cell to the current chemistry zone keeps the spread of chosen zoning variables (such as T and φ) within prescribed limits.
3. If the current cell being zoned cannot be put into the most recently created zone, a new zone is created with the current cell being the first in that zone.

This method greatly simplifies zone creation, and allows establishment of hard limits on parameters like ΔT and $\Delta\varphi$ within each zone. Further, adding additional variables to enhance zoning such as the internal energy of formation u_f (as proposed in Kodavasal et al. [13]) to model special cases like diesel premixed compression ignition (PCI) does not require significant code modification. The determinate limits of ΔT and $\Delta\varphi$ also facilitate zone resolution studies to determine optimum values of ΔT and $\Delta\varphi$ that maintain computational efficiency while still capturing ignition and burn rates as predicted by the detailed approach where chemistry is done in every cell.

Once chemistry is solved in a zone, species information is remapped back onto the cells comprising the zone based on the approach proposed by Babajimopoulos et al. [12], which is uses the following equation:

$$m_{k,cell} = \frac{ch_{cell}}{ch_{zone}}\, m_{k,zone}\,, \tag{2.13}$$

where m_k represents the mass of the k^{th} species and ch is defined by the number of carbon atoms and hydrogen atoms, excluding carbon and hydrogen atoms from complete combustion products, CO_2 and H_2O, as follows:

$$ch = 2C^{\#}_{-CO_2} + \frac{H^{\#}_{-H_2O}}{2} \quad (2.14)$$

Equations (2.13) and (2.14) are used to remap all species except CO_2, H_2O, oxygen (O_2) and nitrogen (N_2), which are subsequently redistributed to the cells so that the following conditions are satisfied:

1. The mass of each cell in the zone is conserved.
2. The mass of each individual species in the zone is conserved.
3. The number of C, H, O and N atoms in each cell is conserved.

Since it is not possible to know the exact species concentrations that must be mapped back onto each cell without performing chemistry calculations in every cell, this remapping approach aims to ensure that the thermodynamic properties of the cells are not changed significantly by the remapping process.

2.4 Fully coupled CFD/kinetics model performance evaluation

This section describes the evaluation of the fully coupled CFD/kinetics simulation's performance in terms of reproducing HCCI engine experiment results. Representative HCCI engine experiments from Olesky et al. [14], performed at the University of Michigan's Walter E. Lay Automotive Laboratory are used to evaluate the CFD model.

2.4.1 HCCI Engine Configuration

The engine used by Olesky et al. [14] is a single cylinder research engine based on a gasoline Ricardo Hydra block. The engine features a pent-roof head with a side mounted direct injector which is mounted between the two intake valves. The fuel spray is aimed at the piston bowl. There is a spark plug centrally mounted in the cylinder head and is always enabled for engine start and warm-up. Once in HCCI mode however, the

spark discharge is disabled. The compression ratio for this engine is higher than typical gasoline engines, to enable HCCI ignition by means of achieving higher in-cylinder pressures and temperatures. Engine specifications are provided in Table 2.2.

This engine is equipped with a Fully Flexible Valve Actuation (FFVA) system built by Sturman Industries, which enables application of a wide range of valve timings. This feature of the valve-train allows the implementation of unconventional valve strategies such as NVO, where both the intake and exhaust valves may be simultaneously closed for a significant portion of the gas-exchange process, enabling retention of significant amounts of residuals from the previous combustion cycle. Moreover, valve timings may be varied on-the-fly, thus varying the level of NVO, and amount of internal residual as desired. The engine also has provision for externally heating intake air by means of intake air heaters, since the charge heating provided by internal residuals or internal EGR (iEGR), even at very high levels of NVO is insufficient to achieve HCCI ignition under naturally aspirated conditions in this engine. This engine will be referred to simply as the "FFVA engine" henceforth within this document.

2.4.2 CFD model setup

A 3-D mesh of the FFVA engine (shown in Figure 2.1) is used for the model performance evaluation. This mesh has approximately 22,000 computational cells within the cylinder at TDC, and features intake and exhaust ports as well as moving valves. Crevices are not modeled in this mesh. The turbulence model used is the standard KIVA-3V SKE model. Standard KIVA-3V wall functions and the log-law of the wall approach are used to model heat losses to the cylinder liner, head, piston and valves. The spray breakup model used for fuel spray is the in-built Taylor Analogy Breakup (TAB) model.

The simulation is set up to run without chemical kinetics calculations up to IVC, after which gasoline kinetics in conjunction with the 4-component surrogate described

earlier is used. The fully-coupled CFD/kinetics approach (described in section 2.3) is employed, with chemistry being solved in zones created from the computational mesh. The chemistry zone resolution is set such that ΔT within each zone is under 5 K and $\Delta\varphi$ within each zone is under 0.03. This resolution is chosen based on comparison of performance, in terms of ignition prediction and burn rate predictions, against a case where chemistry is solved in every CFD cell.

2.4.3 Performance evaluation

Combustion phasing sweep

First, a combustion phasing (or ignition timing) sweep at a typical HCCI operating point from the Olesky et al. experiments [14] is considered. In this sweep, the level of NVO is fixed at 157° CA, and combustion phasing is swept by means of manipulating intake temperature (T_{in}), using intake air heaters in the experiment. This sweep was performed under naturally aspirated conditions, with a fueling rate of approximately 9.5 mg/cycle injected during the NVO portion, with start of injection (SOI) timing at 330° CA bTDC and injection duration of 14.5° CA. The load, represented by net mean effective pressure (NMEP) was roughly 3 bar. Engine speed was 2000 RPM. The overall charge dilution, in terms of the ratio of fuel mass to diluent equivalence ratio (Φ') was 0.3, and the residual gas fraction was roughly 50%.

To evaluate the performance of the CFD model in terms of matching experimental trends at different ignition timings (measured by crank angle of 10% fuel energy released, CA10), a corresponding sweep using CFD is performed. Time-variant pressure profiles in the intake and exhaust ports are imposed onto the CFD simulation from the median-value point of the high-speed experimental data. These pressures are shifted for this sweep by +1.75% and -7% respectively to match the compression pressure trace from experiments. The median-value point from experiments is determined based on the point having the

median value of peak pressure. The simulation is initialized at 80° CA aTDC from the previous cycle. The initial temperature estimate prescribed to CFD is obtained from heat-release analysis (HRA) on experimental data. The initial temperature is raised by approximately 7.5% over the predictions from the HRA, based on three-pressure analysis (TPA) predictions from GT-Power for a nominal experimental HCCI point, because the TPA analysis (which is considered to be more accurate, since GT-Power models manifold flows using 1-D CFD, while the HRA uses phenomenological models for these flows) predicts a higher value of residual temperature at 80° CA aTDC.

The wall temperature solver in GT-Power is used to get estimates for component temperatures for a nominal point within this sweep. The temperatures imposed to the CFD simulation are roughly 25 K higher than those predicted by the GT-Power wall temperature solver, in order to match the combustion phasing range of the experimental sweep. The component temperatures imposed are specified in Table 2.3. Since there is considerable uncertainty in these predictions from GT-Power, and the primary objective of this portion of the evaluation is to investigate the behavior *at* a given combustion phasing, this manipulation is considered acceptable, and is not expected to vastly alter combustion trends for a given combustion phasing. The intake temperatures imposed on the CFD simulation are identical to those from the experiments.

Figure 2.2 shows pressure traces for three representative points from the combustion phasing sweep. The experimental results (200 cycles per point) are shown (in grey) along with the corresponding prediction from CFD simulation (in black). It is important to note the significant spread within the experimental results for any given point, which becomes larger at later combustion phasing. From Figure 2.2 it may be seen that the pressure predictions from the CFD simulations lie well within the experimental spread for each of the three operating points.

Figure 2.3 shows the comparison of pressure traces predicted by CFD with those from the experimental cycle with closest value of peak pressure compared to CFD

predictions. It is observed that when compared with such a cycle from the experimental data, the peak pressure rise rates match well with the experimental values, with the relative errors being -6.5%, +5.0% and +5.0% for the early, mid and late combustion phasing points respectively. The actual values of peak pressure rise rates from CFD simulations and experimental cycles with closest peak pressure values corresponding to the CFD simulation are given in Table 2.4.

This lends confidence to the performance of the CFD simulation in conjunction with the gasoline kinetics, in terms of capturing to the first order the effect of factors such as stratification and fuel chemistry on burn rates. This sort of model performance evaluation is the best possible given the near impossible nature of actually computing thermal and compositional stratification within all of the charge, since even optical techniques (such as those used in [15] typically only show stratification within a small 2-D window accounting for < 40% of the total area represented by $\pi.(bore^2/4)$.

NVO effects

With confidence in the CFD model in terms of capturing combustion phasing effects, the next test of the model is its ability to capture NVO effects for a fixed combustion phasing. It is believed that NVO generates significant thermal and compositional stratification, in addition to the natural wall heat loss-driven thermal stratification; and that this additional stratification could potentially extend burn duration. Olesky et al. [14] report that trading external charge heating (by heating intake air) for internal charge heating (by trapping hot internal residuals using NVO) results in longer burn durations represented by the crank angle interval between 10% of the fuel energy being released and 90% of the fuel energy being released (CA10-90). Two cases from the Olesky et al. experiments [14] are considered – one with lower NVO (NVO=157° CA) and higher T_{in} (T_{in} = 106° C), and another with higher NVO (NVO=179° CA) and lower

T_{in} (T_{in} = 45° C), such that both cases have the same fueling rate (9.5 mg/cycle) and ignition timing (CA10 ~ 2° CA bTDC). Both cases are run at 2000 RPM. A corresponding pair of low/high NVO CFD simulations is run, with the low NVO case having NVO=157° CA and *T*in = 106° C and the high NVO case having NVO = 181° CA and *T*in = 45° C. Figure 2.4 shows the burn profiles for both cases, from experiments (top) and CFD simulation (bottom). It is seen from the experimental results, that the higher NVO case has a longer burn duration represented by CA10-90. Olesky et al. [14] suggested that this could be because of the higher NVO trapping higher residuals, thus lowering oxygen content within the charge resulting in slower kinetics and heat release for the high NVO case. They also suggest that the higher NVO case probably has a higher level of thermal and compositional stratification which could potentially contribute to slowing down sequential autoignition in the high NVO case, resulting in longer burn duration. The effect of thermodynamic properties of residuals (lower γ and higher C_p) was also suggested as possible explanations for this observation. Obviously, with metal engine experiments alone, it is very hard to isolate these different concurrent effects in order to identify which effects are major and which are minor, which is one of the motivations for the current work. Most important to note from Figure 2.4 is that the CFD simulation (bottom of figure) captures experimental trends in terms of the higher NVO case showing longer burn duration compared to the lower NVO case. Qualitatively, the level of change in burn duration is also similar to experiments for a similar level of NVO change.

These two tests of the performance of the CFD model (capturing phasing effects on pressure trace and burn rates, and capturing NVO effects on burn duration) provide additional confidence in the application of the fully-coupled CFD/kinetics approach to the study of NVO effects and comparing different valve strategies in terms of their effect on HCCI burn duration. It must also be noted that this approach (CFD coupled with chemical kinetics) has been successfully applied by numerous researchers to model HCCI

operation for a range of engine designs and operating conditions, and the individual sub-models, such as sub-models for sprays, heat transfer and fuel chemistry come with their own fundamental validation over a range of conditions of which this nominal HCCI point forms a subset.

2.5 Quasi-dimensional multi-zone model development

2.5.1 Model setup

A quasi-dimensional multi-zone combustion model to simulate HCCI combustion is developed. In chapters 3,4 and 5, this model is used as a diagnostic tool in conjunction with cold-flow CFD simulations to decouple effects such as thermal stratification, compositional stratification and mixture thermodynamic properties in an attempt to understand the contribution of each of these effects to HCCI burn duration in isolation. In Chapter 6, the same model is adapted to function as a stand-alone combustion model intended for system-level simulation of HCCI combustion.

This combustion model divides the contents of the combustion chamber into multiple “zones”, with each zone having its own unique temperature and composition. Each zone can have a different mass, as long as the total mass of all zones equals the mass of all the cylinder contents; however zone masses are constant throughout the simulation. Zones do not exchange heat or mass (species) with each other; and they communicate with each other purely based on compression work to maintain uniform pressure within the cylinder. This multi-zone model falls under a class of quasi-dimensional HCCI combustion models colloquially known as “balloon-type” multi-zone models; since in essence each zone could be considered as a “balloon” of constant mass that is free to interact with the other balloons only by means of compression and expansion to maintain uniform pressure within the cylinder. Each zone may lose heat to the walls in a prescribed fashion, or alternatively, all the zones may be considered

adiabatic if the intent is purely to capture stratification effects on sequential autoignition. Chemical kinetics based on a prescribed chemical kinetic mechanism is used to describe chemical reactions within each zone. The overall cylinder volume varies based on the well-known crank slider kinematics relation, and the individual zone volumes vary in a manner such that the sum of volumes of all the zones at any instant is equal to the overall cylinder volume at that instant. If desired, the cylinder may also be considered as a constant volume chamber, but this is not done in the current work. Initial individual zone temperatures and composition may be imposed as desired, either from a companion non-reacting CFD simulation at some point, say pre-ignition in order to study the effects of stratification on burn duration, or alternatively, the multi-zone model may be used in a stand-alone fashion, and each zone could be allowed to develop its own temperature history based on a prescribed heat loss model. A diagrammatic representation of this model is given in Figure 2.5.

2.5.2 Numerical solution of system states

The total number of chemical species in the chemical kinetic mechanism used is denoted by *nsp*, and the total number of zones is denoted by *N*. Zone index is denoted by the letter *i*, and species index is denoted by the letter *k*. There are then *nsp*+1 system states solved within each zone – one zone temperature T_i and *nsp* species mass fractions $y_{i,k}$ (k=1→*nsp*). Since there are *N* zones, the total number of states for the whole combustion model is $N(nsp+1)$. It must be noted that the system states of one zone are coupled to system states of every other zone, since the overall pressure within the cylinder is uniform at every time-step of the numerical solution. The overall cylinder pressure is not included in the ordinary differential equation (ODE) system; however, it is computed at every time-step based on zone temperatures and composition using the ideal

gas law equation. It must be noted that the effect of heat and species diffusion between zones is not modeled.

Derivation of rate of change of species mass fraction in every zone

By applying mass continuity equations for a species *k* within a zone *i*, we have for any species *k*

$$\frac{dm_{i,k}}{dt} = \sum_{j=1;j\neq i}^{N} \dot{m}_{j\rightarrow i,k} + \dot{\omega}_{i,k} W_k V_i, \tag{2.15}$$

where the term on the left hand side (LHS) of the equation represents the rate of change of the mass of species *k* within zone *i*. The first term on the right hand side (RHS) of the equation represents the total rate of *influx* of mass of species *k* into zone *i* from all other zones given by the secondary zone index *j*. The second term on the RHS represents the rate of generation of species *k* (in terms of mass per unit time of species *k*) within zone *i* due to chemical reactions. Here, $\dot{\omega}_{i,k}$ represents the molar generation rate (in terms of moles per unit second per unit volume) of species *k* within zone *i* due to chemical reactions, which is computed using a chemical kinetic library based on the temperature, pressure and species mass fractions in zone *i*. W_k denotes the molecular mass of species *k*; and V_i denotes the volume of zone *i*. Since mass transfer between zones is not considered in the current model, the first term on the RHS drops out of the equation. Writing $m_{i,k}$ in terms of $y_{i,k}$ (mass fraction of species *k* in zone *i*) and m_i (mass of zone *i*), and V_i in terms of m_i and ρ_i (mass density of zone *i*), we get

$$\frac{m_i dy_{i,k}}{dt} = \frac{\dot{\omega}_{i,k} W_k m_i}{\rho_i} \tag{2.16}$$

Simplifying, we have

$$\frac{dy_{i,k}}{dt} = \frac{\dot{\omega}_{i,k} W_k}{\rho_i}, \tag{2.17}$$

which is the expression for the rate of change of mass fraction of species *k* in zone *i*. This expression is supplied to the numerical integrator used in the combustion model, which computes the rate of generation of every species in every zone at every time step.

Derivation of rate of temperature change in every zone

Applying the 1st law of thermodynamics (energy conservation) to zone *i*, we have

$$\frac{dU_i}{dt} = -\dot{Q}_i - \dot{W}_i , \tag{2.18}$$

where U_i is the total internal energy of zone *i*, $\dot{Q}_i$ is the rate of heat loss suffered by zone *i*, and $\dot{W}_i$ is the rate of pressure-work performed by zone *i*, at any instant. Rewriting U_i in terms of the total enthalpy of zone *i* (H_i), pressure within the zone *i* (*P*, which is identical to overall pressure within the cylinder) and V_i; and using the expression for pressure-work, we obtain

$$\frac{d(H_i - PV_i)}{dt} = -\dot{Q}_i - \frac{PdV_i}{dt}, \tag{2.19}$$

simplifying,

$$\frac{dH_i}{dt} - \frac{V_i dP}{dt} - \frac{PdV_i}{dt} = -\dot{Q}_i - \frac{PdV_i}{dt}, \tag{2.20}$$

$$\frac{m_i dh_i}{dt} - \frac{V_i dP}{dt} = -\dot{Q}_i \tag{2.21}$$

Expanding the first term on the LHS,

$$\frac{m_i dh_i}{dt} = m_i \frac{d}{dt}\sum_{k=1}^{nsp} h_{i,k}.y_{i,k}$$

$$= m_i\left[\sum_{k=1}^{nsp} h_{i,k}.\frac{dy_{i,k}}{dt} + \sum_{k=1}^{nsp} y_{i,k}C_{p,k}.\frac{dT_i}{dt}\right]$$

$$= m_i \sum_{k=1}^{nsp} h_{i,k}.\frac{dy_{i,k}}{dt} + m_i.\frac{dT_i}{dt}\sum_{k=1}^{nsp} y_{i,k}C_{p,k} \qquad (2.22)$$

$$= m_i \sum_{k=1}^{nsp} h_{i,k}.\frac{dy_{i,k}}{dt} + m_i.C_{p,i}\frac{dT_i}{dt}$$

In the above expansion, h_i represents the mass-specific enthalpy of zone *i*; and $C_{p,k}$ and $C_{p,i}$ represent the specific heat at constant pressure (with units of J/kg/K when SI units are employed) of species *k* and zone *i* respectively.

Writing the cylinder pressure using the ideal gas relation for the multi-zone system,

$$P = \frac{\sum_{j=1}^{N} m_j R_j T_j}{V}, \qquad (2.23)$$

where *j* is a secondary zone index, R_j is the average value of gas constant within zone *j*, T_j is the temperature of zone *j*, and *V* is the total volume of the cylinder at any given instant, determined based on crank-slider kinematics. Differentiating equation (2.23) with respect to time,

$$\frac{dP}{dt} = -\frac{\dot{V}}{V^2}\sum_{j=1}^{N} m_j R_j T_j + \frac{1}{V}\sum_{j=1}^{N}\left\{\frac{dm_j}{dt} R_j T_j\right\} + \frac{1}{V}\sum_{j=1}^{N}\left\{m_j T_j \frac{d}{dt}\left(\sum_{k=1}^{nsp}\frac{\bar{R}}{W_k} y_{j,k}\right)\right\} + \frac{1}{V}\sum_{j=1}^{N}\left\{m_j R_j \frac{dT_j}{dt}\right\}, \tag{2.24}$$

where $\dot{V}$ is the rate of change of cylinder volume determined by crank-slider kinematics and $\bar{R}$ is the universal gas constant (in J/mol/K when SI units are used). The second term on the RHS of equation (2.24) is zero in this case, since zones have constant mass. This gives us

$$\frac{dP}{dt} = -\frac{\dot{V}}{V^2}\sum_{j=1}^{N} m_j R_j T_j + \frac{1}{V}\sum_{j=1}^{N}\left\{m_j T_j \frac{d}{dt}\left(\sum_{k=1}^{nsp}\frac{\bar{R}}{W_k} y_{j,k}\right)\right\} + \frac{1}{V}\sum_{j=1}^{N}\left\{m_j R_j \frac{dT_j}{dt}\right\} \tag{2.25}$$

Using equations (2.22) and (2.25), in equation (2.21), we get an expression for the rate of change of temperature in zone *i* as

$$\begin{aligned}\frac{dT_i}{dt} = \frac{1}{-1 + \frac{m_i R_i}{\rho_i C_{p,i} V}}\Bigg[& \frac{1}{\rho_i C_{p,i}}\sum_{k=1}^{nsp}\left\{h_{i,k} W_k \dot{\omega}_{i,k}\right\} + \frac{\dot{Q}_i}{m_i C_{p,i}} \\ & + \frac{\dot{V}}{\rho_i C_{p,i} V^2}\sum_{j=1}^{N}\left\{m_j R_j T_j\right\} \\ & - \frac{\bar{R}}{\rho_i C_{p,i} V}\sum_{j=1}^{N}\left\{m_j T_j \sum_{k=1}^{nsp}\left(\frac{1}{W_k}.\frac{dy_{i,k}}{dt}\right)\right\} \\ & - \frac{1}{\rho_i C_{p,i} V}\sum_{j=1;j\neq i}^{N}\left\{\frac{m_j R_j dT_j}{dt}\right\}\Bigg]\end{aligned} \tag{2.26}$$

It must be noted that in equation (2.26), the rate of change of temperature in any zone is a function of the rate of change of temperature in every other zone, which is contained in the last term on the RHS. This coupling at every instant implies that a system of linear equations with *N* variables comprising of rate of change of temperature of every zone

needs to be solved at every time-step in order to determine the rate of change of temperature in every zone dT_i/dt as a function of known/determinable quantities at that instant.

The values of $dy_{i,k}/dt$ and dT_i/dt for i=1→N and k=1→nsp are thus computed at every time step, which allows the integrator to time-march the system and compute the values of the state variables $y_{i,k}$ and T_i (i=1→N and k=1→nsp) at every time step. The value of cylinder pressure is computed using equation (2.23). Additionally, other quantities of interest, such as mass fraction of fuel energy released may also be computed at every time-step based on the state variables of the system.

2.6 Sequential multi-zone approach

2.6.1 Modeling approach

The balloon multi-zone described in the previous section is used in a sequential manner with non-reacting CFD simulation. This approach is referred to in this document as the sequential multi-zone or sequential MZ approach.

A non-reacting CFD simulation is run starting at 80° CA aTDC of the previous cycle; through the exhaust and intake processes, up to 10° CA bTDC (pre-ignition) of the cycle being studied. The pre-ignition CFD domain is then binned in terms of temperature (T), mole percentage of oxygen (χ_{O2}) and fuel-oxygen equivalence ratio (ϕ_{FO}) into roughly 50-200 bins based on the resolution specified and stratification within the CFD domain. Every bin from the non-reacting CFD simulation is used to create a corresponding zone for the balloon multi-zone, and information such as species mass fractions, total mass and temperature from each CFD bin is mapped onto the corresponding balloon MZ zone. An illustration of this approach is shown in Figure 2.6. The balloon-MZ is thus initialized at this pre-ignition point (10° CA bTDC), and is run

through the combustion process with reactions computed using a supplied chemical kinetic mechanism and a standard thermo-kinetic library.

The primary application of the sequential-MZ approach in this work is to serve as a diagnostic tool, by means of which thermal stratification, compositional stratification and mean composition may be decoupled, and their effects on burn duration studied in isolation. For example, in order to remove compositional stratification effects while preserving thermal stratification effects on burn duration, the balloon MZ could be initialized at pre-ignition by imposing onto every MZ zone the temperature of the corresponding CFD bin and global *mean* composition (i.e. setting $y_{i,k} = \bar{y}_k$, i=1→N , k=1→nsp), instead of imposing composition from the corresponding CFD bin. Another scenario could be to isolate the effects of thermodynamic properties such as the ratio of specific heats of the mixture (γ) from chemical effects such as oxygen concentration, when comparing air dilution to external EGR (eEGR) dilution. For this, the mass fractions of species in the balloon MZ for eEGR dilution may be manipulated in such a way that products of combustion (CO_2 and H_2O) are replaced with N_2, such that the oxygen concentration remains the same as the eEGR case, however, the γ of the new mixture is same as that of the air dilution case. It is difficult to perform such diagnostic studies using the fully-coupled CFD/kinetics approach, whereas these studies are readily performed using the sequential MZ model.

2.6.2 Effect of turbulent diffusion and heat loss during combustion

Two major modeling simplifications in the sequential MZ are the omission of turbulent heat and mass diffusion between the Lagrangian zones, and neglecting wall heat loss from the zones after the CFD domain is mapped onto the balloon MZ. It must be noted however, that these effects are captured by the CFD solution up to the point where the transition is made from CFD to MZ. Thus, for the main combustion portion of the

solution, the turbulent diffusion effects and wall heat loss effects are not captured. This is mainly to simplify the multi-zone model since it is a challenge to accurately prescribe heat and mass diffusion rates between zones. There is not enough information to model the heat loss term $\dot{Q}_i$ in equation (2.26), and since the goal is to capture the effect of factors such as stratification and mean composition on burn duration, adiabatic combustion is assumed for the balloon MZ in the sequential MZ approach. It must be noted that the non-reacting CFD simulation preceding the multi-zone solution is still non-adiabatic, and captures the effect of wall heat losses on thermal stratification. This thermal stratification is then mapped onto the balloon MZ prior to ignition. Further, the motivation of the MZ is to purely capture stratification effects which are thought to be the primary contributors to differences in burn duration when going from one charge preparation strategy to another.

Before evaluating the performance of the sequential MZ against fully-coupled CFD, it is critical to understand the fundamental impact of neglecting turbulent heat and mass diffusion and also neglecting wall heat losses during combustion. Three cases are formulated to capture both mean composition effects and potential stratification effects arising from NVO:

- PVO case with air dilution
- PVO case with eEGR dilution (43% RGF - 36% eEGR, 7% iEGR)
- NVO case with 157° CA of NVO (43% RGF – 43% iEGR)

All cases have premixed fueling to simulate PFI, and same fuel content (9.3 mg) at IVC. The cases are run at an engine speed of 2000 RPM. Ignition timing (CA10) is matched by means of manipulating intake temperature, and is roughly at 2° CA bTDC for all the cases. Operation details for the three cases are provided in Table 2.5.

First, fully-coupled CFD/kinetics simulations for the three cases are performed. Chemical reactions are computed from IVC using a 312-species gasoline mechanism [5]

in conjunction with the four-component gasoline surrogate developed by Mehl et al. [5]. Then, corresponding test cases with fully-coupled CFD/kinetics simulations are performed with turbulent heat and mass diffusion as well as wall heat loss deactivated after ignition. This is achieved by setting the turbulent Prandtl number for heat diffusion and turbulent Schmidt number for mass diffusion to infinity, and setting adiabatic walls, during combustion (after 718° CA which is roughly CA10) for the test cases. The reason for this study is to investigate whether neglecting turbulent diffusion effects and wall driven heat losses during combustion affects relative trends in terms of burn duration for different charge preparation strategies.

Figure 2.7 shows the burn profiles from the fully-coupled CFD simulations including turbulent diffusion effects and wall heat loss during combustion, and Figure 2.8 shows the burn profiles from the fully-coupled CFD simulations where turbulent diffusion effects and wall heat losses are neglected during combustion (from 718° CA, which roughly corresponds to CA10). It may be noted from Figure 2.7 and Figure 2.8 that neglecting turbulent diffusion effects and wall heat loss effects during combustion does not have a significant impact on the overall trends in burn duration for strategies with different composition and potentially different stratification.

This result by itself does not truly confirm that neglecting turbulent diffusion effects and the assumption of adiabatic combustion do not alter relative trends in burn duration since errors from one assumption could potentially fight errors associated with other assumptions. For example, turbulent diffusion of radicals and heat from ignited regions to un-ignited regions during combustion might help accelerate ignition to the un-ignited regions. Thus neglecting turbulent diffusion effects could potentially increase the burn duration predicted. However, neglecting wall heat losses during combustion, could potentially shorten burn duration by not allowing energy to escape to the walls, keeping temperatures high, thus accelerating sequential autoignition. Thus, the act of neglecting turbulent diffusion could potentially mask the effects of neglecting wall heat losses.

To investigate these effects thoroughly, the test cases are run with each of these effects turned off in isolation. That is, the fully coupled simulation for each of the three test cases is restarted at 718° CA (for the main combustion) with:

(a) Turbulent Prandtl number for heat diffusion set to infinity with non-adiabatic walls and turbulent mass diffusion permitted

(b) Turbulent Schmidt number for mass diffusion set to infinity with non-adiabatic walls and turbulent heat diffusion permitted

(c) Adiabatic walls with turbulent heat diffusion and turbulent mass diffusion permitted

Figure 2.9, Figure 2.10 and Figure 2.11 show the burn profiles for the three test cases for restarts (a), (b) and (c) respectively. Comparing burn profile trends with Figure 2.7, where turbulent diffusion effects and wall heat losses are included, it may be noted that the trends in burn duration going from one charge preparation strategy to another are largely unaffected with these simplifying assumptions applied in isolation, which provides confidence in using these assumptions in the context of the sequential MZ applied as a diagnostic.

Effect of turbulent heat diffusion and turbulent mass diffusion on sequential autoignition rate in isolation of wall heat loss effects

After showing that turbulent heat and mass diffusion effects as well as wall heat losses do not affect trends in burn duration with different strategies, it is interesting to investigate the effect of turbulent heat diffusion and turbulent mass diffusion on sequential autoignition rates in isolation of wall heat loss effects. For this three variations of the three test cases described before (PVO-air, PVO-eEGR and NVO-iEGR) are compared. The fully coupled simulation for each of the three test cases is restarted at 718° CA (for the main combustion) with:

(a) Adiabatic walls, turbulent heat diffusion and turbulent mass diffusion permitted

(b) Adiabatic walls, turbulent mass diffusion permitted, but turbulent heat diffusion turned off

(c) Adiabatic walls, turbulent heat diffusion permitted, but turbulent mass diffusion turned off

Comparing burn durations for the three test cases with variations (a) and (b) gives an indication of the importance of turbulent heat diffusion effects between CFD cells on sequential autoignition. Figure 2.12 shows the burn profiles for the three test cases based on the variation (a), shown on top and the variation (b), shown on the bottom. It may be noted that there is an insignificant difference in burn duration as a result of turbulent heat diffusion effects being ignored as in variation (b) compared to variation (a), where they are included. This indicates that turbulent heat diffusion, at least as modeled within KIVA-3V, under these conditions does not play a significant role in accelerating or decelerating the overall sequential autoignition process.

Comparing burn durations for the three test cases with variations (a) and (c) gives an indication of the importance of turbulent mass diffusion effects between CFD cells on sequential autoignition. Figure 2.13 shows the burn profiles for the three test cases based on the variation (a), shown on top and the variation (c), shown on the bottom. It may be noted that there is consistently an increase in burn duration as a result of turbulent mass diffusion effects being ignored as in variation (c) compared to variation (a), where they are included. The relative increase in burn duration for the PVO-air case is +8.7%, that for the PVO-eEGR case is +9.8% and that for the NVO-iEGR case is +9.0%. This indicates that turbulent mass diffusion, at least as modeled within KIVA-3V, under these conditions has a consistent effect of speeding up the autoignition process, however neglecting this effect (as is done in the sequential MZ approach after the CFD domain is mapped onto the balloon multi-zone) does not affect relative trends in burn duration going from one charge preparation strategy to another, at least in the context of the charge preparation strategies studied in the current investigation.

2.6.3 Performance evaluation of sequential MZ against fully coupled CFD/kinetics

For the sequential MZ to serve as a reliable diagnostic tool, it should be able to capture the effect of stratification as well as mean composition on HCCI burn duration. The fully-coupled CFD/kinetics approach has already been evaluated against experiments, and it was shown that this approach performs well in terms of capturing peak pressures, pressure rise rates; as well as the effect of increasing NVO. Further, it was also shown that the simplifying assumptions made during combustion do not impact the trends in terms of burn profiles going from one strategy to another. The sequential MZ is evaluated against the fully-coupled CFD/kinetics approach in terms of its ability to capture mean composition effects as well as effects resulting from different levels of internally trapped residuals on HCCI burn duration.

Corresponding sequential MZ runs are performed for the three test cases described in the preceding sections – PVO-air, PVO-eEGR and NVO-iEGR (by performing a non-reacting CFD run up to 10° CA bTDC and running the balloon MZ by mapping temperature and species from the non-reacting CFD run). For the sequential MZ, the temperature of every zone needs to be raised by a fixed amount (roughly 10-15 K for every case, with all zone temperatures are incremented by the same amount for a given case), to match ignition timing with the fully-coupled CFD/kinetics simulation. This adjustment does not affect the relative temperature distribution between the zones pre-ignition (since the temperature of all the zones is increased by the same quantity), and is required, since for the sequential MZ, the *non-reacted* composition is mapped to the balloon MZ. Thus, the effect of any radicals formed before 10° CA bTDC (captured by the fully-coupled CFD/kinetics approach) is not captured by the sequential MZ approach. It is critical to match ignition timing since burn duration is a strong function of ignition timing, and it is intended to study the effect of other factors such as stratification and mean composition on burn duration *for a given ignition timing.*

For the current evaluation, the binning of computational cells within the CFD domain from the non-reacting CFD run, for creation of balloon MZ zones, is done in such a way that the $\Delta T_{\text{bin}} < 5$ K, $\Delta\chi_{O2bin} < 2\%$ and $\Delta\ \phi_{FO} < 0.05$. This resolution within the "reaction-space" spanned by T, ϕ_{FO} and χ_{O2} results in the creation of 88 zones for the PVO-air dilute case, 55 zones for the PVO-eEGR case and 177 zones in the case of the NVO-iEGR case. This resolution is arrived upon based on comparing the fidelity in overall ignition delay distribution using zone average properties to the ignition delay distribution arrived at by computing ignition delay using the He et al. [16] ignition delay correlation for iso-octane in every CFD cell at 10° CA bTDC for the non-reacting CFD simulation from which zones are formed. This comparison is shown in Figure 2.14 for the three cases. It may be seen from Figure 2.14 that the cumulative ignition delay distribution (which in essence determines sequential autoignition and burn duration) is retained within the balloon MZ for the zoning limits chosen.

Figure 2.15 and Figure 2.16 show the in-cylinder pressure traces and burn profiles for the fully-coupled CFD/kinetics approach and the sequential MZ approach for the three cases studied. From Figure 2.15 it may be seen that the pressure traces are well matched trend-wise when comparing fully-coupled CFD/kinetics results to the sequential MZ results. It is seen from Figure 2.16 that for the fully-coupled CFD/kinetics simulation, the burn duration for the PVO-air dilute case is the shortest, closely followed by the PVO-eEGR dilute case. The NVO-iEGR dilute case has a noticeably longer burn duration than the other two cases for the same ignition timing. The burn duration difference between the PVO-air dilute case and PVO-eEGR dilute case is possibly due to differences in composition of the diluent, and the longer burn duration for the NVO-iEGR case is possibly due to stratification effects. At this point however, the reasons for the differences can only be hypothesized. However, it is more important to note that the sequential MZ captures these differences in the burn durations pretty well compared to the fully-coupled CFD/kinetics approach. The actual burn durations in terms of CA10-90

predicted by the fully-coupled CFD approach are shown in relation to those predicted by the sequential MZ approach (which has several simplifying assumptions such as omitting turbulent diffusion between zones and omitting wall heat losses) in Table 2.6 along with the relative errors.

It must be kept in mind however, that the overall trends in burn duration going from one strategy to another are preserved with the sequential MZ compared to the fully-coupled CFD, which is the primary concern. This gives us confidence to apply the sequential MZ tool as a diagnostic to decouple various concurrent effects and identify the reasons for the differences in burn duration with different diluents and different valve strategies.

2.7 Reaction space analysis method

In order to understand the key factors that contribute to HCCI burn duration it is important to develop an understanding of the reaction space, since HCCI burn duration is a result of sequential autoignition within *reaction space*, with more reactive parcels of charge igniting before less reactive ones, irrespective of their physical location in terms of *x,y* and *z* co-ordinates.

To perform analysis within this reaction space, we need to define a metric for reactivity, as well as choose dimensions to span the reaction space. The ignition delay expression proposed by He et al. [16], based on rapid compression machine (RCM) experiments, is chosen as the reactivity metric in the current work. The expression is as follows:

$$\tau_{ign} = 1.3\text{x}10^{-4}.P^{-1.05}.\phi_{FO}^{-0.77}.\chi_{O_2}^{-1.41}.e^{\frac{33700}{RT}}, \quad (2.27)$$

where τ_{ign} represents ignition delay in milliseconds, *P* represents pressure in atmosphere, ϕ_{FO}represents the fuel-oxygen equivalence ratio, χ_{O2} represents the oxygen mole

percentage, R is the universal gas constant in cal/K/mol and T is the temperature in Kelvin.

This ignition delay is chosen because it has a simple algebraic form, is a direct *qualitative* indicator of reactivity, with lower ignition delays signifying a more reactive mixture. This expression is valid for iso-octane over a range of naturally aspirated conditions, and has been successfully employed to model gasoline HCCI ignition in simple HCCI combustion models [17, 18]. With the development and validation of ignition delay correlations for gasoline, the natural next step would be to adopt a gasoline ignition delay correlation as a more precise metric for reactivity. However, for the purposes of the current study, a qualitative indicator of reactivity is sufficient, since we are not interested in predicting actual ignition timing of the charge.

This ignition delay expression has a constant slope when represented as $\log\tau_{ign}$ versus 1000/T, and does not capture any Negative Temperature Coefficient (NTC)-like behavior. In order to evaluate if capturing this behavior is critical to the analysis done in the current work, which is restricted to naturally aspirated conditions, single-zone, adiabatic constant volume ignition delay computations using the 312-species gasoline mechanism [5] are performed over a range of temperatures at the near-TDC point (at 10° CA bTDC or pre ignition based on the cases in section 2.6.2) with in-cylinder pressure of 24 bar. The composition for these computations was taken to be representative of the mean composition of the PVO-eEGR case and NVO-iEGR case described in section 2.6.2 with a ϕ_{FO} of 0.44 and RGF of 43%. The ignition delays from these computations (taking the time of 10% mass fraction burned in the single-zone simulations to represent ignition timing) are shown alongside the ignition delay predictions from the He et al. [16] correlation for the same conditions in Figure 2.17. From the CFD simulations in section 2.6.2, it was observed that more than 90% of the mass is hotter than 1000 K. Based on Figure 2.17, it may be clearly seen that for this near-TDC pressure (24 bar) resulting from naturally aspirated operation, and for this typical HCCI composition the ignition delay

predictions from the He et al. correlation [16] agree well with those from gasoline kinetics up to roughly $1000/T = 1.0$ or for $T > 1000$ K. Deviation from linear behavior (which cannot be captured by the ignition delay correlation) is shown by the gasoline kinetics only for $1000/T$ values greater than 1.0 which represents temperatures lower than 1000 K. Since we do not typically see temperatures lower than 1000 K in a major portion of the charge from 10° CA bTDC onwards (the hottest 90% of the charge is over 1000 K at 10° CA bTDC based on CFD simulations in section 2.6.2) it is likely that NTC-like behavior does not play a significant role in determining ignition delays under the conditions studied in this work, and that the He et al. [16] correlation is a good qualitative indicator of reactivity within the cylinder pre-ignition. Another observation supporting the reasoning that NTC effects do not play a significant role in ignition determination under these conditions is that the burn profile curves for typical naturally aspirated HCCI conditions simulated using the fully-coupled CFD approach in section 2.6.2 (Figure 2.7) do not show any clear two-step ignition indicative of NTC effects and Low Temperature Heat Release (LTHR). However, it must be noted that under boosted conditions, NTC-like behavior could play a significant role in determining reactivity distribution within the charge. For these conditions, the ignition delays computed using the He et al. [16] correlation might not be representative of actual ignition delays based on kinetics.

The independent dimensions for the reaction space follow directly from the RHS of equation (2.27), where the independent variables T, $\phi_{FO}$and χ_{O2} are chosen to represent the reaction space. The variable P is obviously not chosen as a reaction space dimension, as it is uniform throughout the cylinder. The ignition delays thus computed within every CFD cell serve to provide a metric for reactivity distribution; and in the cumulative form over the charge mass, ignition delay serves as an indicator of "reactivity stratification".

Figure 2.18 shows an illustration of the pre-ignition reaction space (at 10° CA bTDC) visualized for the earliest igniting case from the combustion phasing study

performed in section 2.4.3. This reaction space is visualized based on a CFD run corresponding to that case with chemical kinetics turned off. Temperature bins are shown on the *x*-axis and ϕ_{FO} bins are shown on the *y*-axis. Cells from the CFD domain are put into these bins based on their values of *T* and ϕ_{FO}. The average temperature and composition in each bin is computed, and based on this (along with the cylinder pressure), the ignition delay is computed within each bin using equation (2.27). The bins are colored by this computed value of ignition delay based on the color scale shown in the figure. The figure is also annotated with a lines passing through bins with roughly the same ignition delays. These parallel lines are in a sense iso-reactivity lines. The progress of the HCCI sequential autoignition wave is then perpendicular to these iso-reactivity lines as indicated for illustration in the figure. It may be inferred from the slope of these iso-reactivity lines, that for this illustration case, an increase in ϕ_{FO} of 0.5 is worth an increase in *T* of 50 K in terms of ignition delay. This observation provides some insight into the relative effect of stratification in the ϕ_{FO}dimension and *T* dimension on reactivity. It is important to understand that HCCI sequential autoignition is directly related to *reactivity stratification* and only indirectly related to thermal and compositional stratification.

For a more rigorous analysis of the relative contribution of stratification in the *T*, ϕ_{FO} and χ_{O2} dimensions on reactivity stratification, we take the partial derivates of τ_{ign} to *T*, ϕ_{FO} and χ_{O2} individually and evaluate the sensitivity of τ_{ign} for nominal pre-ignition conditions at 10° CA bTDC of *T*=1050 K, ϕ_{FO} = 0.5 and χ_{O2} = 15%, we get ΔT = 50 K $\equiv\Delta\phi_{FO}$ = 0.5 $\equiv\Delta\chi_{O2}$ = 8% in terms of their effect on $\Delta\tau_{ign}$.

Figure 2.19 shows the reaction space visualized in terms of cumulative mass above a certain ignition delay for this case. From the figure, it may be seen that the earliest igniting 10% of charge mass has ignition delays within 1 ms, which corresponds to 12° CA at this engine speed (2000 RPM). This gives us a rough prediction of the time delay between this pre-ignition point at 10° CA bTDC and the actual CA10 value when

10% of the charge has burned. It turns out that for this case CA10 is approximately at 2° CA bTDC which represents an 8° CA interval between this pre-ignition point and the CA10 point. Thus the prediction of 12° CA is very close to the actual ignition delay. The actual CA10 point occurs slightly earlier than what we would expect from the snapshot of the reaction space at 10° CA bTDC, since these ignition delays are for constant volume; however in the actual simulation, the volume is constantly reducing (and pressure increasing as a consequence) due to compression from the piston, which serves to increase the reactivity within all of the charge as the piston moves toward TDC.

It is also seen from Figure 2.19 that the 90% of the charge mass has an ignition delay lower than 5 ms, if we consider constant volume combustion. However, this is not the case in reality, as once the most reactive regions ignite and expand, increasing the overall cylinder pressure and compressing the initially less reactive regions, the reactivity of these regions increases rapidly, causing them to in reality have an ignition delay far lower than 5 ms. However, this pre-ignition snapshot provides a qualitative picture of the reactivity stratification within the cylinder and can be directly related (in terms of trends) to the ultimate 10-90 burn duration. This is a valuable technique to compare two different charge preparation strategies in a qualitative manner, head to head, pre-ignition, in terms of their stratification, and try to understand the impact of various kinds of stratification on burn duration.

Table 2.1 – Gasoline surrogate composition taken from Mehl et al. [5]

Simulation Type	**Mass Fraction**
iso-octane	0.5413
n-heptane	0.1488
toluene	0.2738
2-pentene	0.0361

Table 2.2 – UM-FFVA engine specifications used in CFD simulations

Cylinder displacement (L)	0.540
Bore/Stroke (mm)	86.0/94.3
Connecting Rod Length (mm)	152.2
Compression Ratio	12.22:1
IVC/EVO	130°bTDC/148°aTDC
Swirl Ratio	0.3

Table 2.3 – Component temperatures used in CFD simulation

$\mathbf{T_{head}}$	450 K
$\mathbf{T_{piston}}$	480 K
$\mathbf{T_{liner}}$	450 K
$\mathbf{T_{exh.\ valve}}$	490 K
$\mathbf{T_{int.\ valve}}$	480 K

Table 2.4 – Peak pressure rise rates –CFD versus experimental cycle (with closest peak pressure to CFD), for combustion phasing sweep with fixed NVO of 157°

Case	CA10 (°CA aTDC)	Expt. $\mathbf{PRR_{max}}$ (bar/°CA)	CFD $\mathbf{PRR_{max}}$ (bar/°CA)	% error CFD vs. expt.
Early	-1	4.74	4.43	-6.5
Mid	0	3.62	3.80	+5.0
Late	3	2.14	2.25	+5.0

Table 2.5 – Operating conditions for test cases based on three different charge preparation strategies

Parameter	PVO-air dilution	PVO-eEGR dilution	NVO-iEGR dilution
Fueling	PFI	PFI	PFI
NVO	0° CA	0° CA	157° CA
$\boldsymbol{\phi_{FO}}$ (mean)	0.33	0.44	0.44
$\boldsymbol{\chi_{O2}}$ (mean)	20%	15%	15%
T_{in}	213°C	241°C	98°C
Internal Residual	7%	7%	42%
External Residual	0%	36%	0%
Total RGF	7%	43%	42%

Table 2.6 – Burn duration predictions from CFD and sequential MZ for the three test cases (charge preparation strategies) studied

Case	Fully-coupled CFD CA10-90 (° CA)	Sequential MZ CA10-90 (° CA)	% error seq. MZ vs. CFD
PVO-air	5.0	4.3	-14
PVO-eEGR	5.5	4.8	-13
NVO-iEGR	7.2	6.5	-10

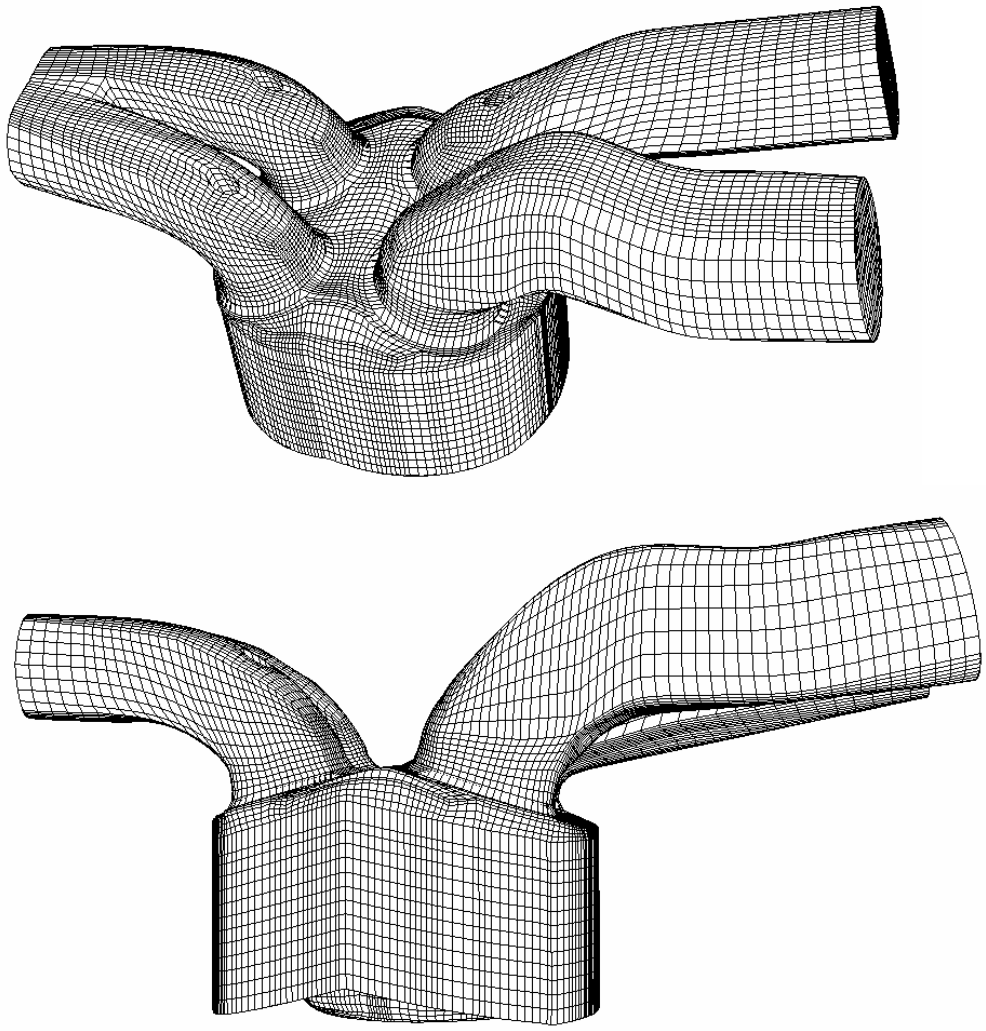

Figure 2.1 – CFD mesh of FFVA engine used in simulations

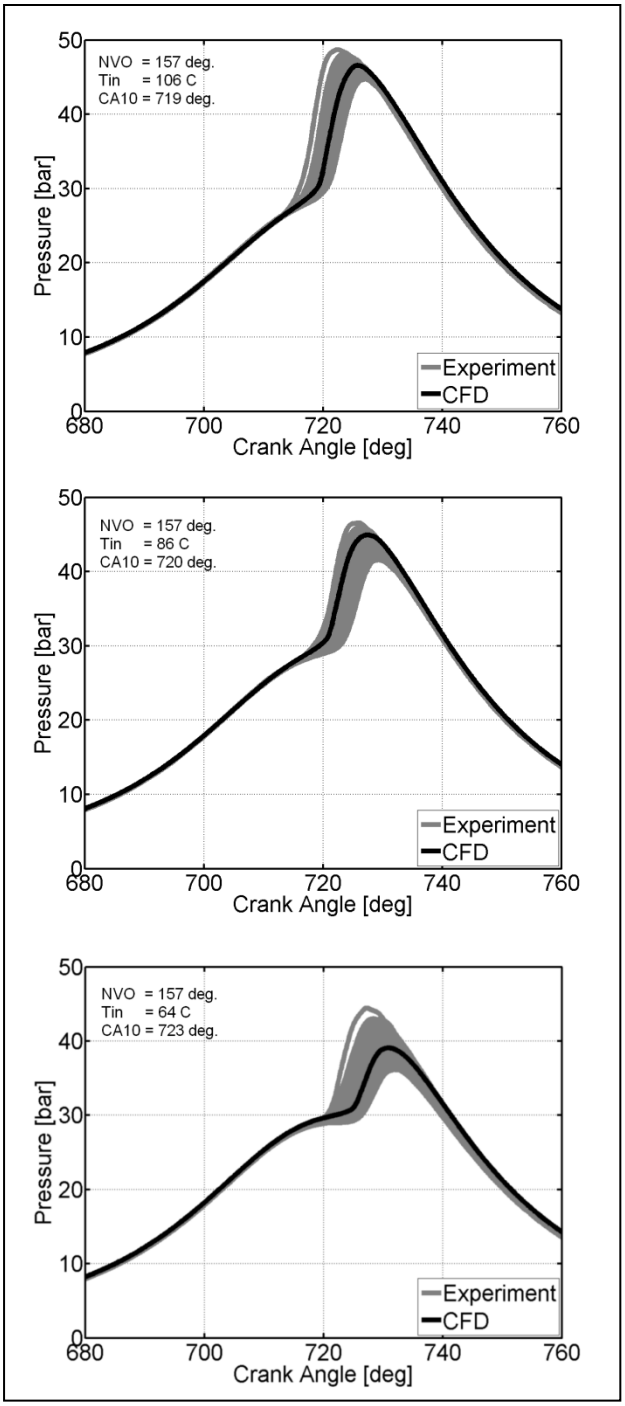

Figure 2.2 – Pressure traces from combustion phasing sweep; experiments versus CFD: 9.4 mg/cycle injected, fixed NVO (157°), T_{in} = 106°C (top), 86°C (middle), 64°C (bottom), RGF (experiment) = 48%, RGF (CFD) = 43%, Φ (experiment) = 0.6, Φ (CFD) = 0.55, Φ'(experiment) = 0.3, Φ'(CFD) = 0.3

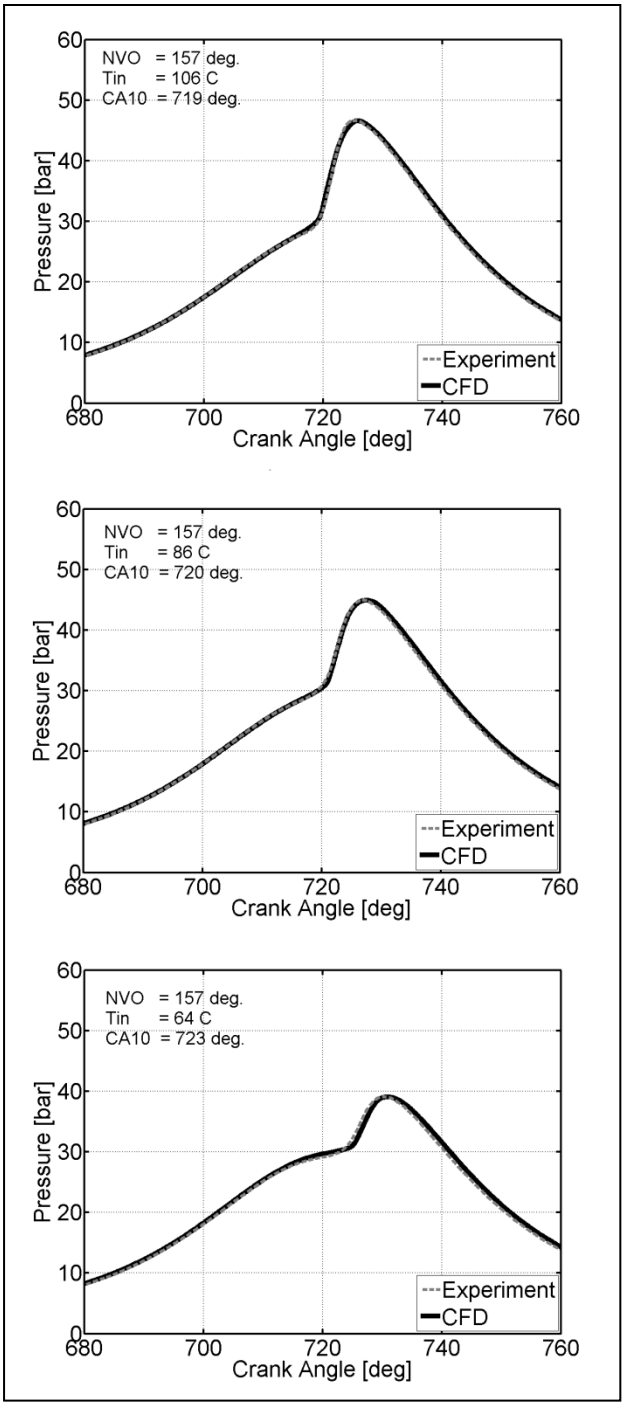

Figure 2.3 – Pressure traces from combustion phasing sweep; experiments versus CFD: 9.4 mg/cycle injected, fixed NVO (157°), T_{in} = 106°C (top), 86°C (middle), 64°C (bottom), RGF (experiment) = 48%, RGF (CFD) = 43%, Φ (experiment) = 0.6, Φ (CFD) = 0.55, Φ'(experiment) = 0.3, Φ'(CFD) = 0.3. Experimental cycle with closest peak pressure to CFD predictions shown.

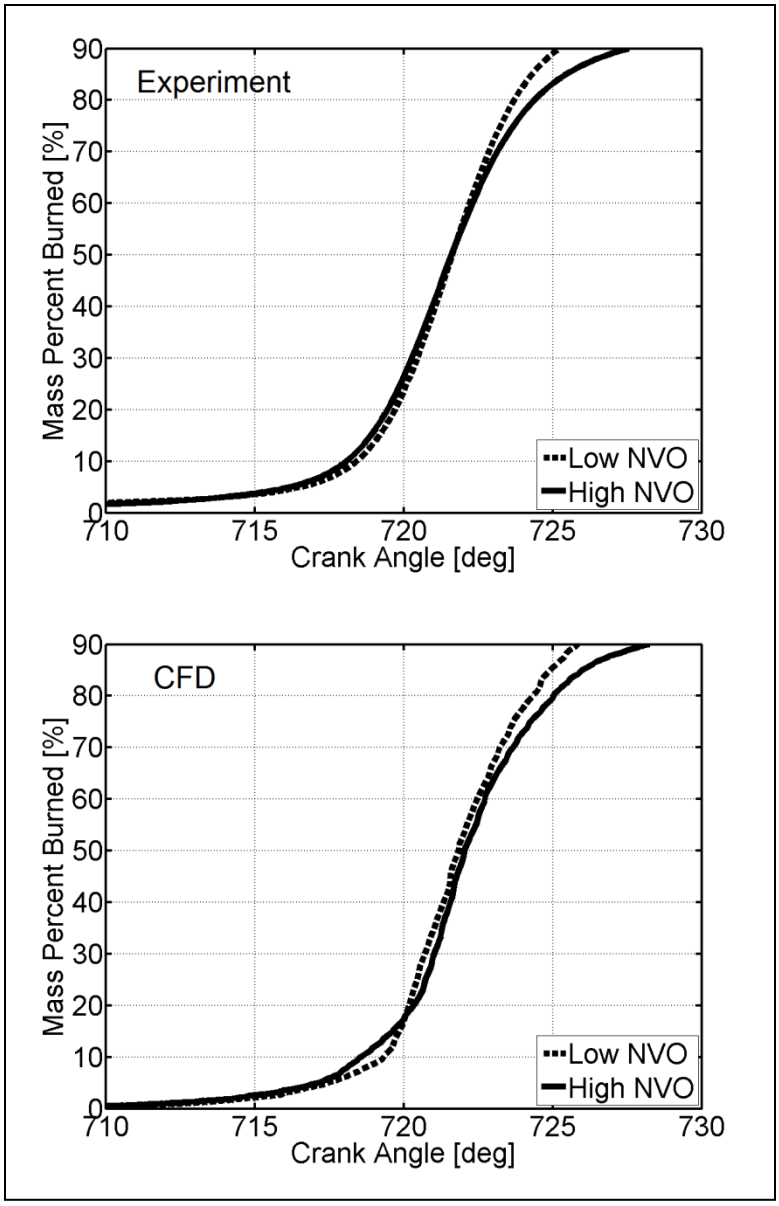

Figure 2.4 – Comparison of burn profiles for high and low NVO cases – experiments and CFD results, experiment: high NVO = 179°, low NVO = 157°; CFD: high NVO = 181°, low NVO = 157°

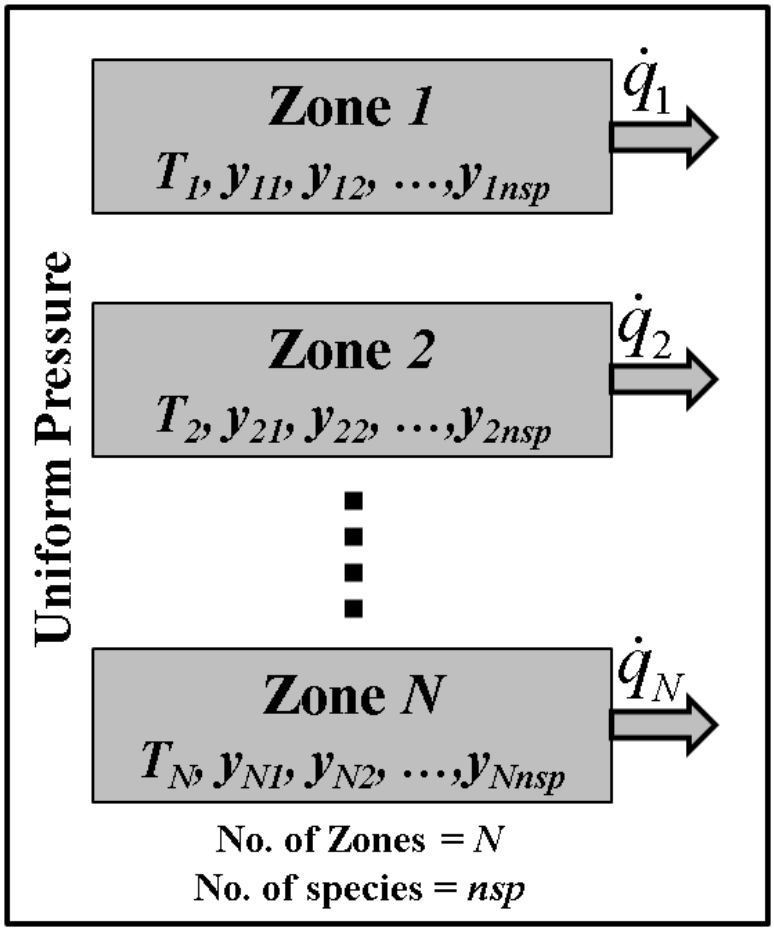

Figure 2.5 – Illustration of balloon MZ setup

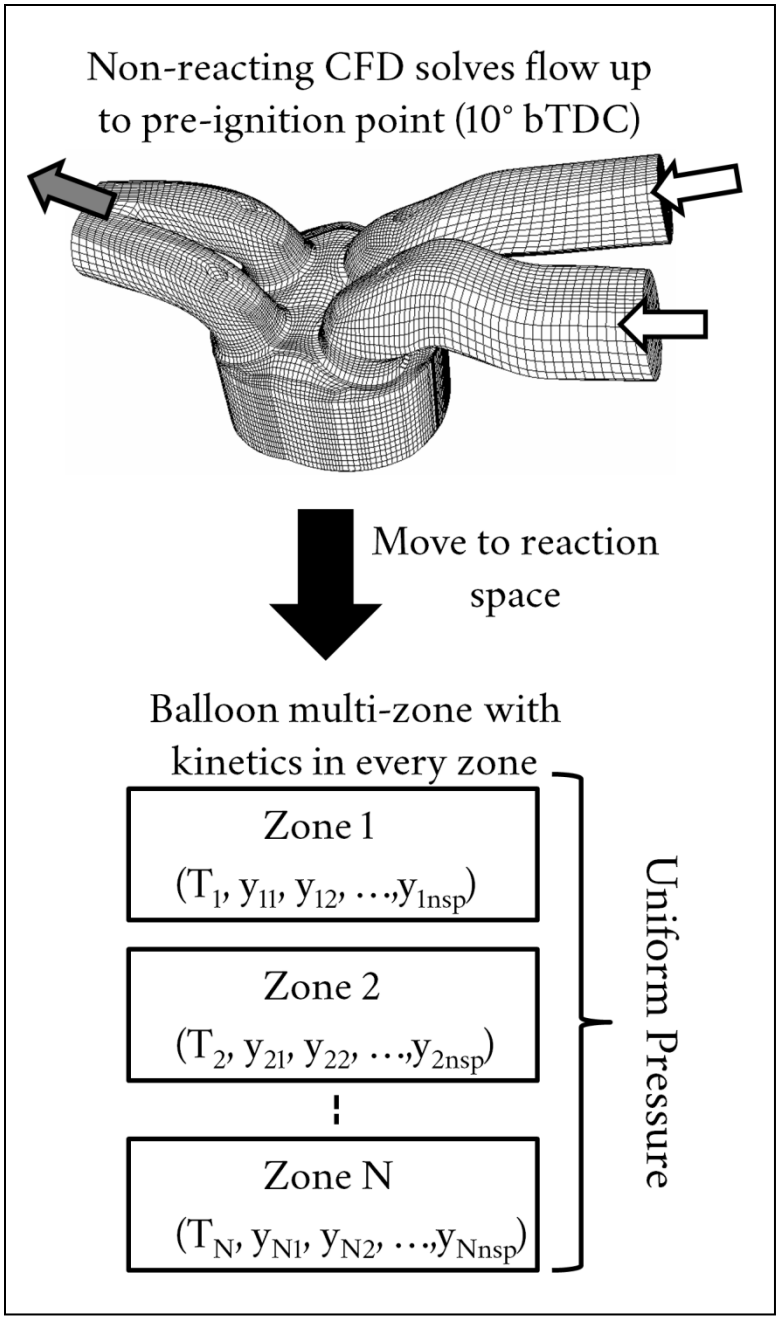

Figure 2.6 – Illustration of sequential MZ setup

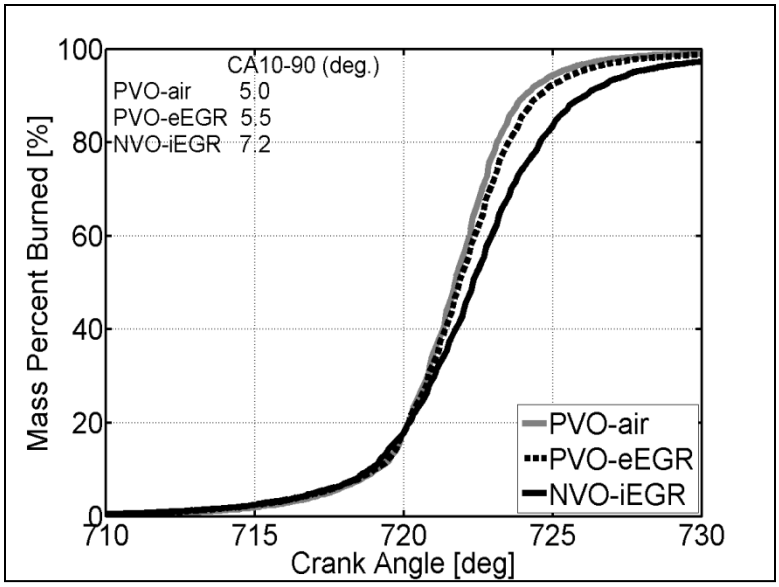

Figure 2.7 – Mass percentage burned profiles for PVO-air dilution, PVO-eEGR dilution and NVO-iEGR dilution; predictions from CFD with turbulent diffusion effects considered and non-adiabatic walls during combustion

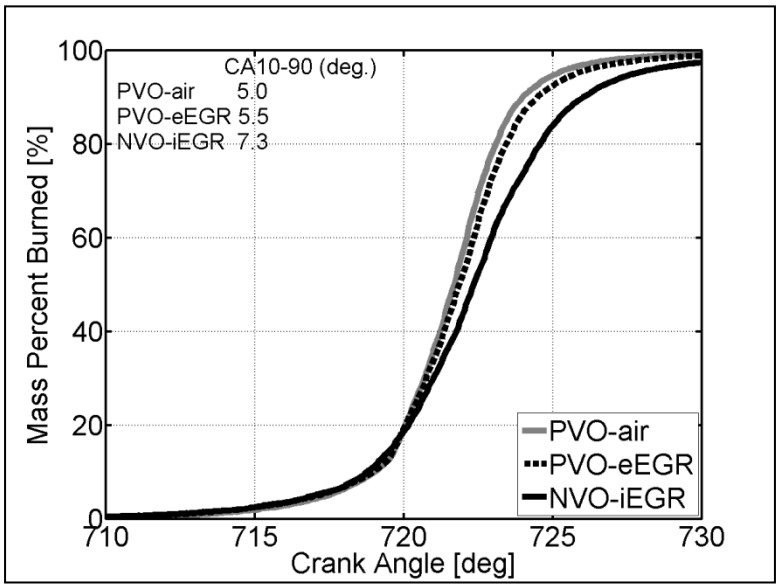

Figure 2.8 – Mass percentage burned profiles for PVO-air dilution, PVO-eEGR dilution and NVO-iEGR dilution; predictions from CFD with turbulent diffusion effects neglected along with the assumption of adiabatic walls during combustion (after 718° CA)

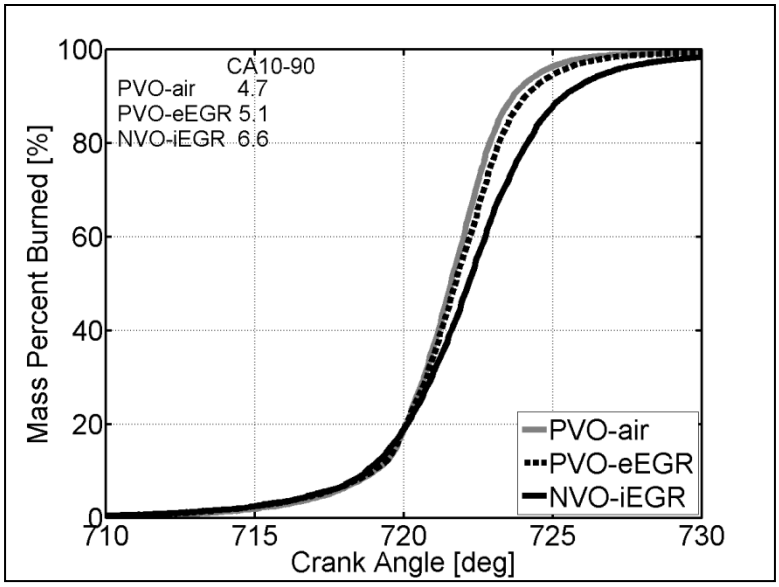

Figure 2.9 – Mass percentage burned profiles for PVO-air dilution, PVO-eEGR dilution and NVO-iEGR dilution; predictions from CFD with turbulent heat diffusion effects neglected during combustion (post 718° CA) while turbulent mass diffusion considered along with non-adiabatic walls (It must be noted that turning off turbulent heat diffusion in effect turns off wall heat losses too in KIVA-3V, since wall heat loss fluxes are based on the turbulent Prandtl number)

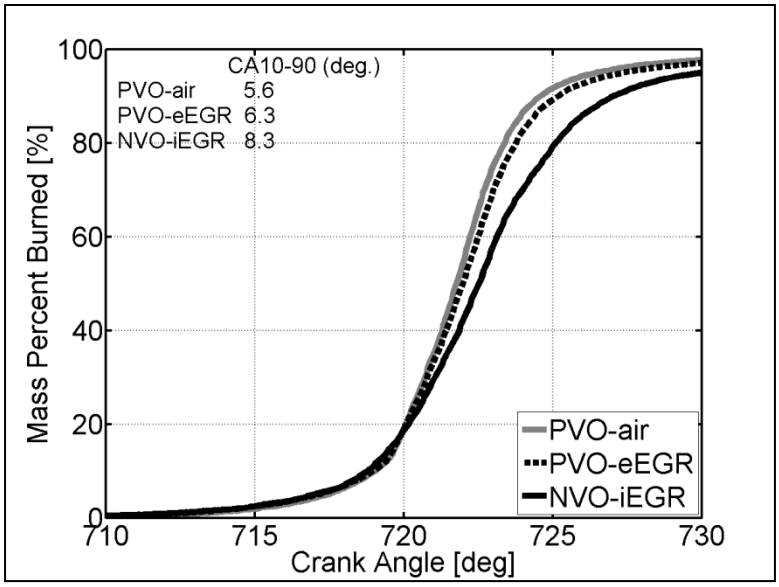

Figure 2.10 – Mass percentage burned profiles for PVO-air dilution, PVO-eEGR dilution and NVO-iEGR dilution; predictions from CFD with turbulent mass diffusion effects neglected during combustion (post 718° CA) while turbulent heat diffusion is allowed throughout along with non-adiabatic walls throughout

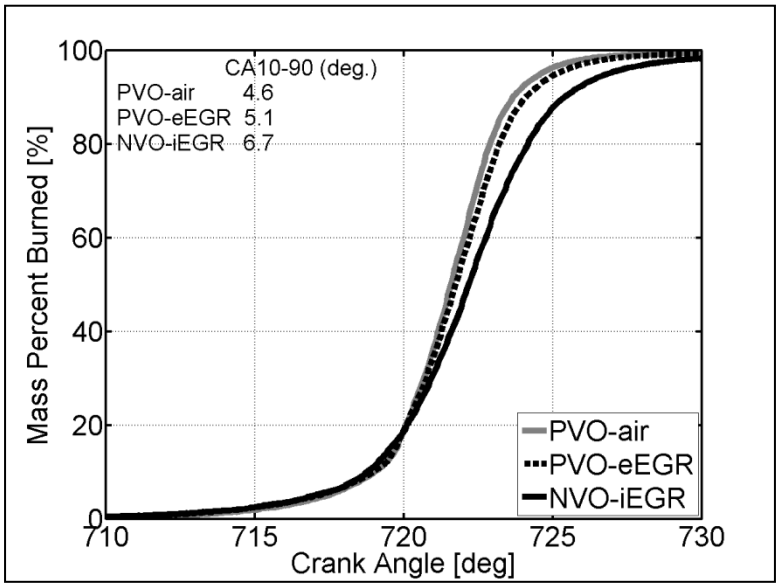

Figure 2.11 – Mass percentage burned profiles for PVO-air dilution, PVO-eEGR dilution and NVO-iEGR dilution; predictions from CFD with adiabatic walls during combustion (post 718° CA) while turbulent heat and mass diffusion are allowed throughout the simulation

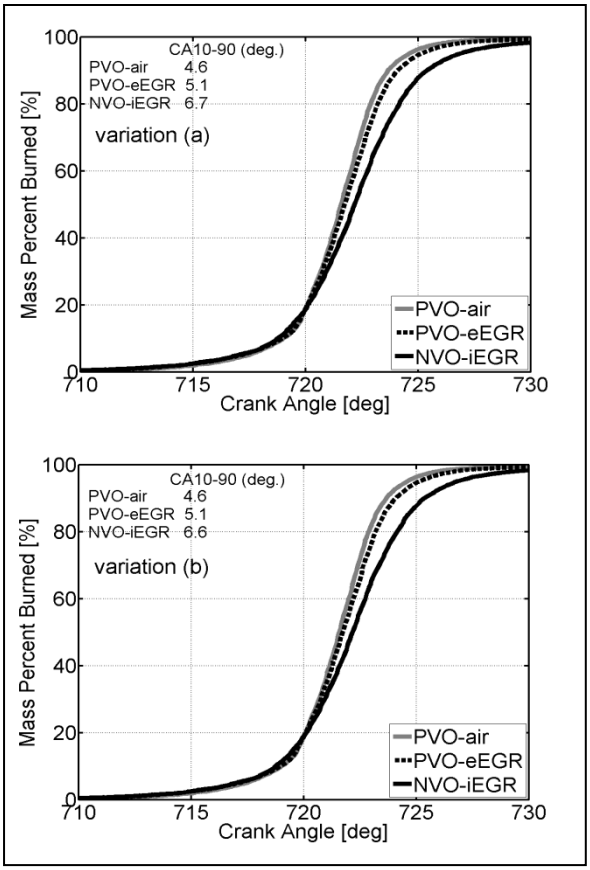

Figure 2.12 – Effect of turbulent heat diffusion on sequential autoignition: Mass percentage burned profiles for PVO-air dilution, PVO-eEGR dilution and NVO-iEGR dilution; predictions from CFD based on variation (a) – adiabatic walls during combustion (post 718° CA) with turbulent heat and mass diffusion included and variation (b) – adiabatic walls and no turbulent heat diffusion during combustion (post 718°CA), with turbulent mass diffusion allowed throughout

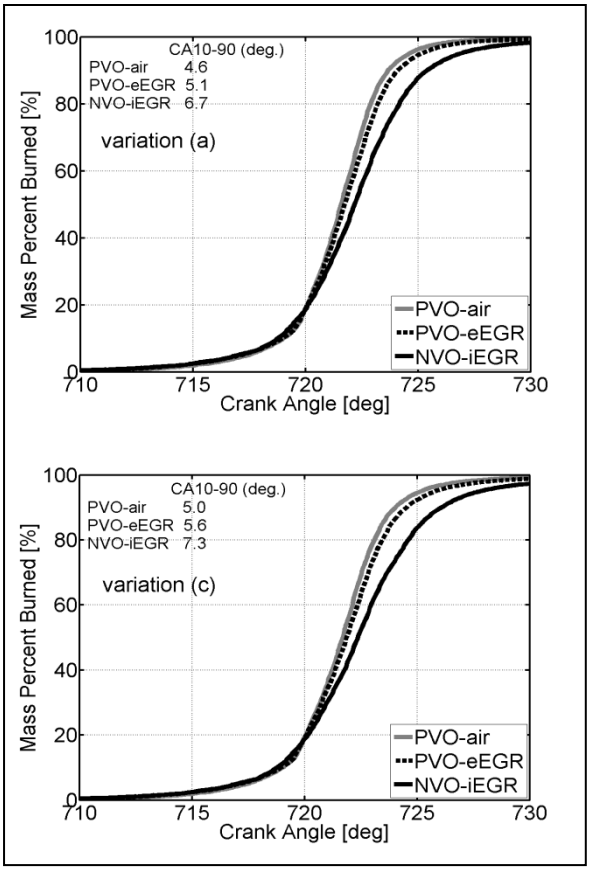

Figure 2.13 – Effect of turbulent mass diffusion on sequential autoignition: Mass percentage burned profiles for PVO-air dilution, PVO-eEGR dilution and NVO-iEGR dilution; predictions from CFD based on variation (a) – adiabatic walls during combustion (post 718° CA) with turbulent heat and mass diffusion included and variation (c) – adiabatic walls and no turbulent mass diffusion during combustion (post 718°CA), with turbulent heat diffusion allowed throughout

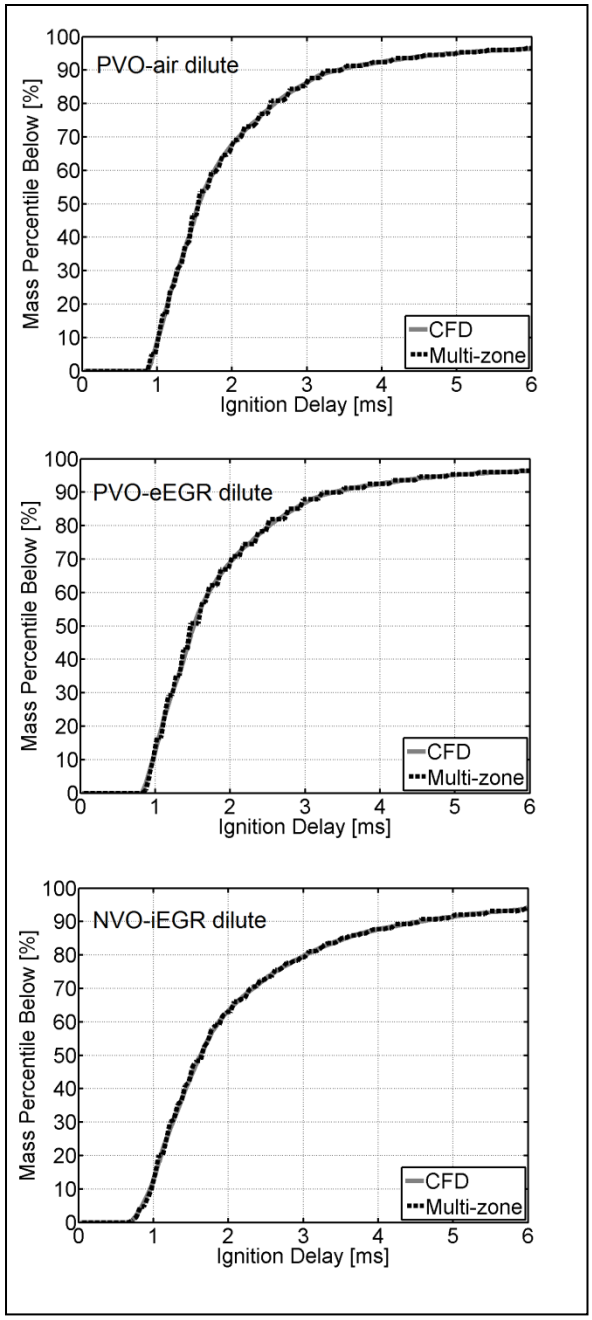

Figure 2.14 – Ignition delay computations for CFD (in every cell) versus computation in every zone based on binning resolution used

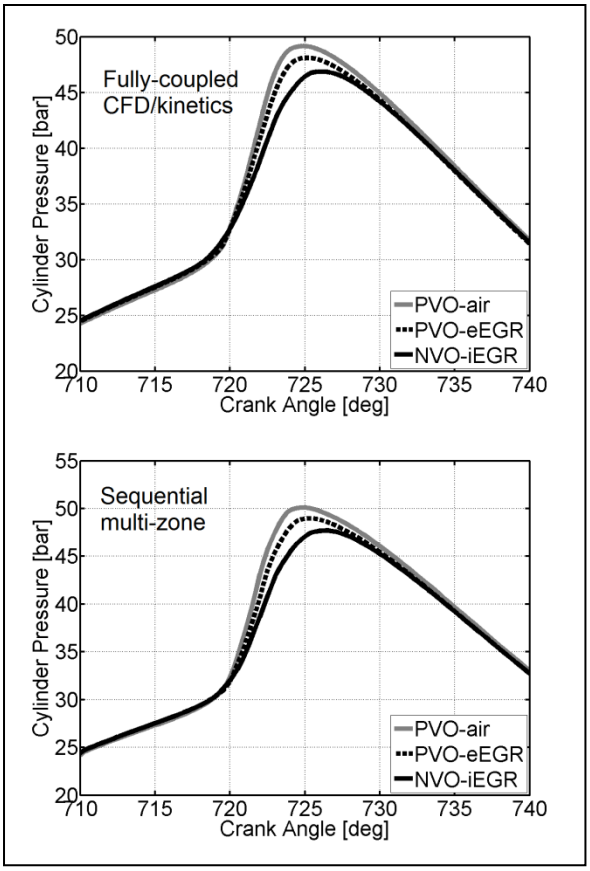

Figure 2.15 – In-cylinder pressure traces for PVO-air dilution, PVO-eEGR dilution and NVO-iEGR dilution; predictions from CFD (top) and sequential multi-zone (bottom)

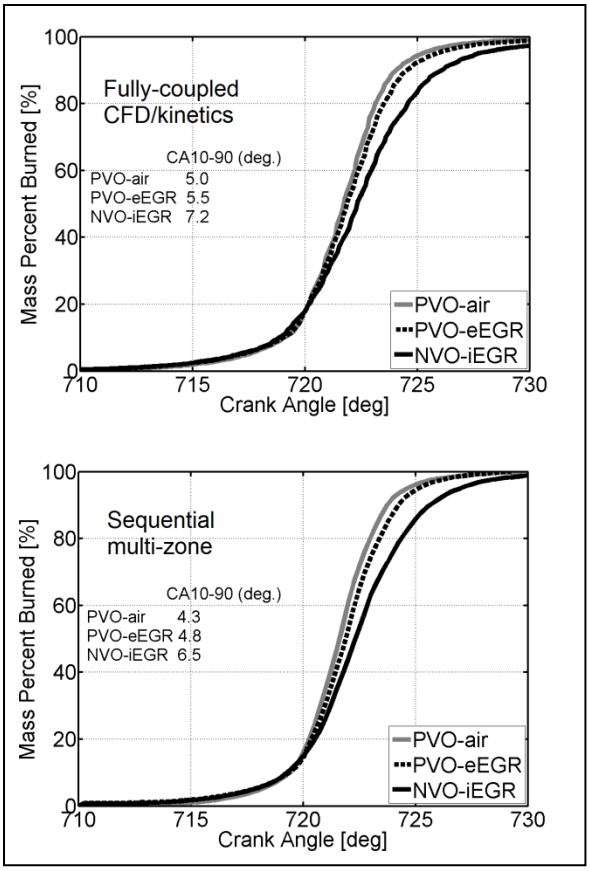

Figure 2.16 – Mass percentage burned profiles for PVO-air dilution, PVO-eEGR dilution and NVO-iEGR dilution; predictions from CFD (top) and sequential multi-zone (bottom)

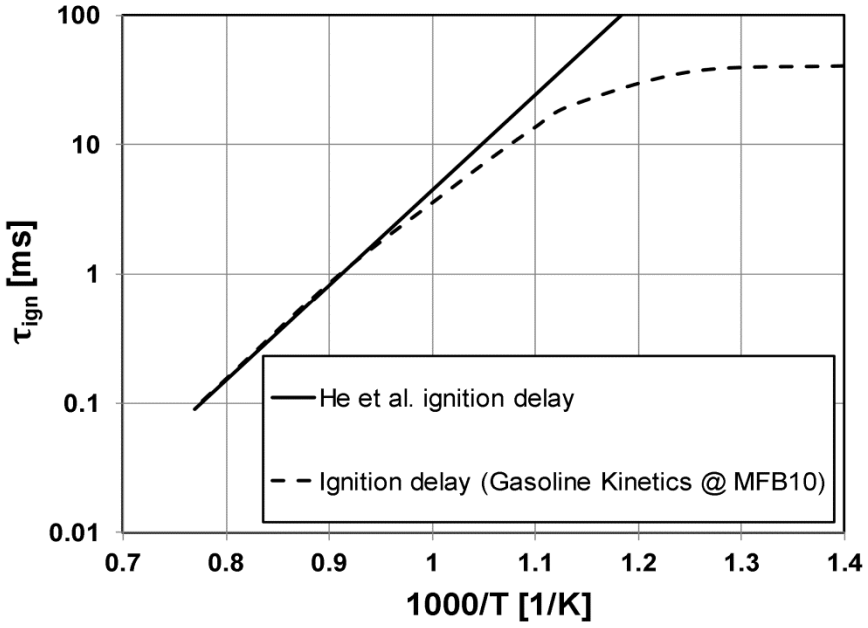

Figure 2.17 – Comparison of ignition delay predictions based on the He et al. [16] correlation against ignition delay predictions (where ignition is considered at 10% mass fraction burned) from adiabatic, constant volume reactor simulations using the 312-species gasoline kinetics [5] under pre-ignition conditions (at 10° CA bTDC) corresponding to CFD simulations (Phi = 0.44, RGF = 43%, P = 24 bar)

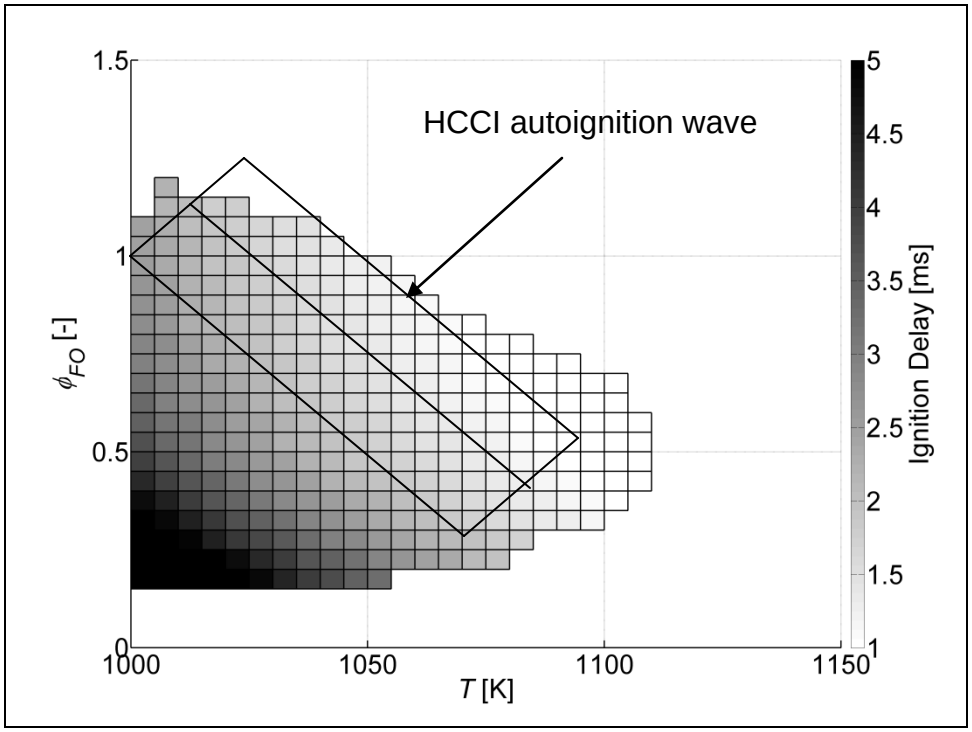

Figure 2.18 – Pre-ignition reaction space (at 10° CA bTDC), visualized in *T* and ϕ_{FO}space for a case with 157° NVO, direct injection with SOI at 330° CA bTDC, and CA10 at approximately 2° CA bTDC; computed from CFD simulation

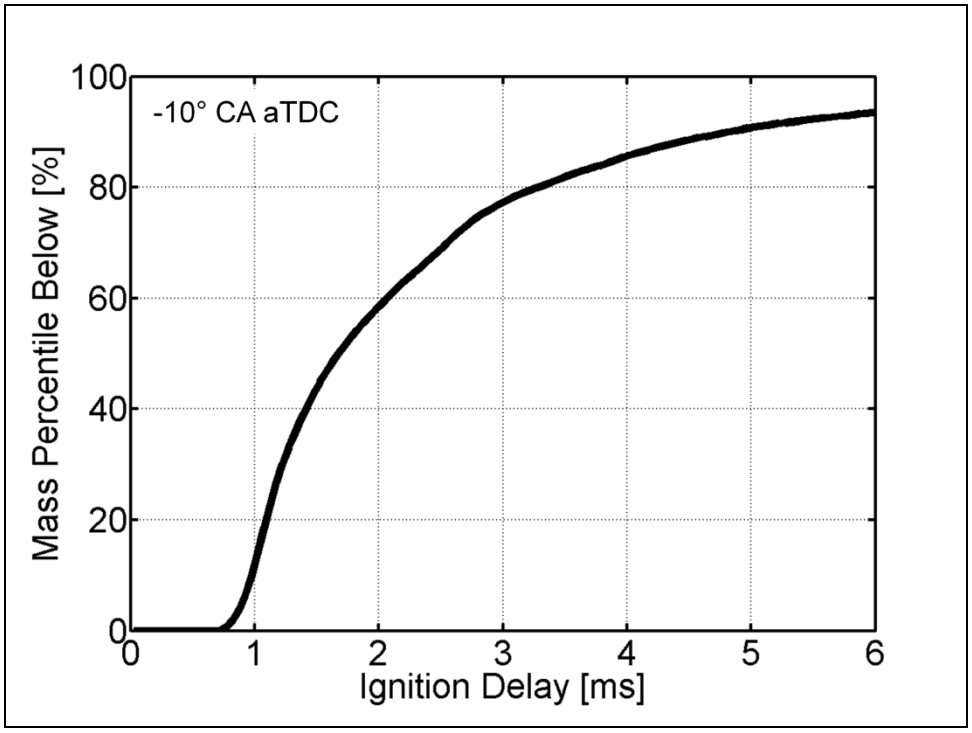

Figure 2.19 – Pre-ignition reaction space (at 10° CA bTDC) visualized in terms of cumulative charge mass below a certain ignition delay, for a case with 157° NVO, direct injection with SOI at 330° CA bTDC, and CA10 at approximately 2° CA bTDC; computed from CFD simulation

2.8 References

1. Amsden, A.A., "KIVA-3V: A Block Structured KIVA Program for Engines with Vertical or Canted Valves," Los Alamos National Laboratory Report LA-13313-MS, 1997.

2. Amsden, A. A., Ramshaw, J. D., O'Rourke, P. J., and Dukowicz, J. K., "KIVA: A Computer Program for Two- and Three-Dimensional Fluid Flows with Chemical Reactions and Fuel Sprays," Los Alamos National Laboratory Report LA-10245-MS, 1985.

3. Amsden, A. A., O'Rourke, P. J., and Butler, T. D., "KIVA-II: A Computer Program for Chemically Reactive Flows and Sprays," Los Alamos National Laboratory Report LA-11560-MS, 1989.

4. Han, Z. and Reitz, R.D., "Turbulence Modeling of Internal Combustion Engines Using RNG k-ε Models," *Combustion Science and Technology*, Vol. **106**, Issues 4-6, pp. 267-294, 1995.

5. Mehl, M., Chen, J.Y., Pitz, W.J., Sarathy, S.M., and Westbrook, C. K., "An Approach for Formulating Surrogates for Gasoline with Application toward a Reduced Surrogate Mechanism for CFD Engine Modeling," *Energy & Fuels*, Vol. 25, Issue 11, pp. 5215-5223, 2011.

6. Mehl, M., Pitz, W.J., Westbrook, C.K., and Curran, H.J., "Kinetic Modeling of Gasoline Surrogate Components and Mixture Under Engine Like Conditions," *Proceedings of the Combustion Institute*, **33**:193-200, 2011.

7. Mehl, M., Pitz, W.J., Sarathy, M., Yang, Y., and Dec, J.E., "Detailed Kinetic Modeling of Conventional Gasoline at Highly Boosted Conditions and the Associated Intermediate Temperature Heat Release," SAE Paper 2012-01-1109, 2012.

8. Dec, J.E., and Yang, Y., "Boosted HCCI for High Power without Engine Knock and with Ultra-Low NOx Emissions – using Conventional Gasoline," SAE Paper 2010-01-1086, 2010.

9. Kong, S. –C., Marriot, C. D., Reitz, R. D., and Christensen, M., "Modeling and Experiments of HCCI Engine Combustion Using Detailed Chemical Kinetics with Multidimensional CFD," SAE Paper 2001-01-1026, 2001.

10. Agarwal, A., and Assanis, D., "Multi-Dimensional Modeling of Natural Gas Ignition under Compression Ignition Conditions Using Detailed Chemistry," SAE Paper 980136, 1998.

11. Sankaran, R., and Im, H. G., "Effects of Mixture Inhomogeneity on the Auto-Ignition of Reactants Under HCCI Environment," *Proceedings of the 42nd AIAA Aerospace Sciences Meeting and Exhibit*, AIAA Paper 2004-1328, 2004.

12. Babajimopoulos, A., Assanis, D.N., Flowers, D.L., Aceves, S.M., and Hessel, R.P., "A fully coupled computational fluid dynamics and multi-zone model with detailed chemical kinetics for the simulation of premixed charge compression ignition engines," *International Journal of Engine Research*, Vol. 6, Issue 5, pp. 497-512, 2005.

13. Kodavasal, J., Keum, S., and Babajimopoulos, A., "An extended multi-zone combustion model for PCI simulation," *Combustion Theory and Modelling*, 2011, Vol. **15**, Issue 6, pp. 893-910, 2011.

14. Olesky, L. M., Vavra, J., Assanis, D., and Babajimopoulos, A., "Internal residual vs. elevated intake temperature: how the method of charge preheating affects the phasing limitations of HCCI combustion," *Proceedings of the ASME 2012 Internal Combustion Engine Spring Technical Conference*, ICES2012-81127.

15. Rothamer, D. A., Snyder, J. A., Hanson, R. K., Steeper, R. R., and Fitzgerald, R. P., "Simultaneous imaging of exhaust gas residuals and temperature during HCCI combustion," *Proceedings of the Combustion Institute* **32**:2869-2876, 2009.

16. He, X., Donovan, M. T., Zigler, B. T., Palmer, T. R., Walton, S. M., Wooldridge, M. S., and Atreya, A., "An experimental and modeling study of iso-octane ignition delay

times under homogeneous charge compression ignition conditions," *Combustion and Flame*, Vol. 142, pp. 266-275, 2005.

17. Babajimopoulos, A., Challa, V. S. S. P., Lavoie, G. A., and Assanis, D. N., "Model-Based Assessment of Two Variable Cam Timing Strategies for HCCI Engines," *Proceedings of the ASME Internal Combustion Engine Division 2009 Spring Technical Conference*, ICES2009-76103.

18. Mamalis., S., Babajimopoulos, A., Guralp, O., and Najt, P., "Optimal Use of Boosting Configurations and Valve Strategies for High Load HCCI – A Modeling Study," SAE Paper 2012-01-1101, 2012.

CHAPTER 3

EFFECT OF DILUENT COMPOSITION

3.1 Background

HCCI operation requires high levels of charge dilution to achieve acceptable rates of energy release as well as low combustion temperatures. Low combustion temperatures are needed to ensure that engine-out NOx emissions from HCCI are not greater than tail-pipe out NOx from SI operation (generally < 20 ppm), since unlike stoichiometric SI operation, lean HCCI exhaust cannot be treated for NOx using a TWC, as the exhaust products need to be close to stoichiometric for effective NOx reduction in the TWC. Moreover, low combustion temperatures have the added advantage of lower heat transfer losses. The most common ways to achieve charge dilution are:

- Using excess (of stoichiometric) air, by operating unthrottled or boosted
- Using EGR - recirculating products of combustion (comprised of major species such as H_2O, CO_2 along with N_2 and unused O_2) from the previous cycle

A combination of air and EGR dilution might also be employed to achieve the overall level of dilution required to lower energy release rates and combustion temperatures. When EGR is used as a means to achieve dilution, it is primarily inducted as cooled, external EGR (eEGR). An eEGR loop is set up wherein the EGR is tapped from the exhaust runner, then passed through an EGR cooler to reduce its temperature, and is finally mixed with the intake air typically at the intake runner. A throttle on the exhaust side typically controls the back-pressure which in turn is used to control the flow of

eEGR back into the intake, thus controlling the eEGR fraction in air/eEGR mixture entering the intake port.

In order to ensure that the eEGR is well mixed with the incoming air, researchers such as Dec et al. [1] mix the eEGR with intake air well before the intake plenum and use a series of bends in the plumbing to the intake plenum to further enhance mixing. The goal is to deliver a homogenous diluent charge (air plus eEGR) to the cylinder.

The diluent composition affects the thermodynamic and chemical kinetic properties of the charge. Since eEGR contains the tri-atomic molecules of H_2O and CO_2, the overall specific heat of the mixture (C_p) increases with an increase in the eEGR fraction within the charge. In addition, the ratio of specific heats of the charge (C_p/C_v, γ) is lowered with increasing eEGR fraction.

The lower γ affects the temperatures at the end of compression, and with all other parameters being the same, increasing the fraction of eEGR within the charge serves to retard ignition. Researchers such as Dec et al. [2] use products of combustion to control combustion phasing under boosted conditions, when intake temperatures (T_{in}) need to be lowered significantly to achieve the required combustion phasing. Here, the primary purpose of eEGR is not to achieve dilution (to control burn duration and NOx emissions); rather, it serves as a means to achieve control over ignition timing. Dec et al. [2] indicate that under boosted conditions, with pure air-dilution, intake temperatures lower than 330 K were required to properly phase combustion to comply with ringing limits. Although their experimental setup allows T_{in} to be reduced as low as about 300 K, T_{in} = 330 K was selected as the lower limit in their engine performance study as it is representative of intercooler-out temperatures for production boosted engines; further, maintaining T_{in} = 330 K prevents condensation of water from the eEGR.

Dec et al. [1] were interested in understanding the effect of eEGR dilution on gasoline HCCI energy release rates and NOx emissions in isolation from its effect on ignition timing. Intake charge heating was used to compensate for combustion retard

caused by eEGR. They found that eEGR addition results in a small reduction in peak Heat Release Rate (HRR) even when the combustion phasing (represented by the crank angle of 50% burn, CA50) was matched. They report that Pressure Rise Rate (PRR) within the cylinder was reduced from 5 → 4 bar /°CA when 51% eEGR was applied. They also found that under the conditions studied within their work, using eEGR resulted in an increase in NOx emissions as they increased overall fueling rate to maintain Gross Indicated Mean Effective Pressure (IMEPg) the same as the air-dilute case, which resulted in higher peak combustion temperatures with eEGR operation. They merely reported the observations pertaining to HRR and did not attempt to explain the reasons for these observations; since these were done on a metal engine with minimal diagnostic capabilities.

Despite the work of Dec et al. [1], there remains a misconception in the engine-community that eEGR serves to increase burn duration and lower NOx emissions. The primary reason for the observations of increased burn duration and lower NOx emissions with the use of eEGR appears to be a natural consequence of combustion retard (brought about by using eEGR) which may alternatively be achieved by other means such as cooling the intake. It is of interest to understand the fundamental impact of eEGR on combustion characteristics such as burn duration and NOx emissions *for a given ignition timing*. In other words, it is interesting to explore the possibility of using eEGR as a means to control burn duration independent of combustion phasing (which may be controlled by some other means such as level of iEGR or intake temperature). It is also important to understand the benefits of replacing air with eEGR in reducing NOx emissions for a fixed combustion phasing determined by other operating constraints

3.2 Conditions for current CFD study

In this work, it is attempted to isolate the effects of eEGR on HCCI combustion characteristics independent of the effect of eEGR on ignition timing. Full cycle CFD simulations at 2000 RPM with the FFVA engine mesh are performed using PVO valve lifts (with valve overlap ~ 0° CA). We use PVO with negligible overlap to minimize possible effects due to stratification caused by internal residuals from the previous cycle. The internal residuals contribute to approximately 7% of the total charge mass in this study for both the air and eEGR cases. We use PFI for both cases, and for the simulation, we impose a fully-premixed fuel-air/fuel-air-eEGR composition to the intake runner. The intake composition in each case is manipulated to achieve 9.3 mg of fuel trapped within the cylinder at IVC, so that both cases have the same fuel-energy content available for combustion. For the eEGR case, air is replaced by products of complete combustion (which also include excess O_2, since overall combustion is lean, and N_2) such that at IVC, the overall Residual Gas Fraction (RGF) for the air-dilute case is 7% (completely from internal residuals) and for the eEGR-dilute case is 43% (a combination of 7% internal residual and 36% externally imposed EGR at the intake). The overall dilution levels for both the cases are similar with $\Phi' \sim 0.3$. The air-dilute case has a mole-percentage of oxygen (χ_{O2}) of approximately 20% and the eEGR-dilute case has $\chi_{O2} \sim 15\%$. This difference results in the overall fuel-oxygen equivalence ratios (ϕ_{FO}) to vary for the two cases; $\phi_{FO} = 0.33$ for the air-dilute case and $\phi_{FO} = 0.44$ for the eEGR dilute case. The 312-species gasoline mechanism [3] is used in both cases in conjunction with the 4-component surrogate [3] described in Chapter 2. Both cases required heating of the intake charge, with the eEGR case heated to a greater extent (T_{in} = 241°C) compared to the air-dilute case (T_{in} = 213°C) in order to match ignition timing defined by CA10, which for both cases is approximately at 2° CA bTDC. These differences are also summarized in Table 3.1.

3.3 Differences in pressure traces and burn profiles

Figure 3.1 compares the in-cylinder pressure traces for the two cases at this operating condition. From the figure, we observe that the eEGR-dilute case has a slightly lower pressure rise rate and a lower peak pressure. Looking at the burn profiles (shown in Figure 3.2), we note that the eEGR dilute case has a slightly slower burn. The burn duration in terms of CA10-90 for the air-dilute case is 5.0° CA, while for the eEGR-dilute case it is 5.5° CA, representing a 10% increase in burn duration with eEGR dilution under these conditions. These observations are in agreement with those of Dec et al. [1] who found a small reduction in energy release rates when replacing air dilution with eEGR dilution.

3.4 Analysis of pre-ignition reaction space at 10°bTDC

In order to understand the reasons for these differences in burn duration, we analyze the reaction space for both cases prior to ignition. Figure 3.3 shows the reaction space for both cases at 10° CA bTDC at which point roughly 1% of the charge is burned (CA1). The *x*-axis is spanned by *T*; the *y*-axis is spanned by ϕ_{FO}, and χ_{O2} is represented by a color-scale. The first thing we observe from Figure 3.3 is that both the air-dilute and eEGR-dilute cases have negligible stratification in composition. The standard deviations in ϕ_{FO} and χ_{O2} are minimal compared to the standard deviation in temperature. We have $\sigma\phi_{FO} < 0.005$ and $\sigma\chi_{O2} < 0.1\%$ for both cases, while σT is 37 K for the air-dilute case and 39 K for the eEGR dilute case. Based on the discussion in Chapter 2, stratification in temperature of the order of σT = 40 K is equivalent to a corresponding stratification in ϕ_{FO} of the order $\sigma\phi_{FO}$= 0.4, or a stratification in χ_{O2} of the order $\sigma\chi_{O2}$= 6.4%. Clearly the stratification that is present in the composition dimensions of ϕ_{FO} and χ_{O2} is orders of magnitude lower than the amount needed to make a major difference to the overall

reactivity stratification (distribution of ignition delay), which is dominated by thermal stratification in both these cases.

The mean values of ϕ_{FO} and χ_{O2} for both cases at the pre-ignition point shown in Figure 3.3 are the same as those at IVC. The mean temperature for the eEGR case is around 14 K higher at this pre-ignition point. This is an important point to note, as it indicates that the unburned temperature needed to achieve ignition for the eEGR case is higher than that for the air-dilute case. Thus, in order to match ignition timing with the air-dilute case, not only do we have to compensate for the lower γ in the case of eEGR dilution (which reduces compression temperatures), but we must further increase the pre-ignition temperature, to possibly compensate for the changes in chemical kinetic properties (like lower χ_{O2}) that affect ignition.

After observing that we have low stratification in terms of composition for both cases, we look at the temperature stratification arising from each of the strategies shown in Figure 3.4. We observe in Figure 3.4 that the foot of the temperature distribution, in terms of the hottest temperatures, is shifted to lower temperatures for the air-dilute case compared to the eEGR-dilute case. Further, we observe that in general the overall temperature distribution is also shifted to the right (colder) for the air-dilute case compared to the eEGR-dilute case. The overall thermal stratification is almost identical for both cases, with thermal stratification primarily driven by wall heat loss when the levels of internal residual are low as in the case with PVO operation.

In-spite of the leading edge of the temperature distribution being hotter for the eEGR-dilute case, the ignition timing for both cases is matched. To better understand the reason for this, we compare the "reactivity stratification" for both cases, based on computing ignition delay in every CFD cell using the He et al. [4] ignition delay correlation introduced in Chapter 2. Figure 3.5 shows a scatter-plot of the ignition delay evaluated using the He et al. correlation in every CFD cell at 10° CA bTDC based on non-reacting simulations corresponding to the reacting simulations (for which pressure

traces and burn profiles are shown in Figure 3.1 and Figure 3.2 respectively) for both the air-dilute and eEGR-dilute cases. The *x*-axis is 1000/*T* and the *y*-axis is a log-axis denoting ignition delay. We observe that the "feet" of both curves (air and eEGR) have approximately the same ignition delay, even though they are offset in temperature, with the foot of the eEGR distribution being hotter. This is because the higher temperature for the eEGR case compensates for deficiency in oxygen, in effect causing the ignition delay to be matched for the hottest 10% of the mass based on our definition of ignition timing as CA10.

3.5 Decoupling thermodynamic effects from chemical kinetic effects

Figure 3.6 shows the cumulative reactivity distribution expressed in terms of ignition delay. From Figure 3.6 we see again that the air-dilute and eEGR-dilute case have the leading edge (most reactive 10%) of the reactivity distribution matched, based on the earlier discussion. In addition, we notice that the reactivity for the rest of the charge also happens to be almost perfectly matched for the two cases. However, from Figure 3.2 we noted that the burn duration for the eEGR case is about 10% higher than that for the air-dilute case, in-spite of having similar reactivity throughout the charge prior to ignition.

In order to explain this behavior, we begin by hypothesizing that the differences in burn duration may be explained based on differences in thermodynamic properties and not differences in reactivity, as reactivity is matched. Figure 3.7 shows the distribution of γ for the whole CFD domain over reactivity (represented by ignition delay) for both air-dilution and eEGR-dilution. Both cases have a higher γ in regions with longer ignition delays. This is because regions with longer ignition delays are generally colder, and γ is a thermodynamic property that increases with temperature. More interesting to note however, is that the γ for the eEGR-dilute case is lower than that for the air-dilute case

over the whole ignition delay space. It is hypothesized that the lower γ for the eEGR case leads to a slower rate of increase in end gas temperatures (unburned temperatures) post-ignition due to compression work from the burning regions; thus leading to a slower increase in reactivity in the end-gas post ignition of the earliest burning regions.

In order to test the validity of this hypothesis and isolate the γ effect, we use the sequential MZ approach as a diagnostic tool. We use the temperature and composition distribution from the non-reacting CFD simulations corresponding to the reacting CFD simulations for the air-dilute and eEGR-dilute cases to initialize a quasi-dimensional balloon-type MZ model at 10° CA bTDC in the manner described in Chapter 2. We then run the quasi-dimensional balloon multi-zone with the same 312-species gasoline mechanism used in the fully-coupled CFD simulations. A consistent shift on the order of 15 K to the initial temperature profiles for both the air-dilute and eEGR-dilute cases was needed to attain the same ignition timing as the fully-coupled CFD case. This is possibly because for the sequential MZ approach we impose non-reacted fuel species onto the MZ at the pre-ignition point, which results in a slightly longer ignition delay compared to the fully-coupled CFD/kinetics case wherein the fuel species have a longer time to break down with kinetics beginning from IVC. With the ignition timing matched, we see similar characteristics as the fully-coupled CFD/kinetics results in terms of 10-90 burn duration (Figure 3.8), with the eEGR-dilute case having longer burn duration than the air-dilute case. In order to decouple the γ effect, we introduce a third diagnostic case (which we call N_2-dilute) using the sequential MZ which is identical to the sequential MZ eEGR case, except that upon initializing the MZ at 10° CA bTDC, we replace a certain fraction of CO_2 and H_2O in every zone of the MZ with N_2 such that the overall γ of the mixture is matched with that of the air-dilute case. However, this N_2-dilute case retains the same level of oxygen concentration as the eEGR-dilute case (χ_{O2} = 15%). Figure 3.8 shows the burn profile for the N_2-dilute case, in relation to the burn profiles for the air-dilute and

eEGR-dilute cases. It can be seen from Figure 3.8 that the N_2-dilute case has a similar burn profile as the air-dilute case, even though they have different levels of χ_{O2}.

Figure 3.9 shows the variation of γ for the three sequential CFD-MZ cases and Figure 3.10 the variation in specific heat C_p with the progress of combustion. It may be seen from Figure 3.9 that the γ is matched for the air-dilute and N_2-dilute cases through the combustion process; while from Figure 3.10 it may be seen that through the combustion process, the C_p of the N_2-dilute case is higher than the C_p of the air-dilute case. In-spite of having a higher C_p (more thermal sink effect) and lower χ_{O2}, both of which would theoretically serve to extend burn duration, we note that with the γ matched, the burn profiles for the air-dilute and N_2-dilute cases are almost identical. This indicates that with the overall reactivity stratification matched for the air-dilute and eEGR-dilute cases, the difference in γ is the factor responsible for the eEGR-dilute case having a 10% longer burn duration than the air-dilute case.

3.6 Analysis of NOx emissions

Both the air-dilute and eEGR-dilute cases have low levels of NOx (under 1g/kg of fuel Emissions Index NOx, EINOx). The air-dilute case has an EINOx of 0.23 g/kg fuel and the eEGR-dilute case has an EINOx of 0.14 g/kg fuel. However, it is still beneficial to look at the distribution of charge in the post-combustion reaction space and identify NOx forming regions, since this understanding is critical to develop NOx mitigating charge preparation strategies if NOx becomes an issue at other operating conditions.

Figure 3.11 shows the distribution of charge in the post-combustion reaction space (at 6° CA aTDC which corresponds approximately to CA90 for both cases) for both air-dilute and eEGR-dilute operation; visualized in terms of ϕ_{atomic} and T. The quantity ϕ_{atomic} is an "atomic" equivalence ratio which remains a constant with the

progress of combustion, unlike the ϕ_{FO} which goes to zero as combustion progresses. It is computed in each CFD cell as follows:

$$\phi_{atomic} = \frac{2C^{\#} + \frac{H^{\#}}{2}}{O^{\#}}, \tag{3.1}$$

Where $C^{\#}, H^{\#}$ and $O^{\#}$ represent the number of carbon, hydrogen and oxygen atoms respectively in the CFD cell. We observe that in both cases, there is not a significant amount of stratification in ϕ_{atomic}, and that the maximum combustion temperatures in both cases at this crank angle are under 2100 K. The mean combustion temperature for the air-dilute case is 1942 K and that for the eEGR-dilute case is 1920 K. The slightly higher levels of EINOx for the air-dilute case might be because of the slightly higher post-combustion temperatures and also because of the higher concentration of oxygen available in the burned mixture, as may be seen in Figure 3.12; which shows the concentration of oxygen available in the post-combustion reaction space for the air-dilute case (top) and eEGR-dilute case (bottom). In Figure 3.11 as well as in Figure 3.12, it may be seen that for the eEGR dilute case, the bin with the hottest temperature has lower NO formation compared to the adjacent, colder bin. This is explained based on the *total mass* contained within each of these bins. Even though the hotter bin has a higher temperature compared to adjacent colder bin, it has a lower total charge mass contained within it compared to the other colder bin, thus resulting in overall NO generated (which is an absolute measure) within the hotter bin being lower than that generated within the adjacent colder bin. This is made clearer in Figure 3.13, which shows the reaction space for the eEGR case as in Figure 3.11, colored by total NO generated, with the added dimension of mass contained in every bin.

3.7 Summary

It was shown that under the conditions studied in this work, when ignition timing is fixed, the difference between air dilution and eEGR dilution on HCCI burn duration is small with the eEGR case showing a 10% increase in burn duration compared to the air-dilute case. A critical point to note is that these simulations do not take into account cyclic variations in eEGR which could potentially occur in automotive engines. These observations are however in line with the steady state experimental observations of Dec et al. [1]. Reaction space analysis performed on the CFD simulations shows that the pre-ignition reactivity distribution for both cases is almost identical. Further, using the sequential MZ approach, it is shown that the small differences in burn duration at constant ignition timing are due to thermodynamic effects, and not lower oxygen concentration for the eEGR case; since the lower oxygen concentration is compensated for by higher temperatures, compared to the air-dilute case. NOx emissions were low for both air-dilute and eEGR dilute operation.

Table 3.1 – Operating conditions: Air versus eEGR dilution

Parameter	**Air dilution**	**eEGR dilution**
Fueling	PFI	PFI
NVO	0° CA	0° CA
$\boldsymbol{\phi_{FO}}$ (mean)	0.33	0.44
$\boldsymbol{\chi_{O2}}$ (mean)	20%	15%
T_{in}	213°C	241°C
Internal Residual	7%	7%
External Residual	0%	36%
Total RGF	7%	43%

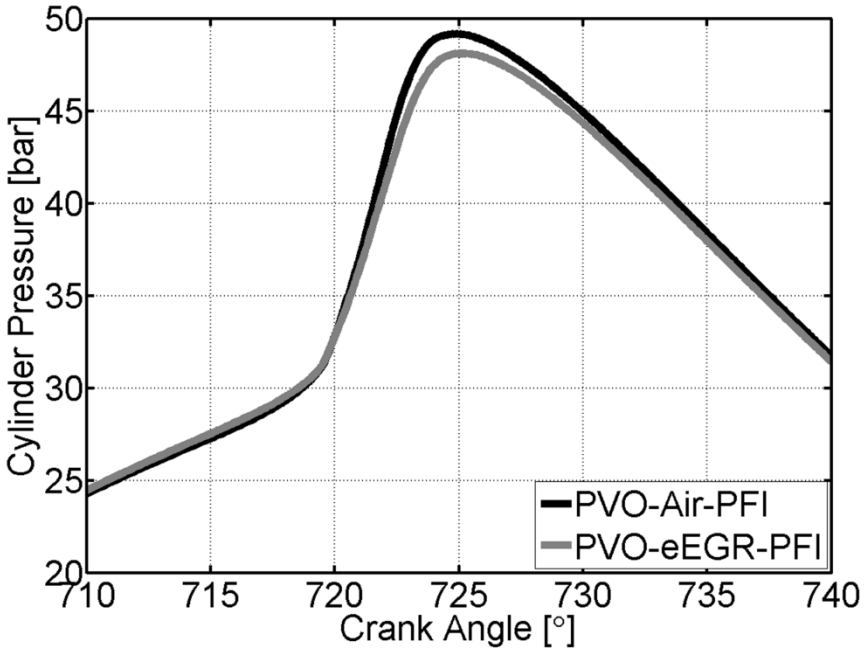

Figure 3.1 – In-cylinder pressure traces from full CFD simulation for air dilution and eEGR dilution cases

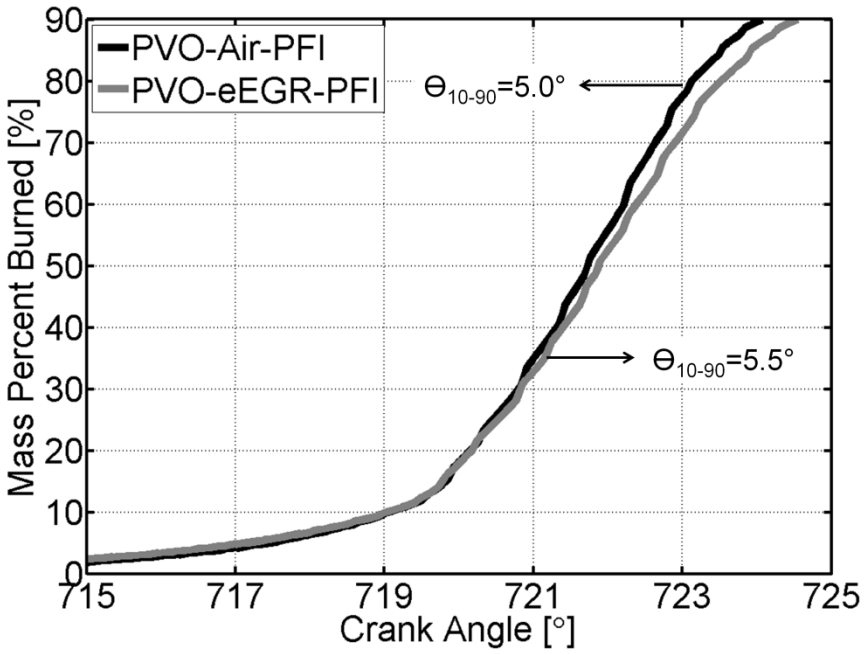

Figure 3.2 – Mass percentage burned profiles from full CFD simulation for air dilution and eEGR dilution cases

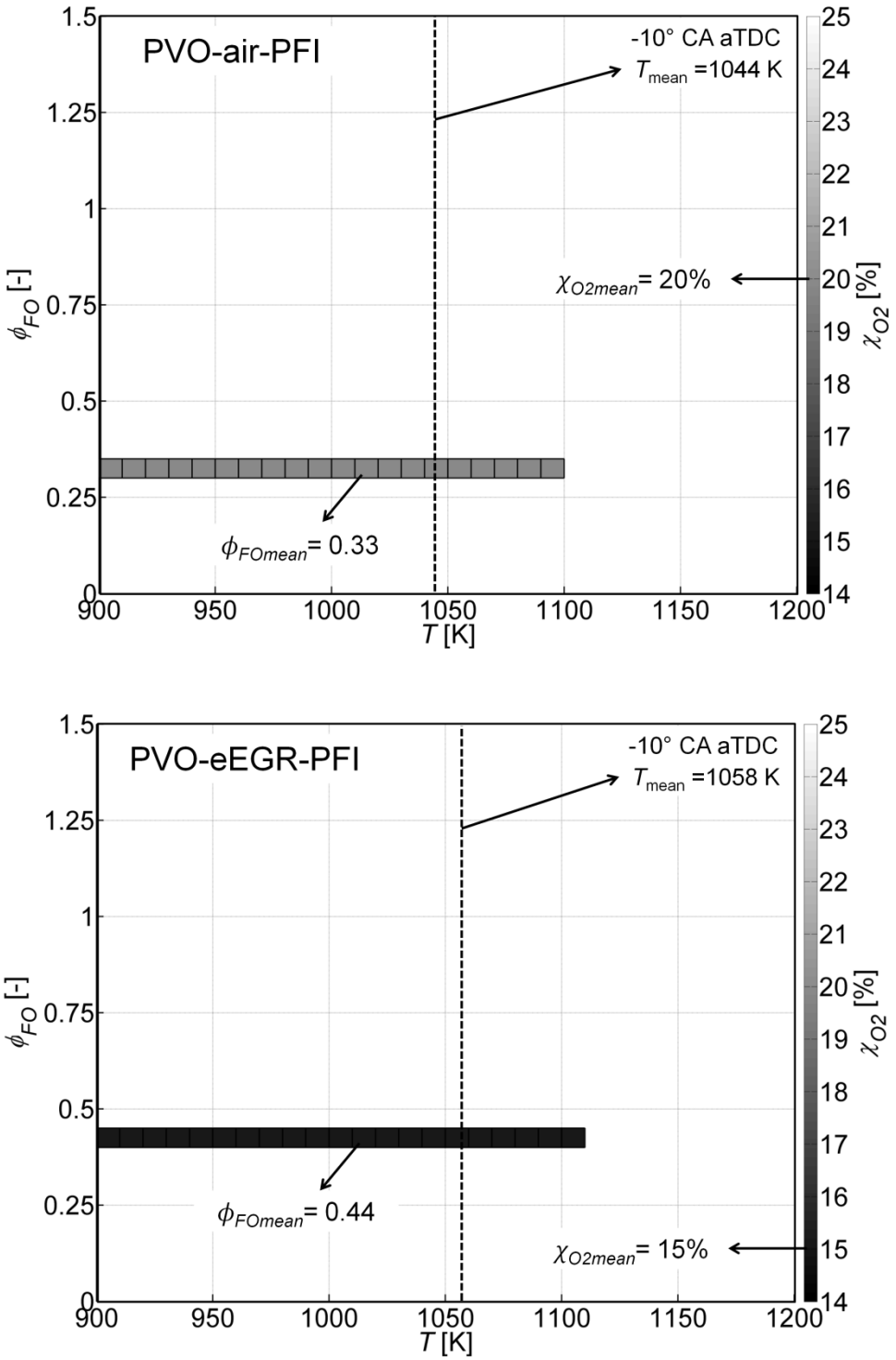

Figure 3.3 – Pre-ignition reaction space (10° CA bTDC) for air dilution case (top) and eEGR dilution case (bottom) from CFD simulations

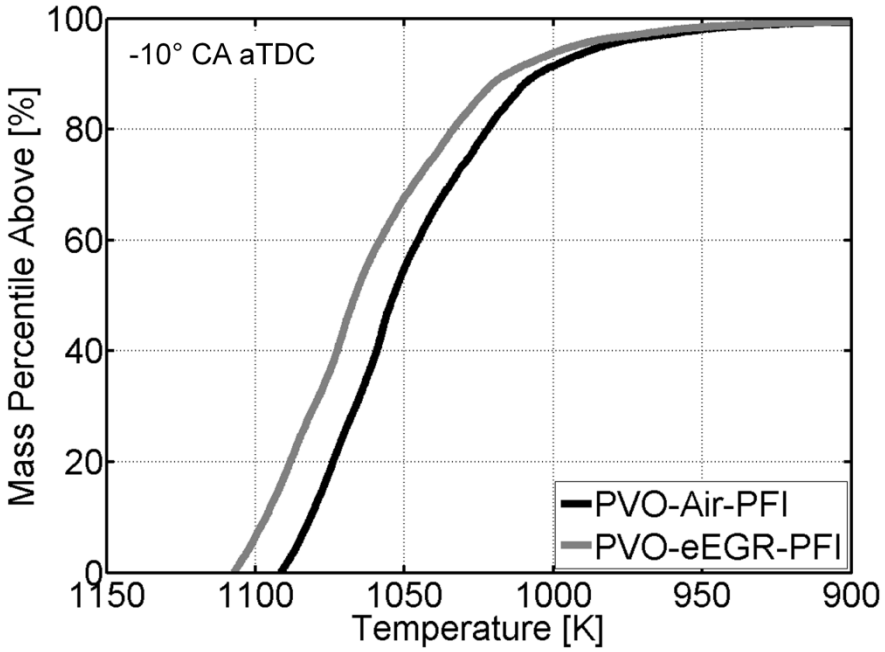

Figure 3.4 – Pre-ignition (10° CA bTDC) temperature distribution from CFD simulation for air dilution and eEGR dilution cases

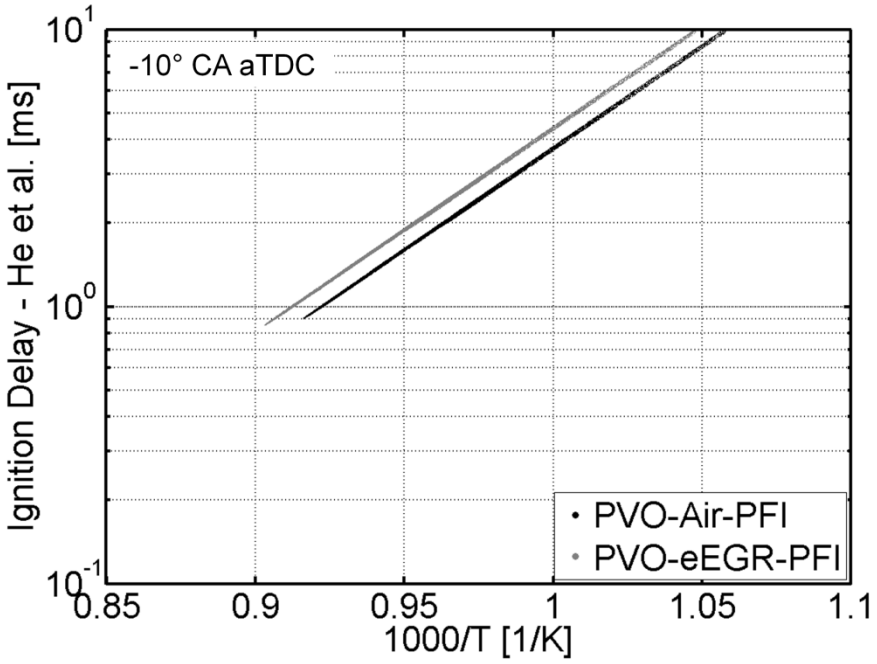

Figure 3.5 – Pre-ignition (10° CA bTDC) ignition delay scatter from CFD simulation for air dilution and eEGR dilution cases

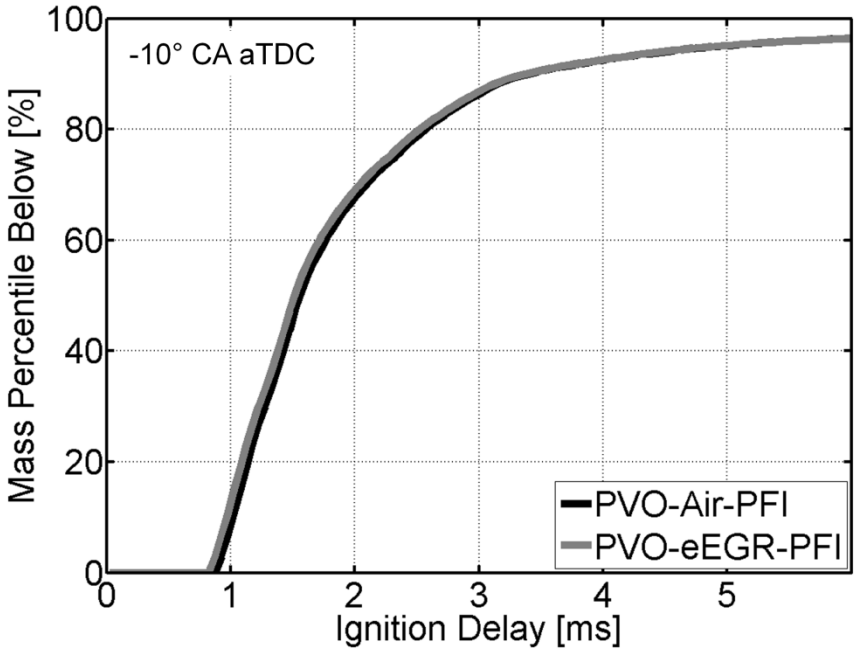

Figure 3.6 – Pre-ignition (10° CA bTDC) reactivity distribution from CFD simulation for air dilution and eEGR dilution cases

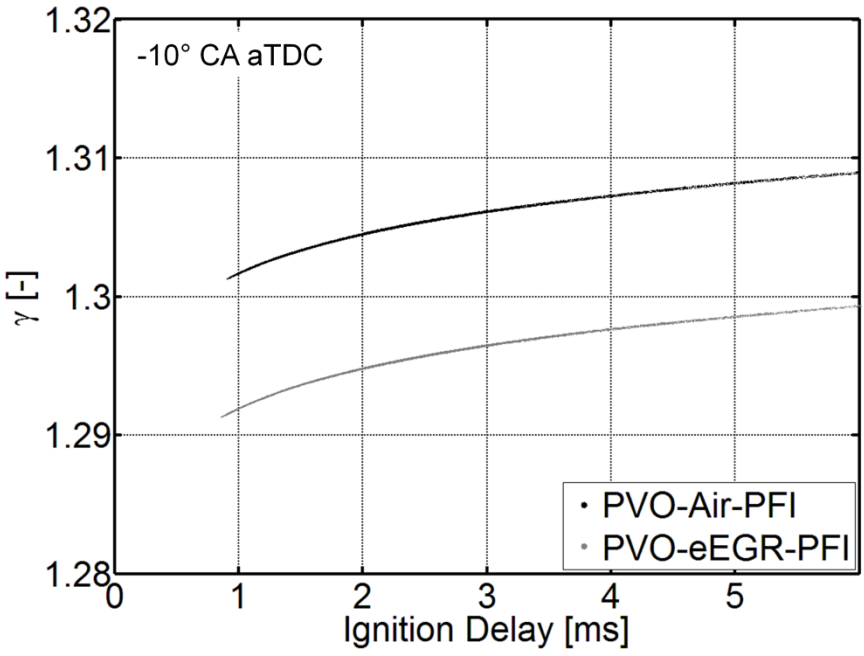

Figure 3.7 – Pre-ignition (10° CA bTDC) distribution of γ from CFD simulation for air dilution and eEGR dilution cases

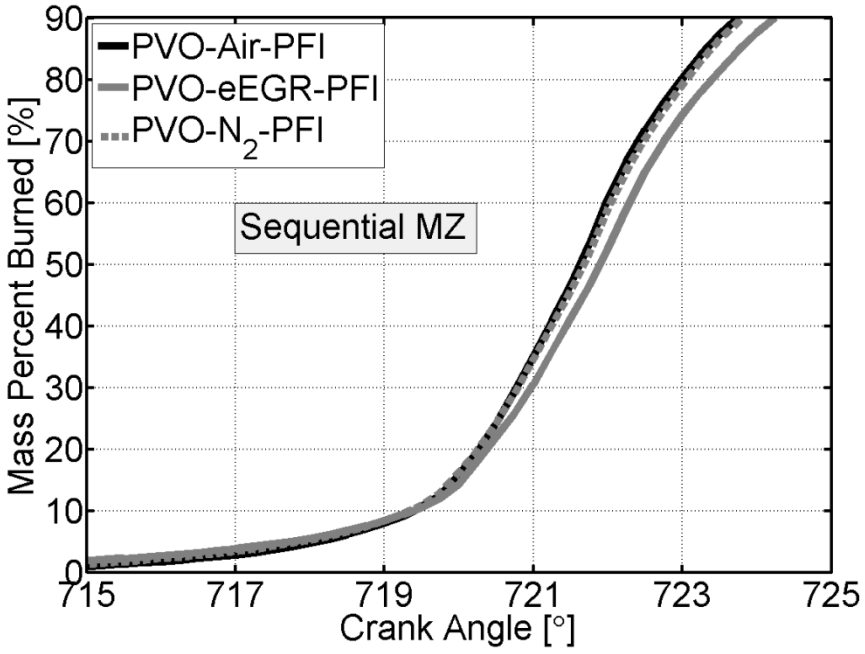

Figure 3.8 – Application of sequential MZ to decouple thermodynamic effects; air dilution, eEGR dilution and N_2 dilution shown

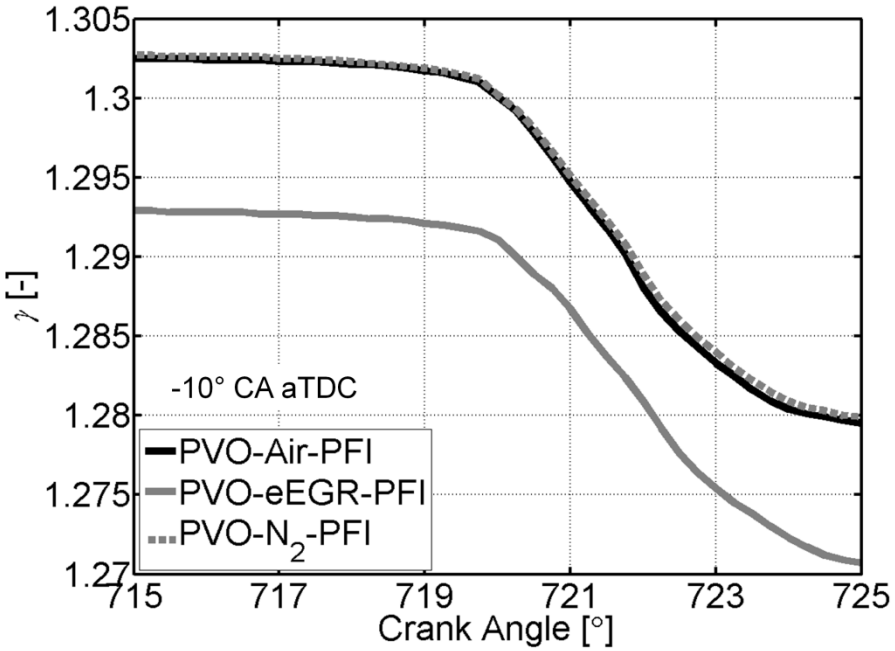

Figure 3.9 – Variation of γ with the progress of combustion

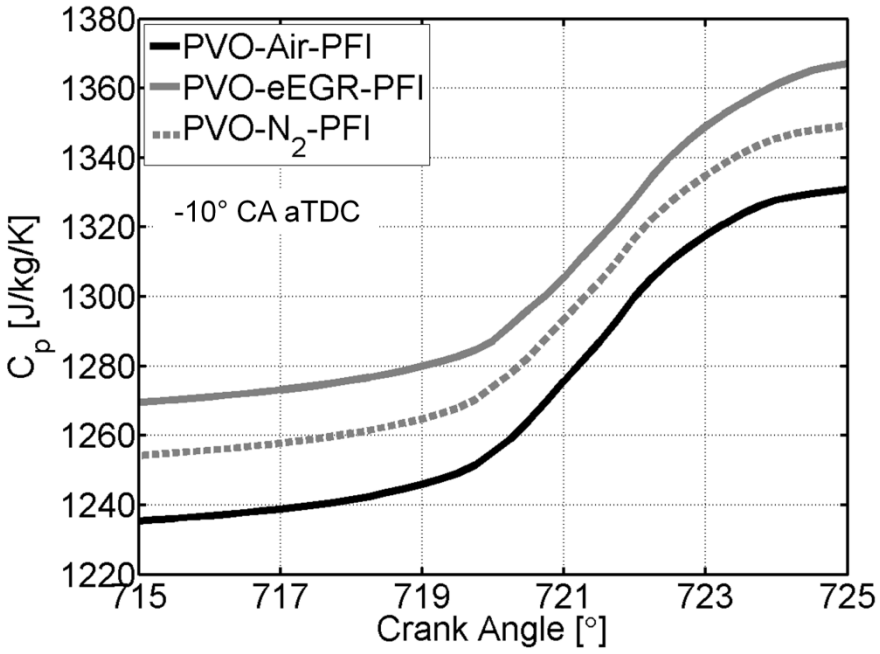

Figure 3.10 – Variation of C_p with the progress of combustion

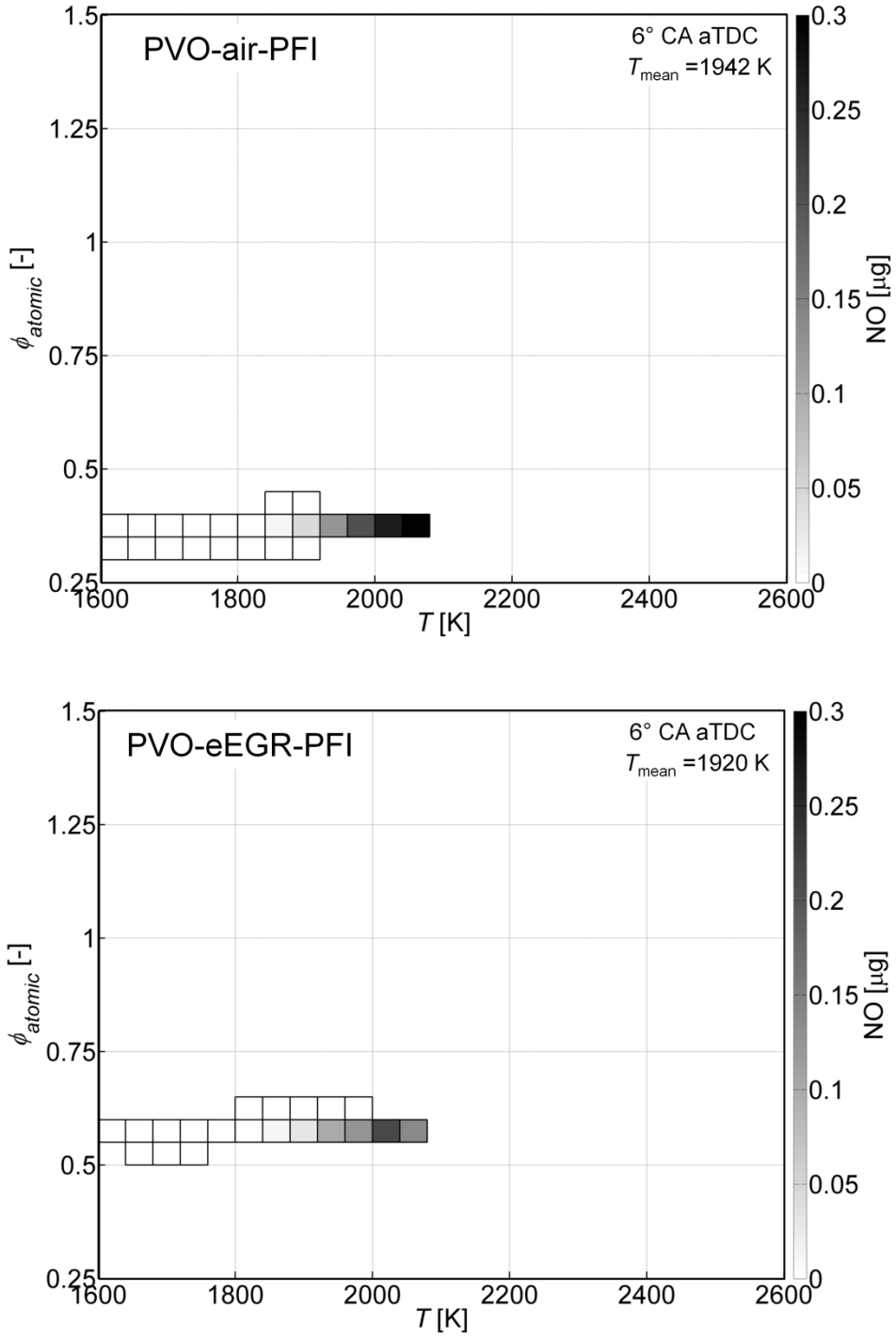

Figure 3.11 – Post-combustion (6° CA aTDC) distribution in ϕ_{atomic} and T colored by NO from CFD simulation for air dilution and eEGR dilution cases

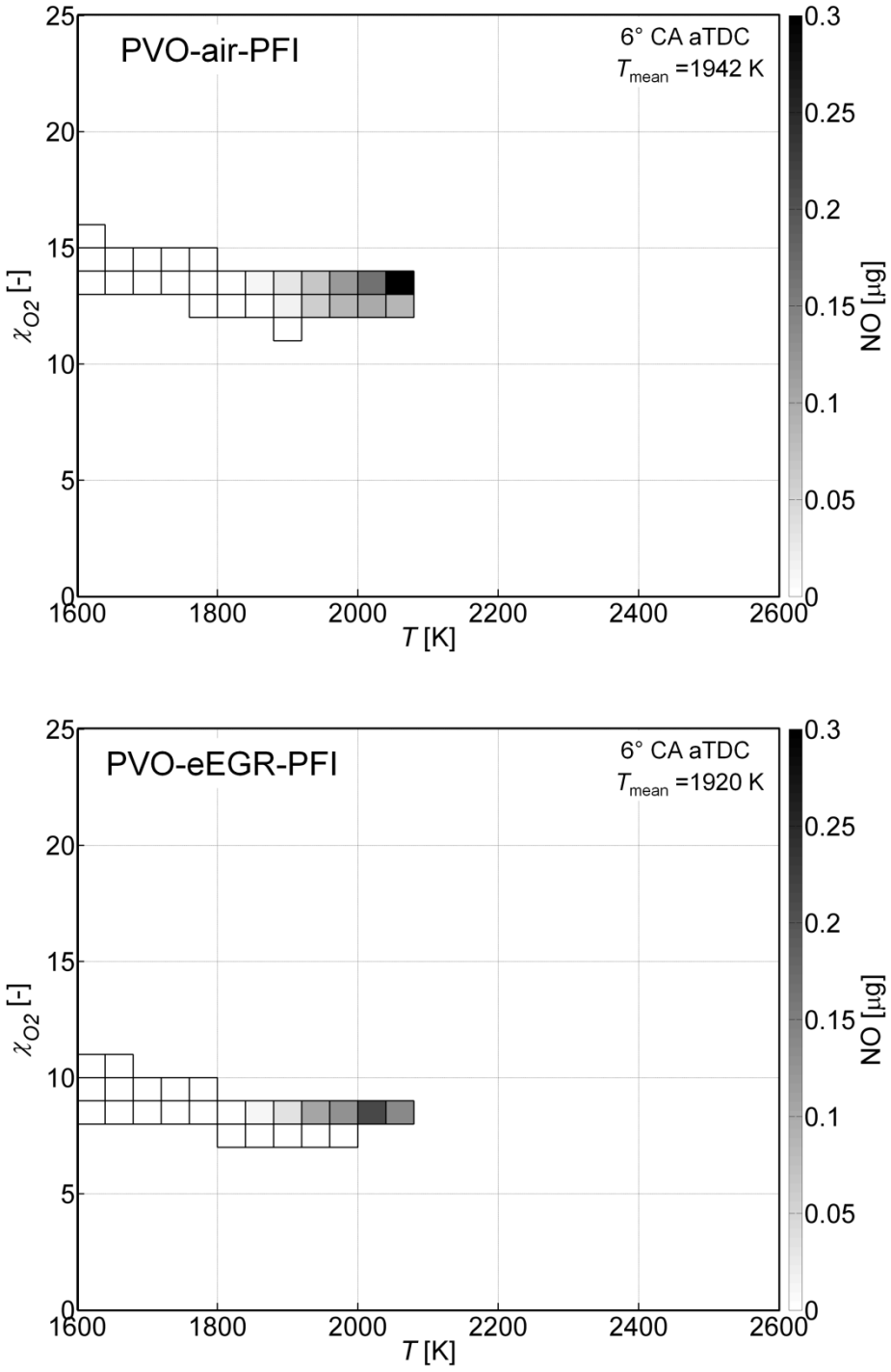

Figure 3.12 – Post-combustion (6° CA aTDC) distribution in χ_{O2} and T colored by NO from CFD simulation for air dilution and eEGR dilution cases

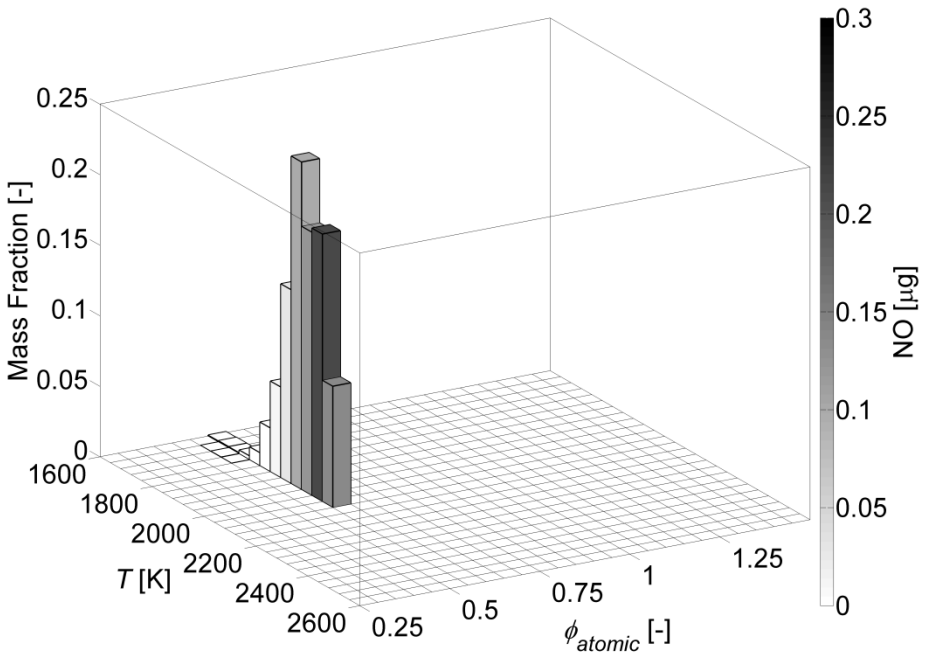

Figure 3.13 – Post-combustion (6° CA aTDC) distribution in ϕ_{atomic} and *T* colored by NO, showing mass fraction contained in ϕ_{atomic} -*T* bins from CFD simulation of eEGR dilution case

3.8 References

1. Dec, J. E., Sjöberg, M., and Hwang, W., "Isolating the Effects of EGR on HCCI Heat-Release Rates and NOx Emissions," SAE Paper 2009-01-2665, 2009.

2. Dec, J.E., and Yang, Y., "Boosted HCCI for High Power without Engine Knock and with Ultra-Low NOx Emissions – using Conventional Gasoline," SAE Paper 2010-01-1086, 2010.

3. Mehl, M., Chen, J.Y., Pitz, W.J., Sarathy, S.M., and Westbrook, C. K., "An Approach for Formulating Surrogates for Gasoline with Application toward a Reduced Surrogate Mechanism for CFD Engine Modeling," *Energy & Fuels*, Vol. **25**, Issue 11, pp. 5215-5223, 2011.

4. He, X., Donovan, M. T., Zigler, B. T., Palmer, T. R., Walton, S. M., Wooldridge, M. S., and Atreya, A., "An experimental and modeling study of iso-octane ignition delay times under homogeneous charge compression ignition conditions," *Combustion and Flame*, Vol. 142, pp. 266-275, 2005.

CHAPTER 4

IMPACT OF STRATIFICATION FROM NVO

HCCI operation typically requires higher unburned temperatures than conventional gasoline SI operation [1], since ignition is primarily controlled by chemical kinetics and there is no spark discharge to initiate combustion. To achieve the required temperature for ignition, gasoline HCCI engines typically employ an increased compression ratio, along with some form of charge heating, either internal (typically using trapped residuals from the previous cycle by means of NVO [2-6]) or external (by means of using external charge heaters [7], or by bypassing the intercooler in a turbocharged system [8]).

NVO operation has gained increasing interest within the HCCI research community, as this is relatively easy to implement in a production engine using cam-phasing technology compared to intake air heaters. Moreover, it offers a quicker control over CA50 compared to external heaters, which makes NVO operation attractive for transient operation. There is thus great interest to understand the fundamental impact on combustion and emissions from NVO operation compared to conventional PVO valve events; primarily in the context of the possible high levels of stratification in temperature and composition brought about by NVO operation. Preliminary work by Rothamer et al. [9] indicate that there is an increased stratification in temperature and EGR distribution within the charge going from PVO to NVO operation, though it is not clear what impact this stratification has on HCCI burn duration and NOx emissions.

Further, it is important to isolate the stratification effects of NVO operation from mean composition effects (in terms of mean thermodynamic and chemical kinetic properties of EGR). A means for isolating stratification effects is needed to compare the effect of using iEGR for dilution versus eEGR for dilution, if combustion phasing is fixed and control over CA50 is achieved by some other means such as intake air heating or intercooler bypass. This chapter describes the effect of NVO operation on thermal and compositional stratification, and how this added stratification in the reaction space affects HCCI burn duration and NOx emissions.

4.1 Conditions for study

Full cycle CFD simulations are performed based on the FFVA engine mesh using KIVA-3V coupled with kinetics calculations being performed for the closed portion of the main combustion cycle (kinetics from IVC onwards). The engine speed is 2000 RPM for this investigation. Two cases are studied: the first case is the same as the eEGR case from the previous chapter and uses a PVO profile with negligible overlap; the second case is an iEGR case which uses an NVO valve profile with a negative overlap of 157° CA. Both cases employ premixed fueling, representative of PFI into the intake to avoid complications associated with fuel stratification from direct injection. The mean composition for both cases is identical at IVC, with both cases having ~43% RGF. For the NVO-iEGR case all the residual is internal, whereas for the PVO-eEGR case, 7% of the RGF is internal residual while 36% of the residual is external. Both cases have the same mean oxygen concentration (χ_{O2} = 15%) and also the same mean fuel-oxygen equivalence ratio (ϕ_{FO} = 0.44). The NVO-iEGR case requires a lower level of intake air heating owing to the elevated internal energy of the charge brought about by the high levels of trapped residuals. The NVO-iEGR case has T_{in} = 98°C while the PVO-eEGR case has T_{in} = 241°C. Both cases have similar ignition timing (defined as CA10), and

ignite approximately at 2°CA bTDC. The fully-coupled CFD-chemical kinetics approach is used, with chemistry turned on after IVC. The same 312-species gasoline mechanism [10] in conjunction with the 4-component gasoline surrogate of Mehl et al. [10] is used in these simulations. The operating conditions for the two strategies are summarized in Table 4.1.

4.2 In-cylinder pressure traces and burn profiles

Figure 4.1 shows the in-cylinder pressure traces for the two cases while Figure 4.2 shows the mass fraction burned profiles for both the PVO-eEGR case and the NVO-iEGR case. We note from Figure 4.2 that both cases have a similar ignition timing (CA10), however, the NVO-iEGR case has a slower pressure rise rate, lower peak pressure (Figure 4.1) and a pronounced longer burn duration (Figure 4.2). The burn duration for the iEGR case is 7.2° CA, which represents a 30% increase in burn duration over the eEGR case which has a burn duration of 5.5° CA.

4.3 Analysis of the pre-ignition reaction space (at 10° CA bTDC)

In order to understand the differences in burn duration between the NVO-iEGR case and the PVO-eEGR case, we take a closer look at the pre-ignition reaction space for both cases. Figure 4.3 shows the pre-ignition reaction space generated by post-processing the CFD results and grouping individual CFD cells into bins based on temperature and ϕ_{FO}. The bins are colored by χ_{O2}. As noted previously, the compositional stratification for the PVO-eEGR case is negligible. For the NVO-iEGR case, however, we observe stratification in both ϕ_{FO} as well as in χ_{O2}. The stratification in ϕ_{FO} in terms of $\sigma\phi_{FO}$ is 0.02 and that in χ_{O2} in terms of $\sigma\chi_{O2}$ is around 0.01%. It should also be noted that the stratification in composition for the NVO-iEGR case is correlated to the stratification in temperature, with the hotter regions (comprised mostly of burned residuals from the

previous cycle) having a lower ϕ_{FO} and lower χ_{O2} than the colder end gas (comprised of the colder intake charge that contains fuel and oxygen), since the fueling is premixed along with the intake. This compositional stratification from NVO operation, though higher than that in the PVO-eEGR case (the PVO-eEGR case has $\sigma\phi_{FO}$< 0.005 and $\sigma\chi_{O2}$ < 0.1%), is still insignificant relative to the thermal stratification which in terms of σT is around 48 K for the NVO-iEGR case. The thermal stratification for the PVO-eEGR case in terms of σT is 39 K. Based on the analysis in Chapter 2, a σT of around 50 K has an equivalent impact on ignition delay stratification as a $\sigma\phi_{FO}$ of 0.5 and a $\sigma\chi_{O2}$ of 8%. Clearly, the compositional stratification present with NVO-iEGR operation in terms of $\sigma\phi_{FO}$ and $\sigma\chi_{O2}$, though higher than that in the PVO-eEGR case, is not significant enough to generate a first order impact on reactivity stratification which is dominated by thermal stratification.

Figure 4.4 shows the cumulative distribution of temperature within the charge for both the PVO-eEGR case and the NVO-iEGR case. It may be seen from Figure 4.4, that there is a marked increase in the thermal stratification with NVO operation. Sjöberg et al. [11] use a "thermal width" metric to quantify thermal stratification at BDC. They contend that since the distribution of temperature is non-normal, thermal width is a better metric to quantify temperature stratification compared to standard deviation. We also employ such a metric to quantify the spread in temperature within the cylinder prior to ignition at 10° CA bTDC. We define (Thermal Width)$_{10\text{-}90}$ or $TW_{10\text{-}90}$ as the difference in temperature between the temperature above which 10% of the charge mass is at, and the temperature above which 90% of the charge mass is at. The $TW_{10\text{-}90}$ for the PVO-eEGR case pre-ignition is 81 K and that for the NVO-iEGR case is 110 K, representing a 35% increase in thermal width with NVO operation.

Figure 4.5 shows a scatter-plot of the ignition delay evaluated using the He et al. correlation [12] in every CFD cell at 10° CA bTDC based on non-reacting simulations corresponding to the reacting simulations for both the PVO-eEGR and NVO-iEGR cases.

The *x*-axis is 1000/*T* and the *y*-axis is a log-axis denoting ignition delay. There is a slight spread in ignition delay for a given temperature for the NVO-iEGR case due to the compositional stratification. In order to understand how the increased thermal width affects reactivity stratification, we visualize the cumulative distribution of reactivity (in terms of ignition delay computed in every CFD cell using the He et al. [12] correlation) prior to ignition (at 10° CA bTDC), shown in Figure 4.6. From Figure 4.6, we note that the leading edge of the reactivity distribution up to the 10% point is roughly matched as the ignition delay for the two cases is matched. However, we note that the reactivity in the later igniting regions of the charge is not matched, with the NVO-iEGR case having longer ignition delays in the later igniting regions, and overall larger reactivity stratification, which explains the longer burn duration for the NVO case seen in Figure 4.2.

4.4 Decoupling thermal and compositional stratification

In the previous section, we noted that NVO operation (iEGR case) introduces both compositional and thermal stratification; and that the overall reactivity stratification is greater for the iEGR case compared to the eEGR case, even when mean composition and temperature are very similar.

In order to truly understand the relative contribution of each kind of stratification we need to isolate thermal stratification effects from compositional stratification effects. To do this, we re-compute the ignition delay in every CFD cell at 10° CA bTDC for the iEGR case using the temperature of each cell along with the global mean composition (ϕ_{FO} = 0.44 and χ_{O2} = 15%) instead of the actual composition in every cell. This in effect removes any effect of compositional stratification from the computation of reactivity stratification. Figure 4.7 shows the reactivity distribution for the NVO-iEGR case

computed in this manner (indicated as “NVO-iEGR-PFI-mean comp” in the figure) alongside the original reactivity distributions for the NVO-iEGR and PVO-eEGR cases.

Comparing the NVO-iEGR-PFI-mean composition case with the NVO-iEGR-PFI case, we notice that there is hardly any difference in the reactivity distribution, indicating that under these conditions, the compositional stratification generated by NVO operation is not a major contributor to overall reactivity stratification, which appears to be dominated by thermal stratification. If we look closely, however, we note that neglecting the compositional stratification for the NVO-iEGR case in fact increases the reactivity stratification by slightly shortening the ignition delays for the leading edge while increasing ignition delays in the end-gas. Thus, including compositional stratification results in a reduction in reactivity stratification compared to the mean composition case. This seems counter-intuitive, since it is generally assumed that any compositional stratification would serve to increase overall reactivity stratification.

This may be explained based on Figure 4.3, where we see that for the iEGR case, the distribution in composition is such that the hotter regions of the charge have lower ϕ_{FO} as well as lower χ_{O2} compared to the colder regions of the charge. Based on the He et al. [12] ignition delay correlation, increasing the values of *T*, ϕ_{FO} or χ_{O2}, all result in a lower ignition delay. With compositional stratification for the iEGR case, we now have temperature being negatively correlated with ϕ_{FO} or χ_{O2}. Thus, there is an increase in ignition delay in the hotter leading edge of the charge and a reduction in the ignition delay in the colder end-gas due to the presence of this compositional stratification that is *negatively* correlated to the thermal stratification in terms of its effect on ignition delay. Thus, the compositional stratification in this case makes the hottest regions less reactive, and the colder regions more reactive than the case with mean composition, in effect *reducing* the overall reactivity stratification.

However, as stated before, this effect is minor, and for the NVO-iEGR-PFI case, the major effect of NVO operation is the added thermal stratification which serves to

widen the reactivity stratification. This is also clear from Figure 4.8 where burn profiles from the PVO-eEGR case, the NVO-iEGR case and the NVO-iEGR case with mean composition assumed are shown. These results were generated using the sequential MZ approach in the same manner as done in Chapter 3. For the NVO-iEGR case with mean composition, the quasi-dimensional balloon multi-zone was initialized at pre-ignition (10° CA bTDC) with overall cylinder mean composition prescribed to every zone (the species mass fraction vector is the same for every zone), while maintaining the thermal stratification from the NVO-iEGR case. From Figure 4.8 it is clear that neglecting compositional stratification generated by NVO operation for the iEGR case does not affect the burn profile significantly, and the thermal stratification generated by NVO operation is the most important factor contributing to the longer burn duration compared to the eEGR (PVO) case.

Figure 4.9 shows the pre-ignition distribution of γ for both cases. From Figure 4.9, it is clear that the thermodynamic mixture properties for both strategies (NVO and PVO) is almost identical. This further reinforces the fact that the difference in burn duration for the two valve strategies are is dominated by differences in thermal stratification.

4.5 Analysis of NOx emissions

The NOx emissions from both cases are very similar, and well under 1g/kg fuel EINOx. The NOx emissions for the eEGR case are 0.14 g/kg fuel EINOx while those for the iEGR case are 0.11 g/kg fuel EINOx. Figure 4.10 shows the post-combustion reaction space visualized in terms of ϕ_{atomic} and T at 6° CA aTDC. The mass percent burned for the NVO case is 92% and that for the PVO case is 97% at this crank angle. Both cases have low stratification in ϕ_{atomic}, and have sufficient dilution to keep peak combustion temperatures under 2100 K.

4.6 Summary

In this chapter, the effect of retaining residuals from the previous cycle using an NVO strategy is compared to conventional PVO operation, using full-cycle CFD simulations. The thermal and compositional stratification resulting from NVO operation with 157° CA negative overlap is computed. Mean composition effects from retaining residuals is isolated from stratification effects by using eEGR in the PVO case to ensure that the mean composition (in terms of oxygen concentration and fuel-oxygen equivalence ratio) is kept the same for the two valve strategies. The results from CFD simulation show a significant increase in burn duration (by around 30% under the conditions studied) for the same ignition timing. Post processing the CFD results indicates that there is a significant increase in thermal stratification from NVO operation with a 35% increase in thermal width prior to ignition. It is also shown that the compositional stratification (in oxygen concentration and fuel-oxygen equivalence ratio) is minimal under the conditions studied. The sequential MZ approach is employed to decouple the effects of thermal and compositional stratification, and it is shown that the effect of compositional stratification arising from NVO operation is insignificant on burn duration. Switching to an NVO strategy does not have a significant impact on NOx emissions, with emissions for both NVO and PVO operation being low.

Table 4.1 – Operating conditions: eEGR (PVO) versus iEGR (NVO) dilution

Parameter	**eEGR dilution**	**iEGR dilution**
Fueling	PFI	PFI
NVO	0° CA	157° CA
$\boldsymbol{\phi_{FO}}$ (mean)	0.44	0.44
$\boldsymbol{\chi_{O2}}$ (mean)	15%	15%
T_{in}	241°C	98°C
Internal Residual	7%	42%
External Residual	36%	0%
Total RGF	43%	42%

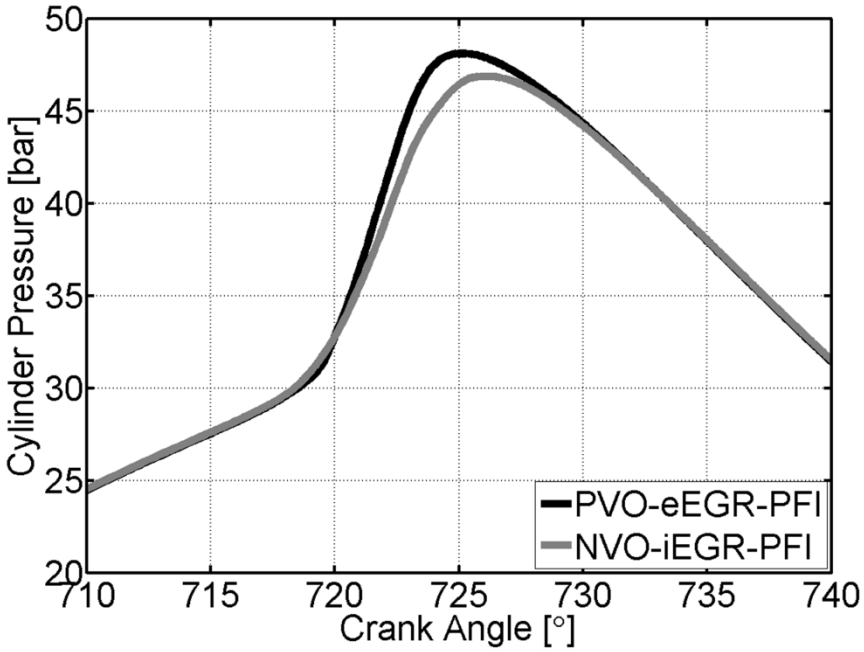

Figure 4.1 – In-cylinder pressure traces from CFD simulation of PVO-eEGR-PFI case and NVO-iEGR-PFI case

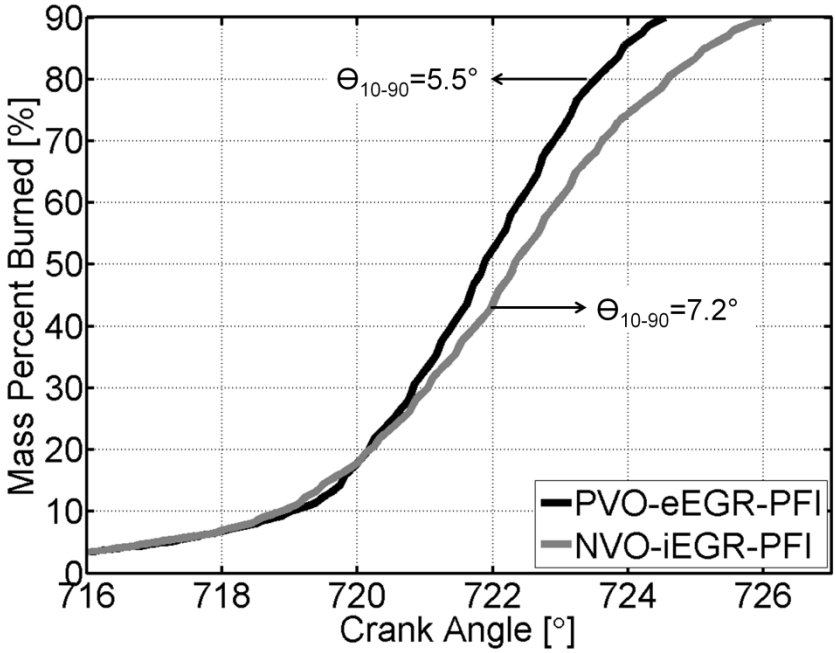

Figure 4.2 –Burn profiles from CFD simulation of PVO-eEGR-PFI case and NVO-iEGR-PFI case

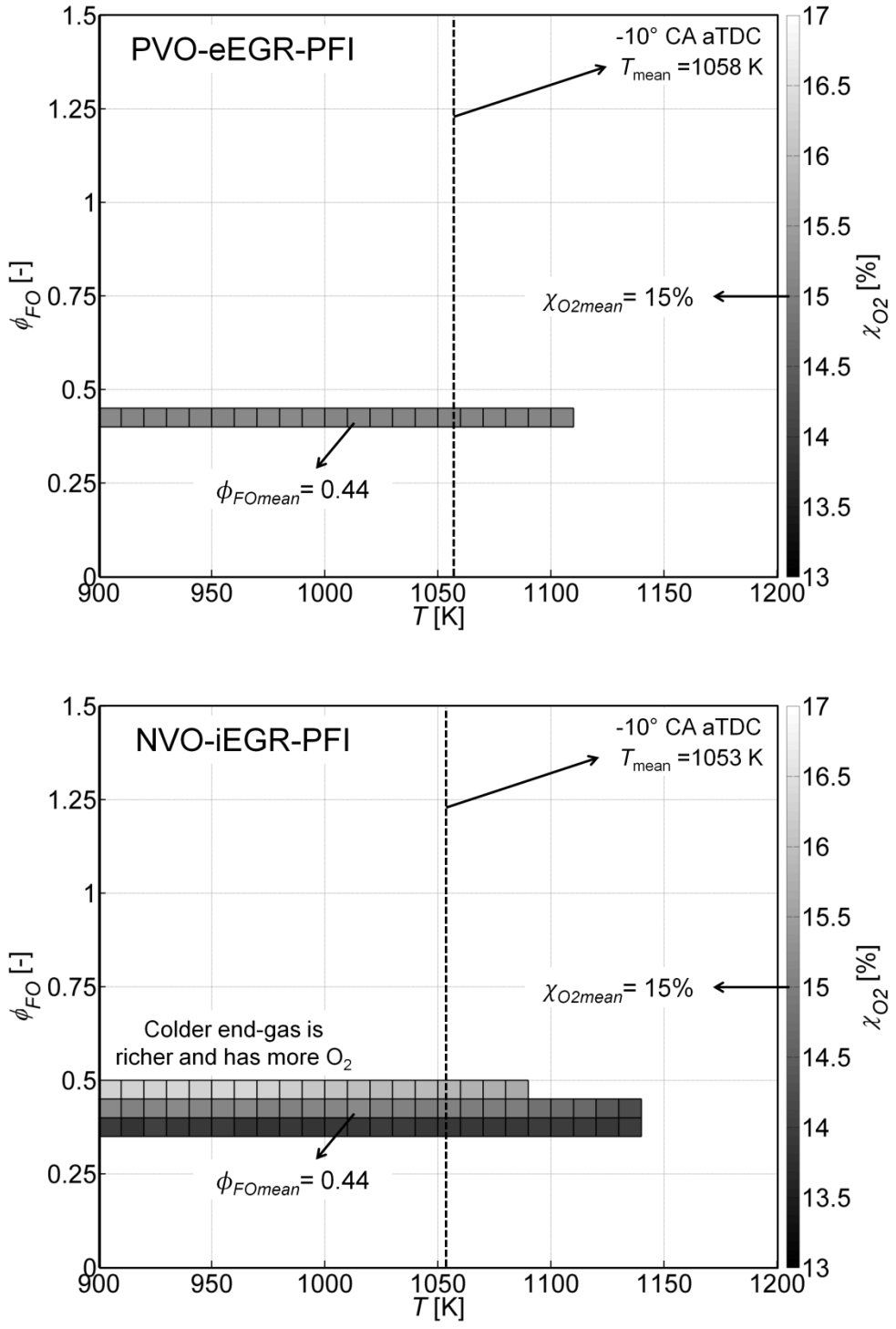

Figure 4.3 – Pre-ignition (10° CA bTDC) reaction space from CFD simulation visualized in terms of reaction space variables ϕ_{FO}, χ_{O2} and T

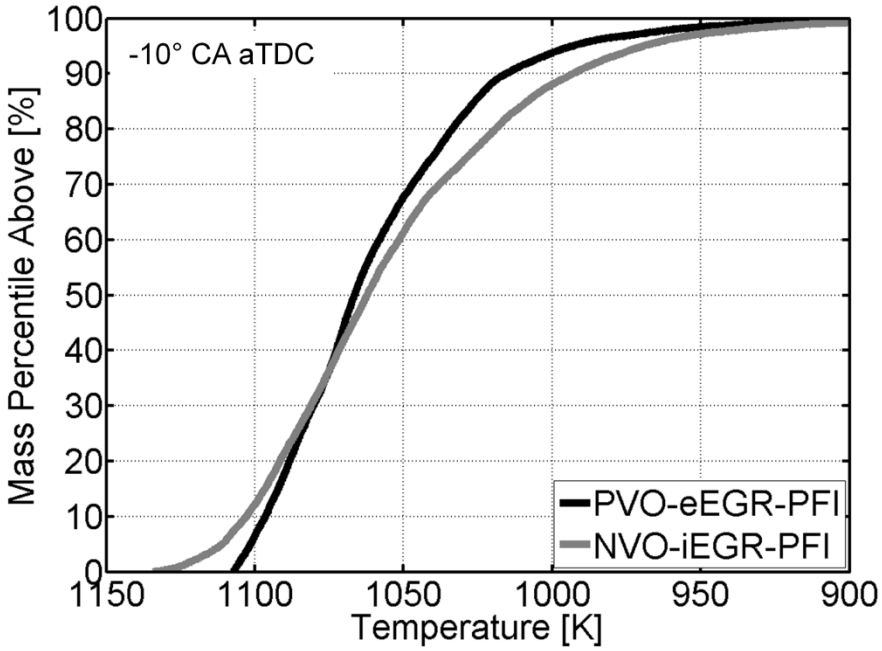

Figure 4.4 – Pre-ignition (10° CA bTDC) cumulative distribution in temperature from CFD simulation

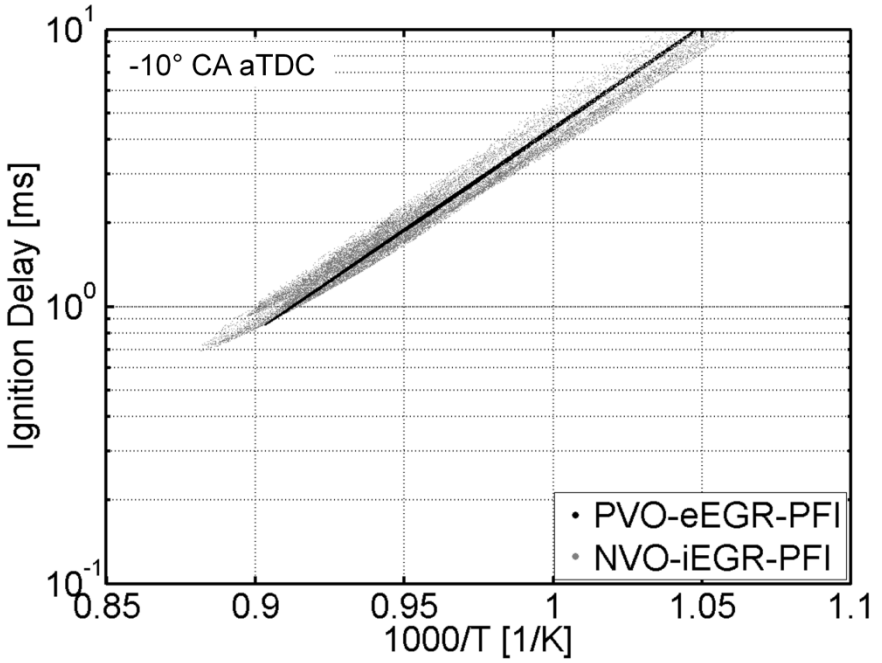

Figure 4.5 – Pre-ignition (10° CA bTDC) ignition delay scatter from CFD simulation

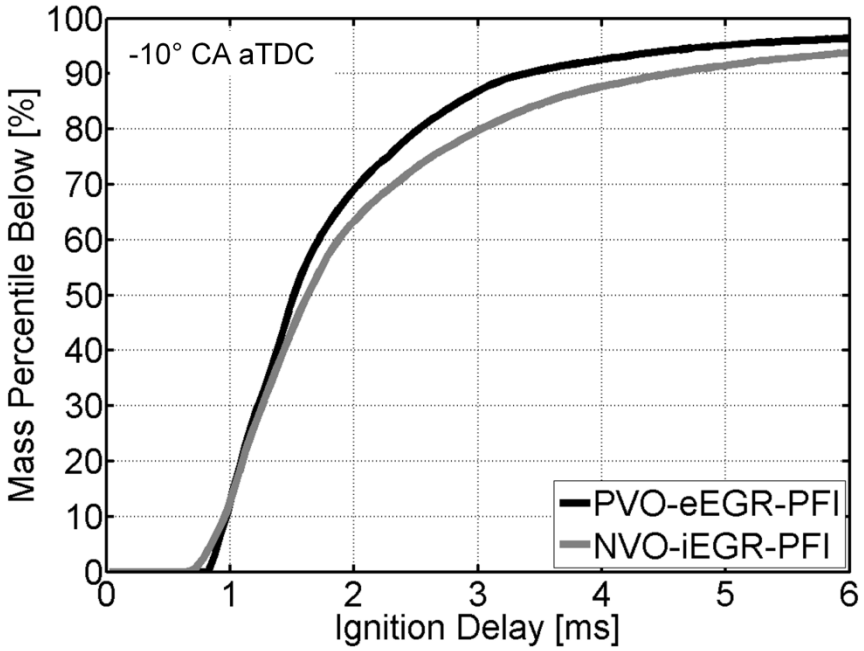

Figure 4.6 – Pre-ignition (10° CA bTDC) reactivity distribution in cumulative terms from CFD simulation

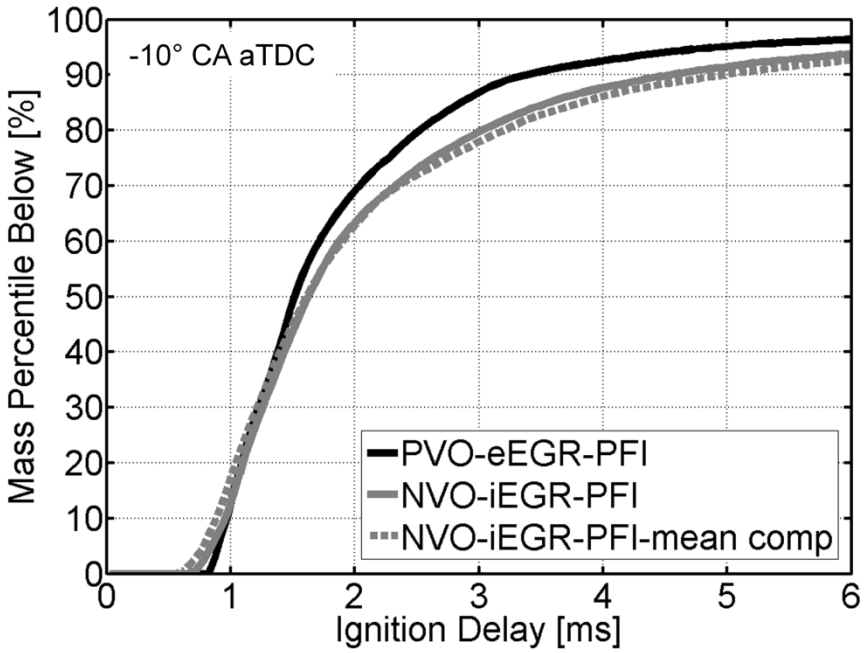

Figure 4.7 – Pre-ignition (10° CA bTDC) reactivity distribution in cumulative terms from CFD simulation of PVO-eEGR-PFI, NVO-iEGR-PFI and NVO-iEGR-PFI with mean composition assumed in all cells

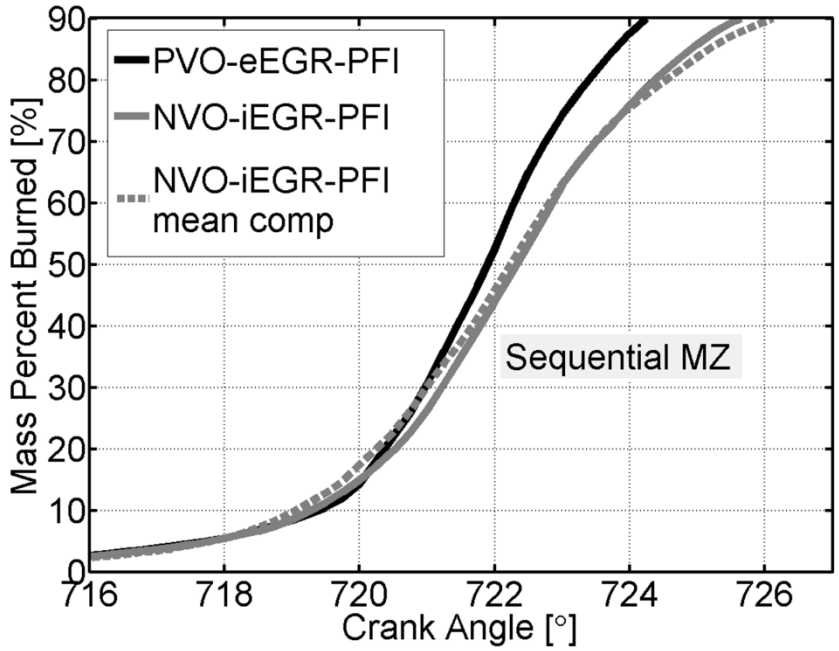

Figure 4.8 – Sequential MZ used to decouple thermal stratification from compositional stratification; burn profiles obtained from the sequential MZ for PVO-eEGR-PFI, NVO-iEGR-PFI and NVO-iEGR-PFI with mean composition shown

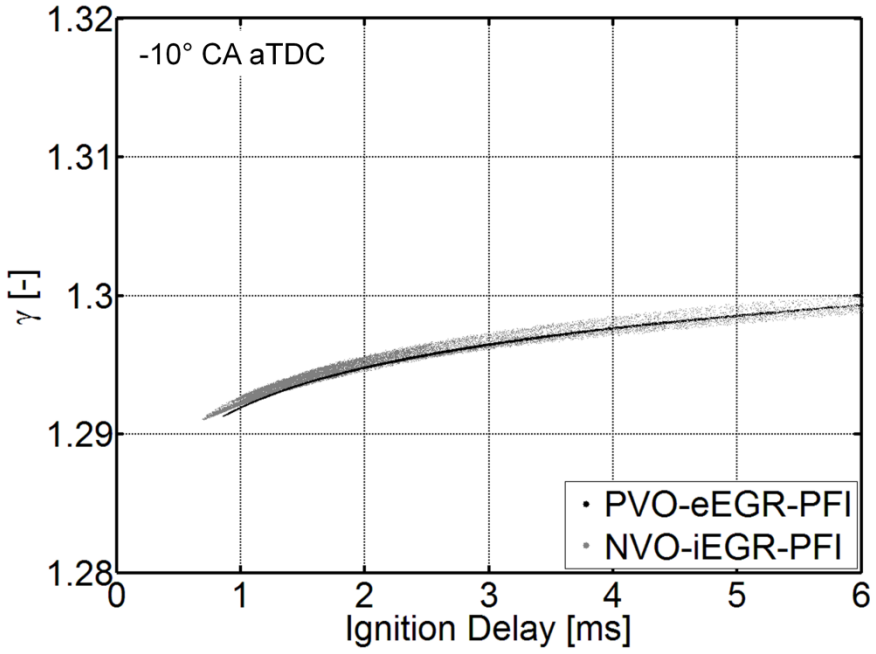

Figure 4.9 – Pre-ignition (10° CA bTDC) scatter in γ from CFD simulation

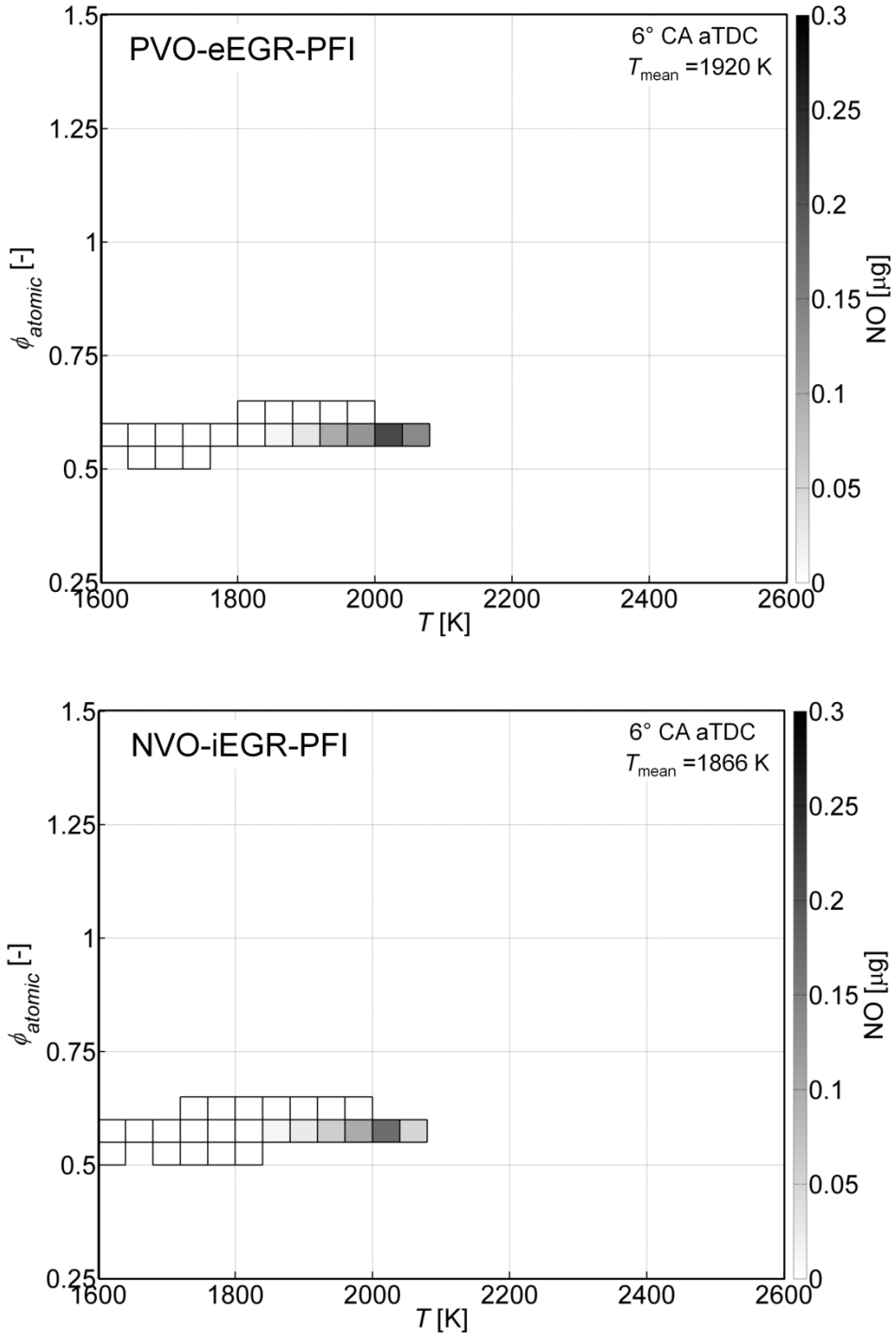

Figure 4.10 – Post-combustion (6°CA aTDC) reaction space from CFD simulation showing distribution of NO formation

4.8 References

1. Lavoie, G. A., Martz, J., Wooldridge, M., and Assanis, D., "A Multi-mode Combustion Diagram for Spark Assisted Compression Ignition", *Combustion and Flame*, Vol. 157: 1106-1110, 2010.

2. Kontarakis, G., Collings, N., and Ma, T., "Demonstration of HCCI Using a Single Cylinder, Four-Stroke SI Engine with Modified Valve Timing," SAE Paper 2000-01-2870, 2000.

3. Koopmans, L., and Denbratt, I., "A Four Stroke Camless Engine, Operated in Homogeneous Charge Compression Ignition Mode with Commercial Gasoline," SAE Paper 2001-01-3610, 2001.

4. Allen, J., and Law, D., "Variable Valve Actuated Controlled Auto-Ignition: Speed Load Maps and Strategic Regimes of Operation," SAE Paper 2002-01-0422, 2002.

5. Hiraya, K., Hasegawa, K., Urushihara, T., Iiyama, A., and Itoh, T., "A Study on Gasoline Fueled Compression Ignition Engine ~ A Trial of Operation Region Expansion," SAE Paper 2002-01-0416, 2002.

6. Milovanovic N., Chen R., and Turner J., "Influence of the Variable Valve Timing Strategy on the Control of a Homogeneous Charge Compression Ignition Engine", SAE Paper 2004-01-1899.

7. Dec, J.E., and Yang, Y., "Boosted HCCI for High Power without Engine Knock and with Ultra-Low NOx Emissions – using Conventional Gasoline," SAE Paper 2010-01-1086, 2010.

8. Mamalis, S., Babajimopoulos, A., Guralp, O., and Najt, P., "Optimal Use of Boosting Configurations and Valve Strategies for High Load HCCI – A Modeling Study," SAE Paper 2012-01-1101, 2012.

9. Rothamer, D. A., Snyder, J. A., Hanson, R. K., Steeper, R. R., and Fitzgerald, R. P., "Simultaneous imaging of exhaust gas residuals and temperature during HCCI combustion," *Proceedings of the Combustion Institute* 32: 2869-2876, 2009.

10. Mehl, M., Chen, J.Y., Pitz, W.J., Sarathy, S.M., and Westbrook, C. K., "An Approach for Formulating Surrogates for Gasoline with Application toward a Reduced Surrogate Mechanism for CFD Engine Modeling," *Energy & Fuels*, Vol. **25**, Issue 11, pp. 5215-5223, 2011.

11. Sjöberg, M., Dec, J. E., and Cernansky, N. P., "Potential of Thermal Stratification and Combustion Retard for Reducing Pressure-Rise Rates in HCCI Engines, Based on Multi-Zone Modeling and Experiments," SAE Paper 2005-01-0113, 2005.

12. He, X., Donovan, M. T., Zigler, B. T., Palmer, T. R., Walton, S. M., Wooldridge, M. S., and Atreya, A., "An experimental and modeling study of iso-octane ignition delay times under homogeneous charge compression ignition conditions," *Combustion and Flame*, Vol. 142, pp. 266-275, 2005.

CHAPTER 5

EFFECT OF FUELING STRATEGY

The method used to deliver fuel into the cylinder is a topic of interest for HCCI operation. With the increasing trend towards injecting fuel directly into the residuals during NVO to take advantage of possible fuel-reforming and NVO heat release [1-3], it is important to understand how injecting fuel into hot residuals affects development of the pre-ignition reaction space for HCCI and what effects this has on burn duration and NOx emissions compared to conventional fully premixed fueling, as may be achieved by PFI into the intake port. It is also important to understand the differences in reaction space development with injection into hot residuals during NVO versus injection into fresh incoming charge during the intake event under PVO operation.

5.1 Direct injection under NVO conditions

Full cycle CFD simulations using the FFVA engine mesh are performed to compare the PFI and DI fueling strategies. Both cases employ an NVO of 157° CA and the engine speed is 2000 RPM. For the DI case, injection is during the expansion portion of the recompression event with SOI timing at 330° CA bTDC, with injection duration of 14.5° CA. For the PFI case, the fuel is assumed premixed in the intake. In both cases, the fuel mass at IVC is 9.3 mg. With the same valve events, the amount of internal residual is nearly identical in both cases with 42% iEGR for the PFI case and 43% iEGR for the DI case. Neither case employs external residual. The mean χ_{O2} is 15% and the mean ϕ_{FO} is

0.44. The ignition timings for the two cases are matched with CA10 approximately at 2° CA bTDC. The intake temperature for the PFI case is 98°C and that for the DI case is 106°C. Non-reacting CFD simulation is performed during the breathing process after which fully-coupled CFD/kinetics solution is employed from IVC onwards. Gasoline kinetics consisting of 312 species developed by Mehl et al. [4] along with the four-component gasoline surrogate proposed by them is used as in chapters 3 and 4. The operating conditions for the two cases are also summarized in Table 5.1

5.1.1 In-cylinder pressure traces and burn profiles

Figure 5.1 shows the in-cylinder pressure traces from the two cases, and Figure 5.2 shows the burn profiles. From Figure 5.1 and Figure 5.2, it is seen that in general the combustion characteristics in terms of pressure rise rates and burn duration are similar. The 10-90 burn duration for the PFI case is 7.2° CA while that for the DI case is around 6.5° CA. To better understand the impact of DI on stratification and sequential autoignition, we take a look at the reaction space.

5.1.2 Analysis of the pre-ignition reaction space at 10° CA bTDC

Figure 5.3 shows the pre-ignition reaction space at 10° CA bTDC for both cases, visualized by binning post-processed CFD results in terms of T and χ_{O2} in every CFD cell. The color axis indicates the mass within each of these bins. From Figure 5.3 it seems that the overall stratification in χ_{O2} is similar for the two fueling strategies, which indicates that distribution in the oxygen concentration dimension is a function of valve strategy and *not* fueling strategy. Both cases show lower χ_{O2} in the leading edge in terms of temperature (representing residual) and higher χ_{O2} in the colder regions (representing the charge coming from the intake port). In the preceding analysis of the PVO versus NVO strategy, it was shown that this level of compositional stratification in the oxygen

dimension is insufficient to cause any significant changes in the overall reactivity stratification and burn duration.

Figure 5.4 shows the pre-ignition reaction space at 10° CA bTDC for both cases visualized in terms of *T* and ϕ_{FO}. We immediately observe a significant difference in the distribution of ϕ_{FO} for the two cases. The PFI case shows a similar distribution of ϕ_{FO} as χ_{O2} with respect to temperature, with hotter regions of the charge being leaner and colder regions of the charge being richer; as the fuel, like oxygen, is also associated with the intake charge (colder) in case of PFI. However, in the DI case, we note that correlation between ϕ_{FO} and *T* is in the opposite direction as that in the PFI case. Here we note that the *hotter* regions of the charge are *richer*, while the *colder* regions of the charge are *leaner*. This is because for the DI case, injection is done during NVO, into the hot residuals, while the colder intake charge does not contain any fuel initially. Additionally, it may be seen from Figure 5.4 that the extent of stratification in the ϕ_{FO} dimension is higher for the DI case compared to the PFI case. In terms of standard deviations in ϕ_{FO}pre-ignition (at 10° CA bTDC) , $\sigma\phi_{FO}$for the NVO-PFI case is 0.02 and that for the NVO-DI case is 0.17. Thus, there is almost an order of magnitude increase in compositional stratification in the ϕ_{FO} dimension with direct injection into residuals. The stratification in temperature in terms of σT for the NVO-DI case is around 42 K. Based on the analysis in Chapter 2, a stratification in *T*, represented by σT = 40 K is worth a stratification in ϕ_{FO} of $\sigma\phi_{FO}$ = 0.4, in terms of effects on reactivity stratification. Thus, the stratification in $\phi_{FO}$with direct injection into residuals during NVO ($\sigma\phi_{FO}$= 0.17) is on the same order as stratification in *T* for this case; and may be important in determining overall reactivity stratification and burn duration.

5.1.3 Effect of ϕ_{FO} distribution from injecting into residuals

In order to isolate the effect of ϕ_{FO} stratification on burn duration, the distribution in reactivity space (defined by ignition delay) is calculated for the DI case based on *T*, χ_{O2} and ϕ_{FO} of every CFD cell. Another companion-calculation of ignition delays is made based on the *T* and χ_{O2} of every cell, but using the global mean $\phi_{FO,}$ in effect ignoring any ϕ_{FO} stratification within the CFD domain. This is done to decouple the effect of ϕ_{FO} stratification on reactivity stratification. The results of these calculations in terms of cumulative reactivity distributions are shown together in Figure 5.5. It is seen from Figure 5.5 that ignoring ϕ_{FO} stratification results in a *shorter* reactivity width. This is because DI into the residuals results in a "favorable" ϕ_{FO} stratification, which acts in the same direction as *T* stratification, such that hotter regions of the charge are also richer in terms of ϕ_{FO}, while colder regions of the charge are leaner and less reactive chemically.

This effect is clearer in Figure 5.6, which shows the distribution of ϕ_{FO} over ignition delay for both the NVO-PFI case and the NVO-DI case. For the NVO-PFI case, as discussed in Chapter 4, colder regions (representing the intake charge) have longer ignition delays (since reactivity stratification is dominated by T). We see that these regions are also richer in terms of ϕ_{FO}, as the fuel is premixed with the intake. For the NVO-DI case, we note that the more reactive regions with lower ignition delay (which correspond to higher temperature regions), also have higher ϕ_{FO}, as now, with NVO-DI we inject fuel into the *hot* residuals.

Thus, the ϕ_{FO} stratification in the case of NVO-DI now causes the hotter regions of the charge to be *more* reactive than if these regions were at the global mean ϕ_{FO}; while the colder regions of the charge are made *less* reactive than they would be were they at the global mean ϕ_{FO}. This causes the overall reactivity stratification to be enhanced by the ϕ_{FO} stratification from DI into residuals during NVO. However, in spite of this

increase in reactivity stratification brought about by the added ϕ_{FO} stratification, the burn duration for the DI case is even shorter than the PFI case. To understand the reason for this, the temperature and reactivity stratifications are compared for the two cases.

5.1.4 Comparison of thermal and reactivity stratification

Figure 5.7 shows the pre-ignition (at 10° CA bTDC) thermal stratification in terms of cumulative temperature distribution based on CFD simulations for both cases. From Figure 5.7 it is immediately apparent that the DI case has a smaller distribution in temperature compared to the PFI case. The $TW_{10\text{-}90}$ for the NVO-PFI case is 110 K and that for the NVO-DI case is 89 K. The reasoning is as follows - spray vaporization within the hot residuals due to injecting fuel during NVO results in the hottest regions of the charge getting cooled down to a certain extent which results in a lower maximum temperature (T_{max}) of the charge prior to ignition. To compensate for the spray-induced cooling, the intake temperature needs to be *increased* for the DI case compared to the PFI case, in order to match ignition timing, with $T_{in,\ DI}$ = 106°C and $T_{in,\ PFI}$ = 98°C. This results in an increase in temperature of the end-gas (intake) prior to ignition, in effect increasing the minimum temperature within the charge (T_{min}) and reducing the temperature difference between the leading edge and the end-gas. This results in an overall reduction in the 10-90 thermal width compared to the PFI case. Thus DI into residuals effectively reduces the overall thermal stratification prior to ignition due to cooling of the hot residuals (lower T_{max}) and increased intake air heating requirement compared to PFI (higher T_{min}). The mean temperature and mean composition for both cases prior to ignition (at 10° CA bTDC) is identical with mean T = 1053 K, mean ϕ_{FO} = 0.44 and mean χ_{O2} = 15%.

Figure 5.8 shows ignition delay computed in every CFD cell at 10° CA bTDC using the He et al. [5] correlation for both the NVO-PFI and NVO-DI cases. The *x*-axis is

1000/T and the y-axis is the logarithm of the ignition delay. It can be seen from Figure 5.8 that there is significant scatter in ignition delay for a given temperature for the NVO-DI case, and this is attributed to the increased ϕ_{FO} stratification arising from direct injection into the residuals.

Figure 5.9 shows the cumulative reactivity stratification based on ignition delay calculations in every CFD cell at 10° CA bTDC for the NVO-PFI and NVO-DI cases. It is seen that the leading 10% of the reactivity (lowest ignition delays) is approximately matched for the two cases, which is why the CA10 angles are matched for the two cases. Even though the leading edge of the DI distribution is cooler than the PFI case, it is also richer than the leading edge of the PFI distribution (since fuel is associated with the hottest regions for DI) which compensates in terms of reactivity as computed using the ignition delay correlation. Thus, under the conditions studied, it seems that the increase reactivity stratification brought about by additional ϕ_{FO} stratification in the same direction as thermal stratification is compensated for by the lower *overall* thermal stratification as a result of spray cooling and additional intake air heating for the DI case. Consequently the burn durations for the two fueling strategies are similar with the DI case burning slightly faster.

It is important to point out though, that post ignition of the most reactive portions of the charge, the reactivity stratification within the unburned charge (yet to ignite) drastically changes compared to the pre-ignition values (computed at 10° bTDC) due to temperature rise in the unburned regions brought about by compression from the ignited, burning regions of the charge. Thus, comparing the reactivity stratification pre-ignition does have its limitations. For example, if we take a closer look at the reactivity stratification pre-ignition for the two cases in Figure 5.9, it may be seen that the ignition delay below which 90% of the charge mass is at is slightly *lower* for the PFI case compared to the DI case; thus, we would expect a slightly shorter burn duration for PFI compared to DI. However, in reality, the burn duration of the DI case (6.5° CA) is shorter

than that of the PFI case (7.2° CA). This is possibly because the early stages of combustion are faster for the DI case, which accelerates the ignition of the unburned portions of the charge to a greater extent than in the PFI case, resulting in an overall faster burn. This effect cannot be easily discerned from the pre-ignition reactivity distribution. However, save for these small details, looking at the reactivity stratification prior to ignition is a powerful tool to understand the interaction between thermal and compositional stratification, and understanding the relative importance of stratification in the different reactivity dimensions, *T*, $\phi_{FO}$and χ_{O2}.Unlike the previous studies (diluent composition and NVO versus PVO), the sequential MZ code is not used in this study to decouple stratification effects from fueling due to the inability of the code to handle the level of stratification associated with direct injection, arising from numerical issues with the ODE solver/kinetics.

5.1.5 Comparison of NOx emissions

Figure 5.10 shows the mean in-cylinder temperatures for the two fueling strategies. It may be seen from Figure 5.10 that the peak mean combustion temperatures are similar for the two cases. Figure 5.11 shows the evolution of NO formation for the two cases (computed using the extended Zeldovich mechanism taken from Heywood [6] used in conjunction with the 312-species gasoline mechanism [4]). From Figure 5.11 it is observed that the NO produced post-combustion for the two cases vastly differs, with the DI case (engine-out EINOx = 1.07 g/kg fuel) producing roughly an order of magnitude higher NO compared to the PFI case (engine-out EINOx = 0.11 g/kg fuel).

To explain this significant difference in engine-out NOx for the two cases in spite of them having similar peak mean combustion temperatures, the post-combustion reaction space (6° CA aTDC) which represents a mass percent burned of roughly 90% for both cases, and also represents the location of the peak mean in-cylinder combustion

temperatures. Figure 5.12 shows the post-combustion reaction space for both cases, with PFI shown on top and DI shown below it in the figure. The reaction space is visualized based on binning CFD results in temperature (x-axis) and ϕ_{atomic} (y-axis) dimensions. As indicated in Chapter 3, the value of ϕ_{atomic} is unaltered by the progress of combustion and thus serves as a good marker of dilution history. The bins are colored by total NO content in the bin at 6° CA aTDC.

The post-combustion temperatures for both cases is roughly 1900 K, however, it is clear from Figure 5.12 that the DI case has a larger distribution in local combustion temperatures. Moreover, the highest local post combustion temperatures for the DI case are around 2500 K while those for the PFI case do not exceed 2100 K. In both pictures within the figure, another curve is shown which qualitatively represents the variation in post-combustion temperatures with equivalence ratio, which in this case is ϕ_{atomic}, a proxy for local dilution levels. The average ϕ_{atomic} for both cases is roughly 0.6. The variation of local ϕ_{atomic} about this value is minimal for the PFI case, in line with the observations in Chapter 4 which show minimal compositional stratification as a result of NVO alone with premixed fueling. For the DI case, however, it is seen that there is significant stratification in ϕ_{atomic} about the mean ϕ_{atomic}, with significant portions of the charge having near-stoichiometric ϕ_{atomic}, and correspondingly lower local dilution. These locally “less-dilute” regions burn to high combustion temperatures, and there is enough mass in such regions to significantly increase overall NO output for the DI case compared to the PFI case. These results indicate that the poor mixing resulting from DI during NVO might cause significant problems with NOx emissions, and a PFI or PDI (combination of PFI and DI) strategy might help under such conditions.

5.2 Reaction space effects of early DI versus PFI for PVO operation

5.2.1 Conditions for study

The aim of this study is to understand the impact of fueling strategy on HCCI combustion characteristics when a PVO valve strategy is used. Using full-cycle CFD simulations coupled to 312-species gasoline kinetics by Mehl et al. [4], two cases are evaluated – one with PFI, and the other with DI having SOI at 330° CA bTDC and injection duration of 14.5° CA. Identical PVO valve lifts with minimal positive overlap are used in both cases. Both cases operate with external residuals, with eEGR representing 36% of the total charge mass. The iEGR as a result of retained residuals is low for both cases and represents 7% of the total charge mass. Thus the total RGF for both PFI and DI is 43%. For the DI case, injection is during the intake event, even though the SOI timing is the same as used in the NVO-DI case in section 5.1. Both cases are run naturally aspirated at an engine speed of 2000 RPM. At IVC, the mean ϕ_{FO} is 0.44 and mean χ_{O2} is 15% for both strategies. The intake temperature for the DI case is higher than that for the PFI case with $T_{\text{in, DI}}$ = 251°C and $T_{\text{in, PFI}}$ = 241°C, such that both cases have the same ignition timing with CA10 at approximately 2° CA bTDC. The fueling is adjusted such that the fuel mass at IVC is 9.3 mg for both strategies. The operating conditions for the two strategies are summarized in Table 5.2.

5.2.2 In-cylinder pressure and burn profiles

Figure 5.13 shows the in-cylinder pressure traces from the CFD simulations of the two cases. It is seen from Figure 5.13 that the pressure traces are almost identical, with similar peak pressures and pressure rise rates. From the comparison of burn profiles, shown in Figure 5.14 it is observed that both cases have similar burn rates and have an identical 10-90 burn duration of 5.5° CA.

5.2.3 Comparison of pre-ignition reaction space at 10° CA bTDC

Figure 5.15 shows the distribution of charge within the cylinder visualized in terms of *T* and χ_{O2} during the pre-ignition crank angle of 10° CA bTDC for the PVO-PFI case (top) and PVO-DI case (bottom). The bins are colored by mass fraction of the total cylinder charge contained within them. From the figure, it may be seen that there is little stratification in the χ_{O2} dimension, with $\sigma\chi_{O2}$ < 0.07% which based on the analysis in the preceding chapters is not significant to affect reactivity distribution. Figure 5.16 shows the distribution of charge within the cylinder visualized in terms of *T* and ϕ_{FO} during the pre-ignition crank angle of 10° CA bTDC for the PVO-PFI case (top) and PVO-DI case (bottom). The bins are colored by mass fraction of the total cylinder charge contained within them. The stratification in ϕ_{FO} for the PVO-PFI case (top) is negligible with $\sigma\phi_{FO}$ = 0.002; whereas for the PVO-DI case (bottom), there seems to be a more noticeable stratification in ϕ_{FO}, with $\sigma\phi_{FO}$ = 0.06 due to the direct injection. This level of stratification with PVO-DI is now comparable to NVO-DI which has a $\sigma\phi_{FO}$= 0.17; however it is about a third in terms of standard deviation compared to the NVO case.

Looking at the pre-ignition (10° CA bTDC) reactivity stratification for the two cases in Figure 5.17, we notice that the reactivity stratification for the PVO-DI case is almost identical to that of the PVO-PFI case, in spite of there being a noticeable ϕ_{FO} stratification. The reason for the identical reactivity stratification for the PVO-DI case is because unlike the NVO-DI case, where the ϕ_{FO} stratification is coupled with the temperature distribution, the ϕ_{FO} distribution for the PVO-DI case is not correlated to the dominant thermal distribution. The average temperature distribution over ignition delay for the two cases (PVO-PFI and PVO-DI) is shown in Figure 5.18. We note from the figure that for both cases, the regions with higher reactivity (lower ignition delay) also have higher temperature, and that ignition delay is well correlated with temperature.

Moreover, the distribution of average temperature over ignition delay for both cases is nearly identical for PVO-PFI and PVO-DI operation.

Figure 5.19 shows the cumulative distribution in temperature for both the cases. The thermal widths ($TW_{10\text{-}90}$) for the two cases are nearly identical with $TW_{10\text{-}90}$ approximately equal to 80 K for both cases. Thus, with DI associated with a PVO strategy, there is no change in overall thermal stratification to match ignition delay unlike with NVO operation, where NVO-DI has a significantly lower thermal stratification prior to ignition compared to NVO-PFI.

Even though the stratification in ϕ_{FO} for the PVO-DI case is lower than in the NVO-DI case; there is still an order of magnitude higher ϕ_{FO} stratification for the PVO-DI case compared to the PVO-PFI case. Still, the burn profiles and reactivity stratification are almost identical for the two cases. Figure 5.20 shows the distribution of average ϕ_{FO} over reactivity (represented by ignition delay) for the PVO-PFI and PVO-DI cases. For the PVO-PFI case, as expected, there is no variation in ϕ_{FO} over reactivity due to premixed operation; however for the PVO-DI case there seems to be a distribution in ϕ_{FO}. However, unlike in the NVO-DI case, whose distribution in average ϕ_{FO} over reactivity is shown in Figure 5.6, where the more reactive regions with lower ignition delay and higher temperatures, also have higher ϕ_{FO}, there is no correlation between reactivity and ϕ_{FO} for the PVO-DI case, since the fuel is not associated with "hotter" or "colder" regions of the charge. This is because fuel is injected into the intake stream (containing air and external residuals at a uniform temperature), and there is no significant *second* stream (i.e. internal residual), as in the case of NVO-DI. Since there is no correlation between ϕ_{FO} and T in the PVO-DI case, the cumulative distribution in reactivity is unaffected by the ϕ_{FO} stratification. This is made even clearer in Figure 5.21 where ignition delay is computed in every CFD cell for the PVO-DI case based on both the actual ϕ_{FO} within the cell (shown with a solid line), and based on the overall cylinder-average ϕ_{FO} (shown with a dashed line). We see from Figure 5.21 that imposing

the ϕ_{FO} stratification in the manner it exists (uncorrelated to *T*) for the PVO-DI case, does not impact overall reactivity stratification.

5.2.4 Comparison of NOx emissions

Figure 5.22 shows the mean in-cylinder temperature traces for the PVO-PFI and PVO-DI cases. The mean temperature profiles for both fueling strategies under PVO operation look identical. Figure 5.23 shows the evolution of NO formation in terms of EINOx for both cases. The overall engine-out NOx for both fueling strategies with PVO valve profile is well below the 1 g/kg fuel EINOx limit. The EINOx for the PFI case is 0.14 g/kg fuel and for the DI case is 0.19 g/kg fuel. Figure 5.24 shows the distribution of NOx in the post-combustion reaction space (shown at 6° CA aTDC) for both cases in terms of ϕ_{atomic} and *T* from the post-processing of the CFD results. The DI case has a greater initial stratification in ϕ_{atomic} which results in portions of the charge burning less dilute compared to the mean composition within the cylinder, thus reaching higher temperatures post-combustion. However, the stratification is not as significant as in the NVO-DI case where significant portions of the charge burn with less dilution.

5.3 Comparison of DI effects under PVO and NVO conditions

In this chapter, we have until now compared DI to PFI under NVO and PVO conditions respectively. It is also interesting to understand the inherent differences between NVO and PVO operation in the context of direct fuel injection particularly in terms of mixing of the fuel spray. Table 5.3 shows the comparison of the operating conditions for the CFD simulations to compare NVO-iEGR-DI to PVO-eEGR-DI operation. Both cases have the same mean composition at IVC (). The CFD simulations are full-cycle with gasoline kinetics from IVC. The engine speed simulated is 2000 RPM. Figure 5.25 compares the pressure traces and Figure 5.26 compares the burn profiles for

the PVO-DI-eEGR and NVO-DI-iEGR cases. From Figure 5.26 we observe that the NVO case has a longer burn duration compared to the PVO case; the 10-90 burn duration for the PVO case is 5.5° CA and that for the NVO case is 6.5° CA. Figure 5.27 shows the reactivity stratification for the two cases prior to ignition (at 10° CA bTDC). From Figure 5.27 it is clear that the NVO-iEGR-DI case has a higher stratification in reactivity compared to the PVO-eEGR-DI case, which is in line with the longer burn duration observed in the NVO case compared to the PVO case.

Figure 5.28 compares the distribution in reaction space in terms of ϕ_{FO} and T prior to ignition (at 10° CA bTDC) for the two cases. The PVO case has lower stratification in ϕ_{FO}compared to the NVO case with $\sigma\phi_{FO}$=0.06 for the PVO case, and $\sigma\phi_{FO}$=0.17 for the NVO case. The reason for the lower ϕ_{FO} stratification for the PVO-DI case compared to the NVO-DI case is possibly because of the longer intake event for the PVO case compared to the NVO case. To achieve NVO, EVO and IVC are kept fixed; while EVC is advanced and IVO is retarded by an equal amount such that the NVO is symmetric about the gas-exchange TDC. This results in shorter intake and exhaust events with increasing NVO. Figure 5.29 shows the evolution of TKE through the cycle for both the PVO-DI and NVO-DI cases. Since a major portion of the turbulent kinetic energy (TKE) for mixing is provided by the intake event, the shorter intake event for the NVO case results in less TKE being available to mix the fuel with the rest of the charge, resulting in more stratification in ϕ_{FO} present pre-ignition compared to the PVO case. It must be noted that the injection timing, and duration of injection are identical for both the cases; thus both the NVO and PVO cases with direct injection have the same time available for mixing to occur up to the pre-ignition point of 10° CA bTDC. The IVC timing for both cases is at 590° CA aTDC of the previous combustion cycle, or 130° CA bTDC of the current combustion cycle. The intake duration for PVO is longer than that for the NVO case as indicated in the figure, with the IVO timing for the PVO case being significantly earlier than that of the NVO case. It may be seen from Figure 5.29, that

there is a sharp increase in TKE with the beginning of the intake event, and the TKE within the cylinder remains high through most of the intake event for both cases, compared to the value of TKE during the rest of the cycle. Injection in both cases is at 330° CA bTDC of the current cycle, or 390° CA aTDC of the previous cycle. The injection for the PVO case is during the intake event and into the fresh, high kinetic-energy intake charge, whereas in the NVO case, injection is during the NVO portion, with the fuel being injected into the hot residuals from the previous cycle. The mixing is more vigorous for the PVO case due to the longer intake event, and longer duration for which the value of in-cylinder TKE is high, resulting in less overall stratification in ϕ_{FO} compared to the NVO case at IVC and consequently at the pre-ignition point.

The higher pre-ignition ϕ_{FO}stratification for the NVO-DI case compared to the PVO-DI case with direct injection, results in higher NO emissions from NVO operation, with EINOx for the NVO-DI case being 1.07 g/kg of fuel, and that for the PVO case being 0.19 g/kg of fuel. The reason for this is apparent looking at the post-combustion reaction space visualized in terms of ϕ_{atomic} and *T*. shown in Figure 5.30. The color of the bins represent the amount of NO generated in that bin. The higher level of stratification in ϕ_{FO}(and thus ϕ_{atomic}) prior to ignition due to poorer mixing of the directly injected fuel with the rest of the charge for the NVO-DI case results in the less dilute regions achieving relatively high post-combustion temperatures. This results in a significant increase in NO generation within these regions. Due to the better mixing of injected fuel with diluents in the PVO-DI case, there are no regions of the charge that burn to high relatively high post-combustion temperatures, thus the overall NO is significantly lower than the NVO-DI case.

5.4 Summary

PFI and DI fueling strategies are compared under NVO and PVO conditions. Full-cycle CFD simulation are performed with DI SOI timing for both cases is 330° CA bTDC which for the NVO case results in all the fuel being injected during the negative valve overlap portion. For the NVO-DI case, injecting fuel into the hot residuals results in a global ϕ_{FO} stratification that is in the same direction as the thermal stratification which serves to increase reactivity stratification. However, the overall thermal stratification is reduced compared to NVO-PFI due to DI into the hot residuals for the NVO-DI case, which serves to decrease reactivity stratification. A combination of these two effects results in the overall reactivity stratification to be similar to the NVO-PFI case, and consequently the burn duration of the NVO-DI case is similar to that of the NVO-PFI case when ignition timing is matched. With NVO-DI, as a result of incomplete mixing of fuel with the rest of the charge, significant pockets of charge burn with low dilution, resulting in an order of magnitude increase in NOx emissions compared to the NVO-PFI case. Switching to DI under PVO conditions does not seem to affect HCCI combustion characteristics. The ϕ_{FO} stratification as a result of DI under PVO conditions is localized in nature, and is not related to the global thermal distribution, which results in the global reactivity stratification being identical for the PVO-DI and PVO-PFI cases. NOx emissions are also low for the PVO-DI case, because of better mixing compared to the NVO-DI case, due to the longer intake event, and associated increase in turbulent kinetic energy kinetic energy available for mixing.

Table 5.1 – Operating conditions: NVO-PFI versus NVO-DI

Parameter	**PFI**	**DI**
Fueling	PFI	DI; SOI@330° bTDC
NVO	157° CA	157° CA
$\boldsymbol{\phi_{FO}}$ (mean)	0.44	0.44
$\boldsymbol{\chi_{O2}}$ (mean)	15%	15%
T_{in}	98°C	106°C
Internal Residual	42%	42%
External Residual	0%	0%
Total RGF	42%	42%

Table 5.2 – Operating conditions: PVO-PFI versus PVO-DI

Parameter	**PFI**	**DI**
Fueling	PFI	DI; SOI@330° bTDC
NVO	0° CA	0° CA
$\boldsymbol{\phi_{FO}}$ (mean)	0.44	0.44
$\boldsymbol{\chi_{O2}}$ (mean)	15%	15%
T_{in}	98°C	106°C
Internal Residual	7%	7%
External Residual	36%	36%
Total RGF	43%	43%

Table 5.3 – Operating conditions: PVO-DI versus NVO-DI

Parameter	**PVO-DI**	**NVO-DI**
Fueling	DI; SOI@330° bTDC	DI; SOI@330° bTDC
NVO	0° CA	157° CA
$\boldsymbol{\phi_{FO}}$ (mean)	0.44	0.44
$\boldsymbol{\chi_{O2}}$ (mean)	15%	15%
T_{in}	251°C	106°C
Internal Residual	7%	43%
External Residual	36%	0%
Total RGF	43%	43%

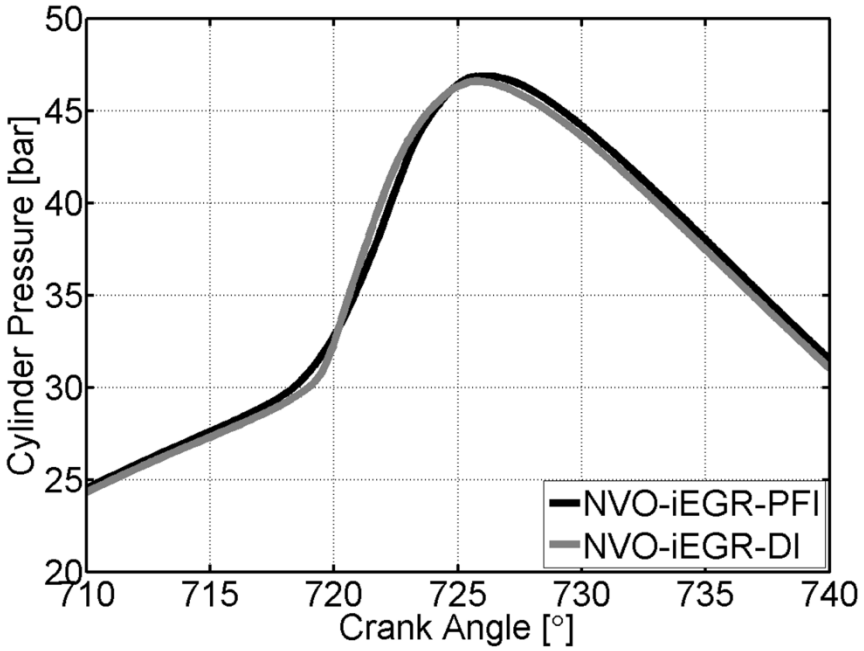

Figure 5.1 – In-cylinder pressure traces from CFD simulation of NVO-iEGR-PFI and NVO-iEGR-DI cases

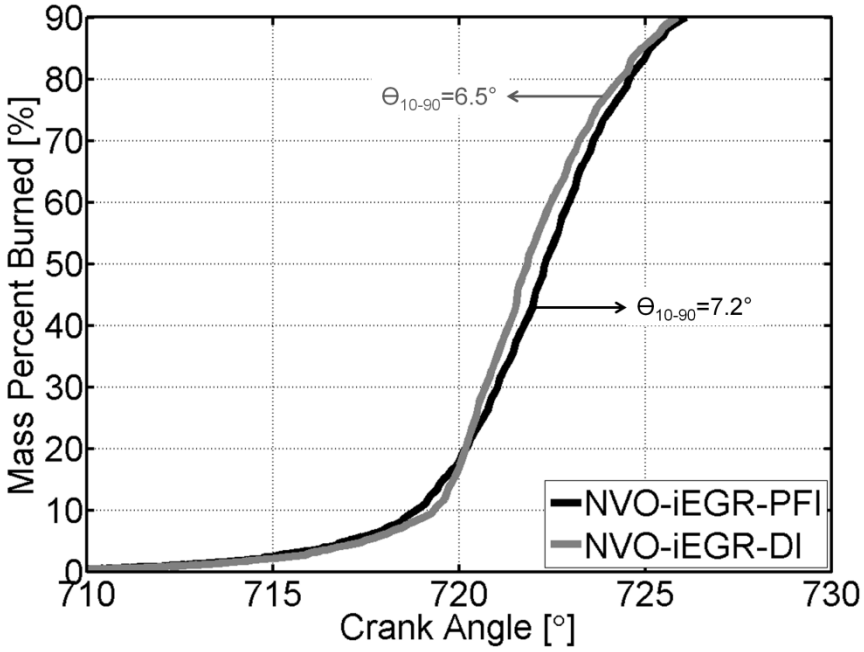

Figure 5.2 – Burn profiles from CFD simulation of NVO-iEGR-PFI and NVO-iEGR-DI cases

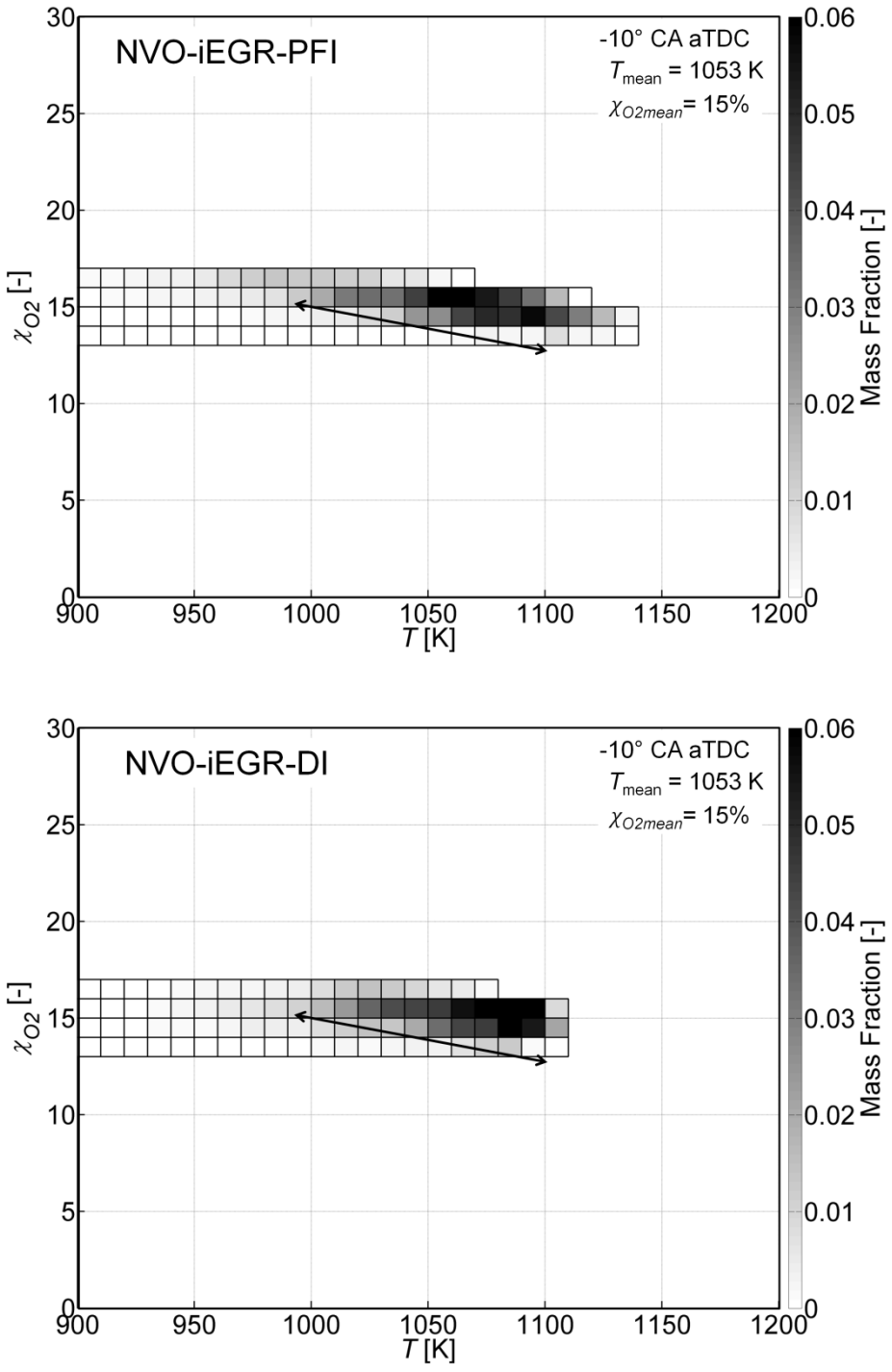

Figure 5.3 – Pre-ignition (10° CA bTDC) visualized in T and χ_{O2} dimensions from CFD simulation of NVO-iEGR-PFI and NVO-iEGR-DI cases

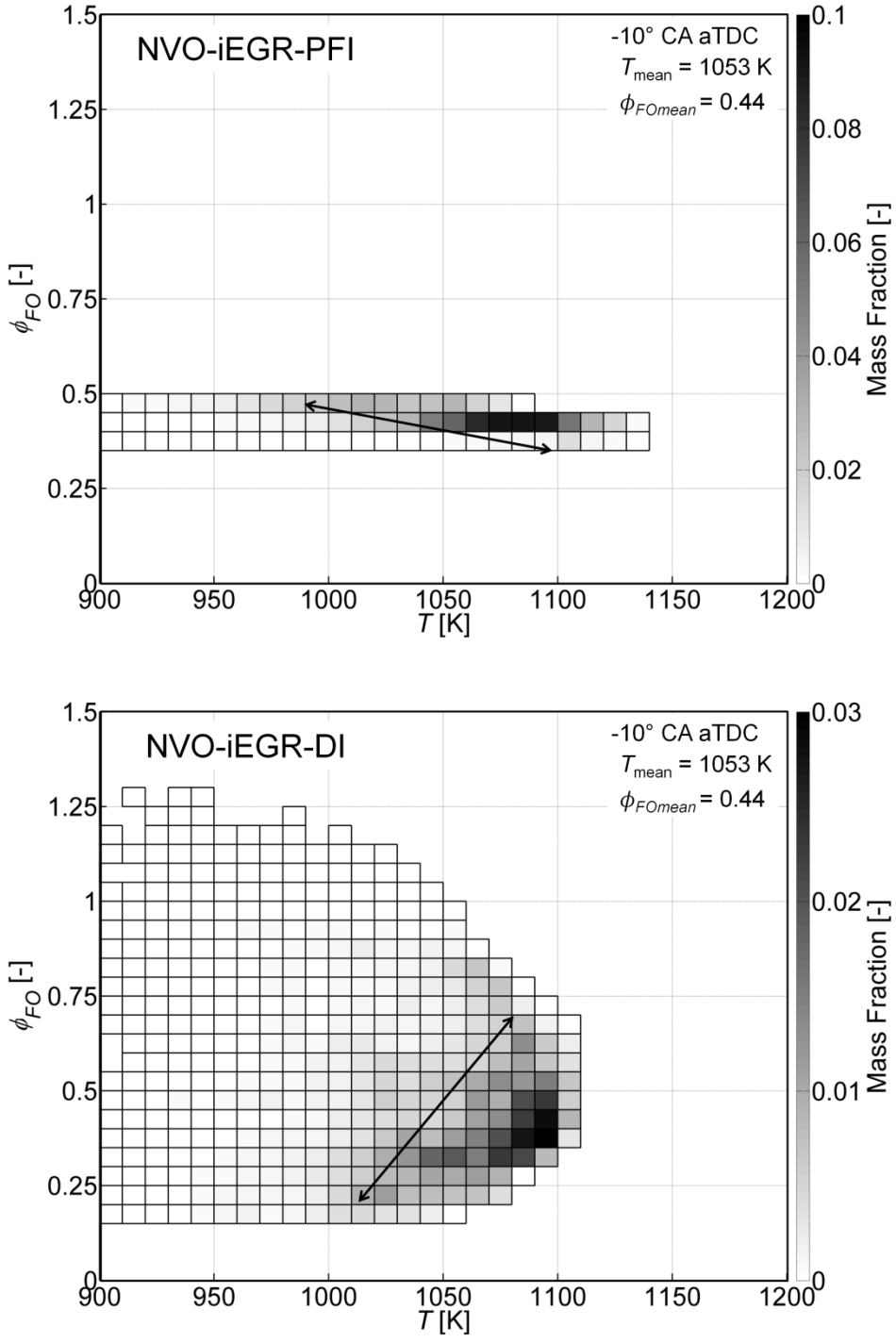

Figure 5.4 – Pre-ignition (10° CA bTDC) visualized in T and ϕ_{FO} dimensions from CFD simulation of NVO-iEGR-PFI and NVO-iEGR-DI cases

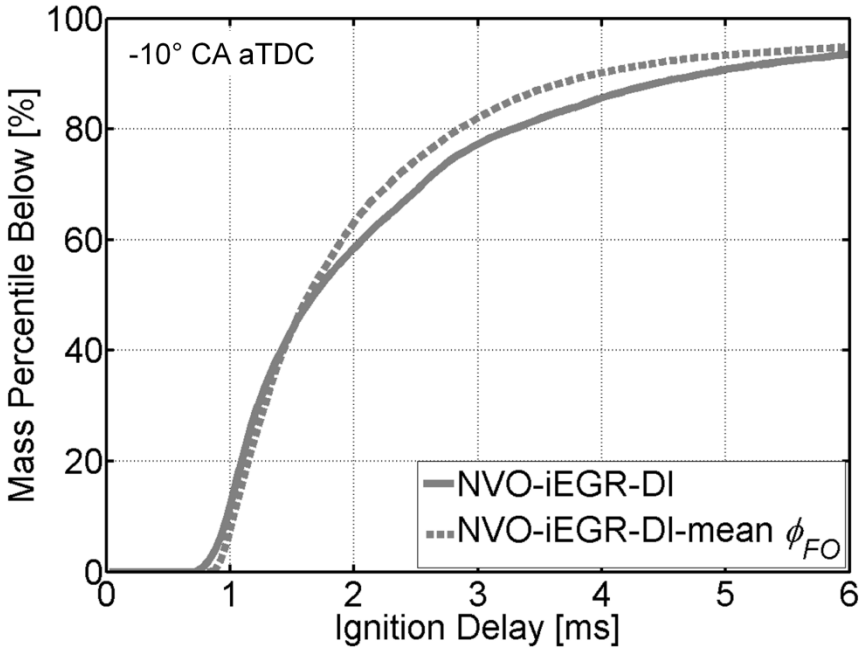

Figure 5.5 – Decoupling ϕ_{FO} stratification from *T* stratification for NVO-iEGR-DI case. Pre-ignition (10° CA bTDC) reactivity distribution (in terms of ignition delay) from CFD simulation of NVO-iEGR-DI shown with and without considering ϕ_{FO} stratification

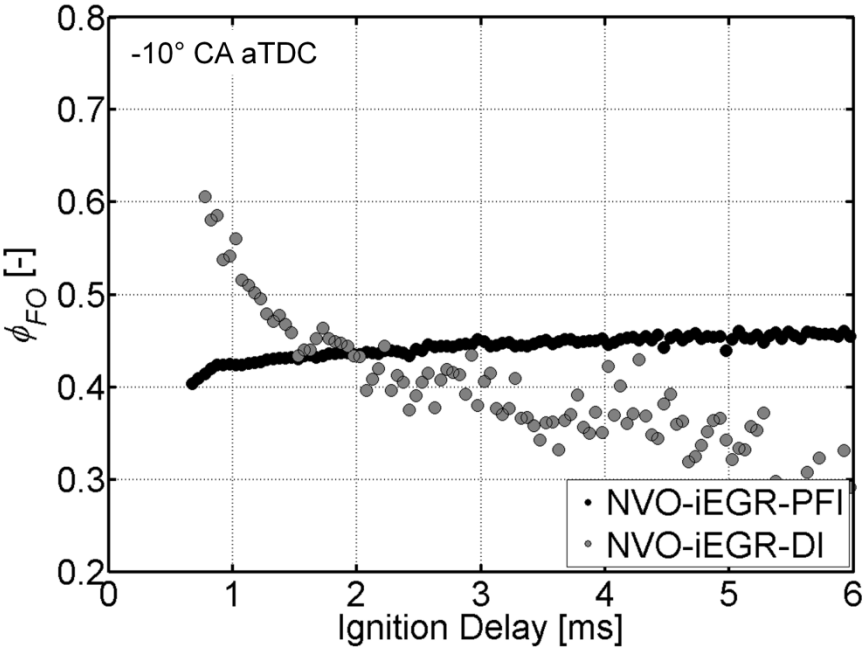

Figure 5.6 – Pre-ignition (10° CA bTDC) distribution of ϕ_{FO} over ignition delay for NVO-iEGR-PFI and NVO-iEGR-DI

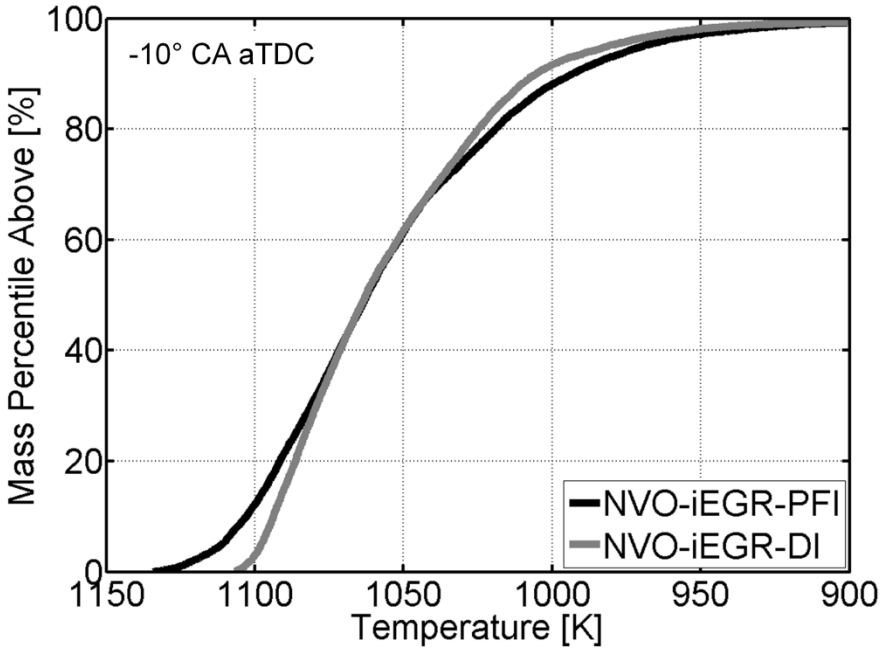

Figure 5.7 – Pre-ignition (10° CA bTDC) temperature distribution in cumulative terms from CFD simulation of NVO-iEGR-PFI and NVO-iEGR-DI cases

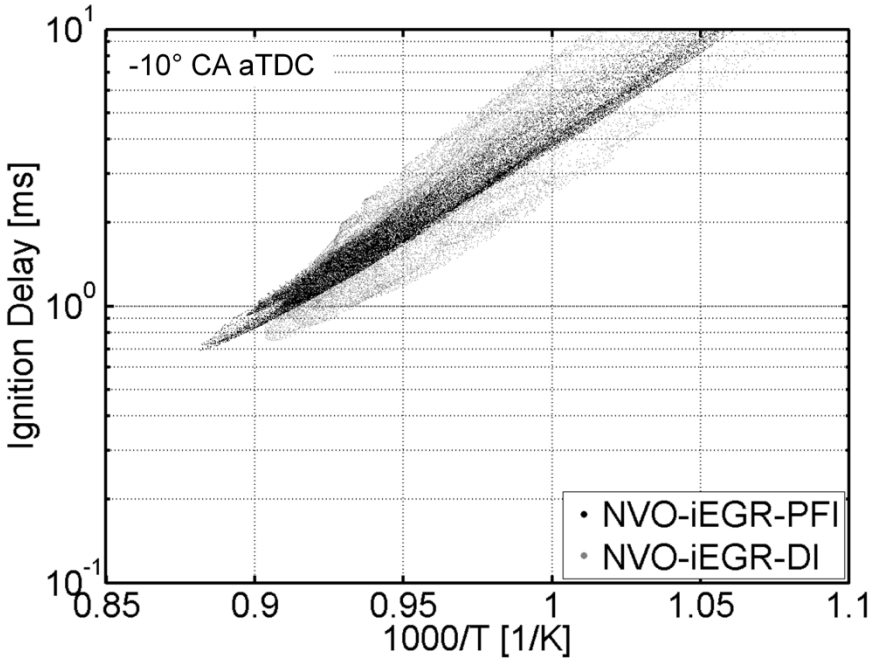

Figure 5.8 – Pre-ignition (10° CA bTDC) ignition delay scatter from CFD simulation of NVO-iEGR-PFI and NVO-iEGR-DI cases

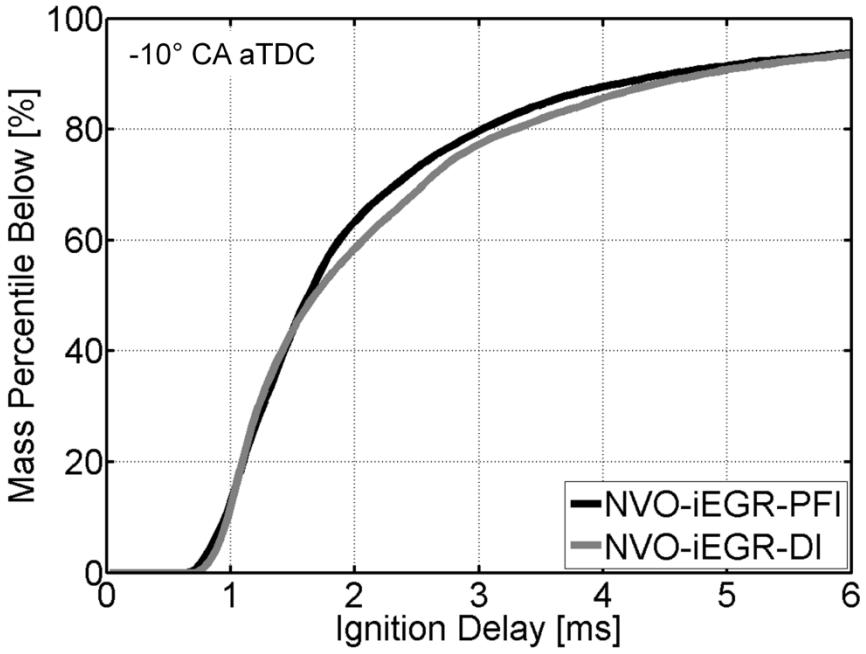

Figure 5.9 – Pre-ignition (10° CA bTDC) reactivity distribution (in terms of ignition delay) from CFD simulation of NVO-iEGR-PFI and NVO-iEGR-DI cases

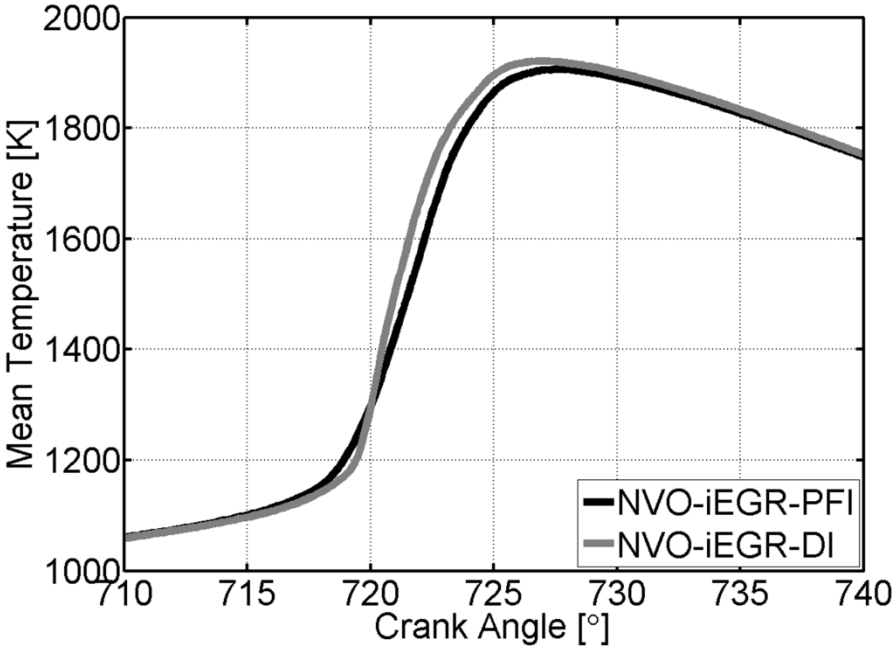

Figure 5.10 – In-cylinder temperature traces from CFD simulation of NVO-iEGR-PFI and NVO-iEGR-DI cases

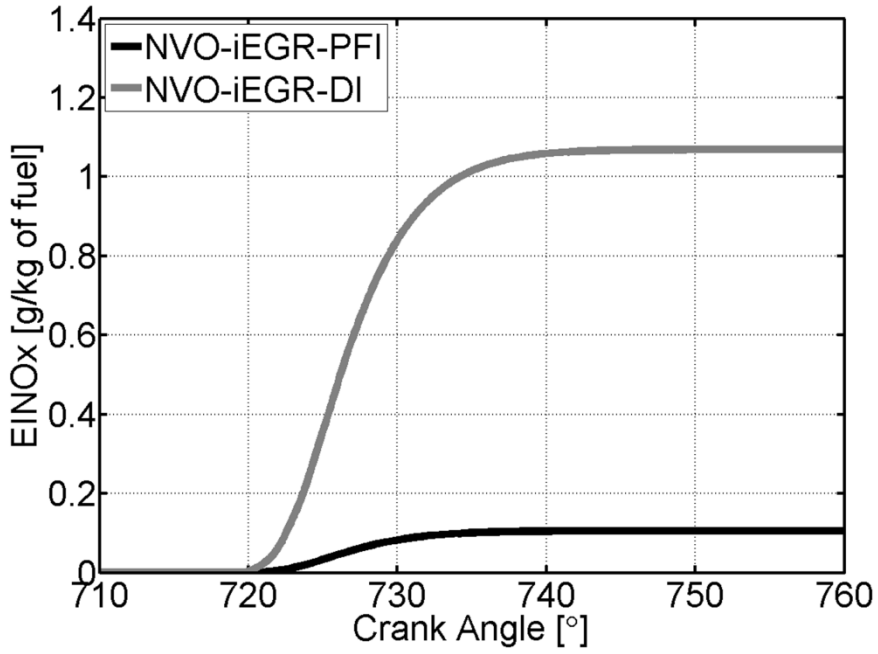

Figure 5.11 – NO formation with respect to crank angle (in terms of $EINO_X$) from CFD simulation of NVO-iEGR-PFI and NVO-iEGR-DI cases

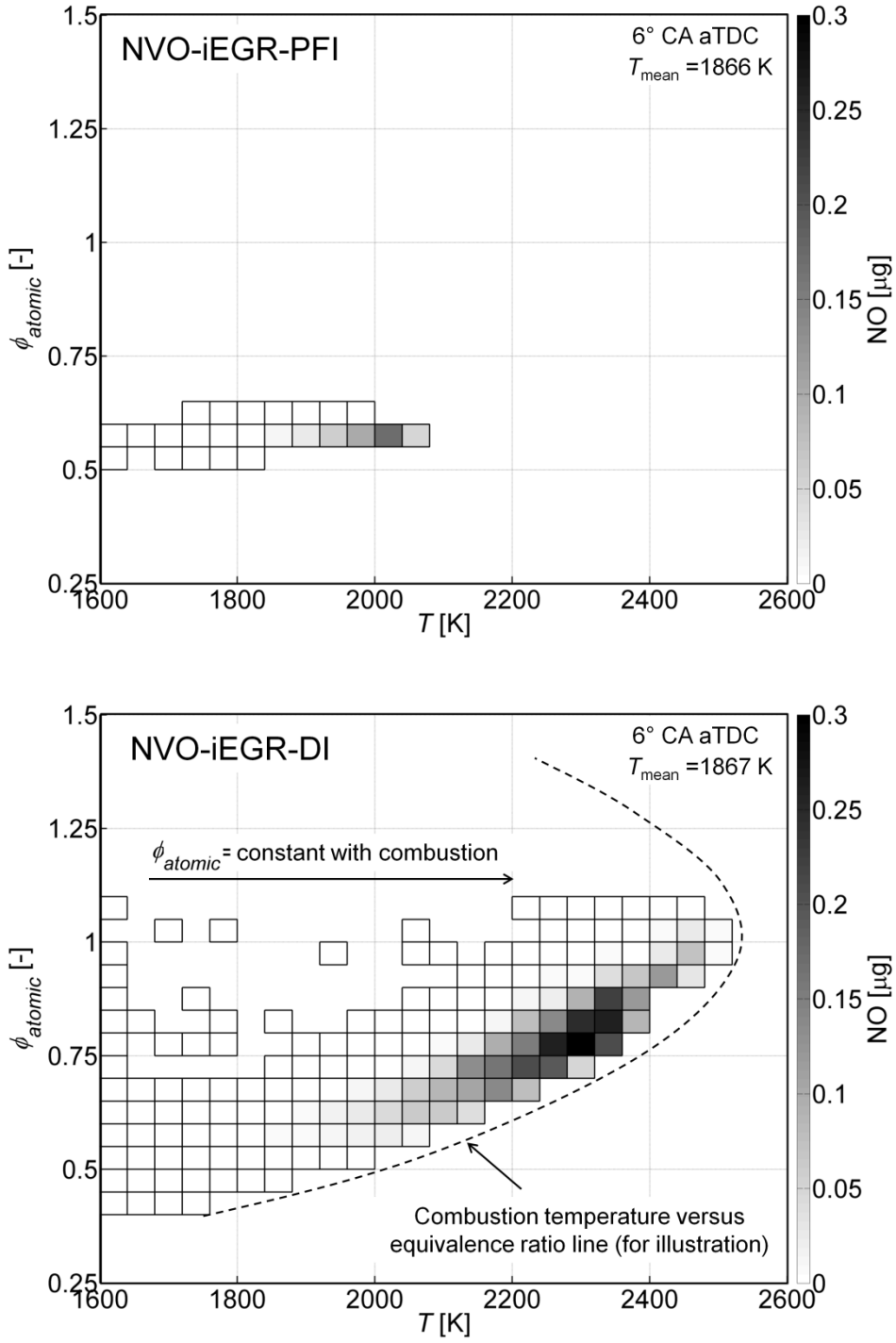

Figure 5.12 – Post-combustion (6° CA aTDC) reaction space from CFD simulation of NVO-iEGR-PFI and NVO-iEGR-DI cases showing NO distribution

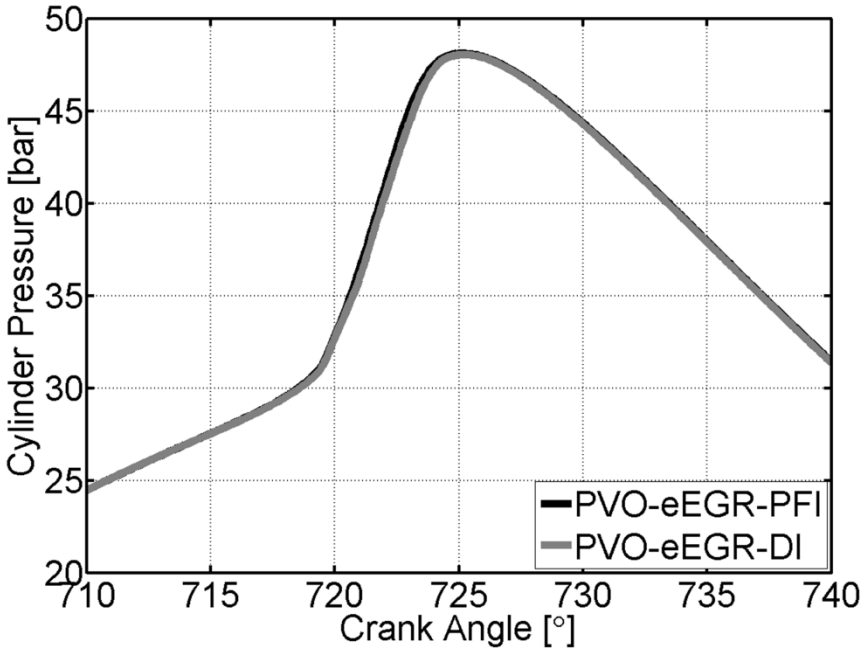

Figure 5.13 – In-cylinder pressure traces from CFD simulation of PVO-eEGR-PFI and PVO-eEGR-DI cases

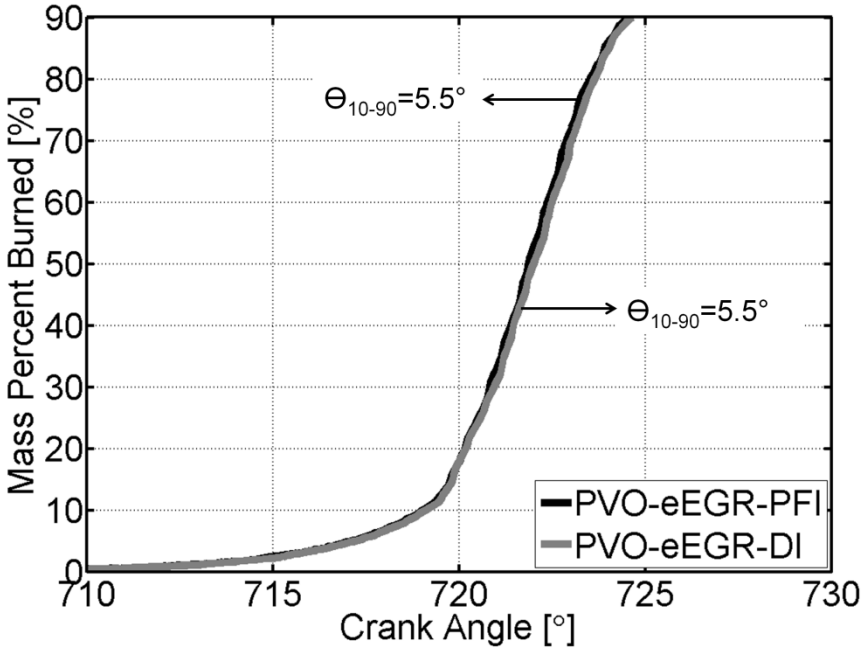

Figure 5.14 – Burn profiles from CFD simulation of PVO-eEGR-PFI and PVO-eEGR-DI cases

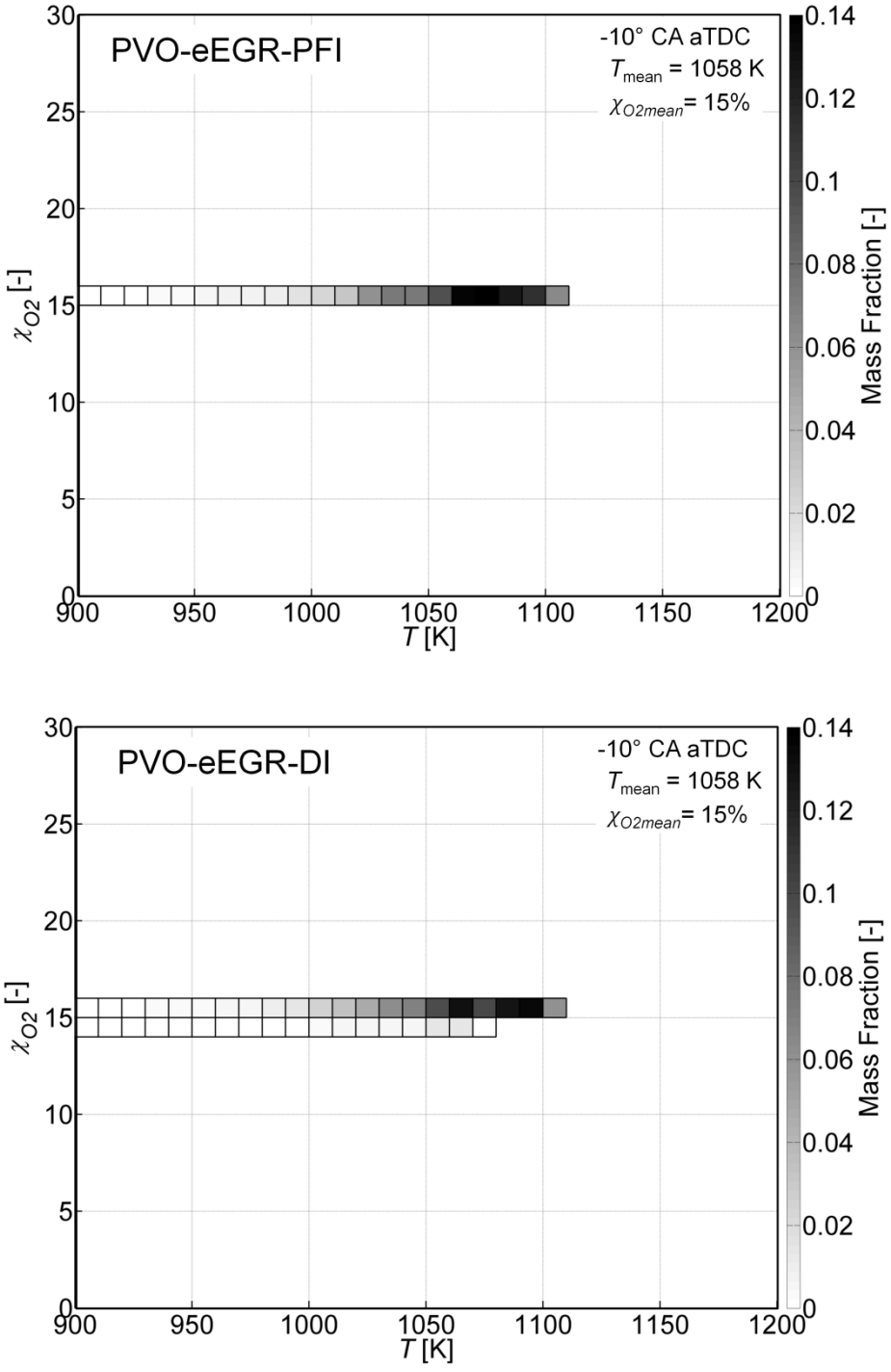

Figure 5.15 – Pre-ignition (10° CA bTDC) reaction space visualized in terms of T and χ_{O2}

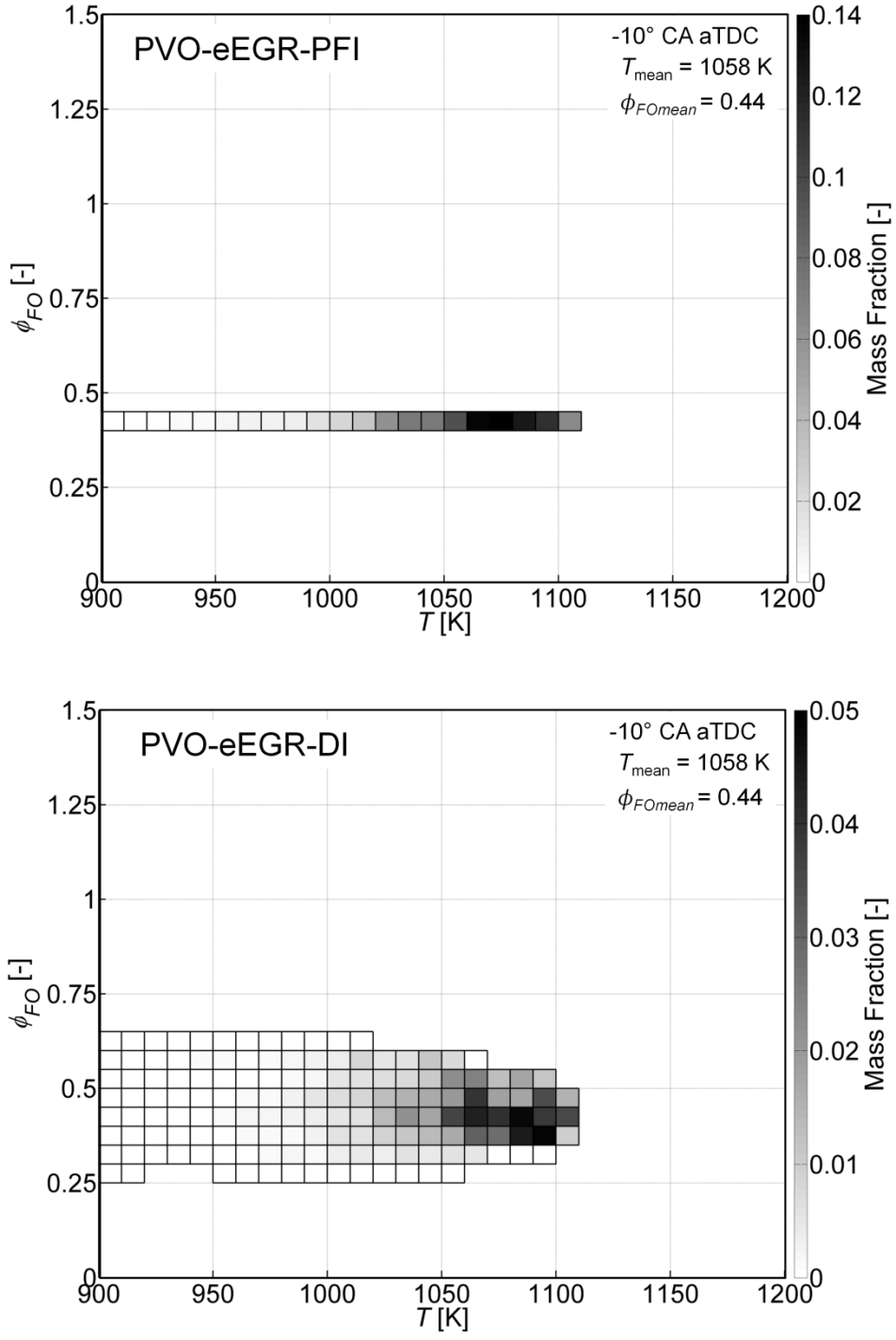

Figure 5.16 – Pre-ignition (10° CA bTDC) reaction space visualized in terms of T and ϕ_{FO}

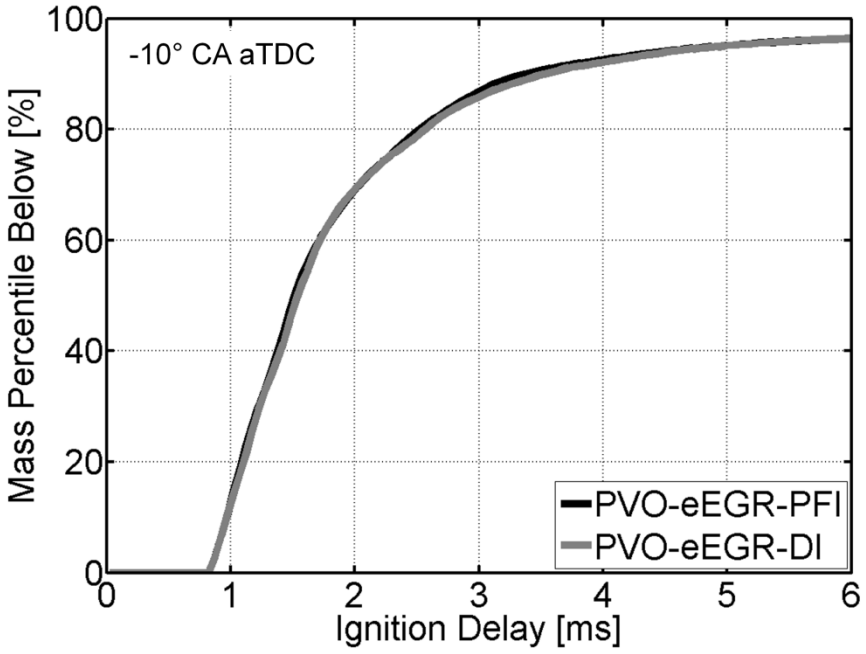

Figure 5.17 – Cumulative distribution of reactivity in terms of ignition delay for PVO-PFI and PVO-DI cases

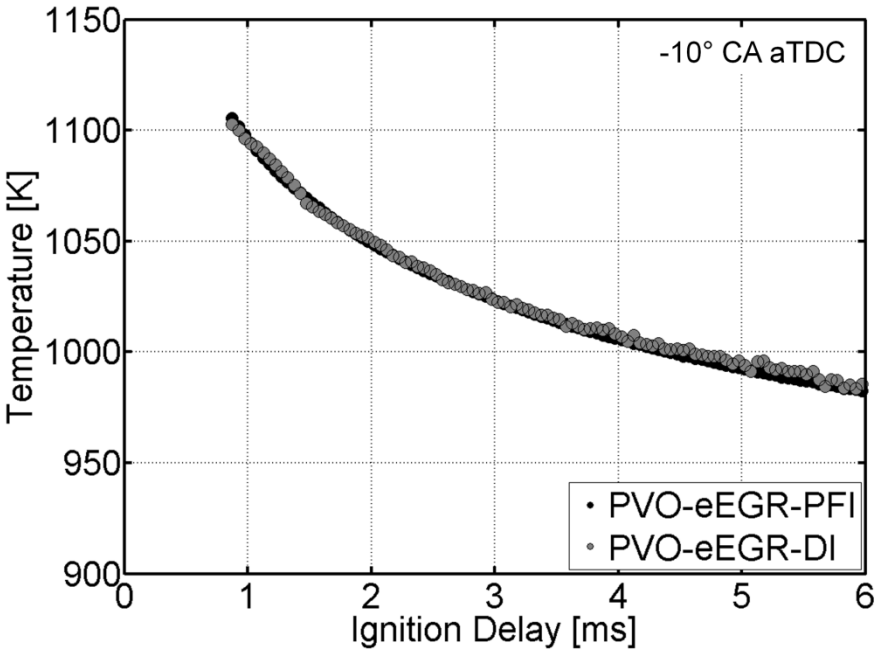

Figure 5.18 – Average temperature distribution over ignition delay for PVO-PFI and PVO-DI cases

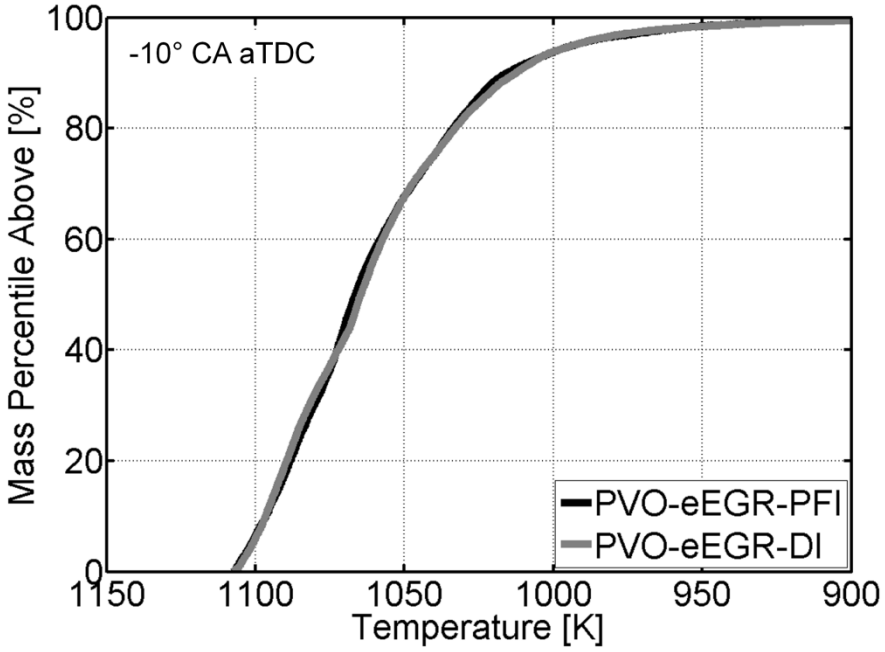

Figure 5.19 – Cumulative distribution in temperature for PVO-PFI and PVO-DI cases

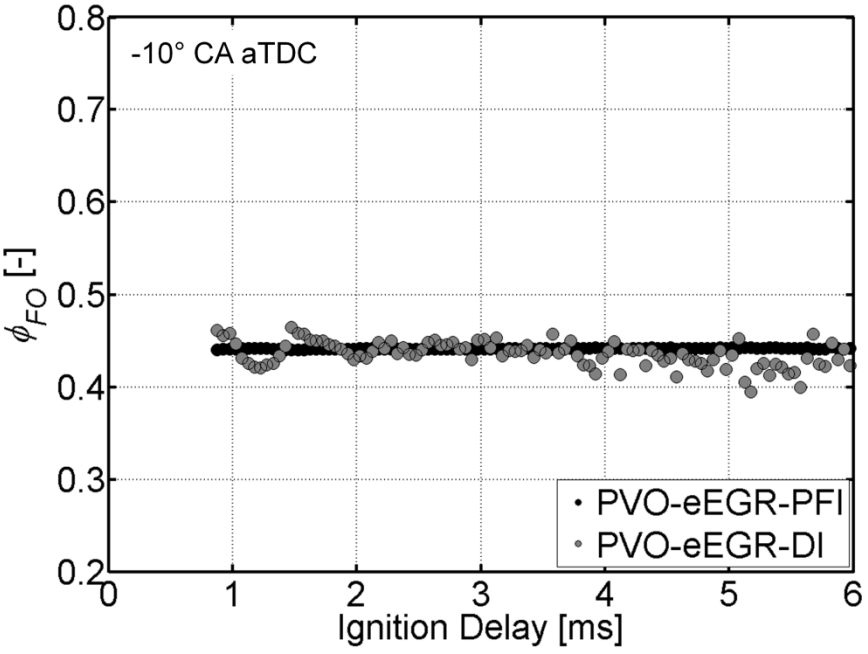

Figure 5.20 – Average ϕ_{FO} over ignition delay for PVO-PFI and PVO-DI cases

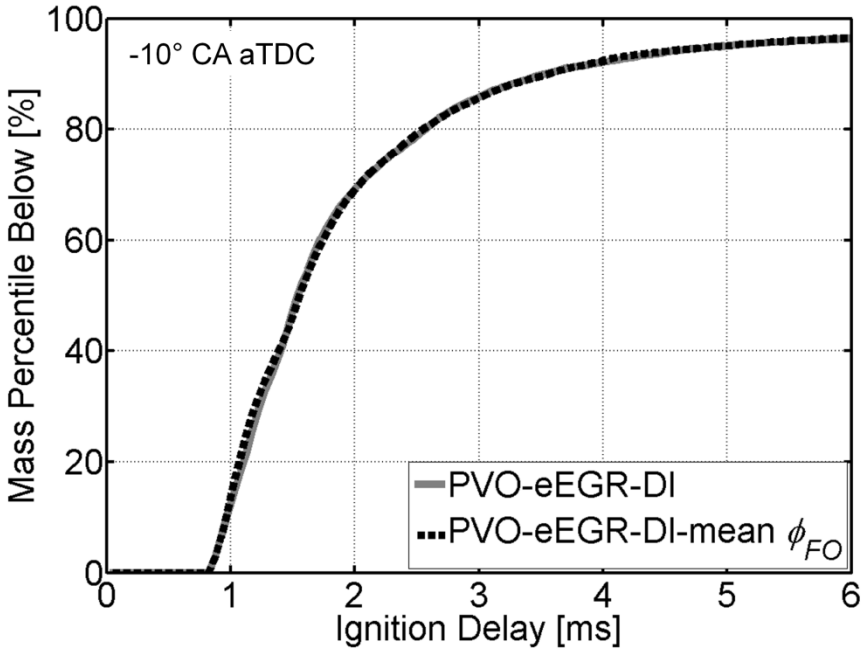

Figure 5.21 – Cumulative distribution of reactivity in terms of ignition delay for PVO-DI and PVO-DI with mean ϕ_{FO}

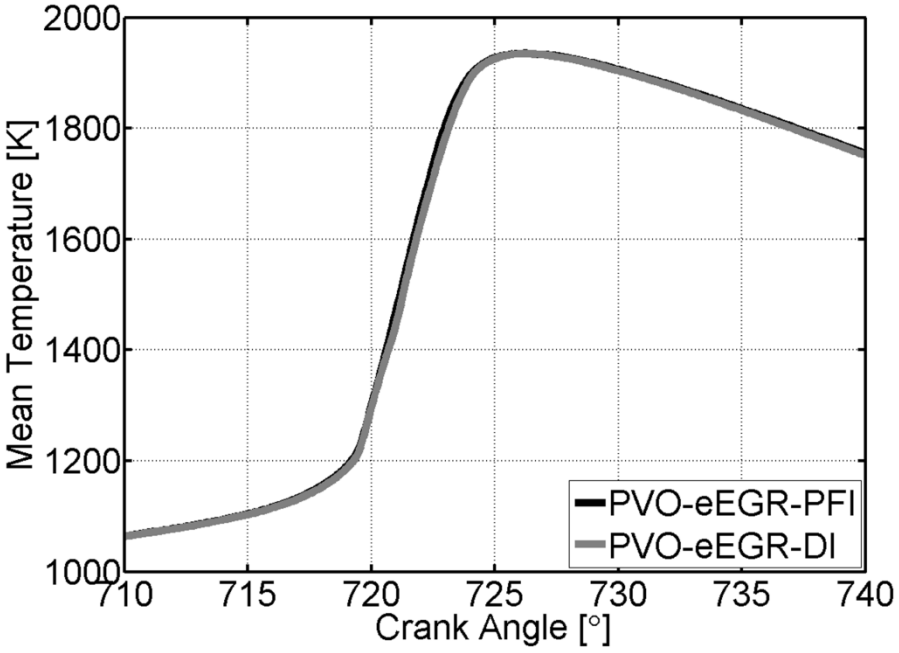

Figure 5.22 – In-cylinder temperature trace for PVO-PFI and PVO-DI cases

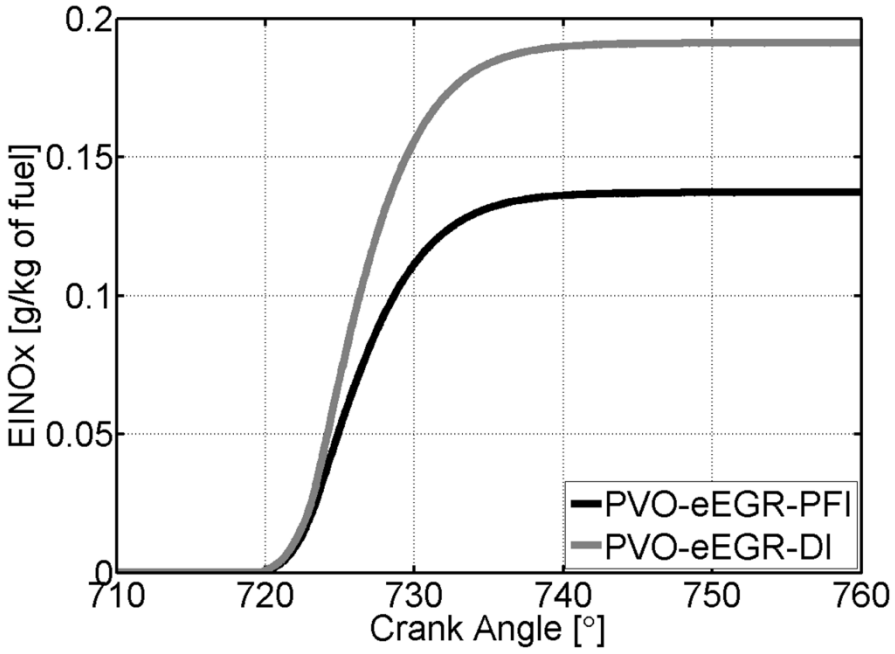

Figure 5.23 – Evolution of NOx with respect to crank angle for PVO-PFI and PVO-DI cases

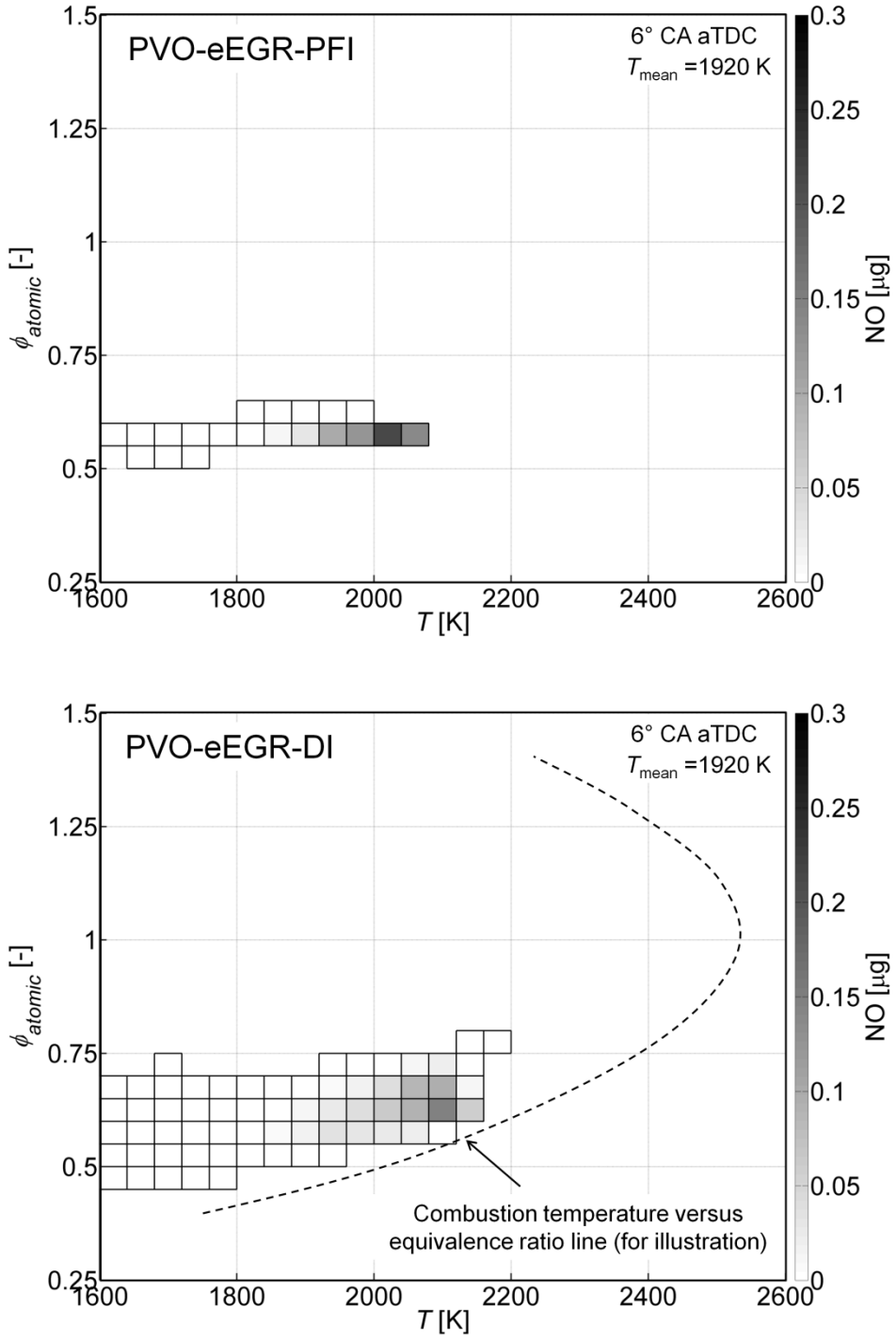

Figure 5.24 – Post-combustion (6° CA aTDC) reaction space from CFD simulation of PVO-eEGR-PFI and PVO-eEGR-DI cases showing NO distribution

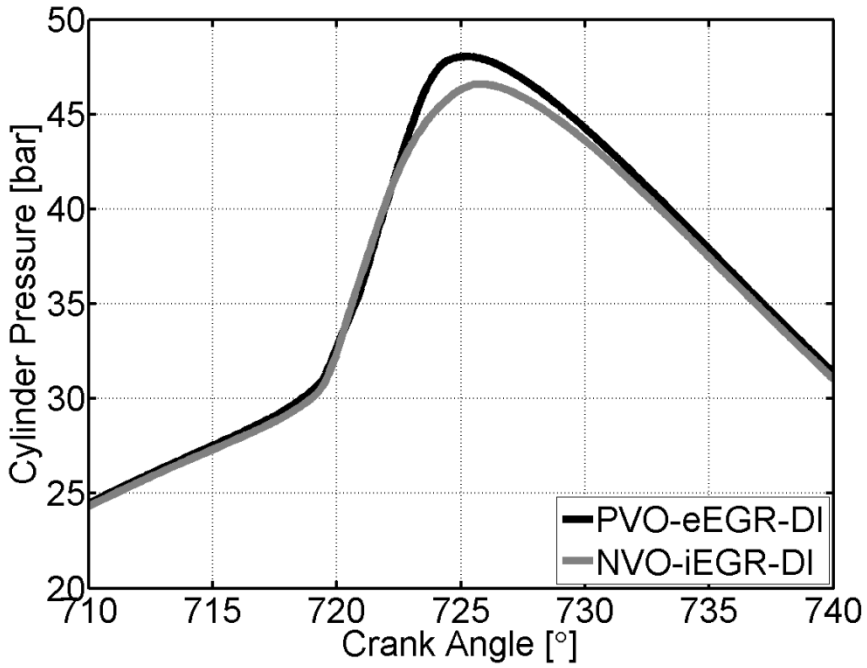

Figure 5.25 – In-cylinder pressure traces from CFD simulation of PVO-eEGR-DI and NVO-iEGR-DI cases

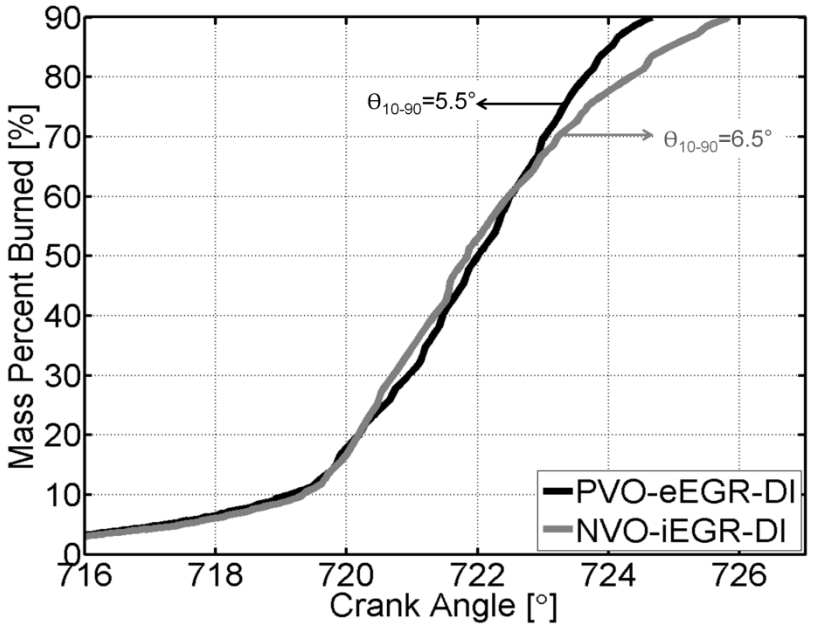

Figure 5.26 – Burn profiles from CFD simulation of PVO-eEGR-PFI and NVO-iEGR-DI cases

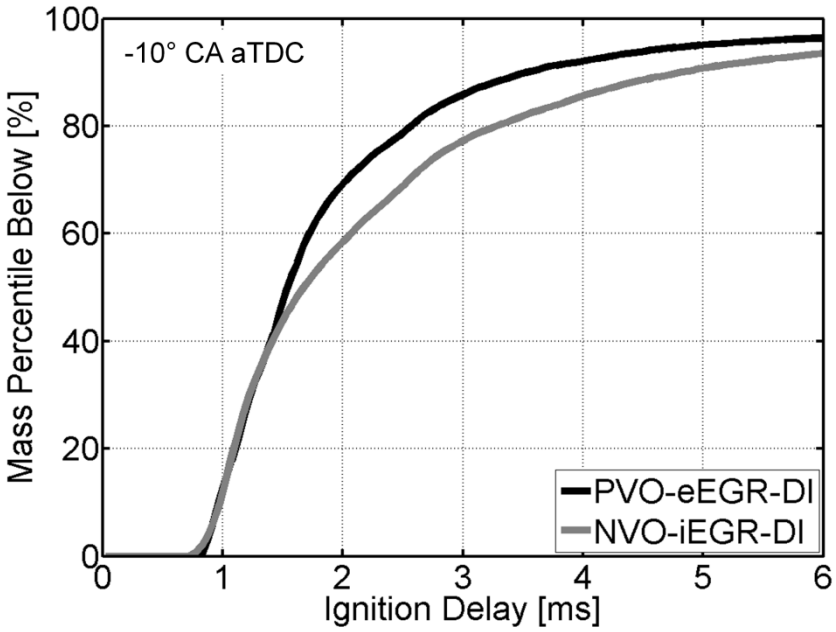

Figure 5.27 – Pre- ignition (10° CA bTDC) reactivity distribution (in terms of ignition delay) from CFD simulation of PVO-eEGR-DI and NVO-iEGR-DI cases

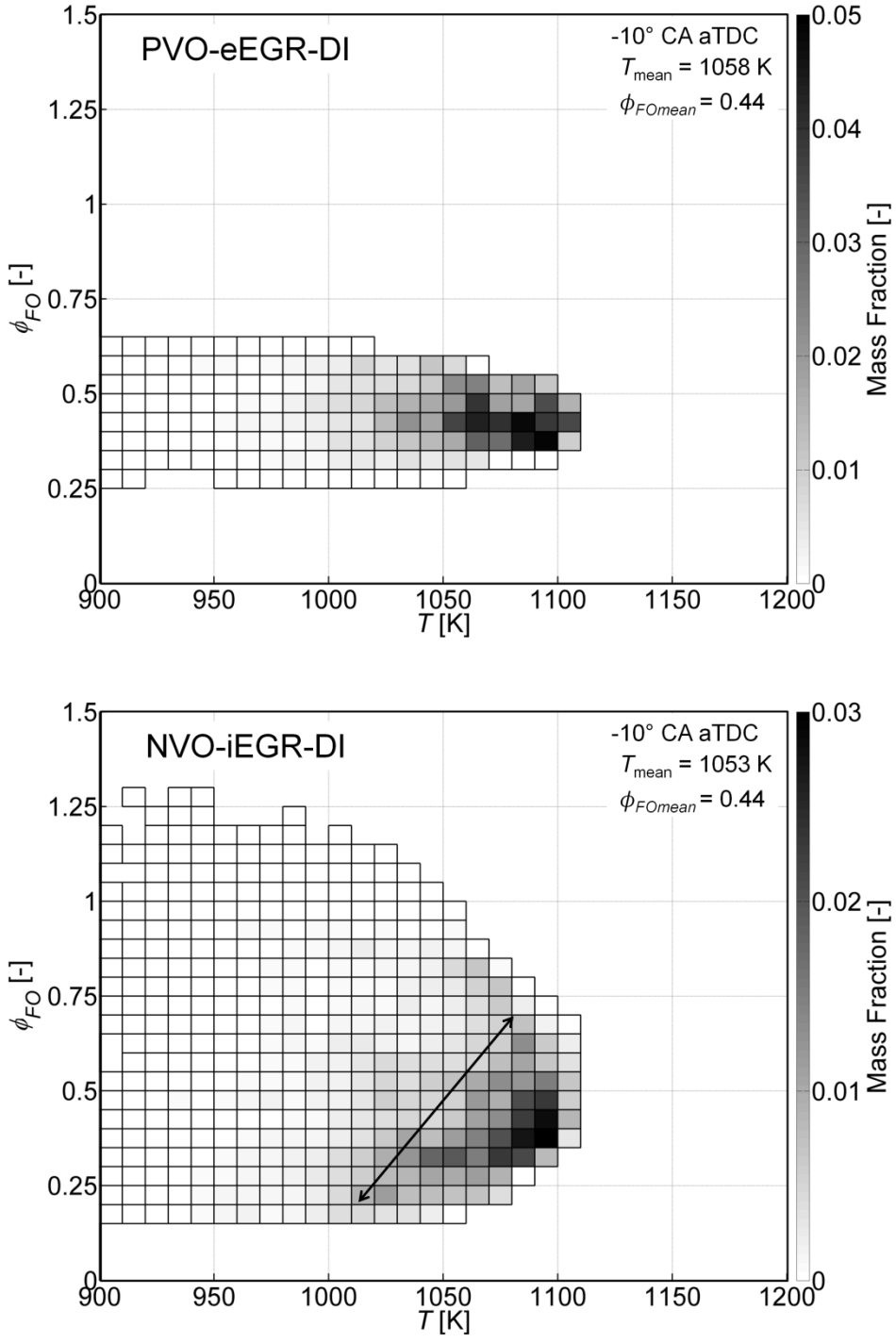

Figure 5.28 – Pre-ignition (10° CA bTDC) reaction space visualized in terms of T and ϕ_{FO} from CFD simulations of the PVO-eEGR-DI and NVO-iEGR-DI cases

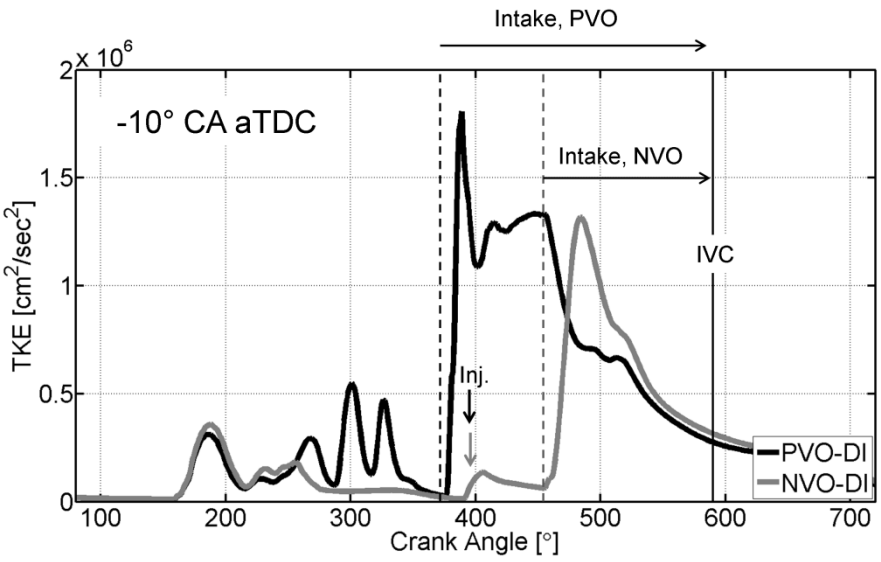

Figure 5.29 – Evolution of turbulent kinetic energy (TKE) for PVO-DI compared to NVO-DI showing injection event and intake events

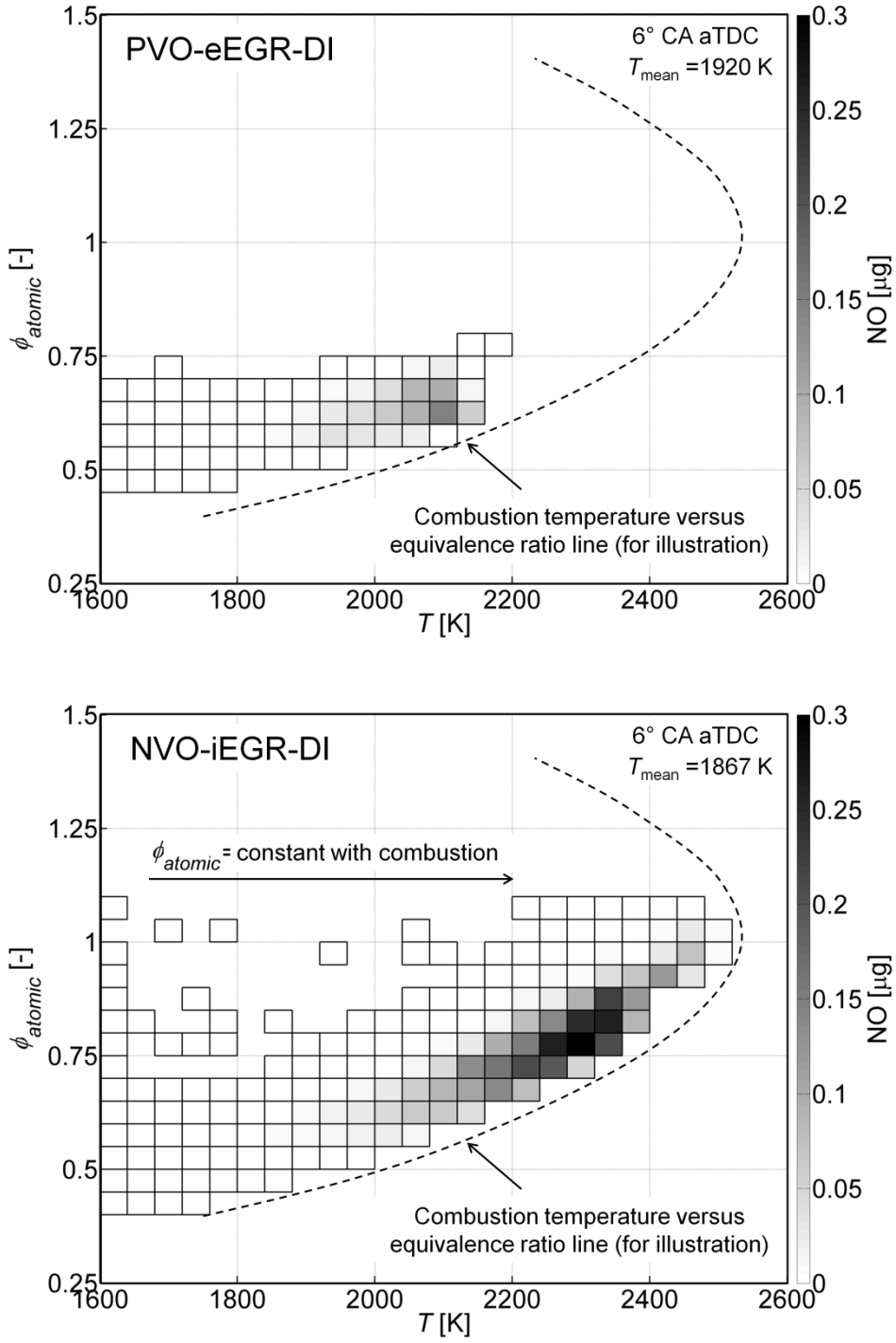

Figure 5.30 – Post- combustion (6° CA aTDC) reaction space from CFD simulation of PVO-eEGR-DI and NVO-iEGR-DI cases showing NO distribution

5.5 References

1. Koopmans, L., Ogink, R., and Denbratt, I., “Direct Gasoline Injection in the Negative Valve Overlap of a Homogeneous Charge Compression Ignition Engine,” SAE Paper 2003-01-1854, 2003.

2. Guohong, T., Zhi, W., Jiaxin, W., Shijin, S., and Xinliang, “HCCI Combustion Control by Injection Strategy with Negative Valve Overlap in a GDI Engine,” SAE Paper 2006-01-0415, 2006.

3. Kulzer, A., Hathout, J-P., Sauer, C., Karrelmeyer, R., Fischer, W., and Christ, A., “Multi-Mode Combustion Strategies with CAI for a GDI Engine,” SAE Paper 2007-01-0214, 2007.

4. Mehl, M., Chen, J.Y., Pitz, W.J., Sarathy, S.M., and Westbrook, C. K., “An Approach for Formulating Surrogates for Gasoline with Application toward a Reduced Surrogate Mechanism for CFD Engine Modeling,” *Energy & Fuels*, Vol. **25**, Issue 11, pp. 5215-5223, 2011.

5. He, X., Donovan, M. T., Zigler, B. T., Palmer, T. R., Walton, S. M., Wooldridge, M. S., and Atreya, A., “An experimental and modeling study of iso-octane ignition delay times under homogeneous charge compression ignition conditions,” *Combustion and Flame*, Vol. 142, pp. 266-275, 2005.

6. Heywood, J. B., 1988, *Internal Combustion Engine Fundamentals.* McGraw-Hill, New York.

CHAPTER 6

ACCELERATED MULTI-ZONE COMBUSTION MODEL FOR HCCI

6.1 Guidelines for a simplified HCCI combustion model

Based on the studies performed in chapters 3, 4 and 5, it is possible to describe some of the main features a simple HCCI combustion model intended for use in system-level codes should be able to capture.

Under PVO conditions, with minimal internal residual, the primary driver for thermal stratification is heat loss to the walls. A simple combustion model should be able to capture the effect of wall heat loss driven thermal stratification in a computationally efficient manner. NVO operation results in additional thermal stratification brought about by internally trapped hot residuals, which was shown in Chapter 4 to have a significant impact on burn duration. For a simple HCCI combustion model to predict burn duration under NVO conditions correctly, accurate description of the thermal stratification at IVC brought about by trapping residuals, and subsequent evolution of this thermal stratification through the compression stroke (as a result of mixing) needs to be captured.

Additionally, it was shown in Chapter 4 that the compositional stratification brought about from NVO operation does not have a significant impact on the reactivity distribution and burn duration. A simple combustion model for NVO-HCCI could potentially neglect compositional stratification effects from NVO operation and mixing in composition space, thus simplifying model development. However, if the effects of direct injection on burn duration and NO emissions are to be captured, capturing compositional

stratification becomes important for NVO operation. On the other hand, for PVO operation with early injection, it was shown that compositional stratification does not result in significant differences compared to PVO-PFI operation, and a simple combustion model which captures wall heat loss driven thermal stratification could suffice.

In order to capture stratification effects on burn duration, a simple model should also be able to model sequential auto-ignition resulting from different regions with different reactivity igniting at different times. This effect is captured by balloon-type multi-zone models.

Quasi-dimensional multi-zone combustion modeling is a powerful tool to capture the impact of thermal stratification and chemical kinetics on HCCI combustion characteristics (combustion timing and burn duration) in a computationally efficient manner. The availability of high performance computing and better Ordinary Differential Equation (ODE) solvers [1] makes it increasingly feasible to incorporate a high fidelity multi-zone combustion model with realistic gasoline kinetics [2] into a system level simulation framework (e.g. 1-D engine model with 1-D gas exchange for intake and exhaust) while maintaining computational efficiency.

6.2 Multi-zone Combustion Modeling for HCCI

This section presents a brief overview of the current state of the art in quasi-dimensional HCCI combustion modeling. The purpose of quasi-dimensional multi-zone combustion models for HCCI is to transfer the emphasis from resolving small-scale fluid mechanics to resolving thermal stratification and chemical kinetics, because traditional HCCI combustion is primarily governed by chemical kinetics and the fuel-air mixture is relatively homogeneous in composition prior to ignition HCCI.

6.2.1 Balloon-type multi-zone models

In “balloon-type” quasi-dimensional multi-zone combustion modeling, the contents of the engine cylinder are divided into multiple reactors or “zones”. These zones may be considered as deformable fixed mass control volumes (like balloons), and typically do not exchange heat or mass with each other. Each zone loses heat to the cylinder walls in a pre-determined fashion generally based on its volume or area. Typically, the total heat loss is predicted using empirical correlations like Annand [3], Woschni [4], Hohenberg [5], and their variations. The heat loss is then distributed among the zones, generating temperature stratification during the compression stroke. This method generally assumes uniform pressure over all zones at every time- step of the simulation. The temperature distribution aims to reproduce the thermal stratification developed in an engine prior to ignition, which is what leads to sequential autoignition of various parcels of charge in the cylinder. The rate at which this sequential autoignition occurs, which is related to the degree of thermal stratification, determines burn duration and pressure rise rates during combustion.

Andreatta [6] developed one of the first “balloon-type” multi-zone combustion models. This model uses the Woschni [4] correlation for heat loss applied to each zone based on the zone temperature, rather than the average cylinder temperature. Mass transfer is allowed between zones at a prescribed rate. Aceves et al. [7-9] and Babajimopoulos et al. [10] developed the sequential multi-zone combustion model for HCCI, where they use Computational Fluid Dynamics (CFD) to determine the temperature distribution up to a predefined point in the compression stroke, after which a chemical kinetics solver is used in a balloon-type multi-zone framework, with zone initialization based on the temperature distribution predicted by CFD at the point of switching over to chemical kinetics calculations. The reason for using CFD for the non-reacting portion of the computations is to achieve an accurate description of thermal

stratification prior to ignition. Easley et al. [11] developed a multi-zone model that describes the crevice, boundary layer, outer core and inner (adiabatic) core regions. Only the outer core, boundary layer and crevice are allowed to exchange mass to maintain uniform pressure in the combustion chamber. Noda and Foster [12] developed a balloon-type multi-zone combustion model to study strategies to control combustion duration in hydrogen-fueled HCCI. They note that the effect of thermal stratification is more significant than the effect of fuel stratification on HCCI combustion duration. Fiveland and Assanis [13] developed a two-zone HCCI combustion model with a model for boundary layer heat loss. Ogink and Golovitchev [14] developed a model similar to Easley's and coupled it with a cycle simulation software. Xu et al. [15] compare single-zone and multi-zone models with experimental data, emphasizing the need to use a multi-zone model for better prediction of ignition and burn duration. Orlandini et al. [16] also developed a balloon-type multi-zone model to simulate HCCI combustion.

6.2.2 Onion-skin models

"Onion-skin" models divide the combustion chamber into concentric cylindrical zones of definite geometry, typically of constant radii. The height of a zone is determined by the position of the piston. These zones can be thought of as a very coarse CFD grid. However, unlike CFD, transport equations are not explicitly solved between zones. The zones are allowed to exchange heat and mass with each other based on mixing rates determined by turbulent length scales. In these models, only the outermost zone is allowed to lose heat to the walls. The inner zones in turn transfer heat and mass to the outer zones.

The objective of the onion-skin model is also to develop an accurate description of thermal stratification prior to auto-ignition. Notable implementations of this kind of model have been done by Komninos et al. [17]. Early implementations use the Annand

heat loss correlation [3], and in a more recent publication, Komninos and Kosmadakis [18] outline the development of a modified version of the Annand correlation, based on individual zone temperatures rather than average cylinder temperature.

Kongsereeparp and Checkel [19] developed a segregated multi-zone model with a zone configuration scheme that allows for a better geometric description of zone boundary temperatures.

6.2.3 Probability Density Function based models

Another approach to multi-zone HCCI combustion modeling is the Probability Density Function (PDF) approach, which is based on a transformation of coordinates from the physical space in the combustion chamber to coordinates in pure chemistry space, where the chemical kinetics are solved. Zones are created in chemistry space rather than in physical space. Researchers such as Kraft et al. [20] and Maigaard et al. [21] have developed stochastic models for HCCI engine combustion based on the PDF approach. The Representative Interactive Flamelet (RIF) approach, developed by Pitsch et al. [22], is also a PDF based approach to combustion modeling derived from the non-premixed flamelet approach of Peters [23]. Hergart et al. [24] describe a RIF based model for simulating Premixed Charge Compression Ignition (PCCI).

In another vein, HCCI combustion models based on fully-coupled CFD with multi-zone chemical kinetics have been developed by Flowers et al. [25], Babajimopoulos et al. [26], Shi et al. [27], Felsch et al. [28], Kodavasal et al. [29] and others. Narayanaswamy and Rutland [30] implemented detailed CFD models for heat transfer, sprays etc. along with chemical kinetics into a system level simulation tool. However, resolving fluid dynamics by means of these fully-coupled approaches is frequently computationally intensive when modeling multiple engine cycles. Balloon-type multi-zone combustion models are more computationally efficient and can be better

suited for this. This is because in balloon-type models, species transport between zones is not solved. The benefits of this are twofold:

1. As the size of the mechanism increases, the number of species to transport equations (which are non-linear ODEs) increases too, adding a significant computational time penalty for fully-coupled CFD and multi-zone kinetics simulations.
2. For fully-coupled CFD multi-zone reactive simulations, change of zone composition due to mass transfer between the zones, in addition to chemical reactions, generally requires an integrator restart at every CFD time -step and thus recalculation of each individual zone Jacobian, which is computationally expensive when implicit solvers are used, as is generally the case with bigger kinetic mechanisms. This adds to the computational cost associated with generating a new Jacobian and impedes the use of speed up strategies like Jacobian reuse from the previous time–step.

The rest of this chapter focuses on the development and evaluation of a thermal stratification methodology for a balloon-type multi-zone combustion model that is referred to as Accelerated Multi-zone model for Engine Cycle Simulation (AMECS) of HCCI combustion.

6.3 Motivation for a rapid thermal stratification methodology

With the availability of reduced mechanisms and the use of advanced numerics to speed up chemical kinetics computation [1], the bottleneck for implementing a predictive HCCI combustion model in system-level codes is the fluid mechanics solution to determine the thermal distribution prior to ignition. CFD provides a good description of mixing and thermal distribution, however it is too expensive to perform a CFD simulation for every cycle. The objective of this chapter is to develop a methodology to capture the

effect of phenomena like turbulent mixing of heat and mass on thermal stratification prior to ignition, without actually simulating these processes.

This methodology for capturing thermal stratification is then used in conjunction with the multi-zone model formulation described in Chapter 2 with chemical kinetics being solved within every zone. This standalone multi-zone model (AMECS) achieves simulation times on the order of seconds to minutes compared to hours to days as is the case with fully-coupled or sequential CFD-multi-zone approaches, making it an ideal candidate for use in system-level codes.

6.4 AMECS combustion model

6.4.1 Model setup

The AMECS combustion model was developed as part of this doctoral work. It is a balloon-type multi-zone HCCI combustion model, that features block preconditioning of the multi-zone solver, (from McNenly et al. [31]) for computational efficiency, as well as a novel thermal stratification methodology (also developed as part of this work) to determine the relative heat loss from each zone. This methodology eliminates the need to run a non-reacting CFD simulation for every condition, as was required by previous sequential CFD multi-zone approaches [7-10]. The conceptual depiction of this model is shown in Figure 6.1. The cylinder contents are divided into N constant mass zones with a user specified mass distribution; *nsp* denotes the number of chemical species in the kinetic mechanism used, and y_{ik} denotes the mass fraction of species k in zone i, where k goes from 1 to *nsp*, and i goes from 1 to N. T_i denotes the temperature of the i^{th} zone. Uniform pressure is assumed across all the zones at any given time step in the simulation (the ODE system of each zone is coupled to that of every other zone) and $\dot{q}_i$ represents the rate of heat loss from the i^{th} zone at a given time step. The zones do not exchange heat or mass with each other and interact purely based on compression work. It must be noted

that even though the zones have a constant mass distribution, their volume fractions (with respect to total cylinder volume) change throughout the simulation to ensure that uniform pressure is maintained over all the zones.

Zone temperatures (T_i) and species mass fractions (y_{ik}) make up the "states" of the multi-zone system. At every time -step, the ODE solver, or integrator (DLSODPK [32]), updates values of the system states by solving the energy equation in each of the zones. From these basic states, the values of zone volumes and overall pressure are computed at every time step based on the ideal gas law.

6.4.2 Block preconditioning for accelerated calculations

For a system that has M state variables, ODE solvers typically rely on the Jacobian of the system, which is an M x M square matrix that contains the rate of change of every system state variable with respect to every other system state variable at any given instant. This Jacobian is either constructed by the ODE solver, or supplied to the ODE solver externally. The Jacobian matrix is used as part of a modified Newton-Raphson non-linear solver that iteratively solves for the system state at the next time step. Specifically, the non-linear solver requires repeated linear solutions using the Jacobian matrix. The computational expense of factoring a Jacobian scales as $(M)^3$, when treated as a dense matrix. Thus, the computational cost of factoring the Jacobian for the whole AMECS ODE system would scale as $(N.(nsp+1))^3$ as there are $nsp+1$ states (nsp species and one zone temperature, T_i) for each of the N zones.

One multizone approach decouples the different zones, treating them as N individual, independent reactors at every time step, with Jacobian construction costs scaling as $N.(nsp+1)^3$ instead of $(N.(nsp+1))^3$. However, such an approach ultimately has to perform a "pressure-correction" step in every zone at the end of every time step, which in turn changes the temperature of these zones and their initial state for the next time step,

requiring an integrator restart when implicit solvers are used. Accounting for the pressure-coupling between the zones during chemistry calculations (as in AMECS), and treating the whole multizone as a single ODE system comprising of $N.(nsp+1)$ equations does not require an integrator restart at every time step.

With the block preconditioning methodology developed by McNenly et al. [31], the need to construct the whole system Jacobian is eliminated, and instead, N individual zone Jacobians of dimension $nsp+1$ each are constructed. In essence, the zones themselves are coupled at every time step during the chemistry calculation; however, their Jacobians are decoupled. The reasoning behind this is that the rate of change of the concentration of a particular species k, in a particular zone i, (represented by the state y_{ik}) is primarily a function of the concentration of other species in zone i and T_i. It is not a strong function of species concentrations and temperatures in other zones. This permits the decoupling of the whole AMECS ODE system into N smaller ODE systems at every time step, which are then solved quasi-independently. As a result of block-preconditioning of the multi-zone solver, N individual zone Jacobians are factored with a total computational expense of $N.(nsp+1)^3$, which represents a speed up on the order of N^2 over the conventional non-decoupled approach. Since factoring a dense system Jacobian is the most time consuming portion of a reacting simulation, a 40 zone simulation is approximately 3 orders of magnitude faster with the block preconditioned AMECS compared to conventional multi-zone solver approaches.

Unlike fully-coupled CFD/kinetics approaches, which require an integrator restart and Jacobian recalculation at every time step when an implicit solver is used, AMECS reuses individual zone Jacobians over several time steps until convergence at a given time step can no longer be achieved by the iterative solver in a particular zone. It must be noted that the reuse of previous Jacobians does not affect accuracy of the results, as the Jacobian need only provide an estimate of the trajectory slope in the vicinity of the solution. The non-linear solver used in the implicit ODE solver then performs multiple

iterations with this estimate until convergence is reached, as defined by local error tolerances.

The current numerical scheme for block-preconditioning uses the finite-difference approach to generate the individual zone blocks. Using analytical derivation of the Jacobian (instead of finite-difference) and sparse matrix factorization as found in the approaches proposed by Schwer et al.[33], Lu and Law [34] and Perini et al. [35], computational costs for reacting simulations could be further scaled down by two orders of magnitude for large mechanisms (more than a thousand species).

6.4.3 Calculation of system states

The following equations (derived from conservation of mass and energy) are used to supply the integrator with the rate of change of the system states:

$$\frac{dy_{i,k}}{dt} = \frac{\dot{\omega}_{i,k} W_k}{\rho_i} \tag{6.1}$$

$$\frac{dT_i}{dt} = \frac{1}{\rho_i C_{p_i}} \sum_{j=1}^{N} \left(\frac{m_j (R_u / \overline{W}_j)}{V} \cdot \frac{dT_j}{dt} \right) - \frac{\dot{q}_i}{m_i C_{p_i}} - \sum_{k=1}^{nsp} \frac{\dot{\omega}_{i,k} W_k h_{i,k}}{\rho_i C_{p_i}} + \frac{R_u}{\rho_i C_{p_i}} \left\{ \sum_{j=1}^{N} \frac{m_j T_j \sum_{k=1}^{nsp} \frac{dy_{i,k}}{dt}}{\overline{W}_j V} - \frac{\dot{V}}{V^2} \sum_{j=1}^{N} \frac{m_j T_j}{\overline{W}_j} \right\} \tag{6.2}$$

In the above equations, *i* and *j* represent zone indices, while *k* represents species index. *T* denotes temperature , *y* denotes mass fraction of a certain species and *t* denotes time. The symbol $\dot{\omega}$ denotes the chemical rate of generation (in moles per unit volume), *W* represents molecular mass, $\overline{W}$ represents average molecular mass, ρ represents mass

density, C_p represents specific heat on a mass basis at constant pressure, m represents mass, R_u represents the universal gas constant, *V* represents volume, $\dot{q}$ represents rate of heat loss, *h* denotes mass-specific enthalpy and $\dot{V}$ denotes rate of change of volume.

Determining the rate of change of zone temperature as a function of explicitly known quantities requires the solution of a system of *N* linear equations (where *N* is the number of zones), since all zone temperatures are interconnected. The overall pressure (*P*) is computed as follows, using the ideal gas law:

$$P = \frac{\sum_{i=1}^{N} m_i (R_u / \overline{W}_i) T_i}{V} \tag{6.3}$$

A significant point to note is that the term $\dot{q}_i$ (instantaneous rate of heat loss from a particular zone) needs to be supplied or modeled. In this work, $\dot{q}_i$ is computed based on a thermal stratification methodology (developed as part of this work) described in subsequent sections.

6.5 Thermal Stratification

6.5.1 Background

Thermal stratification refers to spatial non-uniformity in the temperature of the cylinder contents. For an engine with Port Fuel Injection (PFI) or fully premixed Direct Injection (DI) and conventional valve events, thermal stratification prior to ignition is primarily developed by heat loss to the cylinder walls, with little contribution from mixing with internal residuals. Snyder et al. [36], in their optical engine work, demonstrated that with conventional valve events and fully premixed direct injection, thermal stratification developed under motoring conditions (with no hot residuals or fuel spray) agrees well with thermal stratification developed under firing conditions.

Combustion chamber walls are typically colder than the air-fuel charge, resulting in net heat transfer to the walls. The air and fuel closer to the boundaries (typically outer regions and boundary layer) lose more heat than air and fuel further away (typically inner regions). Heat flows from the inner regions to the outer regions of the charge, and from the outer regions to the walls. Under NVO conditions, it is believed that residual mixing also contributes to thermal stratification [37]; however the current work focuses on HCCI engines with conventional valve events and fully premixed operation.

6.5.2 The Adiabatic Core Concept

In the context of an Internal Combustion (IC) Engine, the adiabatic core temperature is the temperature of an infinitesimal, hypothetical "adiabatic" region of mass that does not suffer any heat loss, either to the surrounding mass or to the walls, during the compression and expansion strokes. It is important to note that the temperature of this adiabatic core at any instant is less than the "adiabatic temperature" if the cylinder had adiabatic walls, since this hypothetical "adiabatic" region would not get compressed to the same extent as it would if all the contents of the cylinder were adiabatic. This is because the outer regions that lose heat, contract to a greater extent than due to purely compression from the piston (they contract additionally due to heat loss). The hypothetical "adiabatic core" would therefore compress less than it would due to pure piston motion, as it would need to compensate for the cooling compression of the outer regions, with the overall cylinder volume being determined by crank-slider dynamics at any given instant.

The value of the adiabatic core temperature at any crank angle (θ) during the compression stroke can be easily obtained by assuming isentropic compression of the adiabatic core from IVC up to the pressure of the cylinder contents at θ. The thermodynamic state variables of pressure and temperature at are sufficient to establish a

unique thermodynamic state at IVC. The entropy at IVC (S_{IVC}) is then a determinate quantity and is readily obtained using equation (4) based on the pressure, temperature and composition at IVC (P_{IVC}, T_{IVC} and $\bar{y}_{IVC}$)

$$S_{IVC} = fn(P_{IVC}, T_{IVC}, \bar{y}_{IVC}) \tag{6.4}$$

$\bar{y}_{IVC}$ represents the composition in terms of mass fractions of the constituents of the gas mixture, which for a motored case may be approximated as 23.3% O2 and 76.7% N2 by mass. Clearly, the gas composition ($\bar{y}$) remains unchanged from IVC up to any angle θ. Also, the entropy of the gas mixture comprising the adiabatic core also remains a constant, since pressure-work is the only mode of energy exchange between this infinitesimal adiabatic core and its surroundings. Thus, based on the initial entropy (S_{IVC}), and the cylinder pressure at any crank angle, the adiabatic core temperature is a well defined and determinate thermodynamic state, expressed as:

$$T_{adia-core,\theta} = fn(P_{\theta}, S_{IVC}, \bar{y}_{IVC}) \tag{6.5}$$

6.5.3 Thermal Stratification Methodology

The most critical aspect of a multi-zone model is accurately capturing thermal stratification prior to ignition, as this is what determines the rate of heat release. At any crank angle (θ) during the compression stroke, the adiabatic core temperature represents the maximum temperature that any zone within the engine cylinder *could* theoretically reach were it not to lose any heat. The cumulative heat loss from a region or a "zone" within the cylinder is the main factor responsible for the deficit in that zone's temperature at a given time relative to the adiabatic core temperature defined in the previous section.

In the methodology developed in this work, the heat loss from each zone is taken to be a fraction of the total heat loss predicted by the modified Woschni global heat loss correlation (developed by Chang et al. [38]) applied to the average in-cylinder temperature. This fraction is calculated by multiplying the mass fraction of a zone by the zone heat loss multiplier (C_i, where i refers to the zone number) determined by post-processing a baseline motoring CFD simulation.

For a given engine, a CFD simulation is performed for a baseline motoring condition, at a certain engine speed and intake pressure. These results are then used to determine zone heat loss multipliers (C_i values). It is extrapolated that these heat loss multipliers calculated at the baseline motoring condition may then be applied to different operating conditions (for that engine), assuming that within the range of intake pressures and speeds of boosted HCCI operation, thermal stratification characteristics of an engine are primarily a function of geometry rather than operating conditions. This hypothesis is partly supported by the Snyder et al. [36] optical work which shows that for a given engine, thermal stratification characteristics under motoring and firing conditions are very similar.

In this work, a 40 zone setup is used for model performance evaluation. Further, 20 zone and 10 zone setups are also explored to understand sensitivity to zone resolution. The zone mass distribution used in all the cases is such that there is higher resolution in the hotter and colder regions of the charge. These distributions are shown in Figure 6.2.

Figure 6.3 illustrates the procedure used in determining the zone heat loss multipliers from a baseline motored CFD run (40 zone case shown).The cylinder contents at TDC from the motored CFD simulation are binned into zones with a specified mass

distribution based on decreasing temperature. The mass distribution used in the illustration corresponds to the 40 zone mass distribution (shown in Figure 6.2) that is also used in the AMECS multi-zone model.

Using the concept of the adiabatic core temperature (determined based on the pressure at TDC and entropy at IVC), and based on the distribution of temperature at TDC obtained from the motored CFD simulation results binned into zones, zone heat loss multipliers are calculated in the following manner:

$$C_i = \frac{T_{adia-core,TDC} - T_{i,TDC,CFD}}{T_{adia-core,TDC} - T_{avg,TDC,CFD}} \tag{6.6}$$

Here, C_i is the heat loss multiplier for the i^{th} zone (of AMECS), $T_{adia\text{-}core}$ is the temperature of the adiabatic core at TDC, $T_{i,TDC,CFD}$ is the TDC temperature of the i^{th} CFD "zone" (bin) and $T_{avg,TDC,CFD}$ is the cylinder average temperature at TDC from post-processed CFD results. The instantaneous rate of heat loss from every zone for the AMECS model is then given by:

$$\dot{q}_i = C_i . \frac{m_i}{m_{tot}} . \dot{q}_{overall} \tag{6.7}$$

Here $\dot{q}_i$ is the rate of heat loss from i^{th} AMECS zone at any given time, $\dot{q}_{overall}$ is the overall rate of heat loss predicted by the modified Woschni correlation based on the average in-cylinder temperature. In the above equation, m_i and m_{tot} respectively represent the mass of the i^{th} zone, and the total mass of the cylinder contents. It must be noted that $\sum_{i=1}^{N} m_i C_i$ equals m_{tot}, to ensure that the sum of the heat losses from the individual zones at any given instant is equal to the global heat loss predicted by the modified Woschni correlation at that instant. This is based on the definition of average

temperature, which in this case is mass-average temperature, where $\frac{1}{m_{tot}}\sum_{i=1}^{N} m_i T_i = T_{av}$. During compression, when the composition is uniform and unchanging, mass average temperature is equivalent to molar average temperature. The C_i values thus determined are then used unchanged for a given engine at various operating conditions. These conditions are far removed from the baseline motoring simulation for which they were obtained. It must be noted that our thermal stratification methodology to determine zone heat loss could be also be applied based on thermal stratification obtained from optical engine experiments.

Post ignition, the heat loss multipliers used to obtain stratification are no longer used since these were developed based on the average heat loss characteristics during compression in order to capture stratification prior to ignition. In the current model, ignition is defined when the hottest zone reaches 1100 K, after which the overall heat loss predicted by the modified Woschni correlation is distributed among the zones based on their mass fraction and temperature difference with respect to the wall in the following manner:

$$\dot{q}_i = \left(\frac{1}{\varepsilon}\right).\left(\frac{T_i - T_{wall}}{T_{avg} - T_{wall}}\right).\left(\frac{m_i}{m_{tot}}\right).\dot{q}_{overall} \tag{6.8}$$

The quantity ε is a normalization quantity determined at every time step as follows to ensure that the sum of the zone heat loss rates is equal to the overall heat loss rate predicted by the modified Woschni correlation:

The reason for switching to the expression given in equation (6.8) for zone heat loss from the earlier C_i approach is because post-ignition, the heat loss from a zone is additionally dominated by the temperature differential between the zone and the wall.

$$\varepsilon = \sum_{i=1}^{N} \left(\frac{T_i - T_{wall}}{T_{avg} - T_{wall}} \right) . \left(\frac{m_i}{m_{tot}} \right) \quad (6.9)$$

The C_i approach does not capture this effect; it primarily captures the effect of proximity of a zone to the wall. It must be noted that the expression given by equation (6.8) is purely an "engineering" solution and is a simplistic representation of the heat loss rate from a zone given the challenges associated with modeling this phenomena post-ignition, when large temperature gradients exist within the charge.

6.6 Model performance evaluation with respect to CFD

The performance of the AMECS model compared to CFD is evaluated using two very different engine designs:

1. The Sandia boosted gasoline HCCI engine (referred to as Sandia engine henceforth), which is based on a single cylinder of a six-cylinder Cummins B-Series diesel engine with Compression Ratio (CR) of 14 [39]. The CFD grid is a two-dimensional (2-D) axisymmetric grid, with around 800 computational cells at TDC that has a lowered CR of 13.83 to account for blow by losses. Specifications of the CFD grid are provided in Table 6.1 and the grid is shown in Figure 6.4.
2. The University of Michigan Fully Flexible Valve Actuation (UM-FFVA) engine, which is based on a 12.5:1 CR single cylinder gasoline engine with a Ricardo Hydra crankcase [40]. The CFD grid used (specifications in Table 6.2) is a 3-D grid shown in Figure 6.5 that has a CR of 12.22 and approximately 22,000 computational cells at TDC.

Firstly, the thermal stratification predicted by AMECS under motoring conditions is evaluated against CFD predictions for both the engines over a range of operating

conditions. Then, the combustion characteristics predicted by AMECS are evaluated against fully-coupled (fluid mechanics and chemical kinetics) reacting CFD simulations performed for both engines.

KIVA-3V [41] is the CFD software used throughout. The same chemical kinetics library is used within the CFD and in the AMECS simulations. For the fully-coupled reacting CFD simulations, the fully-coupled CFD/kinetics approach developed by Babajimopoulos et al. [26] and Kodavasal et al. [29] is used, where similar CFD cells are grouped into zones for chemical kinetics solution.

6.6.1 Thermal Stratification Prediction

The computed TDC adiabatic core temperature for the Sandia engine is 1064 K and that for the FFVA engine is 1095 K. The zone heat loss multipliers (C_i values) for both engines are computed based on these TDC adiabatic core temperatures and the temperature distribution obtained from the corresponding baseline motoring CFD simulations.

For both the Sandia and the UM-FFVA engines, the thermal stratification prediction by AMECS with zone heat loss multipliers is evaluated at 3 different motoring conditions–

Sandia engine:

a) 1200 RPM, 100 kPa intake pressure (baseline)
b) 2000 RPM, 100 kPa intake pressure (higher RPM)
c) 1200 RPM, 240 kPa intake pressure (higher boost)

UM-FFVA engine:

a) 2000 RPM, 100 kPa intake pressure (baseline)
b) 3000 RPM, 100 kPa intake pressure (higher RPM)
c) 2000 RPM, 200 kPa intake pressure (higher boost)

For each of these cases, the thermal stratification predicted by the AMECS model is compared to that predicted by CFD at 3 different crank angles through the compression stroke : -20° CA after TDC (aTDC), -10° CA aTDC and at 0° CA aTDC. A 40 zone simulation is used, with the zone mass fraction distribution and zone heat loss multipliers from Figure 6.2.

Figure 6.6 (Sandia engine) and Figure 6.7 (UM-FFVA engine) show that the AMECS predictions of thermal distribution near TDC correspond well with CFD predictions over range of intake pressures and speeds. For each engine, the C_i values used are the same in all the cases. For the Sandia engine, the AMECS simulation uses a CR of 13.83 while the UM-FFVA uses a CR of 12.35. The CR used in AMECS is determined based on matching in-cylinder pressure and temperature predictions from an adiabatic CFD simulation.

6.6.2 Prediction of combustion characteristics

Reacting fully-coupled CFD chemical kinetics simulations are compared to reacting simulations using AMECS (40 zones), for a range operation conditions for both the engines –

Sandia engine (100 kPa – 240 kPa intake pressure sweep):

a) 1200 RPM
b) 2000 RPM
c) 1200 RPM, colder walls (component temperatures reduced by 40° C)

UM-FFVA engine (100 kPa – 200 kPa intake pressure sweep):

a) 2000 RPM
b) 3000 RPM

The component temperatures used for the Sandia cases are based on estimates of the same from fire deck temperatures obtained from John Dec of Sandia National Labs

for a 100 kPa intake pressure case. This case is taken from the experiments reported in Dec and Yang [39], which were run with a coolant temperature of 100° C. The procedure used to obtain the component temperatures from fire deck temperatures was developed by Sjöberg et al. [42]. The component temperatures for the UM-FFVA simulations are set at a constant 400 K due to lack of fire deck data.

For comparison with CFD, the fuel considered is PRF 90 (90% isooctane by mass and 10% n-heptane by mass). We use a small 33-species chemical kinetic mechanism developed by Tsurushima [43] for this comparison with CFD. All the cases are at an equivalence ratio of 0.3 with no residuals. The pressure traces are shown in Figure 6.8 (Sandia engine) and Figure 6.9 (UM-FFVA engine). The IVC temperature prescribed to AMECS is adjusted such that the peak pressure is matched with CFD. The required adjustments for all the cases are minor, and within 5.0 K of the IVC temperature prescribed in the CFD simulations. The AMECS and CFD results agree well in terms of in-cylinder pressure for the whole range of intake pressures and RPM studied. Departure from the baseline RPM (the condition at which heat loss multipliers were developed from the motored CFD simulation) and component temperatures results in the agreement being slightly poorer but still acceptable considering the computational expense saved by not performing detailed fluid mechanics computations. The same zone heat loss multipliers and zone mass fractions are used for all conditions with a given engine geometry. Also shown for reference in Figure 6.8 is the in-cylinder pressure prediction from a single-zone simulation for the 100 kPa intake pressure case at 1200 RPM (standard component temperatures). The single-zone simulation clearly over predicts pressure rise rate and peak pressure. Moreover, the IVC temperature for the single-zone simulation had to be increased by 20 K with respect to the IVC temperature of the corresponding CFD simulation to match combustion timing.

6.6.3 Computational cost savings compared to CFD

Table 6.3 shows the computational cost savings associated with avoiding fluid mechanics computations for the two engine grids under motoring and firing conditions. The reduction in computational time for the motoring simulations indicates the speed up achieved by eliminating fluid mechanics calculations which scales with the resolution (number of cells) of the CFD grid used. Under motoring conditions, AMECS represents a speed up of over two orders of magnitude compared to the CFD simulation performed using the 3-D UM-FFVA engine grid, and one order of magnitude speed up compared to the 2-D Sandia engine grid, while still capturing the relevant thermal stratification characteristics. Thus, the speed up associated with using the thermal stratification methodology scales with the size and resolution of the computational grid used in CFD, and presents an attractive alternative to sequential CFD multi-zone approaches [7-10] as well as fully coupled CFD multi-zone approaches [25- 29].

The simulation times of AMECS for the reacting simulations, which are on the order of a minute, for the 33-species PRF mechanism [43] used, emphasize the potential for using chemical kinetics in a multi-zone framework within system level codes.

6.7 Model performance evaluation with respect to experiments

In this section, the performance of AMECS is evaluated against a subset of boosted gasoline HCCI experiments by Dec and Yang [39]. A sensitivity study on the effect of reducing the number of zones is also performed. A 4-component gasoline surrogate by Mehl et al. [2] is used as the fuel for evaluation of the model with respect to experiments as well as for the sensitivity study based on reducing the number of zones. The chemical kinetic mechanism used is a 252-species reduced gasoline mechanism developed by the J.Y. Chen group [2].

6.7.1 Comparison with boosted gasoline HCCI experiments

Dec and Yang [39] suggest that certain early combustion reactions occurring at temperatures above those of low temperature heat release are instrumental in keeping the temperature of the cylinder contents from decreasing prior to the main heat release, during the very early part of expansion stroke near TDC, permitting later combustion phasing. They call this phenomenon Intermediate Temperature Heat Release (ITHR), and note that to achieve temperatures high enough for hot autoignition, the ITHR must be sufficiently high, so that temperatures in the hottest regions of the charge keep rising even during the expansion stroke, up to the late ignition point. They note that ITHR is more pronounced at higher intake pressures (and therefore higher near-TDC pressures), thus allowing for a greater combustion retard with boost. The objective of the Sandia experiments is to investigate the potential of boosted operation and ITHR (characteristic of gasoline fuel chemistry), in allowing for later combustion phasing and lower pressure rise rates. Under boosted conditions of 180 kPa intake pressure and beyond, the Sandia researchers use simulated stoichiometric exhaust called Combusted Stoichiometric Products (CSP) representative of external EGR to phase combustion. The composition of the initial charge varies from $\Phi = 0.48$ and 0% CSP at an intake pressure of 100 kPa to $\Phi = 0.92$ and 58% CSP at the highest level of boost studied (325 kPa intake pressure). All the experiments are at 1200 RPM and 14:1 compression ratio.

In the simulations with AMECS, a reduced gasoline mechanism consisting of 252 species and 1038 reactions is used to capture the effects of ITHR. This mechanism has been developed by the J.Y. Chen group [2], reduced from a detailed 1389 species, 6000 reaction gasoline surrogate mechanism developed at Lawrence Livermore National Laboratory (LLNL) by Mehl et al. [44]. The gasoline surrogate (Mehl et al. [2]) includes 4-components (Table 6.4). The same intake composition as experiments is used, and the

component temperatures are determined based on fire deck temperatures from the experiments using the method developed by Sjöberg et al. [42]

Figure 6.10 shows pressure traces from the Sandia experiments and from the AMECS model (40 zones) using gasoline kinetics with the same intake composition as the experiments. The IVC temperatures (initial temperatures) in the AMECS simulation are adjusted to match the location of peak pressure in the experiments. The trends in HRR from the Sandia experiments are reproduced quite well by AMECS in terms of shape and peak values (Figure 6.11). The AMECS heat release rates shown are subjected to a consistent moving average filter for all cases since results from multi-zone simulations are typically choppy. The filtering does not affect the general shape and location of the peak HRR, though the values of the peak HRR were reduced. It is observed that after ignition (during the main heat release), there appear to be two distinct phases of heat release predicted by the AMECS model, evident from the “bump” in the pressure traces and heat release curves. This could be a characteristic of the gasoline mechanism, as the same behavior is shown in an adiabatic single-zone model with no thermal stratification. Both the LLNL detailed 1389-species and the J.Y. Chen reduced 252-species gasoline mechanisms demonstrate this behavior, which is observed to be more pronounced with later combustion phasing. An illustration of the two-stage heat release after ignition (during the main heat release) is shown in Figure 6.12 for the 240kPa intake pressure case, which has a relatively retarded combustion phasing. These results are obtained using a single-zone, adiabatic variable volume reactor simulation, and thus do not have any stratification effects.

In their experiments, Dec and Yang [39] demonstrate the effect of ITHR on the normalized heat release rate (prior to the main heat release). Mehl et al. [45] also demonstrated that their gasoline mechanism captures ITHR with their single-zone simulations based on the Sandia experiments. It is seen that the AMECS model using the 252-species gasoline kinetics also reproduces ITHR under boosted conditions. This is

shown in Figure 6.13 where the normalized heat release rate curves have been shifted so that the occurrence of the peak heat release rate coincides with TDC. It must be noted that this feature is different from the “bump” in the main heat release (discussed earlier) shown only by the AMECS simulation. It may be seen in Figure 6.13 that the normalized heat release curves for the boosted cases (in both experiment and simulation) indicate some heat release (ITHR), prior to the main heat release. Thus, AMECS used in conjunction with high fidelity chemical kinetics captures critical gasoline chemistry features like ITHR, and can serve as a reliable tool for strategy evaluation in cases where gasoline fuel chemistry is exploited to extend the HCCI high load limit.

Carbon Monoxide (CO) and Hydrocarbon (HC) predictions from the model do not agree well with the experiments (Figure 6.14). The possible reason is that CO and HC are formed by mass flow into the crevice, which is not captured by the current model, as it does not permit mass exchange between zones. Flowers et al. [46] noted that modeling the mass flow between zones is critical to accurately resolve CO and HC formation. Another factor that might contribute to better predictions of CO and HC is improved resolution of the colder zones representing the boundary layer. Nitrogen Oxide (NO) emissions are in general over-predicted by the model (Figure 6.14) possibly because of the simplistic extended Zeldovich NOx mechanism [47] used in the current simulations, though they correspond well with the experiments in terms of order of magnitude and trends.

6.7.2 Effect of zonal resolution

The pressure traces and heat release rates predicted by AMECS using 40, 20, and 10 zones are compared to the Sandia experiment in order to study the relationship between the number of zones and the accuracy of the results. The zone mass distributions for the three cases are shown in Figure 6.2. The pressure traces and heat release rates are

shown in Figure 6.15. It can be seen that in-cylinder pressure and heat release rate predictions match particularly well for the 40 and 20 zone cases, while the pressure and heat release rate predictions from the 10 zone case are understandably less smooth due to the lower resolution.

The computational time for the three zone resolutions for the 100 kPa intake pressure case using the 252-species gasoline mechanism [2] is given in Table 6.5. Computational time was calculated from IVC to 25° aTDC (which represents the approximate location of 90% mass fraction burned in this case). For a given chemical kinetic mechanism, computational time (normalized by the number of time steps taken by the integrator) scales approximately with the number of zones. With an increase in the number of zones, the number of "ignition events" that need to be resolved also increases, which results in the integrator having to cut the time step more often. This is reflected in an increase in the overall number of time steps with zone resolution.

6.8 GT-Power Implementation

Computationally efficient HCCI multi-zone combustion models that use chemical kinetics are preferable to combustion correlations for use in system level engine simulations, as they enable the inclusion of relevant physics in terms of stratification and gasoline fuel chemistry. To this end, the AMECS multi-zone combustion model along with the thermal stratification methodology was implemented in the system level engine simulation tool, GT-Power [48]. AMECS starts executing within GT-Power during the closed portion of the engine cycle, and solves the energy equation within the cylinder. This is made possible by using the "External Engine Cylinder Model" option in GT-Power. The implementation is such that the user may supply suitable chemical kinetics, which are then used to simulate the HCCI combustion process, employing multiple

zones. These zones develop a temperature distribution using the thermal stratification methodology.

6.9 Additional applications of thermal stratification methodology

In addition to its application in AMECS to predict stratification in the context of a multi-zone model with kinetics, the thermal stratification methodology developed in this work may also be used in even simpler HCCI combustion models for system-level codes that *do not* feature chemical kinetics. A potential application in the context of such models is to accurately predict ignition timing, by calculating an auto-ignition integral within the hottest zone. Further, the thermal stratification near TDC predicted by this methodology may be used to develop HCCI burn duration correlations for different engines. Efforts to apply the thermal stratification methodology in such a manner are currently underway at the University of Michigan Walter E. Lay Automotive Laboratory.

6.10 Summary

In this chapter we described the relevant guidelines for simple HCCI combustion models intended for use in system level codes. Development of a quasi dimensional, balloon-type multi-zone HCCI combustion model (AMECS) was described. A computationally efficient methodology (based on zonal heat loss multipliers) to capture thermal stratification driven by wall heat loss, without expensive CFD simulation for every case was proposed and implemented within AMECS. For a given engine, the heat loss multipliers are developed based on an analysis of thermal distribution at TDC of a single non-reacting baseline CFD simulation, and the same heat loss multipliers are used over vastly differing operating points for the same engine, without the need of additional CFD simulation at those points.

It was shown that pre-ignition thermal stratification predicted by AMECS using this methodology agrees well with detailed CFD simulations for two different engine geometries over a range of operating conditions. Additionally, it was shown even under reacting conditions, the AMECS model agrees well with CFD over different levels of boost and engine speed, with simulation times being up to two orders of magnitude lower than those for CFD. The AMECS model with a reduced gasoline mechanism was shown to reproduce experimental trends on a PVO engine in terms of in-cylinder pressure, heat release rate and NO emissions. Predictions of HC and CO emissions from the model do not correspond well with experiments, possibly because crevice flows and mixing are not captured by AMECS.

The application of the thermal stratification methodology developed in this work need not be restricted to models featuring chemical kinetics; even simpler correlation-based HCCI combustion models can stand to benefit from having an accurate description of thermal stratification through the compression stroke.

Table 6.1 – Sandia engine specifications used in CFD simulations

Cylinder displacement (L)	0.981
Bore/Stroke (mm)	102.0/120.0
Connecting Rod Length (mm)	192.0
Compression Ratio	13.83:1
IVC/EVO	158°bTDC/122°aTDC
Swirl Ratio	0.9

Table 6.2 – UM-FFVA engine specifications used in CFD simulations

Cylinder displacement (L)	0.540
Bore/Stroke (mm)	86.0/94.3
Connecting Rod Length (mm)	152.2
Compression Ratio	12.22:1
IVC/EVO	130°bTDC/148°aTDC
Swirl Ratio	0.3

Table 6.3 – Computation times (CFD vs. AMECS) using the 33 species Tsurushima PRF mechanism [43]

Simulation Type	Engine	CFD	AMECS
86.0/94.3	FFVA	4 hours	0.5 minutes
152.2	Sandia	8 minutes	0.5 minutes
12.22:1	FFVA	9 hours	1 minute
130°bTDC/148°aTDC	Sandia	30 minutes	1 minute

Table 6.4 – Gasoline surrogate composition taken from Mehl et al. [2]

Simulation Type	Mass Fraction
iso-octane	0.5413
n-heptane	0.1488
toluene	0.2738
2-pentene	0.0361

Table 6.5 – Computation times for different AMECS zone resolutions (Gasoline 252 species mechanism [2], Sandia engine, 100 kPa P_{in})

No. of zones	**Computation Time[a] (sec)**	**No. of time-steps[b]**	**Normalized Computation Time = (a/b)/(a_{10}/b_{10})**
40	2990	6376	3.7x
20	1095	4618	1.9x
10	407	3203	1.0x

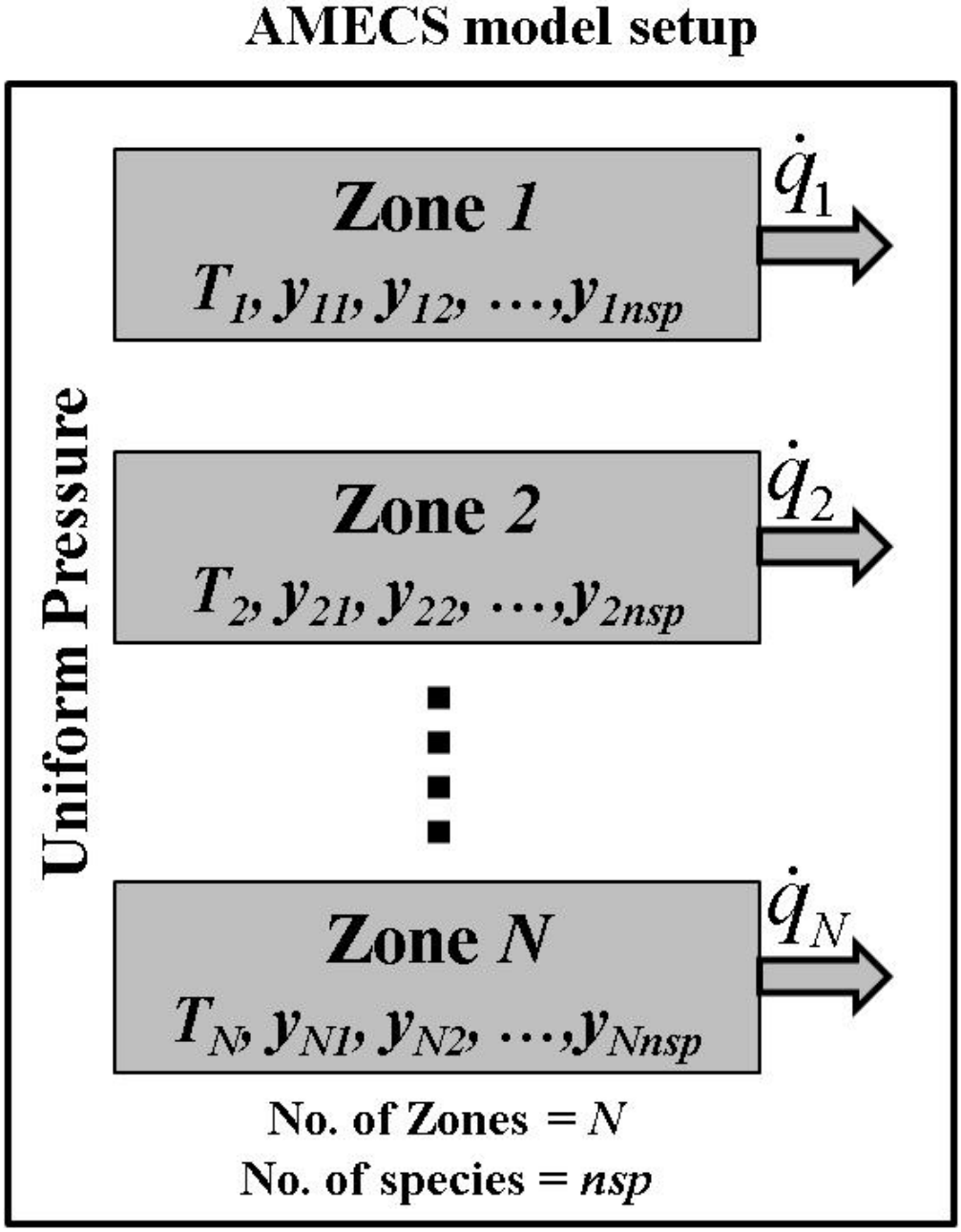

Figure 6.1 – Conceptual picture of the AMECS combustion model

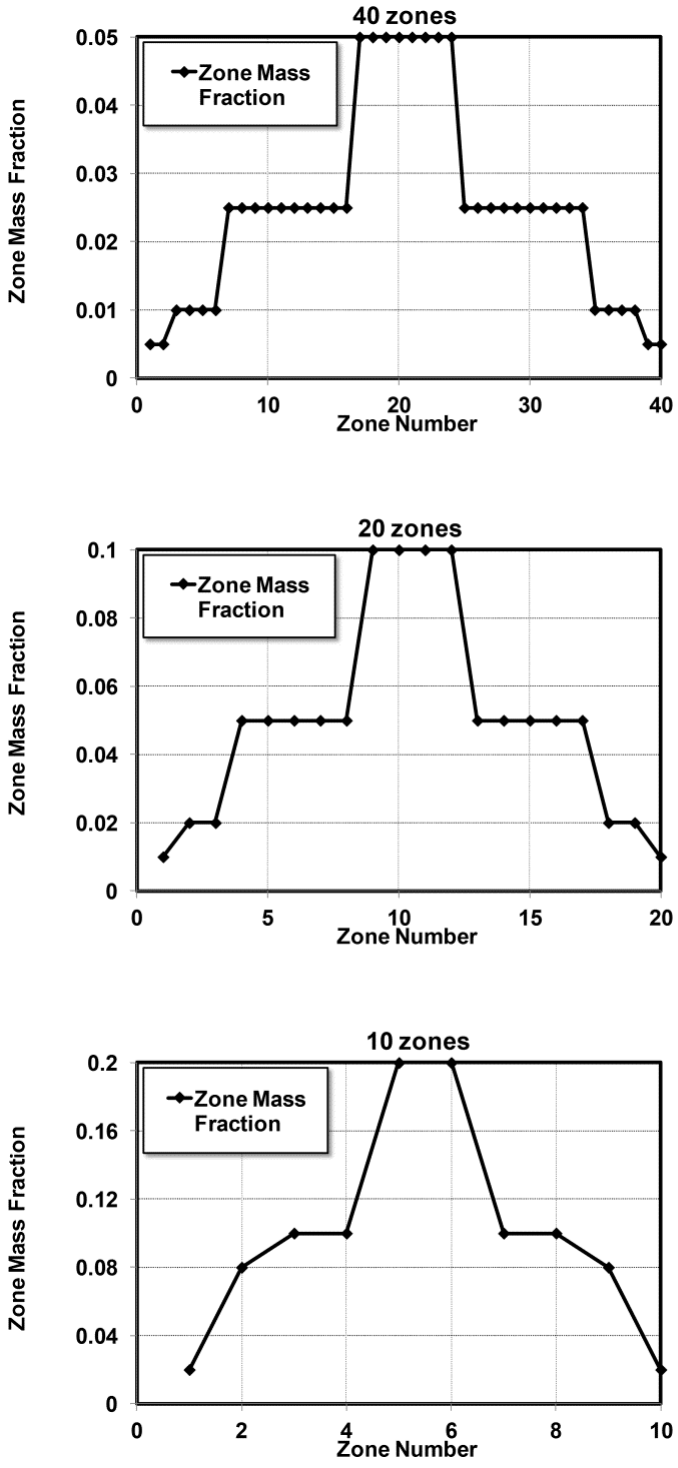

Figure 6.2 – Prescribed zone mass fractions for binning CFD results sequentially from highest temperature (lower zone number) to lowest temperature (higher zone number)

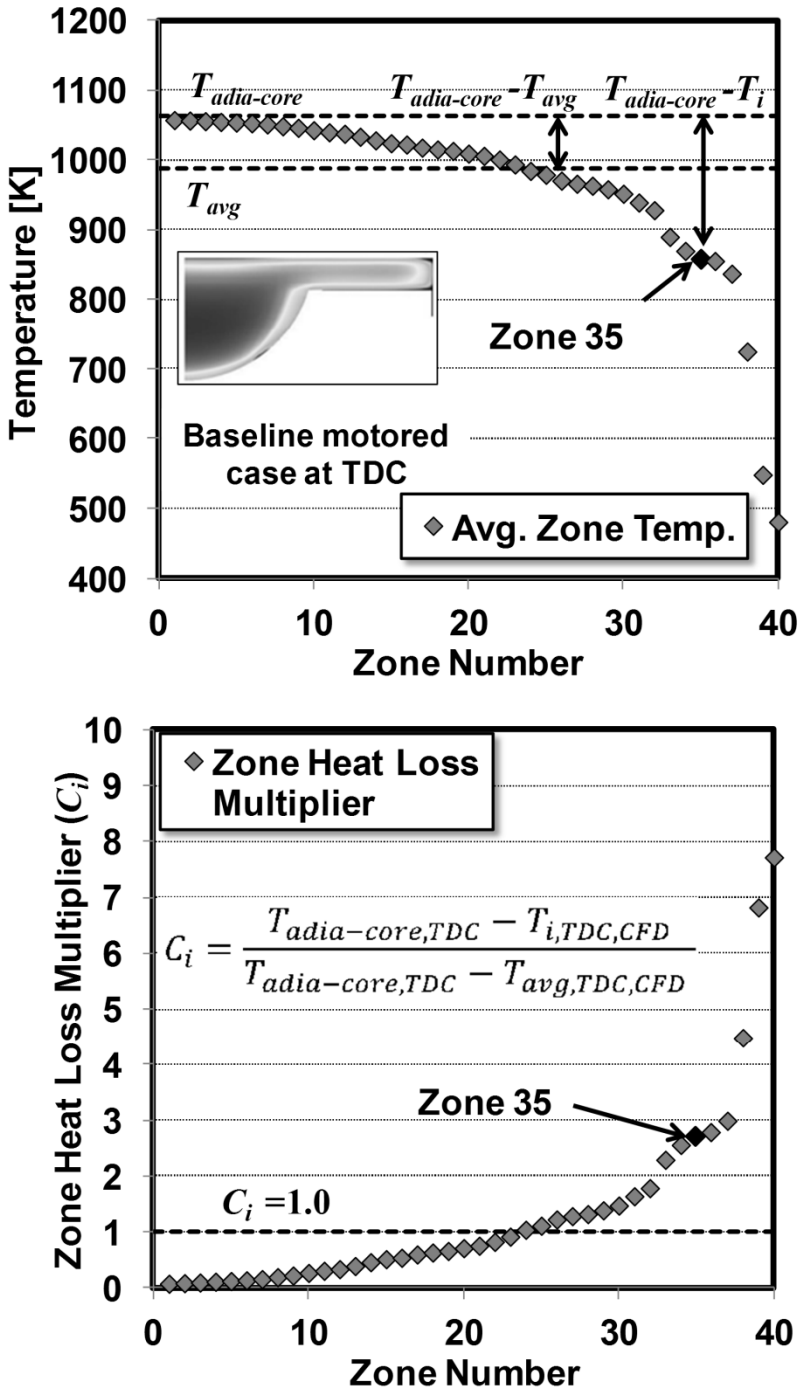

Figure 6.3 – CFD results at TDC from the baseline condition (1200 RPM, 100 kPa P_{in}) binned into 40 temperature zones based on a specified mass fraction distribution (Figure 6.2). As an example, zone 35 is highlighted to illustrate the procedure for obtaining the heat loss multipliers used by AMECS.

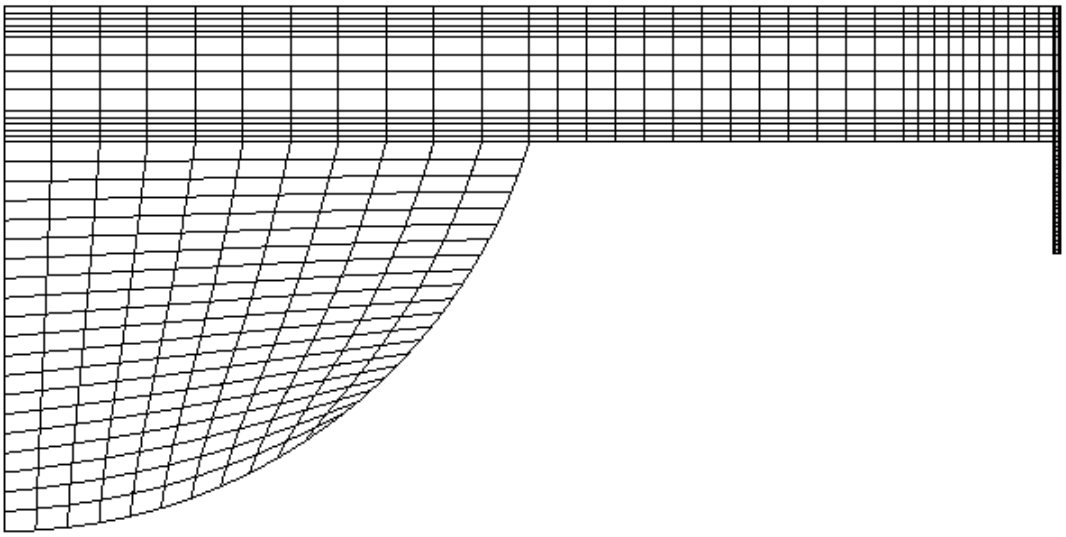

Figure 6.4 – 2D CFD mesh of the Sandia engine used in simulations, shown at TDC.

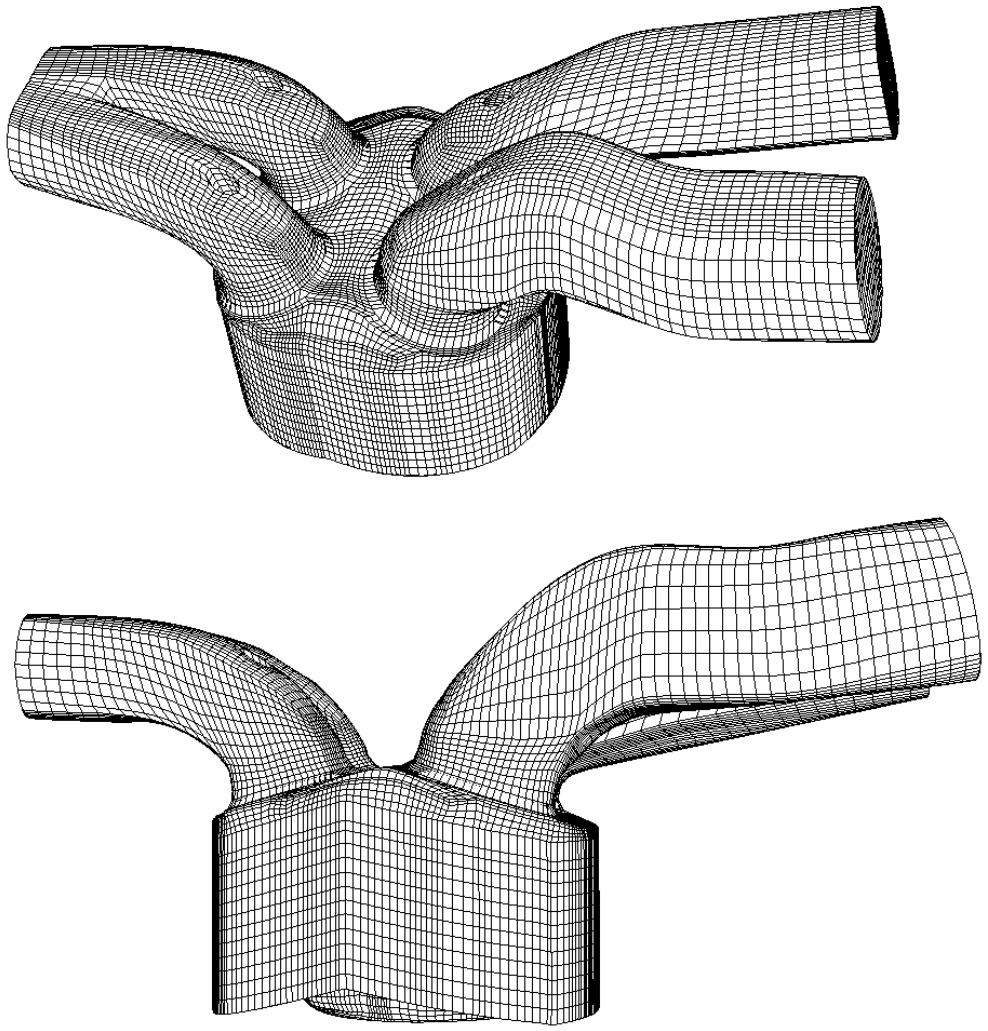

Figure 6.5 – University of Michigan FFVA engine CFD mesh.

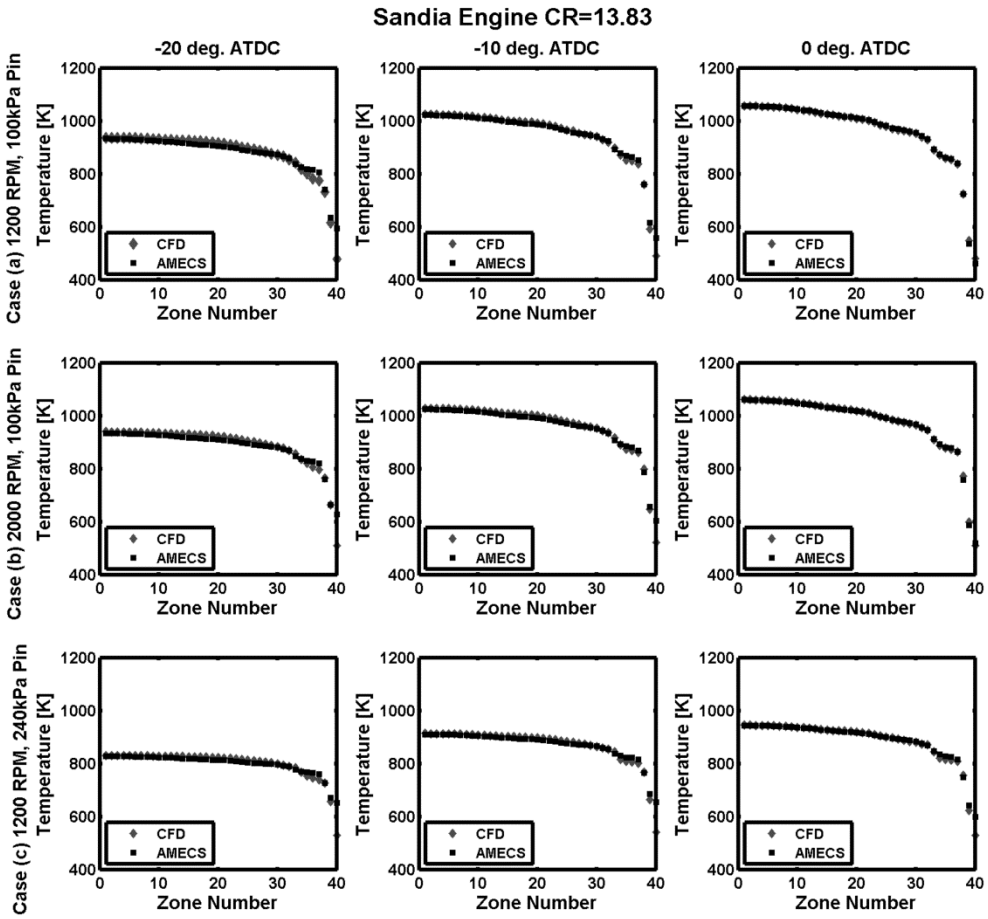

Figure 6.6 – Sandia engine (CR = 13.83): comparison of thermal stratification – motoring CFD results binned into 40 predefined zones compared with temperature distribution prediction from AMECS using the thermal stratification methodology at -20° CA aTDC, -10° CA aTDC and 0° CA aTDC for three cases: Case (a) 1200 RPM, 100 kPa P_{in} (baseline); Case (b) 2000 RPM, 100 kPa P_{in} and Case (c) 1200 RPM, 240 kPa $P_{in.}$

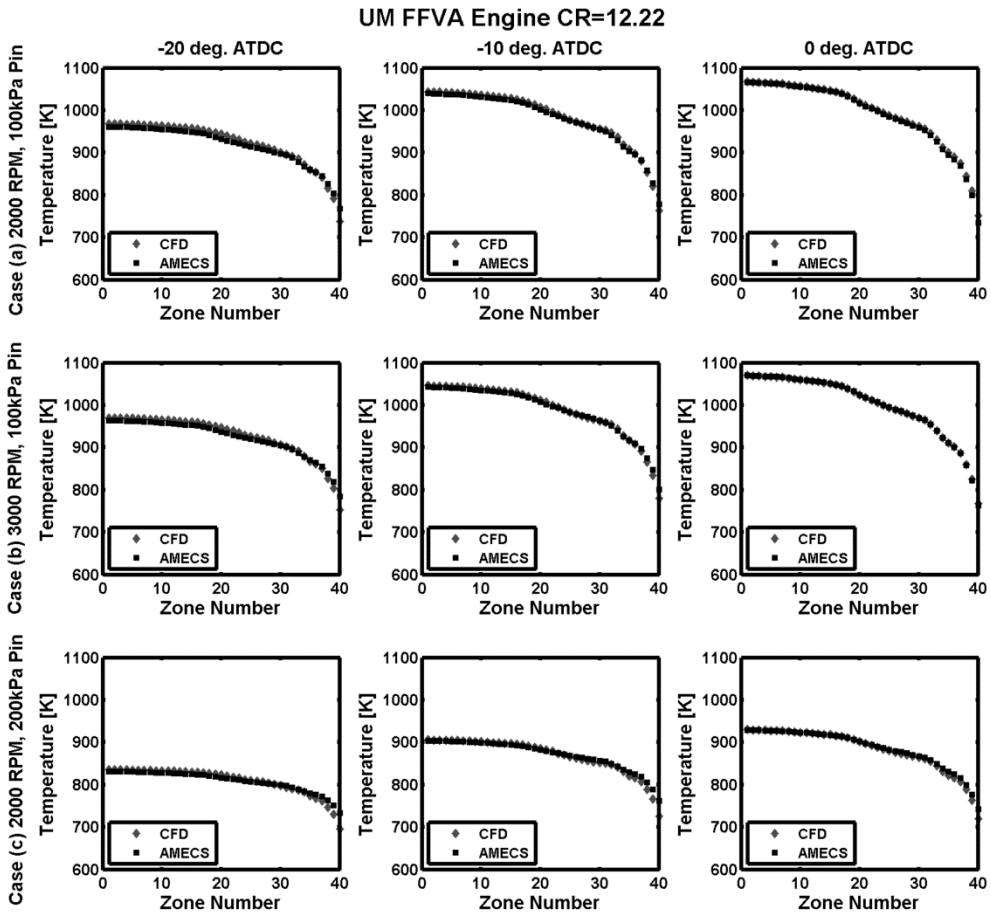

Figure 6.7 – UM-FFVA engine (CR = 12.22): comparison of thermal stratification – motoring CFD results binned into 40 predefined zones compared with temperature distribution prediction from AMECS using the thermal stratification methodology at -20° CA aTDC, -10° CA aTDC and 0° CA aTDC for three cases: Case (a) 2000 RPM, 100 kPa P_{in} (baseline); Case (b) 3000 RPM, 100 kPa P_{in} and Case (c) 2000 RPM, 200 kPa $P_{in.}$

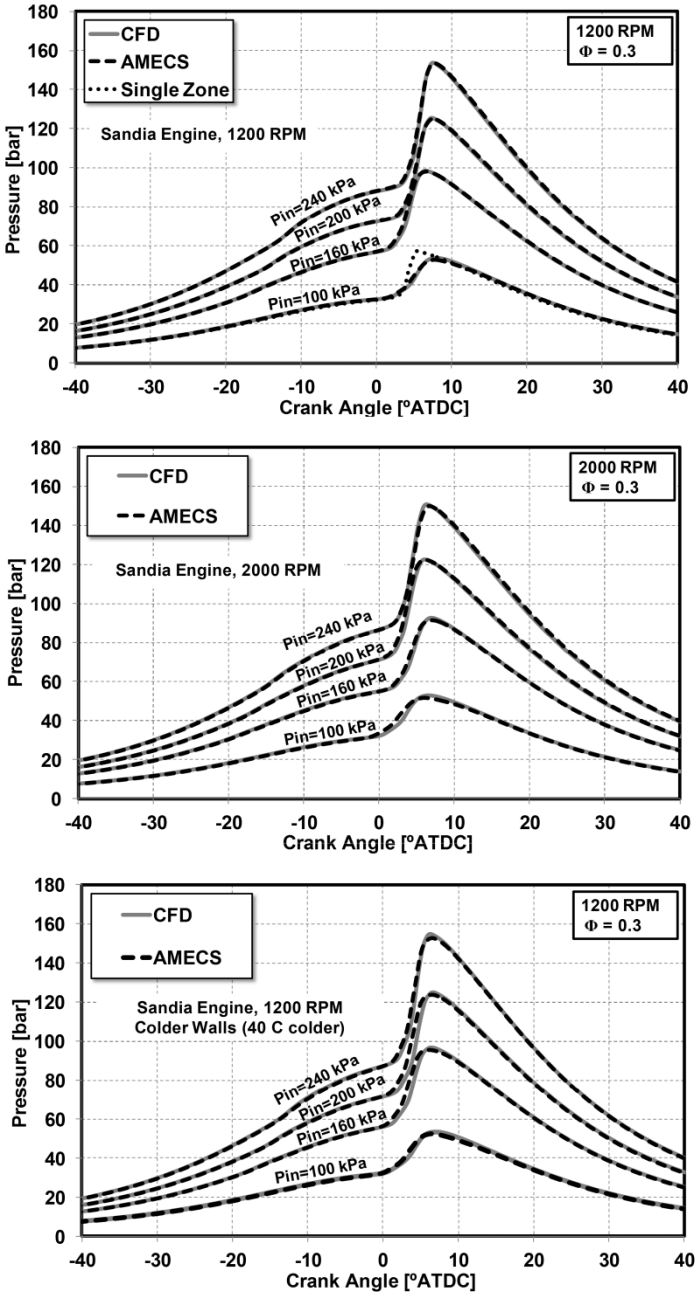

Figure 6.8 – Comparison of AMECS (40 zones) predictions with CFD (fully-coupled CFD/kinetics) results; Φ = 0.3 (PRF 90 and 33-species Tsurushima mechanism [43] used) for the Sandia engine.

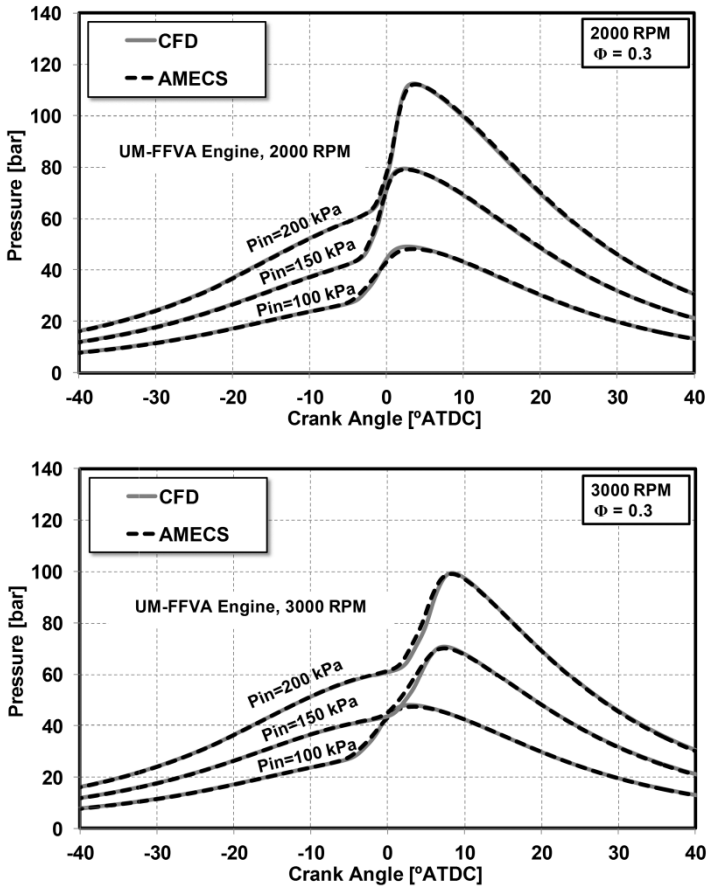

Figure 6.9 – Comparison of AMECS (40 zones) predictions with CFD (fully-coupled CFD/kinetics) results; Φ = 0.3 (PRF 90 and 33-species Tsurushima mechanism [43] used) for the UM-FFVA engine.

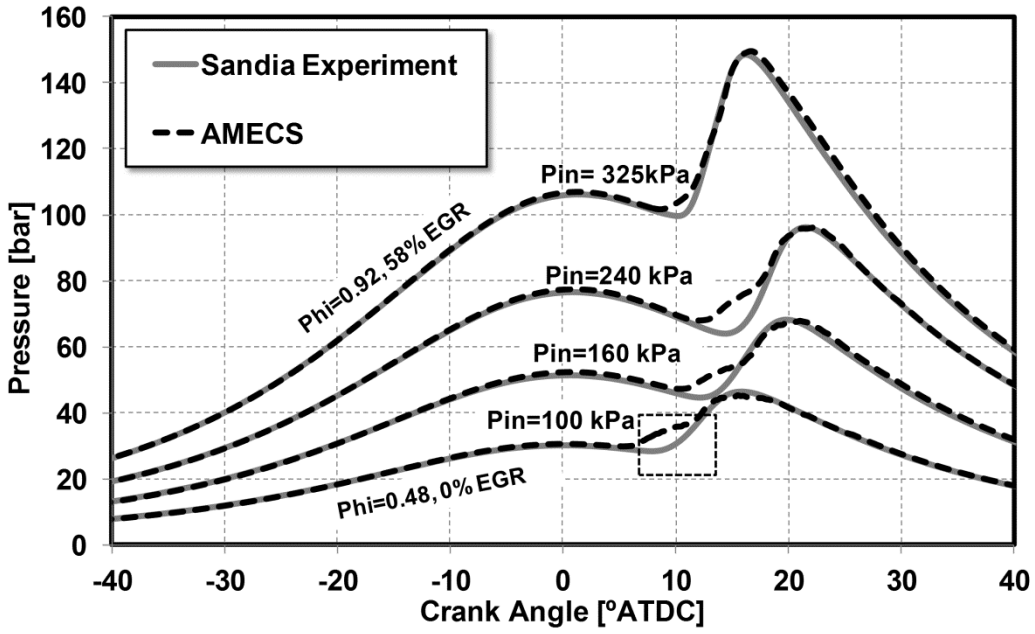

Figure 6.10 – Comparison of AMECS (40 zones) predictions (using the 252-species gasoline mechanism [2]) and surrogate formulation given in Table 6.4 with Sandia boosted gasoline HCCI experiments by Dec and Yang [39]. The dashed box indicates a "bump" in the pressure trace during the main heat release (highlighted here for the 10 kPa P_{in} case), which is possibly an artifact of the gasoline mechanism used.

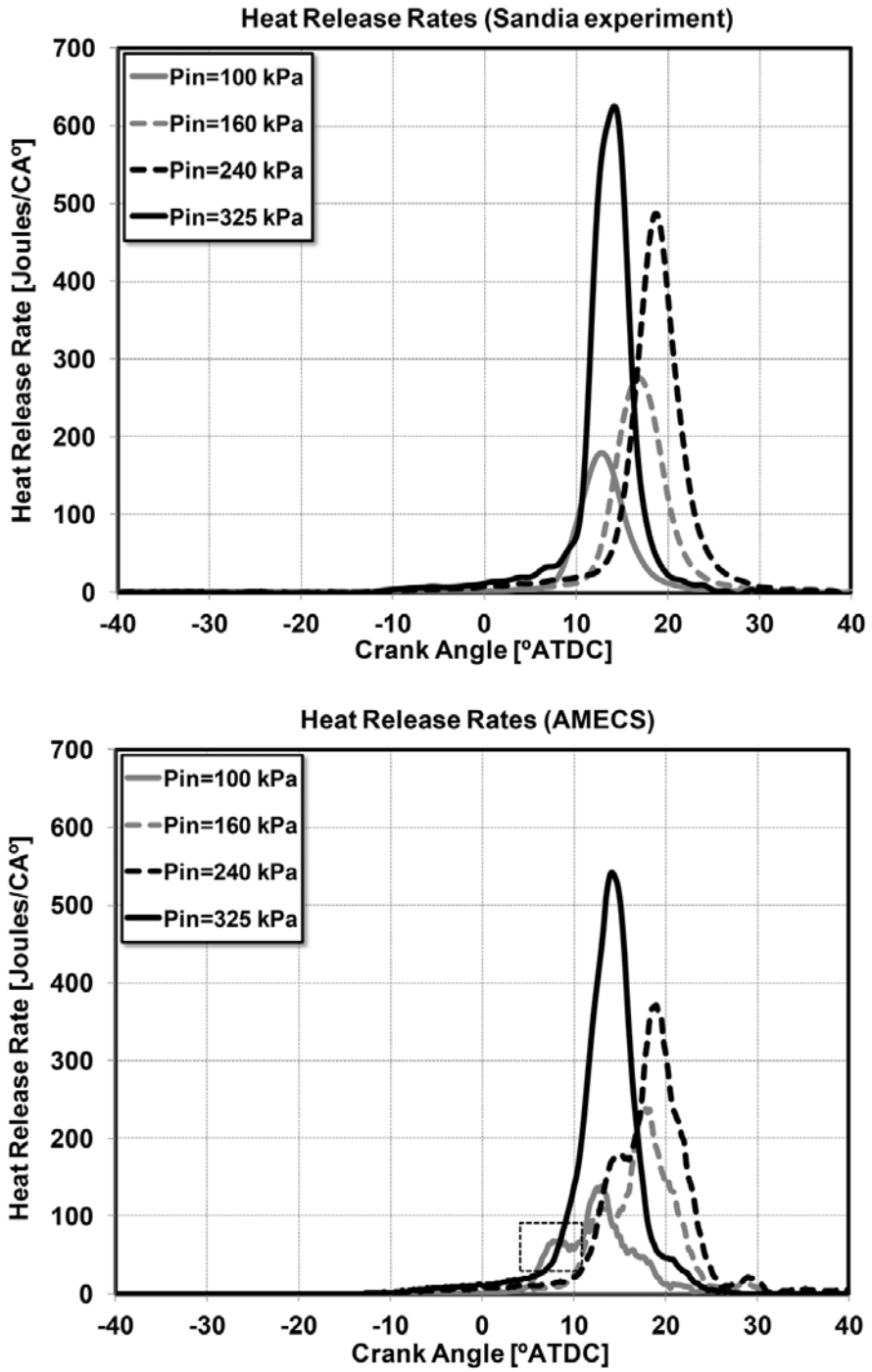

Figure 6.11 – Heat release rates (HRRs) – comparison of AMECS (40 zones using the 252-species gasoline mechanism [2]) predictions with Sandia experiments of Dec and Yang [39]. The dashed box in the AMECS results indicates a "bump" in the HRR predictions from AMECS during the main heat release (highlighted here for the 100 kPa P_{in} case), which is possibly an artifact of the gasoline mechanism used.

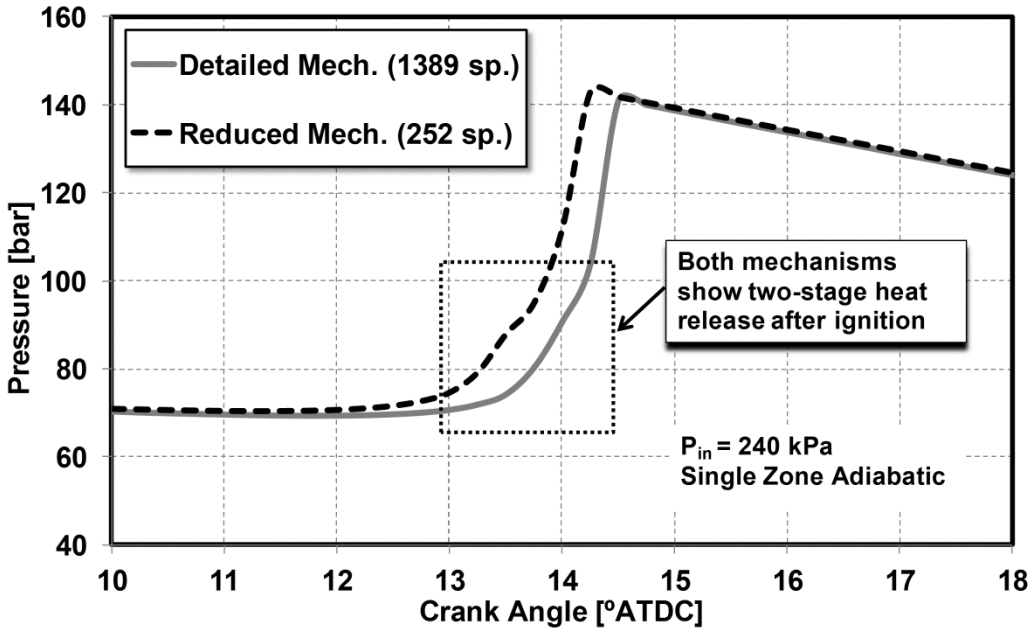

Figure 6.12 – Pressure traces from single-zone adiabatic simulations, with intake pressure of 240 kPa P_{in} and composition as in Sandia experiments, using the 1389-species LLNL detailed gasoline mechanism [44] and the 252-species reduced gasoline mechanism [2]/ The dashed box indicates the "bump" in the pressure trace during the main heat release for both mechanisms.

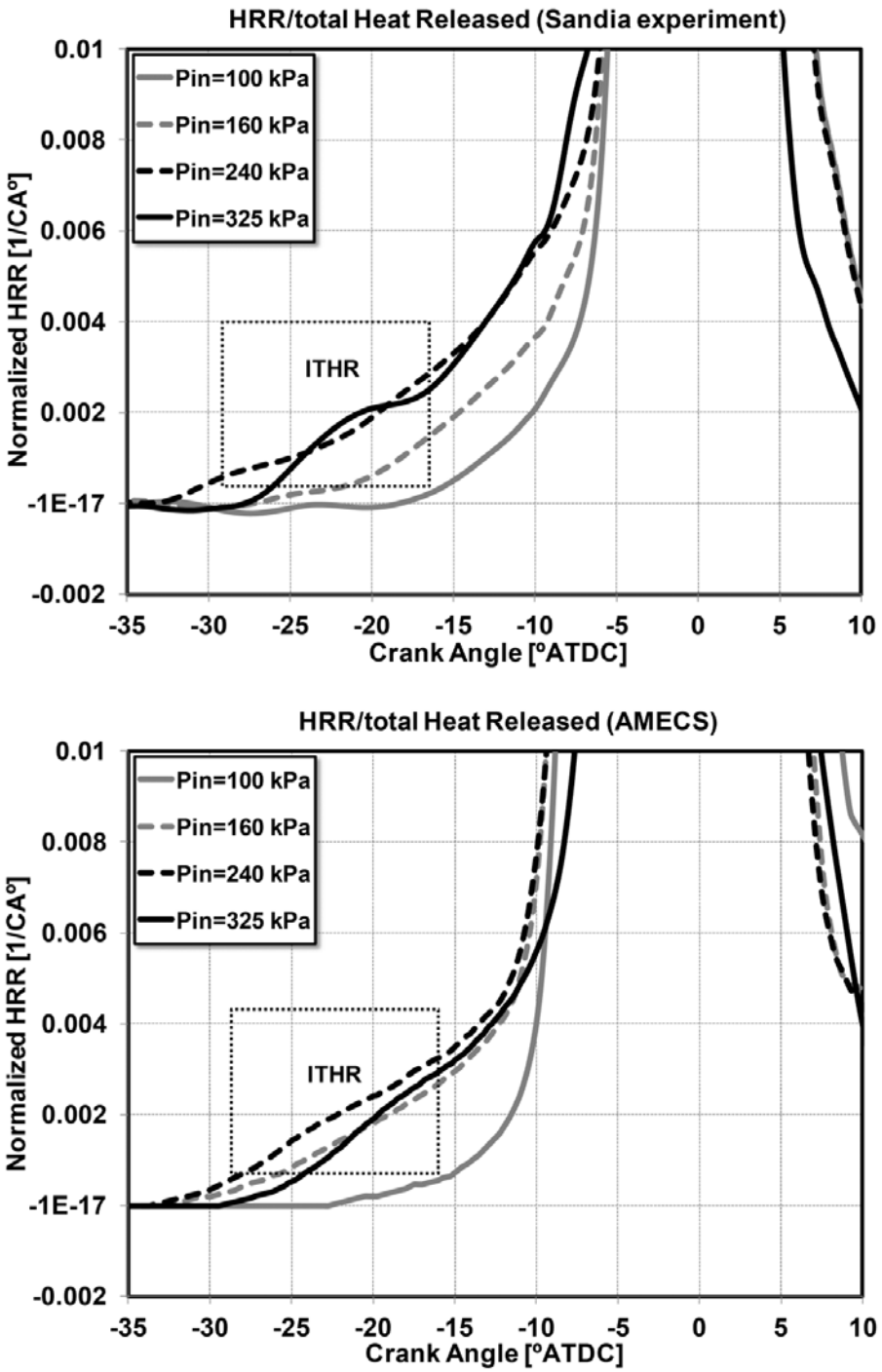

Figure 6.13 – Normalized HRR – comparison of AMECS (40 zones using the 252-species gasoline mechanism [2]) predictions with Sandia experiments of Dec and Yang [39]. Curves are shifted to align peak heat release rate with TDC. The dashed boxes indicate the ITHR (prior to the main heat release) observed by Dec and Yang [39] (top) and that predicted by AMECS (bottom) for boosted conditions.

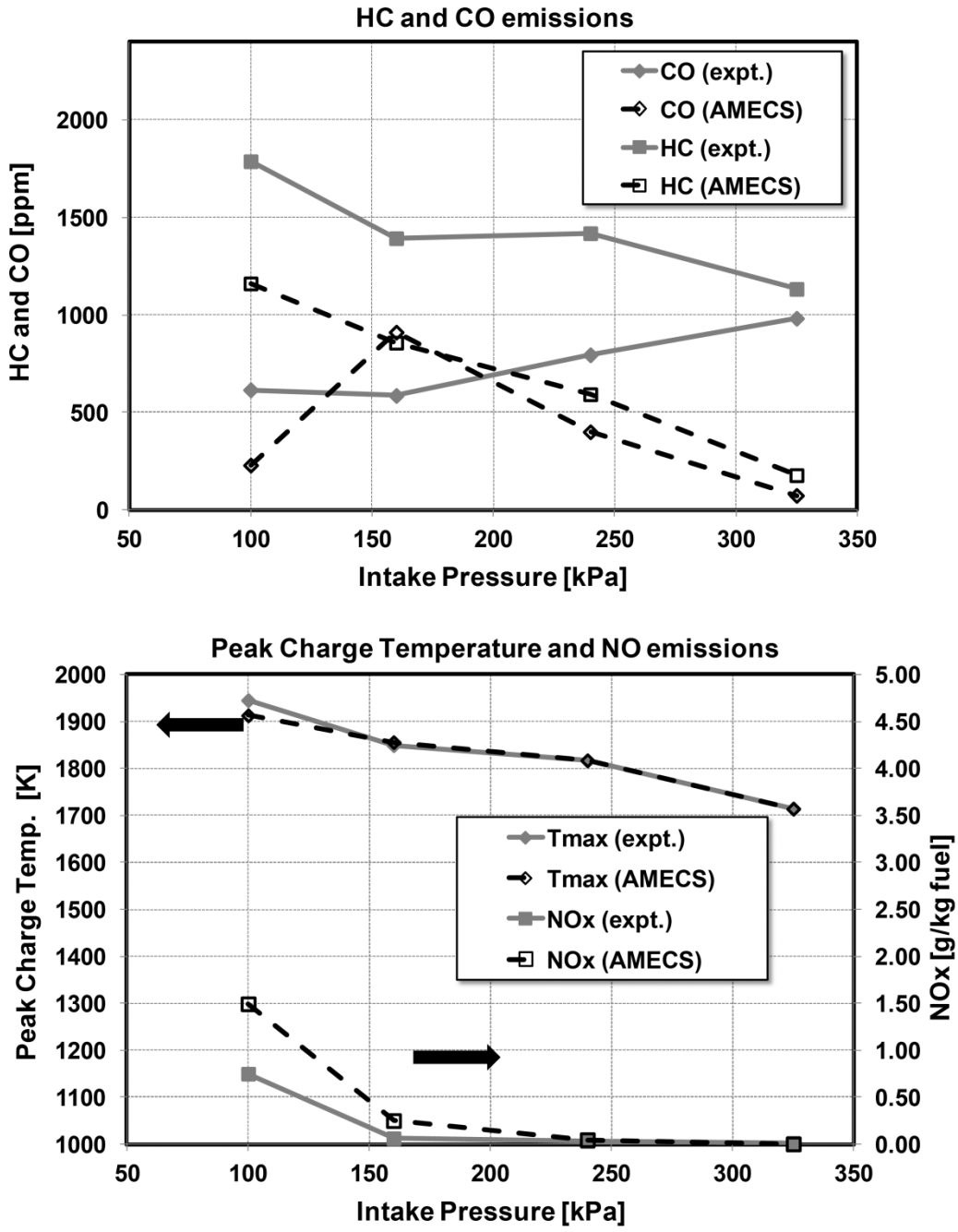

Figure 6.14 – CO and HC emissions (top) and peak charge temperature and NO emissions (bottom) – comparison of AMECS (40 zones using the 252-species gasoline mechanism [2]) predictions with Sandia experiments of Dec and Yang [39].

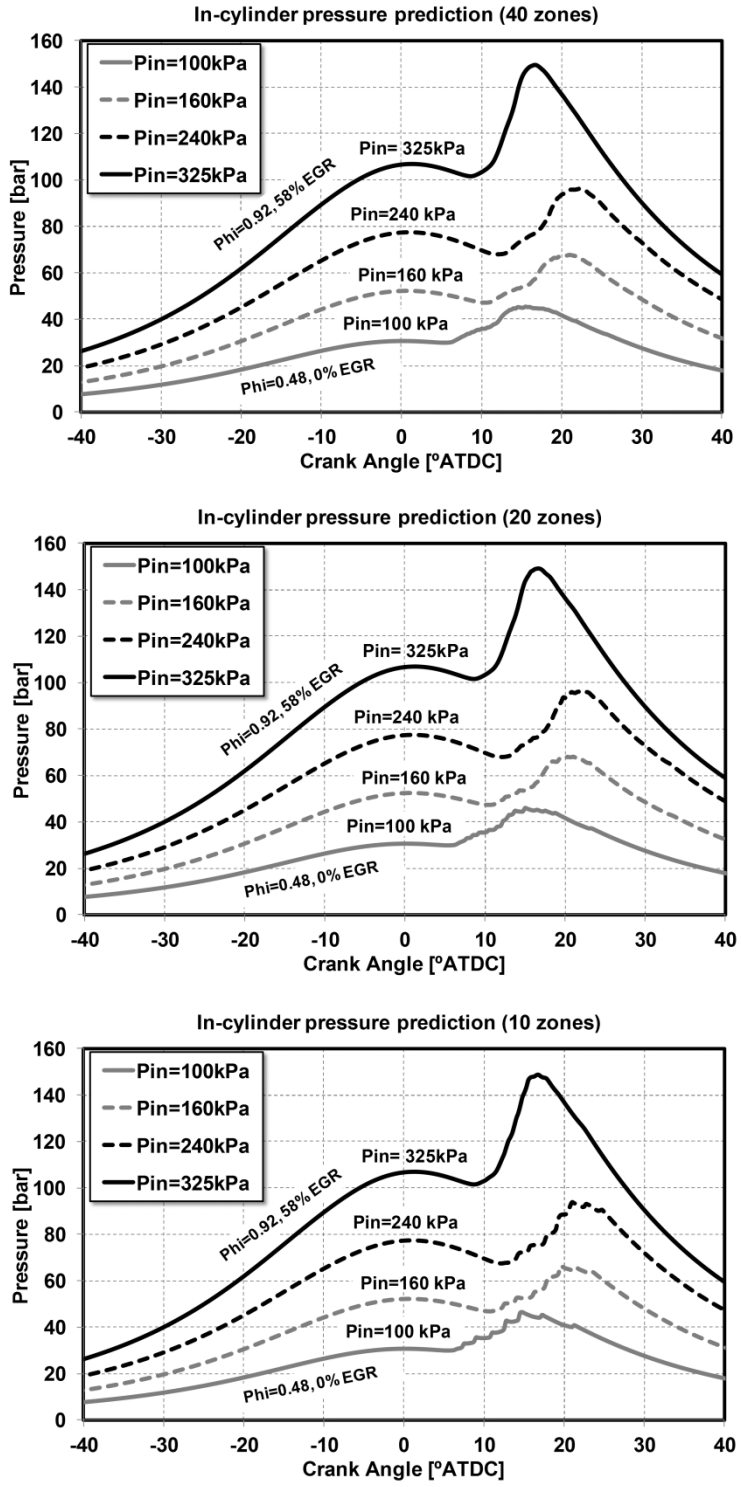

Figure 6.15 – In-cylinder pressure predictions by AMECS using the 252-species gasoline mechanism [2] based on the Sandia data [39] with different zone resolutions.

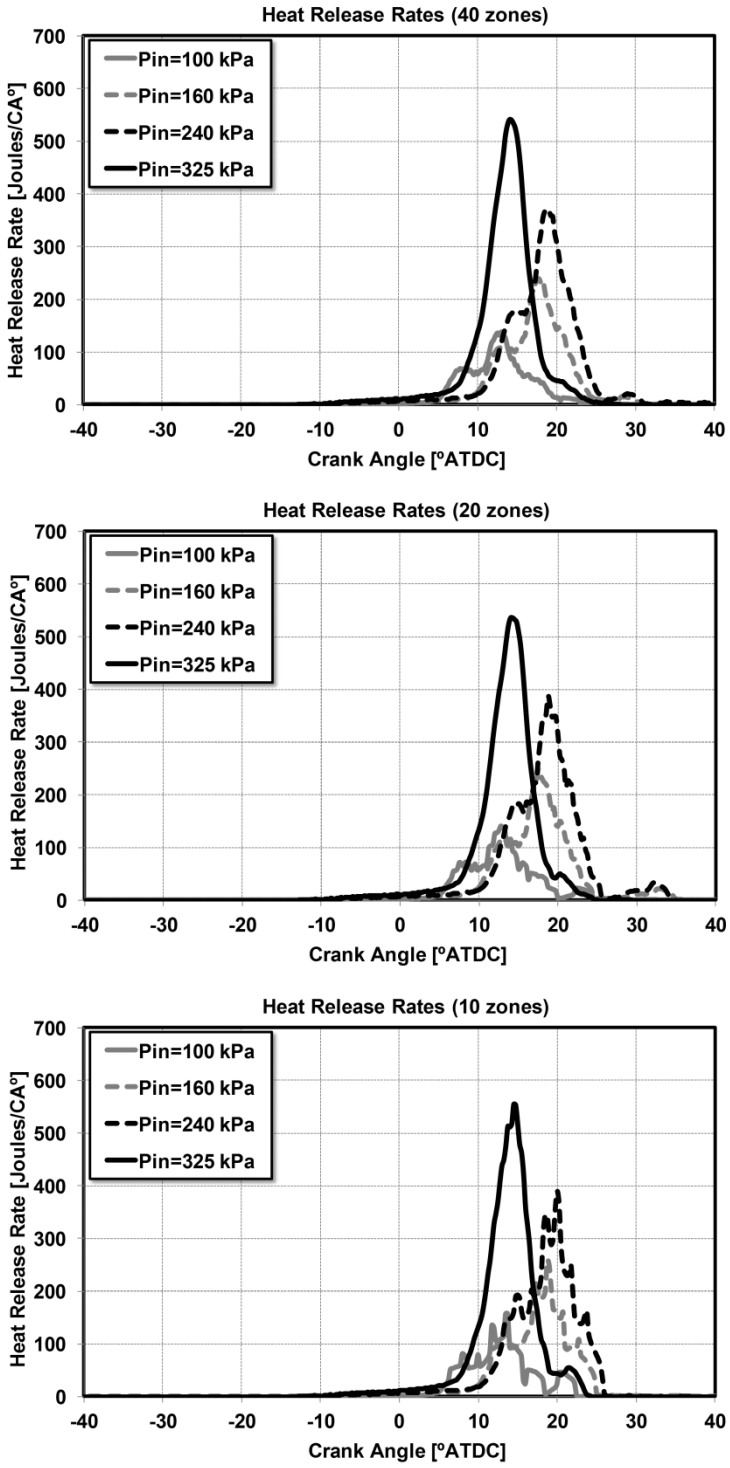

Figure 6.16 –HRR predictions by AMECS using the 252-species gasoline mechanism [2] based on the Sandia data [39] with different zone resolutions.

6.11 References

1. McNenly, M.J., Whitesides, R. A., and Flowers, D. L., "Adaptive Preconditioning Strategies for Integrating Large Kinetic Mechanisms," *8th US National Combustion Meeting organized by the Western States Section of the Combustion Institute*, Paper number 070RK-0377, 2013.

2. Mehl, M., Chen, J.Y., Pitz, W.J., Sarathy, S.M., and Westbrook, C. K., "An Approach for Formulating Surrogates for Gasoline with Application toward a Reduced Surrogate Mechanism for CFD Engine Modeling," *Energy & Fuels*, 2011, 25(11), 5215-52231.

3. Anand, W.J.D., "Heat Transfer in the Cylinders of Reciprocating Internal Combustion Engines," *Proc. Instn. of Mech. Engrs*., 177(36), 973-990, 1963.

4. Woschni, G., "A Universally Applicable Equation for the Instantaneous Heat Transfer Coefficient in the Internal Combustion Engine," SAE Paper 670931, 1967.

5. Hohenberg, G.F., "Advanced Approaches for Heat Transfer Calculations," SAE Paper 790825, 1979.

6. Andreatta, D.A., "The use of reformed natural gas as a fuel for reciprocating engines," Ph.D. dissertation, University of California at Berkeley, Dept. of Mechanical Engineering, 1995.

7. Aceves, S.M., Flowers, D.L., Westbrook, C.K., Smith, J.R., Dibble, R.W., Christensen, M., Pitz, W.J., and Johansson, B., "A Multi-zone Model for Prediction of HCCI Combustion and Emissions," SAE Paper 2000-01-0327, 2000.

8. Aceves, S.M., Flowers, D.L., Martinez-Frias, J., Smith, J.R., Westbrook, C.K., Pitz, W.J., Dibble, R.W., Wright, J.F., Akinyemi, W.C., and Hessel, R.P., "A Sequential Fluid-Mechanic Chemical-Kinetic Model of Propane HCCI Combustion," SAE Paper 2001-01-1027, 2001.

9. Aceves, S.M., Martinez-Frias, J., Flowers, D.L., Smith, J.R., Dibble, R.W., Wright, J.F., and Hessel, R.P., "A Decoupled Model of Detailed Fluid Mechanics Followed by Detailed Chemical Kinetics for Prediction of Iso-Octane HCCI Combustion," SAE Paper 2001-01-3612, 2001.

10. Babajimopoulos, A., Lavoie, G.A., and Assanis, D.N., "Modeling HCCI combustion with high levels of residual gas fraction – a comparison of two VVA strategies," SAE Paper 2003-01-3220, 2003.

11. Easley, W., Agarwal, A., and Lavoie, G.A., "Multi-Zone Modeling of HCCI Combustion and Emissions Using Detailed Chemistry," SAE Paper 2001-01-1029, 2001.

12. Noda, T., and Foster, D.E., "A Numerical Study to Control Combustion Duration of Hydrogen-Fueled HCCI by Using Multi-Zone Chemical Kinetics Simulation," SAE Paper 2001-01-0250, 2001.

13. Fiveland, S.B., and Assanis, D.N., "Development of a Two-Zone HCCI Combustion Model Accounting for Boundary Layer Effects," SAE Paper 2001-01-1028, 2001.

14. Ogink, R., and Golovitchev, V., "Gasoline HCCI Modeling: An Engine Cycle Simulation Code with a Multi-Zone Combustion Model," SAE Paper 2002-01-1745, 2002.

15. Xu, H., Liu, M., Gharahbaghi, S., Richardson, S., Wyszynski, M., and Megaritis, T., "Modeling of HCCI Engines: Comparison of Single-zone, Multi-zone and Test Data," SAE Paper 2005-01-2123, 2005.

16. Orlandini, I., Kulzer, A., Weberbauer, F., and Rauscher, M., "Simulation of Self Ignition in HCCI and Partial HCCI Engines Using a Reduced Order Model," SAE Paper 2005-01-0159, 2005.

17. Komninos, N.P., Hountalas, D.T., and Kouremenos, D.A., "Development of a New Multi-Zone Model for the Description of Physical Processes in HCCI Engines," SAE Paper 2004-01-0562, 2004.

18. Komninos, N.P., and Kosmadakis, G.M., “Heat Transfer in HCCI multi-zone modeling: Validation of a new wall heat flux correlation under motoring conditions,” Applied Energy, 2011, 88(5), 1635-1648.

19. Kongsereeparp, P., and Checkel, M. D., “Novel Method for Setting Initial Conditions for Multi-Zone HCCI Combustion Modeling,” SAE Paper 2007-01-0674.

20. Kraft, M., Maigaard, P., Mauss, F. Christensen, M., and Johansson, B., “Investigation of Combustion Emissions in a Homogeneous Charge Compression Injection Engine: Measurements and a new Computational Model,” *Proc. Combust. Inst.*, 2000, 28(1), 1195-1201.

21. Maigaard, P., Mauss, F., and Kraft, M., “Homogeneous Charge Compression Ignition Engine: A Simulation Study on the Effects of Inhomogeneities,” *J. Eng. Gas Turbines* Power, 2003, 125(2), 466-471.

22. Pitsch, H., Chen, M., and Peters, N., “Unsteady flamelet modeling of Turbulent Hydrogen/Air diffusion flames,” Proc. Combust. Inst., 1998, 27, 1057-1064.

23. Peters, N., “Laminar diffusion flamelet models in non-premixed turbulent combustion,” *Prog. Energy Combust. Sci.*, 1984, 10, 319-340.

24. Hergart, C.-A., Barths, H., and Siewart, R.M., “Modeling Approaches for Premixed Charge Compression Ignition Combustion,” SAE Paper 2005-01-0218, 2005.

25. Flowers, D.L., Aceves, S.M., Martinez-Frias, J., Hessel, R.P., and Dibble, R.W., “Effect of mixing on hydrocarbon and carbon monoxide emissions prediction for iso-octane HCCI engine combustion using a multi-zone kinetics solver,” SAE Paper 2003-01-1821, 2003.

26. Babajimopoulos, A., Assanis, D.N., Flowers, D.L., Aceves, S.M., and Hessel, R.P., “A fully coupled computational fluid dynamics and multi-zone model with detailed chemical kinetics for the simulation of premixed charge compression ignition engines,” *Int. J. Engine Res.*, 2005, 6(5), 497-512.

27. Shi, Y., Hessel, R.P., and Reitz, R.D., "An adaptive multi-grid chemistry (AMC) model for efficient simulation of HCCI and DI engine combustion," *Combust. Theor. Model.*, 2009, 13, 83-104.

28. Felsch, C., Hoffmann, K., Vanegas, A., Drews, P. Barths, H. Abel, D., and Peters, N., "Combustion model reduction for diesel engine control design," *Int. J. Engine Res.*, 2009, 10(6), 359-387.

29. Kodavasal, J., Keum, S., and Babajimopoulos, A., "An extended multi-zone combustion model for PCI simulation," *Combust. Theor. Model.*, 2011, 15(6), 893-910.

30. Narayanaswamy, K., and Rutland, C.J., "Cycle Simulation Diesel HCCI Modeling Studies and Control," SAE Paper 2004-01-2997, 2004.

31. McNenly, M.J., Havstad, M. A., Aceves, S.M., and Pitz, W.J., "Integration Strategies for Efficient Multizone Chemical Kinetics Models," SAE Paper 2010-01-0576, 2010.

32. Hindmarsh, A. C., "ODEPACK, a systemized collection of ODE solvers," In Scientific Computing, Stepleman, R.S. et al. eds., North-Holland, Amsterdam, 55-64, 1983.

33. Schwer, D.A., Tolsma, J.E., Green, Jr., W.H., and Barton, P.I., "On Upgrading the Numerics in Combustion Chemistry Codes," *Combust. Flame.*, 2012, 128(3), 270-291.

34. Lu, T., and Law, C.K., "Toward accommodating realistic fuel chemistry in large-scale computations," *Prog. Energy Combust. Sci.*, 2009, 35(2), 192-215.

35. Perini, F., Galligani, E., and Reitz, R.D., "An Analytical Jacobian Approach to Sparse Reaction Kinetics for Computationally Efficient Combustion Modeling with Large Reaction Mechanisms," *Energy & Fuels*, 2012, 26(8), 4804-4822.

36. Snyder, J., Dronniou, N., Dec, J., and Hanson, R., "PLIF Measurements of Thermal Stratification in an HCCI Engine under Fired Operation," SAE Paper 2011-01-1291, 2011.

37. Rothamer, D.A., Snyder, J.A., Hanson, R.K., Steeper, R.R., and Fitzgerald, R.P., "Simultaneous imaging of exhaust gas residuals and temperature during HCCI combustion," *Proc. Combust. Inst.*, 2009, 32(2), 2869-2876.

38. Chang, J., Güralp, O., Filipi, Z., Assanis, D., Kuo, T.-W., Najt, P., and Rask, R., "New Heat Transfer Correlation for an HCCI Engine Derived from Measurements of Instantaneous Surface Heat Flux," SAE Paper 2004-01-2996, 2004.

39. Dec, J.E., and Yang, Y., "Boosted HCCI for High Power without Engine Knock and with Ultra-Low NOx Emissions – using Conventional Gasoline," SAE Paper 2010-01-1086, 2010.

40. Manofsky, L., Vavra, J., Assanis, D., and Babajimopoulos, A., "Bridging the Gap between HCCI and SI: Spark-Assisted Compression Ignition," SAE Paper 2011-01-1179, 2011.

41. Amsden, A.A., "KIVA-3V: A Block Structured KIVA Program for Engines with Vertical or Canted Valves," Los Alamos National Laboratory Report LA-13313-MS, 1997.

42. Sjöberg, M., and Dec, J.E., "An Investigation of the Relationship Between Measured Intake Temperature, BDC Temperature, and Combustion Phasing for Premixed and DI HCCI Engines," SAE Paper 2004-01-1900, 2004.

43. Tsurushima, T., "A new skeletal PRF kinetic model for HCCI combustion," *Proc. Combust. Inst.*, 2009, 32, 2835-2841.

44. Mehl, M., Pitz, W.J., Westbrook, C.K., and Curran, H.J., "Kinetic Modeling of Gasoline Surrogate Components and Mixture Under Engine Like Conditions," *Proc. Combust. Inst.*, 2011, 33, 193-200.

45. Mehl, M., Pitz, W.J., Sarathy, M., Yang, Y., and Dec, J.E., “Detailed Kinetic Modeling of Conventional Gasoline at Highly Boosted Conditions and the Associated Intermediate Temperature Heat Release,” SAE Paper 2012-01-1109, 2012.

46. Flowers, D.L., Aceves, S.M., Martinez-Frias, J., and Dibble, R.W., “Prediction of Carbon Monoxide and Hydrocarbon Emissions in Iso-octane HCCI Engine Combustion Using Multizone Simulations,” *Proc. Combust. Inst.*, 2002, 29, 687-693.

47. Heywood, J. B., 1988, *Internal Combustion Engine Fundamentals*, McGraw-Hill, New York.

48. Gamma Technologies Inc., *www.gtisoft.com.*

CHAPTER 7

CONTRIBUTIONS AND RECOMMENDATIONS

The effect of diluent composition and thermal/compositional stratification as a result of different charge preparation strategies on HCCI combustion was investigated in this work. Different means of achieving dilution, charge heating and fueling were compared at a fixed ignition timing and fueling using full-cycle CFD simulation with kinetics in an attempt to understand the effect of charge preparation strategy on HCCI burn duration and NOx emissions. Reaction space analysis and a sequential CFD multi-zone model developed as part of this work were used to decouple concurrent effects such as thermal stratification and compositional stratification, in an attempt to understand the importance of each effect in isolation. A methodology to capture thermal stratification driven by wall heat loss was proposed as an alternative to CFD simulation and was implemented into a stand-alone multi-zone HCCI multi-zone combustion model (built as part of this work) intended for use in system-level codes.

7.1 Main findings and insights from this doctoral work

7.1.1 Relative importance of thermal and compositional stratification

Based on the He et al. [1] correlation for ignition delay, the relative importance of distributions in T, $\phi_{FO}$and χ_{O2} in isolation were determined for a nominal HCCI operating point. It was shown that a ΔT of 50 K, $\Delta\phi_{FO}$of 0.5 and a $\Delta\chi_{O2}$ of 8% are all

worth the same change in ignition delay, and thus reactivity stratification. This indicates that significant levels of compositional stratification (in $\phi_{FO}$and χ_{O2}) are required to achieve the same effects as thermal stratification.

It was shown in this work that under typical PVO conditions, the pre-ignition stratification in composition is negligible and the stratification in temperature (primarily driven by wall heat losses) is on the order of 40 K in terms of σT. Under NVO conditions, the compositional stratification is on the order of 0.02 in terms of $\sigma\phi_{FO}$and 0.01% in terms of $\sigma\chi_{O2}$, while the thermal stratification is on the order of 50 K in terms of σT. Thus, even under NVO conditions, thermal stratification dominates. When direct injection is used in conjunction with NVO, the level of stratification in ϕ_{FO} becomes on the order of thermal stratification, with stratification in ϕ_{FO}being roughly 0.17 in terms of $\sigma\phi_{FO}$ and that in temperature being roughly 40 K in terms of σT.

7.1.2 Effect of diluent composition on HCCI combustion

Air dilution and external EGR dilution were compared using full-cycle CFD simulations with gasoline kinetics. It was found that when ignition timing is matched, the HCCI burn rates with air dilution and external EGR dilution are very similar. This finding reinforces the experimental findings of Dec et al. [2], which indicate that EGR dilution has a small effect on burn duration *when combustion phasing is matched*. It must be noted that a significant amount of intake air heating is required to achieve the required combustion phasing for both air-dilute and external EGR-dilute operation under naturally aspirated conditions in Dec et al.'s work [2] as well as in the work presented in this dissertation. However, Dec et al. [2] did not analyze the thermodynamic and chemical kinetic factors at play when replacing air with EGR as diluent while keeping phasing fixed.

In this work, we probe further in order to understand the development in reaction-space for the two dilution methods. It was found that the thermal stratification and reactivity stratification for air and external EGR dilution were very similar when ignition timing is matched. The slight increase in burn duration with external EGR dilution compared to air dilution is primarily due to differences in thermodynamic properties of the two diluents and not differences in chemical reactivity of the charge prior to ignition.

7.1.3 Stratification from NVO and effects on burn duration

A thorough investigation into the effects of trapping large amounts of internal residual (using NVO) on thermal and compositional stratification, and ultimately burn duration was performed using full-cycle CFD simulations with gasoline kinetics. For the first time, the effect of ignition timing and mean composition on burn duration has been decoupled from the effect of stratification resulting from trapping internal residuals. It was shown that trapping internal residuals using NVO introduces noticeable thermal and compositional stratification. It was found that this stratification resulted in a 30% increase in burn duration compared to PVO operation, under the conditions studied. It must be noted that in order to achieve similar combustion phasing with PVO (compared to NVO) the intake needs to be heated significantly, which might not be practical in certain applications such as automotive engines, where NVO would be the strategy of choice for naturally aspirated HCCI operation.

Using reaction-space analysis and by applying the sequential CFD-multi-zone model as a diagnostic tool, it was shown for the first time, in this work, that under PFI conditions, it is the thermal stratification that determines reactivity stratification and ultimately burn duration; compositional stratification from NVO operation does not have a significant impact on combustion characteristics.

One important caveat in these conclusions is the assumption of flameless combustion. Since all of the current work has been performed using RANS, it is not possible to describe small scale fluctuations in temperature and composition which could lead to gradients and possibly local flames. This is a limitation of the current state of the art in CFD simulation, and as LES methods are improved concurrently with advances in computational hardware, higher fidelity simulations such as LES and DNS might provide better insights into the existence of flames under stratified HCCI conditions.

7.1.4 Impact of fueling strategy

It was found that under NVO conditions, direct injection into the residuals results in significant ϕ_{FO} stratification prior to ignition. The shorter intake event with NVO operation (compared to PVO operation) also contributes to the high levels of fuel unmixedness prior to ignition due to lower turbulent kinetic energy available for mixing. With direct injection into hot residuals, there is a significant distribution in ϕ_{FO} that is positively correlated to the temperature distribution. However, the higher level of stratification in ϕ_{FO} from direct injection into the residuals *does not* result in an increase in burn duration compared to premixed fueling, since direct injection into the hot residuals cools down the hottest regions of the charge. To compensate for this and to match ignition timing with the corresponding premixed (PFI) case, the intake temperature (representing the coldest regions of the charge at IVC) needs to be increased. This results in an overall reduction in thermal stratification for NVO-DI operation compared to NVO-PFI operation. The lower thermal stratification, under the conditions studied, counters the added reactivity stratification caused by the ϕ_{FO}distribution from direct injection, which results in the overall reactivity stratification prior to ignition being similar for the two fueling strategies under NVO operation. This results in similar overall HCCI burn duration.

The stratification in ϕ_{FO}caused by insufficient mixing of the fuel with the rest of the charge, arising from direct injection of fuel into the residuals, results in significant pockets of the charge burning less dilute than the mean dilution levels, which in turn results in an order of magnitude increase in NOx emissions when compared to the premixed fueling case for the same ignition timing (due to higher local post-combustion temperatures for the case with direct injection into the residuals). These findings suggest that under conditions where NOx emissions are unexpectedly high with DI during NVO, it may be worthwhile to try PFI fueling in an attempt to reduce potential stratification and NOx.

Under PVO conditions with direct injection, there is better mixing of the fuel with the rest of the charge, resulting in overall low levels of ϕ_{FO}stratification. This is due to due to the longer intake event compared to NVO operation. There is no significant difference in burn duration and emissions with direct injection compared to premixed operation when PVO valve lifts are used.

7.2 Development of a sequential CFD-MZ approach as a diagnostic

In order to probe beyond CFD simulations, a quasi-dimensional, balloon model was developed as a precise diagnostic tool to effectively decouple concurrent effects such as thermal stratification and compositional stratification. This tool is intended to be used in conjunction with CFD. A non-reacting CFD simulation under a certain operating condition is performed up to a certain point prior to ignition after which the reaction space within the CFD domain is mapped onto the balloon model developed. Even though this is not the first implementation of a sequential CFD-MZ tool, the approach followed in this work (wherein this tool is used to decouple concurrent effects) is novel and yielded considerable insights into the individual effects of thermal and compositional

stratification as well as the effect of thermodynamic properties versus chemical kinetic properties on HCCI burn duration.

7.3 Thermal stratification methodology for simple combustion models

A simplified predictive HCCI combustion model for use in system-level codes was developed that can simulate a wide range of HCCI operating conditions under PVO operation. For PVO operation, wall-driven thermal stratification is the primary contributor to reactivity stratification, sequential autoignition and ultimately burn duration.

Prior to this work there did not exist any simplified method to capture wall heat loss driven thermal stratification that had been evaluated against more detailed CFD simulations. In this work, a computationally efficient method to capture wall-driven thermal stratification is developed using fundamental thermodynamic considerations and adiabatic core temperature calculations. This method requires only a single non-reacting CFD simulation to be performed in order to determine the heat loss multipliers for a balloon-type multi-zone HCCI combustion model. The reasoning is that thermal stratification characteristics of an engine are primarily a function of engine design and not operating conditions. These multipliers are then used unchanged over a wide range of engine operating conditions, and show good agreement with CFD predictions of thermal stratification and in-cylinder pressure traces. It must be noted, that even with this thermal stratification methodology, the efforts associated with constructing a CFD mesh are not avoided, since a baseline CFD simulation is required to develop the heat loss multipliers. However, significant computational efforts might be saved by not having to perform a CFD simulation *under every* condition.

It was indicated that the computationally efficient methodology to capture thermal stratification within the cylinder without expensive CFD simulation need not be restricted

to combustion models with chemical kinetics. Even simpler correlation-based combustion models can also stand to benefit from this methodology to better predict ignition timing and burn duration. Efforts to explore the use of the thermal stratification methodology within such correlation-based models is currently underway.

7.4 Standalone balloon multi-zone HCCI combustion model

A standalone balloon multi-zone HCCI combustion model was developed incorporating advanced numerics from LLNL to speed up computations. The thermal stratification methodology developed was incorporated into this multi-zone model and this model was then exercised on two engines with very different geometries. Predictions by this model compared well to CFD results while the computations were done up to two orders of magnitude faster than corresponding CFD simulations. This model also shows good agreement compared to boosted gasoline HCCI engine experiments, with PVO operation, over a range of conditions. This model was implemented into a commercial system-level simulation software called GT-Power, and has cycle simulation times on the order of minutes with a simple kinetic mechanism.

Additionally, this model may also be used to capture the impact of stratification effects on HCCI ignition more accurately by running with chemistry turned on only in the hottest zone. This sort of approach might be useful for even simpler HCCI combustion models that require accurate ignition prediction, after which an algebraic burn correlation is used to predict burn duration.

7.5 Recommendations for future work

Based on the understanding and insights developed in this doctoral work the following recommendations are made for future work:

- Higher fidelity simulations such as LES and DNS under NVO conditions would help develop a better understanding of the impact of NVO operation on thermal stratification, particularly with respect to the effect of small-scale fluctuations in the temperature field on overall burn duration.
- In this work it was shown that inhomogeneities caused by direct injection during NVO could result in significant increases in NO emissions. Higher fidelity spray models in conjunction with finer grid resolution and techniques such as LES might provide further insights into spray development and stratification prior to ignition. These insights might then be used to design advanced injectors that could facilitate better mixing.
- The effect of NVO operation under boosted conditions is also of great interest, particularly because of potential low temperature kinetics associated with gasoline at higher cylinder pressures. A study into the effects of NVO under boosted conditions could be performed with the current simulation tools and kinetic mechanisms as an extension to the studies in this doctoral work. Under boosted conditions, autoignition occurs more readily, and eEGR is typically used to phase combustion rather than iEGR (achieved using NVO) or intake air heating. This work has shown that NVO increases thermal stratification and in turn has significant potential to increase burn duration. Under boosted conditions, NVO could potentially be used to control burn duration rather than just combustion phasing. Since an increase in NVO to increase burn duration would also advance combustion phasing, eEGR could be used in conjunction with iEGR to compensate for the advance in combustion phasing from increasing NVO and thus maintain the desired combustion phasing under boosted conditions.
- A simplified correlation to capture the effect of NVO operation on thermal stratification at IVC and the subsequent evolution of this distribution as a result of

thermal mixing through the compression stroke could be developed for use in simplified combustion models, such as the one developed in this work.

7.6 References

1. He, X., Donovan, M. T., Zigler, B. T., Palmer, T. R., Walton, S. M., Wooldridge, M. S., and Atreya, A., "An experimental and modeling study of iso-octane ignition delay times under homogeneous charge compression ignition conditions," *Combustion and Flame*, Vol. 142, pp. 266-275, 2005.

2. Dec, J. E., Sjöberg, M., and Hwang, W., "Isolating the Effects of EGR on HCCI Heat-Release Rates and NOx Emissions," SAE Paper 2009-01-2665, 2009.